Scuola Internazionale Superiore di Studi Avanzati - Trieste

Clues on the physics of AGN through X-ray spectral, temporal and polarimetric analysis

Elias S. Kammoun

Scuola Internazionale Superiore di Studi Avanzati

A thesis submitted for the degree of

Philosophiæ Doctor

September 2018

SISSA - Via Bonomea 265 - 34136 TRIESTE - ITALY

Supervisor: Prof. Annalisa Celotti (SISSA)
Co-supervisor: Prof. Guido Risaliti (University of Florence)

Main Collaborators:
Prof. Iossif Papadakis (University of Crete)
Dr. Emanuele Nardini (INAF - Arcetri Astrophysical Observatory)
Dr. Michal Dovčiak (Astronomical Institute of the Czech Academy of Sciences)
Dr. Frédéric Marin (University of Strasbourg)

This thesis is dedicated to
some special people
for some special reasons

Prelude

This is not intended to be an acknowledgement in the traditional sense. It is more like a "re-flexion" on the last four years (and beyond). This PhD has changed me, from different perspectives. It made me revisit all my points of view on life, politics, economics, science, philosophy, music, etc... It taught me to seek Completeness instead of Perfection.

Astronomy was, still is, and I hope will continue to be, one of my main passions, since childhood. However, I learned that as any field that involves human beings, it gets more interesting, it gains a new dimension, and may also get tougher. It becomes closer to politics, including all the good and bad aspects. Here comes the role of colleagues, collaborators and supervisors who added various flavours to my experience. They taught me that science cannot and should not be an individualist field. The wise, clear and hard-worker Sifis who I consider my "Astronomy Godfather" and has accompanied me through my carrer since 2013. Collaborating with him is always a pleasure and a great occasion to learn, explore new ways and approaches, looking at things from various points of view. The calm, precise and patient Ema who taught me how to win the fight in the jungle of spectral fits, how to present things in the most complete, detailed and clear way, trying to be always on the safe objective side of science. The busy Guido, with whom it was always great to work (mainly when I visited him in Firenze), discuss new ideas and projects (oops! Some of them are still pending), and who taught me the diplomatic way of doing science (known as the Italian way). Annalisa, who was always there, supportive, despite everything, and could reserve an irreplaceable place for herself. I have learned that science is not only about science but mainly: funds, management, networking, travelling, connections, depression and some bursts of happiness.

Moving to a new society/culture was not that smooth. It needed some compromise, flexibility, and some "surfing" skills. This movement (was totally needed) maturated me on the personal and professional sides. I was introduced to new lifestyles, cultures, habits, ways of thinking, ways of expressing. This cultural exchange is enriching for all the involved parties, which is a thing that "anti-immigration" people do not (want to) consider. This enrichment was amplified by two major factors: 1) friends, 2) travelling. Regarding the first point, I succeeded in building strong friendships that went much beyond a relation between officemates.

All these “crazy” discussions with Gor, meetings in the evening in S.d.F. and V.B. gave an additional dimension to life here, sharing science, sad and happy moments, smart and stupid thoughts, lovely and bad memories, and some hope for the future. Franca; with her wondering eyes, most of the time unsatisfied and trying always to find a meaning in things; Andrej; with his (a bit) conservative scientific attitude and his light presence, trying to reduce accurately all possible errors (good luck with that!); Ricky; with his organized chaos, full of energy and ambition, dreaming about a new world that starts with the independence of Sardinia; all of you guys made these years valuable! As for the friends who are elsewhere, and are many, you should know (but I am sure that you already know) that life would be much harder without your touch (each one of you knows how), especially Alfred, Antoine, Bachar, Joelle, Rim and Rita J. H.. As for the travelling part, I should stress on the effect of two islands that I visited which influenced my view on life and made me reconsider many steps. I mean the authentic Sardinia, more specifically a small beautiful island within the island of Sardinia: The Murgia-Pillosu family, who I consider as a second family for me! The second island is the welcoming Crete which uncovered to me many hidden facts in life that I was not aware of.

Finally, “Love in the time of *PhD*”, well.. let’s not talk in detail about it (“it is beyond the scope of this section”). Briefly, it is hard but much needed! However, the most robust love is the unconditional love of my family, who supported me continuously through all these years, through all the tough and happy moments. I could not accomplish things, the way I did, without them.

Abstract

X-ray emission of active galactic nuclei (AGN) can be considered as a powerful probe of the close environment of supermassive black holes (SMBHs), at the centres of these objects. The X-ray properties of AGN are studied in this dissertation, addressing several open questions in AGN physics:

- the properties of the X-ray corona in AGN (its nature and geometry) ,
- the presence of a population of thermal non-relativistic electrons,
- probing general relativity in the strong-field regime, addressing especially the possibility of estimating accurately the SMBH spin in AGN, through the identification of relativistic reflection features in their X-ray spectra and polarization signal,
- the nature of variability in X-ray light curves, and the identification of the different physical components contributing to it.

In this dissertation, I shed light on these topics by

- Analysing the X-ray spectra and light curves of individual sources, using simultaneous *XMM-Newton* and *NuSTAR* observations. These simultaneous observations can provide the highest signal-to-noise data in the $\sim 0.3-79$ keV band which can be achieved with the current X-ray observatories. By covering the broad X-ray band, *XMM-Newton* (in the 0.3–10 keV) and *NuSTAR* (in the 3–79 keV) allow us to determine with a high precision the various spectral and physical properties of low- and high-redshift AGNs, as well as to identify the various spectral components responsible of the emission in these sources, and study their temporal evolution.
- Simulating high S/N spectra of local AGN, using the instrumental responses of *XMM-Newton* and *NuSTAR*, and assuming a generic model for the X-ray emission in AGN, in order to test the reliability of spin measurements which can be achieved with current instruments.

- Predicting the theoretical spectral and polarimetric signatures of X-ray eclipses, by broad-line region (BLR), clouds which can be used in order to probe the signal arising from the innermost regions of the accretion disc.

Most of the work discussed in this dissertation has already been published in refereed journals.

Chapter 2: Parts of this chapter are published as:

Coronal properties of the luminous radio-quiet quasar QSO B2202-209, **Kammoun, E. S.**, Risaliti, G., Stern D., et al., 2017, MNRAS, 465, 4665.

Bulk Comptonization: new hints from the luminous blazar 4C+25.05, **Kammoun, E. S.**, Nardini, E., Risaliti, G., Ghisellini G., Behar, E. and Celotti, A., MNRAS, 473, L89.

Chapter 3: *Testing the accuracy of reflection-based supermassive black hole spin measurements in AGN*, **Kammoun, E. S.**, Nardini, E., Risaliti, G. 2018, A&A, 614, A44

Chapter 4: *The nature of X-ray spectral variability in MCG-6-30-15*, **Kammoun, E. S.**, Papadakis, I. E., 2017, MNRAS, 472, 3131.

Chapter 5: *Spectral and polarimetric signatures of X-ray obscuration events in AGN*, **Kammoun, E. S.**, Marin, F., Dovčiak, M., Nardini, E., Risaliti, G. and Sanfrutos M., 2018, MNRAS, 480, 3243.

Contents

List of Figures

List of Tables

Beiteddine Opening

https://open.spotify.com/track/0oUb8tMuRKjegiTIGVg3cI

Ziad Rahbany

1 Introduction

Contents

The term Active Galactic Nuclei (AGN) is attributed to the compact regions in galactic centres revealing energetic phenomena which cannot be related obviously to stellar activity. The emission from the central region of an active galaxy can be brighter than the combined emission from all stars in the host galaxy (i.e $\sim 10^{11}\,L_{\odot}$) by a factor of 100 or more. The emission from an AGN covers the whole electromagnetic spectrum, from radio waves to gamma-rays. The overall shape of the AGN spectral energy distribution (SED) is different from the one of a normal galaxy as shown in figure 1.1. AGN show a strong variability in brightness over different timescales which is not seen in normal galaxies.

The first spectrum of an AGN was obtained, in the optical range, at the Lick Observatory for the nebula NGC 1068 by Fath (1909) who noted the presence of strong emission lines. A few years later, Slipher (1917) at Lowell Observatory observed the same nebula at higher spectral resolution. He was able to resolve the emission lines and reported a line-width of hundreds km/s. Hubble (1926) noted,

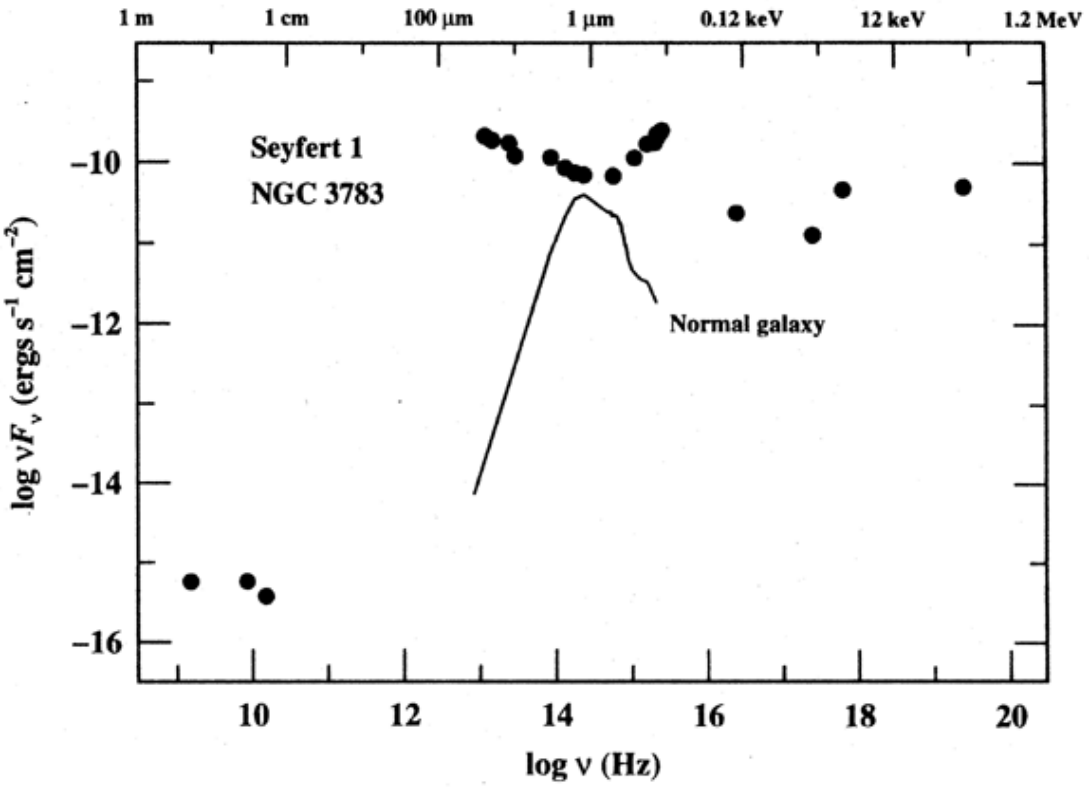

Figure 1.1: The spectral energy distribution (SED), from radio waves to gamma-rays, of the Seyfert 1 galaxy NGC 3783. The SED of a normal galaxy is also shown for comparison. Figure 1.3 in Peterson (1997).

in a study of extragalactic nebulae, strong emission-line spectra of three galaxies: NGC 1068, NGC 4051, and NGC 4151. Seyfert (1943) was the first to identify a class of spiral galaxies having high nuclear surface brightness (stellar-appearing cores). Seyfert found that the optical spectra of these galaxies are characterized by strong nuclear emission lines with a broadness up to 8500 km/s (full width at zero intensity). These galaxies are now known as Seyfert galaxies.

In the late 1950s, quasi-stellar radio sources, later shortened to quasars, were originally discovered as a result of the first radio surveys of the sky. In 1963, Maarten Schmidt was the first to realise that the emission lines in the spectrum of the radio source 3C273, which first did not appear to match any known chemical elements, could be easily interpreted as redshifted Hydrogen lines with a redshift 0.16 (Schmidt 1963). He later studied a large number of quasars and defined their properties as star-like objects identified with radio sources showing broad emission lines, large UV flux, time variability, and found at then-large redshifts (up to 2.37 for 4C25.5; Schmidt & Olsen 1968). As the number of known quasars increased, greater redshifts were identified, and the highest redshift quasar observed to date is ULAS J1342+0928 at $z = 7.54$ (Bañados et al. 2018).

1.1 Black Holes

The current paradigm, or working model, for the AGN phenomenon explains their large inferred luminosity (bolometric luminosity $L_{\rm bol} \sim 10^{9-15}\,L_{\odot}$), as the result of converting the gravitational energy into radiation due to matter falling onto a supermassive compact object of mass $M \sim 10^6 - 10^9 {\rm M}_{\odot}$ (presumably a supermassive black hole, hereafter SMBH). This hypothesis was first introduced by Salpeter (1964), Zel'dovich (1964) and Lynden-Bell (1969). However, the origin of these SMBHs, which are thought to be present at the centres of most galaxies, is not known yet. It is now thought that the engine powering AGN is an accretion disc of gaseous matter spiralling into the gravitational well of the central compact object, through dissipative processes (whose nature remains uncertain), whence it heats up and releases part of its gravitational potential energy into radiation (Shakura & Sunyaev 1973; Novikov & Thorne 1973). In this context, many arguments favour the BH paradigm with respect to other more complicated models based on some stellar precesses that have been proposed in the past. The main arguments can be summarised as follows:

- The release of gravitational energy via accretion can be up to ~ 10 times more efficient (see later for more details) than thermonuclear fusion powering stars. This can explain easily the large luminosities inferred in AGN.

- Standard accretion disc theory (e.g. Shakura & Sunyaev 1973) predicts a peak in the spectrum of the emitted radiation at ultraviolet (UV) wavelengths, assuming SMBH, which is thought to be related to a commonly observed UV feature in the SED of AGN known as the "big blue bump" (see Section 1.3 for more details).

- The BH paradigm by its nature explains intuitively the compactness of, in particular, the X-ray emitting region in AGN deduced from the rapid variability (on timescale of a few 100 seconds) which is observed in their X-ray flux (see Section 1.4 for more details).

Considering a non-rotating central mass M, it is convenient to describe its basic properties using the gravitational radius $r_{\rm g} = GM/c^2$, where G is the gravitational constant, and c is the speed of light. The event horizon, which corresponds to $2r_{\rm g}$ for a non-rotating BH, is the distance below which the gravitational forces require an escape velocity that exceeds the speed of light. The rotating (Kerr) BHs are described using the dimensionless spin parameter, $a^* = Jc/GM^2$, where J is the

angular momentum of the rotation BH which a black hole acquires from its growth history. This parameter is arguably one of the most interesting parameters as it affects the Kerr metrics leading to various properties of astrophysical importance. Theoretically, the spin values range in the [-0.998, 0.998] interval (Thorne 1974). These limits are found without considering magnetohydrodynamics effects. In fact, the magnetic fields of the plunging regions should give rise to torques that tend to reduce the maximum spin ($\sim 0.9 - 0.95$) that can be achieved by a black hole (e.g. Gammie et al. 2004; McKinney & Gammie 2004).

In order to avoid infall, the outward force of radiation pressure has to be counterbalanced by the inward gravitational force. This leads to the definition of the Eddington luminosity,

$$L_{\rm Edd} = \frac{4\pi G c m_{\rm p}}{\sigma_{\rm e}} M \tag{1.1}$$

of a source of mass M, where $m_{\rm p}$ is the proton mass and $\sigma_{\rm e} \simeq 6.65 \times 10^{-25}\,{\rm cm}^2$ is the Thomson scattering cross-section.

The fundamental process in AGN is the conversion of rest mass to electromagnetic radiation due to the infall of a particle from infinity to the innermost stable circular orbit (ISCO), beyond which this particle loses its orbital motion and falls directly into the event horizon. This conversion is done with an efficiency η. Thus, the energy available for a mass M is

$$E = \eta M c^2 \tag{1.2}$$

It should be noted that the efficiency parameter η depends only on the BH properties, assuming all the gravitational energy is converted to electromagnetic radiation. However, there are other cases in which a part of this energy is advected into the BH, thus decreasing the efficiency of the radiation process. Equation (1.2) implies that the rate (L) at which the energy is emitted can be related to the mass accretion rate ($\dot{M}$) by the nuclear source:

$$L = \frac{dE}{dt} = \eta \left(\frac{dM}{dt}\right) c^2 = \eta \dot{M} c^2 \tag{1.3}$$

One can identify the Eddington accretion rate $\dot{M}_{\rm Edd}$ which is the mass accretion rate necessary to power an AGN radiating at the Eddington luminosity $L_{\rm Edd}$,

$$\dot{M}_{\rm Edd} = \frac{L_{\rm Edd}}{\eta c^2} \tag{1.4}$$

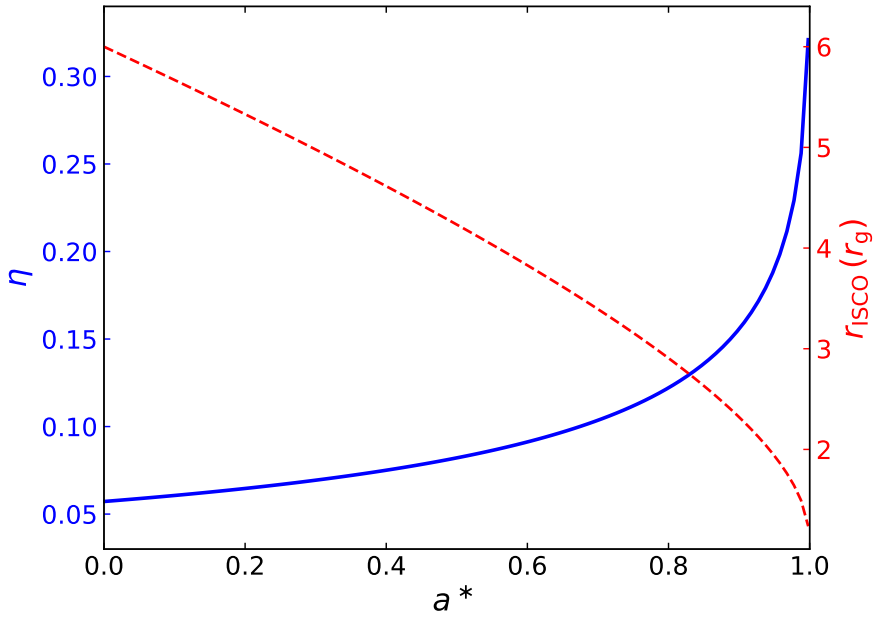

Figure 1.2: Efficiency parameter η (blue) and ISCO position $r_{\rm ISCO}$ (red) as function of the spin parameter a^*.

This value represents the maximum possible accretion rate for a mass M in a spherical accretion. However, this limit can be exceeded with non-spherical models (e.g. equatorial accretion in a disc).

General relativity enables us to calculate the orbits of particles in the vicinity of stationary and rotating BHs. In particular, it allows us to solve for the location of the ISCO. The exact value of $r_{\rm ISCO}$ depends on the value of a^*. The position of the ISCO, in units of $r_{\rm g}$, for an equatorial disc is given by Bardeen et al. (1972):

$$r_{\rm ISCO} = 3 + Z_2 - \left[(3 - Z_1)(3 + Z_1 + 2Z_2)\right]^{1/2} \tag{1.5}$$

where $Z_1 = 1 + (1-a^{*2})^{1/3}\left[(1+a^*)^{1/3} + (1-a^*)^{1/3}\right]$, $Z_2 = \left(3a^{*2} + Z_1^2\right)^{1/2}$ (plotted in Figure 1.2). Hence, for an ISCO at a normalized radius $x = r_{\rm ISCO}/r_{\rm g}$, the general relativistic approximation of the relationship between η and x is,

$$\eta = 1 - \left[1 - \frac{2}{3x}\right]^{1/2} \tag{1.6}$$

Figure 1.2 shows the dependence of η on the spin parameter.

1.1.1 SMBH spins

Measurements of SMBH spins are a key ingredient for understanding the physical processes on scales ranging from the accretion disc out to the host galaxy. In fact,

the spin determines the position of the ISCO of the accretion disc and of the event horizon, which are 1.24 and 1.06 r_g for a maximally rotating black hole, and 6 and 2 r_g for a non-spinning black hole, respectively. Hence, it has been shown that for a Schwarzschild black hole ($a^* = 0$) half of the energy is radiated within $\sim 30\, r_g$, while half of the radiation emerges from within $\sim 5\, r_g$ for a rapidly spinning black hole (e.g. Thorne 1974; Agol & Krolik 2000). This leads to an increase of the radiative accretion efficiency from $\eta = 0.057$ for $a^* = 0$, to 0.32 for $a^* = 0.998$ (see Figure 1.2). Vasudevan et al. (2016) assumed a toy model with a bimodal spin distribution and showed that a SMBH population where only 15% of the sources are maximally rotating can produce 50% of the cosmic X-ray background (CXB) owing to their high radiative efficiency. Moreover, these authors showed that the spin bias is even larger in flux-limited surveys, since half of the CXB can be accounted for if only 7% of the sources have a spin of 0.998 (see also Brenneman et al. 2011).

The SMBH spin distribution is also fundamental for understanding the SMBH-host galaxy co-evolution. In fact, the angular momentum of a black hole matures over cosmic time and its final value is determined by the accretion and merger history of the galaxy. For instance, mergers tend to spin down the black hole (Volonteri et al. 2013), while the SMBH spins up through prograde accretion of material through the galactic disc (King et al. 2008). Spin measurements are also important in order to understand the astrophysical consequences of spin and, particularly, to give observational support to theoretical notions such as the spin-driving of relativistic jets (Blandford & Znajek 1977), which are observed in some AGN. Relativistic jets are one of the main indicators of AGN feedback which, in addition to the high radiative efficiency, seems to play a crucial role in the evolution of the host galaxy and its star formation history. Hence, understanding the growth of SMBHs and their spin distribution is a key point for our understanding of the larger scale structure of the Universe (see Fabian 2012, for a review about AGN feedback).

In addition to the importance of SMBH spin in cosmology and galaxy evolution, the nuclear regions in AGN can be considered as unique laboratories to directly test the effects of general relativity in its strong-field regime, which manifest themselves as extreme physical phenomena such as light bending (e.g. Miniutti & Fabian 2004) and reverberation lags (e.g. Fabian et al. 2009; Emmanoulopoulos et al. 2011a; Kara et al. 2016, see Section 1.4 for more details). This requires a characterisation, with high precision, of signals from within a few gravitational radii of the BH, which can be achieved mainly via high-quality X-ray observations. In fact, AGN are strong X-ray emitters and it is widely accepted that the X-rays arise, from the innermost regions of the accretion disc, due to the Comptonization of UV disc photons by

a hot ($\sim 10^9$ K) transrelativistic medium, usually referred to as the X-ray corona (e.g. Shapiro et al. 1976; Haardt & Maraschi 1993; Petrucci et al. 2001a,b, see Section 1.4 for more details about the X-ray emission in AGN). As the measure of the spin is strongly dependent on the irradiation and subsequent emissivity of the disc, its success is tightly connected to the study of the X-ray corona itself, whose nature and properties are still largely unknown.

1.2 Classes of AGN and unified model

The classification of AGN is based on their observational properties. This classification has evolved significantly due to the higher-quality observations and the better understanding of the physical processes in these sources.

Seyfert galaxies are low-luminosity AGN, with a B-band magnitude $M_B > -23$ (Véron-Cetty & Véron 2003), that have stellar-like nuclei but the host galaxies are clearly detectable. These AGN are classified as radio-quiet AGN [1]. The spectra of these galaxies reveal the presence of strong high-ionization emission lines. Seyfert galaxies are divided into two main subclasses, known as Type-1 and Type-2. Two kinds of emission lines characterize the Type-1 Seyfert galaxies (or Seyfert-1 galaxies). These lines can be superposed on one another. The first are narrow lines (e.g. [O III] λ5007) that have widths on the order of 100 km/s and are characteristic of low-density ionized gas (electron density $n_e \simeq 10^3 - 10^6\,\mathrm{cm}^{-3}$) which defines the narrow-line region (NLR). The low density property of the gas allows forbidden-line transitions to occur instead of collisionally suppressed transitions. The second are the broad lines but seen as permitted-line transitions (e.g. Hα, Hβ) only. These lines have widths up to 10^4 km/s. The absence of broad forbidden-lines indicates that the broad line emission occurs in a high density gas ($n_\mathrm{e} \gtrsim 10^9\,\mathrm{cm}^{-3}$) which defines the broad-line region (BLR). Type-2 Seyfert galaxies differ from the Seyfert-1 galaxies in that only narrow (forbidden and permitted) lines are observed in their spectra. In addition to emission lines, weak absorption lines related to the presence of late-type giant stars in the host galaxy can be observed in both Seyfert 1 and 2 spectra. An interesting subclass of Seyfert-1 galaxies is the Narrow-Line Seyfert-1 (NLS1) galaxies characterized by "narrow" broad lines (FWHM$_{H\beta} < 2000$ km/s), weak forbidden lines with a flux ratio [O III]/H$\beta_{total} < 3$, and strong Fe II emission in the optical/UV (Osterbrock & Pogge 1985; Goodrich 1989).

[1] Radio-quiet/loud AGN are characterized by the radio loudness factor $R = F(5\mathrm{GHz})/\mathrm{F(B)}$ being smaller or larger than 10, respectively (where $F(5\mathrm{GHz})$ is the radio flux at 5GHz and $F(\mathrm{B})$ is the optical B-band (~ 4400 Å) flux) and radio powers $P_{1.4\mathrm{GHz}}$ that are smaller or larger than $10^{24}\mathrm{W\,Hz}^{-1}$, respectively.

Quasars consist of the most luminous subclass of AGN, their B-band magnitude is less than −23 (Véron-Cetty & Véron 2003). In the X-ray band, the approximate dividing line is that quasars have a $2.0 - 10.0\,\mathrm{keV}$ luminosity L_X greater than $\sim 10^{44}\,\mathrm{erg\,s^{-1}}$, whereas the luminosity of Seyfert galaxies is lower than this (Loaring et al. 2003). Nowadays, the term quasar is used interchangeably for both radio-loud and radio-quiet sources[2], in spite of the fact that only around 10% of quasars are strong radio sources that originally defined the quasar class (e.g. Padovani 2011). Using high-resolution observations, astronomers were able to resolve low-redshift quasars ($z < 0.5$) and study their host galaxies (Karhunen et al. 2014).

Another class of AGN is the Low-Ionization Nuclear Emission-lines Region galaxies (LINERs) identified by Heckman (1980). Their spectra resemble those of Seyfert 2 galaxies, except that the low ionization lines like [O I] λ6300, and [N II] $\lambda\lambda$66548,6583 are relatively strong. LINERs are very common and might be present in a large fraction of nearby spiral galaxies (Ho et al. 1997).

Another group of AGN known as "blazars" includes highly variable (on timescales as short as a few minutes in γ-rays) core-dominated radio-loud sources emitting polarized light (observed so far in the radio and optical ranges), in which a jet is aligned closely along the observed line of sight (Blandford & Rees 1978). Blazars are characterised by one or more of the following properties:

1. Intense, variable γ-ray emission (with $L_\gamma \sim 10^{44-48}\,\mathrm{erg\,s^{-1}}$).
2. Intense, variable radio emission associated with a flat radio spectrum and, occasionally, superluminal motion (with a radio power $\sim 10^{43-46}\,\mathrm{erg\,s^{-1}}$).
3. Radio, X-ray, and/or γ-ray jets revealing a relativistic motion.
4. A double-peak SED with a lower-frequency peak at radio-to-X-ray energies and a high-frequency peak at X-ray-to-γ-ray energies (see next section for more details).

Blazars can be divided into BL Lacertae (BL-Lac) objects (after the first source of this type that showed, for years, no sign of emission lines) and flat-spectrum radio quasars (FRSQs). The distinction between BL-Lacs and FRSQs is "historically" based on whether any optical broad emission lines have rest-frame equivalent width below (in the case of BL-Lacs) or above (in the case of FRSQs) 5 Å(e.g. Stickel et al. 1991; Urry & Padovani 1995).

[2]Historically the term "quasi-stellar objects" (QSO) was used to refer to radio-quiet sources, while "quasar" was reserved for radio-loud quasi-stellar sources.

The physical distinction between the two types of blazars is suspected to be caused by the divergent natures of their accretion flows (Maraschi & Tavecchio 2003; Ghisellini & Tavecchio 2008). FSRQs are thought to host geometrically-thin, optically-thick accretion discs that are accreting with Eddington ratios ($L/L_{\rm Edd}$) larger than 0.1. Their optical spectra reveal the presence of broad emission lines from high-velocity clouds, while their infrared spectra show a strong emission from dusty torii. Instead, BL-Lacs are thought to accrete through geometrically-thick, optically-thin accretion discs, in a radiatively inefficient way (e.g. Narayan & Yi 1994), having low Eddington ratios of the order of 0.01. The lack of broad emission lines and dust emission in these objects suggests that the structure of the surrounding medium and the properties of the accretion flow are physically different from FSRQs. Ghisellini et al. (2011) suggested a new classification scheme in order to distinguish between FSRQs and BL-Lacs, based on a physical property of the source. They suggested a definition based on the luminosity of the broad emission lines, normalized to the corresponding Eddington luminosity, with a threshold of $L_{\rm BLR}/L_{\rm Edd} \sim 5 \times 10^{-4}$.

Recently, Padovani (2017) noted that the old classification of radio-quiet and radio-loud AGN may be misleading. The author points out the fact that the classical distinction that is based on the radio loudness (R) or radio power is valid only for broad-line unobsucured AGN. R can be used in quasar samples, where one can safely assume that the optical emission is a proxy of the accretion disc and therefore the radio-to-optical flux density ratio represents a measurement of the jet radio emission as compared to the disc emission. However, the jet-disc ratio cannot act as a measurement of the jet strength if the optical band is dominated by jet emission or by the host galaxy. Moreover, in the case of Seyfert galaxies, the spatial resolution of the optical and radio observations can affect the value of R. In fact, most Seyfert 1 galaxies would be radio loud, by considering their nuclear luminosities. This create more confusion for the classification (Ho & Peng 2001). Thus, Padovani argues that the main and most simple difference between the two AGN classes is a fundamental *physical* one: the presence (or absence) of a strong relativistic jet. Based on this, he suggested "new and better" names: jetted and non-jetted AGN. Hence, I will use hereafter, in this dissertation, the jetted and non-jetted classification referring to the classically classified radio-loud and radio-quiet AGN, respectively.

Unified Model

In order to explain the variety of AGN, Antonucci (1993) proposed a "Unified Model". It is believed that the dichotomy between Type-1 and Type-2 AGN depends on the vantage point. Antonucci & Miller (1985) found the first evidence

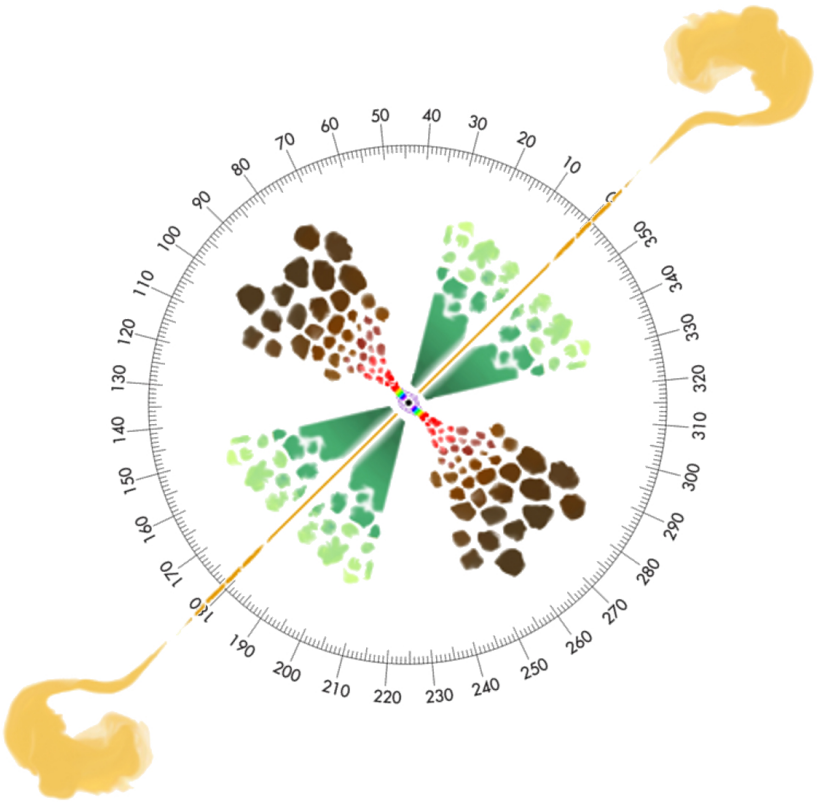

Figure 1.3: Unscaled sketch of the AGN unification theory. A type-1 AGN is seen at inclinations 0-60° while a type-2 AGN is seen at 60–90°, approximately. Color code: the central supermassive black hole is in black, the surrounding X-ray corona is in violet, the multi-temperature accretion disk is shown with the color pattern of a rainbow, the BLR is in red and light brown, the circumnuclear dust in dark brown, the polar ionized winds in dark green and the final extension of the NLR in yellow-green. A double-sided, kilo-parsec jet is added to account for radio-loud AGN (Figure 1 in Marin 2016).

for the unified model. They discovered a hidden Seyfert 1 nucleus in the Seyfert 2 NGC 1068 by polarization measurements.

The basic features of the current unified model, presented in Figure 1.3, are as follows: at the center of an AGN a SMBH is accreting matter through an accretion disc. This disc is surrounded by high-velocity broad-line clouds within a few light months of the center (spanning from 10^{-4} to 10^{-1} pc), from which the permitted lines are emitted. A massive, dusty, and optically thick equatorial molecular torus, whose radius is estimated between 10^{-1} and 10 pc, obscures the central regions. Hundreds of parsecs in extent, lies the low-density narrow-line emitting region in two ionization cones. If one is looking at the central source with low inclination (below $\sim 60°$), then no obscuration is present and both the broad and narrow line regions can be observed (Seyfert 1s). Looking through the torus, the observer will only see

the narrow line region clouds, the broad line regions will be obscured (Seyfert 2s). It should be noted that blazars are observed in the case when a jetted source is observed pole-on (its axis is nearly parallel to the line of sight). It should be also mentioned that several counter examples to the classical original unified model has been presented. For example, Bianchi et al. (2008) presented simultaneous X-ray and optical observations of the type-2 Seyfert NGC 3147 showing no absorption in X-rays, and an absence of broad lines in optical. A revision of the "classical" unified model is thus needed (see for a review, e.g. Netzer 2015).

1.3 AGN broad-band spectra

AGN spectra can range from radio waves to γ-rays. Broadband SEDs for different types of AGNs are shown in Figure 1.4. At energies below $\sim 100\,\mathrm{eV}$, two gaps can be seen. One gap is in the extreme ultraviolet (EUV) part and the other in the millimeter-wavelength regime (between $\sim 1\,\mathrm{cm}$ and $300\,\mu\mathrm{m}$). The 'EUV gap' is due mainly to the opacity of the ISM in our Galaxy (absorption by neutral Hydrogen). The 'millimeter gap' is due to the opacity of the Earth's atmosphere (caused by water vapour absorption) and a lack of sensitive detectors for wavelengths larger than $300\,\mu\mathrm{m}$.

The broadband spectrum of a non-jetted AGN can be divided into three major components: the big blue bump (BBB), the infrared bump, and the X-ray region:

- The BBB continuum component in AGNs extends from the near-infrared at ~ 1 μm up to the UV (~ 1000 Å). This component is attributed to thermal emission that originates from a geometrically thin, optically thick accretion disk (Shakura & Sunyaev 1973). More than half of the bolometric luminosity of an unobscured AGN is typically emitted in this spectral range. However, one of the most important observational problems is that a substantial part of the BBB cannot be observed as it falls within the EUV gap.

- The broad infrared bump extends from ~ 1 to ~ 100 μm. It is accepted that this feature arises from reprocessing of the BBB emission by dust with temperature ranging between ~ 10 and ~ 1800 K (e.g. Barvainis 1987; Sanders et al. 1989) located at a range of distance from the BH. The spectral dip at ~ 1 μm is then naturally explained by the finite sublimation temperature ($\sim$ 1800 K, for graphite grains) of dust. It should be noted also that the infrared bump does not show strong variability on short timescales (e.g. Hunt et al. 1994).

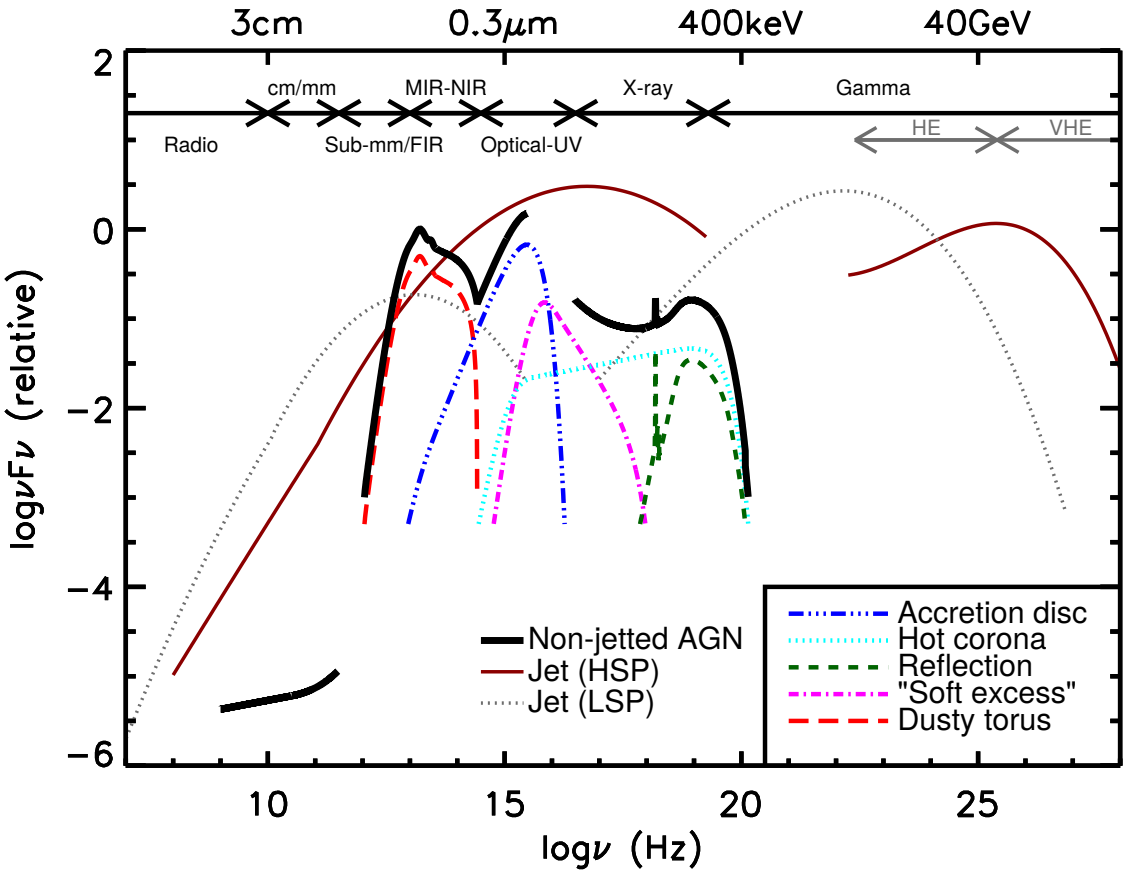

Figure 1.4: A schematic representation of an AGN spectral energy distribution (SED), based on the observed SEDs of non-jetted quasars. The black solid curve represents the total emission and the various coloured curves (shifted down for clarity) represent the individual components. The intrinsic shape of the SED in the mm-far infrared (FIR) regime is uncertain; however, it is widely believed to have a minimal contribution (to an overall galaxy SED) compared to star formation, except in the most intrinsically luminous quasars and powerful jetted AGN. The emission from the AGN accretion disk peaks in the UV region. The jet SED is also shown for a high synchrotron peaked blazar (HSP, based on the SED of Mrk 421) and a low synchrotron peaked blazar (LSP, based on the SED of 3C 454.3). Adapted from Harrison (2014) and Padovani (2017).

- In the X-ray band, the AGN spectrum can be well described by a power law with a spectral index ~ -0.9. It is accepted that this component is due to Compton upscattering of optical/UV photons, arising from the accretion disc, by hot electrons located in the vicinity of the BH (the X-ray emission in AGN is discussed with more details in the next section).

Broad-band SEDs of jetted AGN (shown in Figure 1.4) are dominated by two broad peaks one in the millimeter to near infrared range and one in the X-ray to γ-ray band. There are noticeable distinctions between the broadband SED of BL-Lac objects and FSRQs (high-synchrotron and low-synchrotron peaked quasars,

HSP and LSP, respectively). The former shows lower-luminosity, higher-energy peak emission extending up to several GeV. The high energy peak of the latter is typically in the MeV range. The peaked feature in the millimeter range is attributed to synchrotron emission from the jet. While the high-energy peaked feature is attributed to inverse Compton (IC) emission. This component can be emitted through two different channels at least: internal Compton and external Compton (EC). The former process is the case where the seed-scattered photons are the locally produced synchrotron photons (synchrotron-self Compton, SSC; e.g. Jones et al. 1974; Ghisellini et al. 1985). Such SSC sources show a very high energy Compton peak with a power-law spectrum of the same slope as the synchrotron source. However, the more powerful jets are probably dominated by external seed photons (EC sources). The external radiation field near the boosted core can be of high enough energy density to explain a very powerful IC bump. The dimension of the sub-parsec central radio source in such cases is similar to the typical dimension of the BLR and/or the molecular torus (e.g. Sikora et al. 1994, 2002). IC scattering of photons from the BLR or the torus can produce a high-luminosity, high-energy peak that has higher luminosity but lower frequency compared with the high-energy peak in BL-Lac objects. Other potentially important sources of external photons are the central accretion disk itself (e.g. Dermer et al. 1992), or from the cosmic microwave background at large scales (e.g. Böttcher et al. 2008; Celotti & Fabian 2004).

1.4 The X-ray spectrum of a non-jetted AGN

X-ray emission is a common property of AGN which radiate a considerable fraction of their bolometric luminosity in the 2–10 keV band ($\sim 10\%$ for an AGN radiation at $\lesssim 0.1\,L_{\rm Edd}$; e.g. Vasudevan & Fabian 2007).

X-ray flux variability in AGN is the largest among any of the observed wavelength ranges (e.g. McHardy 1989). This indicates that the X-ray emission arises from a very compact region. Assuming a variability timescale in the order of ~ 1 h accompanied by a change of the observed flux a factor of ~ 2, one can argue that during a phase of uniform brightening or dimming, the linear dimensions of the X-ray source cannot exceed the corresponding light crossing time. For a BH mass of $10^8\ M_\odot$, a variability of ~ 1 h would correspond to $\sim 7\ r_g$. This rough estimate has recently been confirmed by gravitational microlensing studies which suggest that the X-ray emitting source in some quasars may be as small as $\sim 10\ r_g$ (Chartas et al. 2009; Mosquera et al. 2013; Reis & Miller 2013). The production of X-rays requires a high-temperature medium, which, in addition to the rapid X-ray variability, is suggestive that the emitting region is compact, and located in the vicinity of the SMBH.

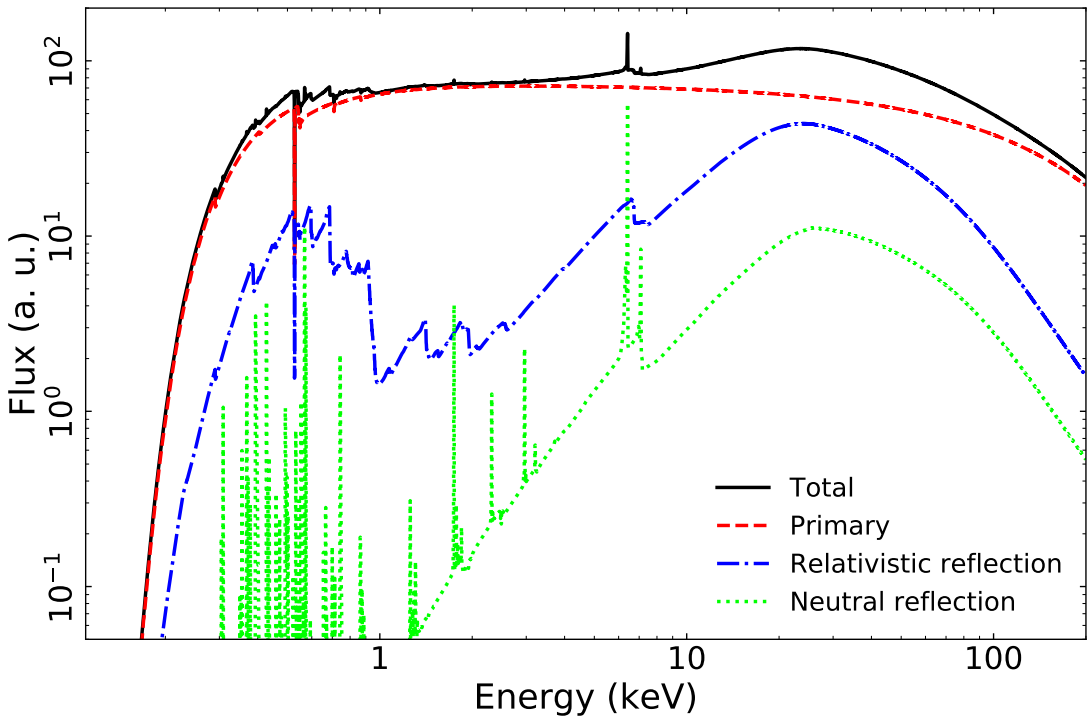

Figure 1.5: A schematic representation of a non-jetted AGN X-ray spectrum (taking into account Galactic absorption only). The black solid curve represents the total emission and the various coloured curves represent the individual components: the primary emission from the hot corona (red dashed line), the ionized blurred reflection (blue dash-dotted line) arising from an accretion disc with a constant ionisation parameter of $\log \xi = 2$, and distant neutral reflection (green dotted line).

1.4.1 The primary emission

It is generally thought that the hard X-ray continuum emission (known as the primary emission) arising around accreting black holes, is due to Compton up-scattering of UV/soft X-ray disc photons off a hot ($T_{\rm e} \sim 10^9$ K), trans-relativistic medium, usually referred to as the X-ray corona (e.g. Shapiro et al. 1976; Haardt & Maraschi 1993; Petrucci et al. 2001a,b). The Compton up-scattering of photons (with mean energy $\langle E \rangle$) by hot electrons occurs when $\langle E \rangle \lesssim 4kT_{\rm e}$. These electrons are thought to be heated and confined by magnetic fields emerging from the ionized accretion disc (e.g. Galeev et al. 1979; Haardt & Maraschi 1991). If the electron gas is optically thin, then the $y-$Compton[3] parameter is in the order of unity, and it can be shown that a power-law with a photon index of

$$\Gamma = \sqrt{\frac{9}{4} + \frac{4}{y}} - \frac{1}{2} \tag{1.7}$$

[3]The $y-$Compton parameter represents the total relative energy change of photons due to scattering. It's given by $y = \frac{4kT_{\rm e}}{m_{\rm e}c^2} \times \max(\tau, \tau^2)$, where τ is the optical depth of the medium and $m_{\rm e}$ is the electron mass.

can describe the emerging spectrum. If $y = 1$, then $\Gamma = 2$ which is comparable to what is commonly observed in non-jetted AGN. As the energy of the photons become comparable to the electron thermal energy, the photons cannot gain energy anymore, and a sharp cutoff is expected in the spectrum at $E_{\rm cut} \simeq 2 - 3kT_{\rm e}$ (see e.g. Petrucci et al. 2001a). As a result, the primary emission arising from the corona (red dashed line in Figure 1.5) can be well approximated by a power-law with a high-energy exponential cutoff of the form

$$F_{\rm prim}(E) = NE^{-\Gamma} \exp\left[-\frac{E}{E_{\rm cut}}\right].$$

The geometry (extended or point-like) and physics (thermal/nonthermal population of electrons, and its heating mechanism) of the X-ray source remain major uncertainties. Several models have been proposed:

- an extended, optically-thin region slab above a cold, optically-thick disc (Haardt & Maraschi 1991),
- a discrete, optically-thin blobs above an optically-thick disc that could be related to magnetic reconnection events which create hot flares above the accretion disc (e.g. Haardt et al. 1994; Nayakshin & Melia 1997),
- a hot accretion flow (e.g. Shapiro et al. 1976; Narayan & Yi 1994),
- a mildly relativistic electrons moving along the axis of a jet ("aborted jet" according to Ghisellini et al. 2004).

Non-jetted AGN show often a sharp rise above the aforementioned primary component, at energies below ~ 1 keV, referred to as the "Soft X-ray Excess" whose origin is still debated since its discovery in 1985 (Singh et al. 1985). The soft excess in many unabsorbed AGN could be fitted by a blackbody model with a best-fit temperature in the range 0.1-0.2 keV (Walter & Fink 1993, e,g), however, this temperature is significantly higher than the maximum temperatures expected in AGN accretion discs. It has been shown that the temperature associated with this region, if fitted by a blackbody model, is constant over a wide range of AGN luminosity and black hole mass (e.g. Walter & Fink 1993; Gierliński & Done 2004; Crummy et al. 2006), favouring an origin through atomic processes instead of purely continuum emission. Several scenarios were proposed in order to explain this feature. It was proposed, for example, that the excess arises due to ionized reflection with light bending, in which soft X-ray lines are relativistically blurred as they are produced very close to the BH (see next section for details; Miniutti &

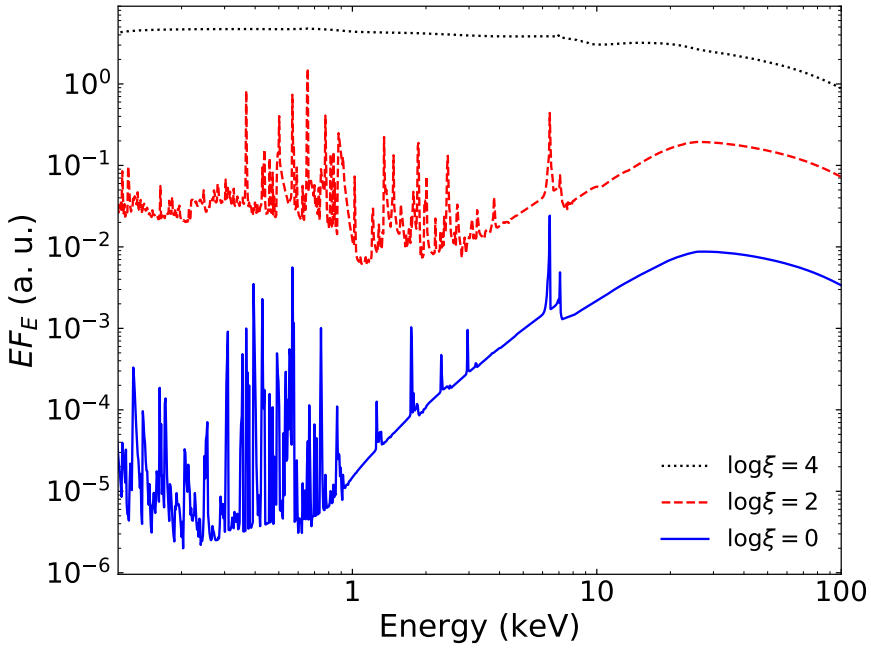

Figure 1.6: Effects of the ionisation level on the shape of the reflection spectra. The reflection spectra were estimated for disc ionisations $\log \xi = 0, 2, 4$ (blue solid, red dashed, black dotted lines, respectively) assuming a power-law primary with $\Gamma = 2$, solar abundance, and an inclination of 30°.

Fabian 2004; Crummy et al. 2006). It has also been proposed that the soft excess could arise from Compton up-scattering of disc photons, in a "warm" medium of an electron population with a temperature much lower and an optical depth much higher than those of the X-ray corona that are responsible for the emission at energies above 2 keV (e.g. Czerny & Elvis 1987; Magdziarz et al. 1998; Petrucci et al. 2013, 2018). It should be noted that both scenarios were able to give acceptable results in terms of spectral fitting.

1.4.2 X-ray reprocessing

In addition to being emitted in the direction of the observer, the primary emission will irradiate and be reprocessed by the accretion disc (e.g. George & Fabian 1991; Ross & Fabian 2005). X-rays incident on the disc will be subjected to Compton scattering by free or bound electrons, and photoelectric absorption followed either by Auger de-excitation or by fluorescent line emission (see e.g. Lightman & White 1988; George & Fabian 1991). The resulting spectrum is known as the reflection spectrum. The dotted and dash-dotted lines in Figure 1.5 represent the reflection spectra expected from ionised/relativistically blurred and neutral material, respectively. The reflection spectrum is characterized by:

- A soft emission due to bremsstrahlung from ionised elements as well a multitude of emission lines, that are prominent for low ionisation material.
- A prominent emission line at $\sim$ 6.4 keV, associated with the iron Kα (Fe Kα) emission line. The presence of strong Fe Kα emission is expected due to its abundance and high fluorescent yield[4]. The Fe Kα (and all emission lines) broadens as the material gets more ionised (see Figure 1.6). In fact, for high ionisation parameters[5], ξ, a significant part of the upper layer of the disc is ionised. Since the lines originate from deep layers of the disc which are more neutral, the emission lines escaping from the disc will be Compton up-scattered and broadened as they interact with the electrons in the upper ionised layers of the disc.
- An Fe K-shell absorption edge at $\sim$ 7 keV which is thought to be the result of an increase in the absorption cross-section for photons with energies larger than the binding energy of Fe K-shell electron.
- A broad component peaked at around 20–30 keV, known as 'Compton hump'. This feature is due to Compton scattering, as the absorption cross-section decreases with increasing energy. Furthermore, it is expected that photons with energies larger than $\sim$ 100 keV will loose a considerable amount of their energy as they escape from the slab upon being scattered down.

It should be noted that the accretion disc is not the only material able to reprocess the primary emission in AGN. Many sources reveal the presence of narrow Fe Kα emission lines (e.g. Bianchi et al. 2009) that could be explained by reflection from distant, dense material such as the BLR or the putative molecular torus invoked in AGN unification models (Ghisellini et al. 1994a).

Relativistic effects on the reprocessed spectrum

In the case of the accretion disc, special and general relativistic effects result in blurring the ionized reflection spectrum and asymmetrically broadening the emission lines owing to the gravitational redshift and the motion of the emitting particles in the disc (see Iwasawa et al. 1996; Fabian et al. 2000a; Miniutti & Fabian 2004; Iwasawa et al. 2004; Miniutti et al. 2007). Let us consider a single emission line, emitted from a rotating ring of the accretion disc:

[4] An element's fluorescent yield is defined as the probability in a particular atomic shell leads to a radiative transition rather than the ejection of an Auger electron.

[5] $\xi = 4\pi F_{\rm inc}/n_{\rm H}$ (in units of erg cm s^{-1}), where $F_{\rm inc}$ is the incident flux of the X-ray source, and $n_{\rm H}$ is the volume density of the reprocessing material.

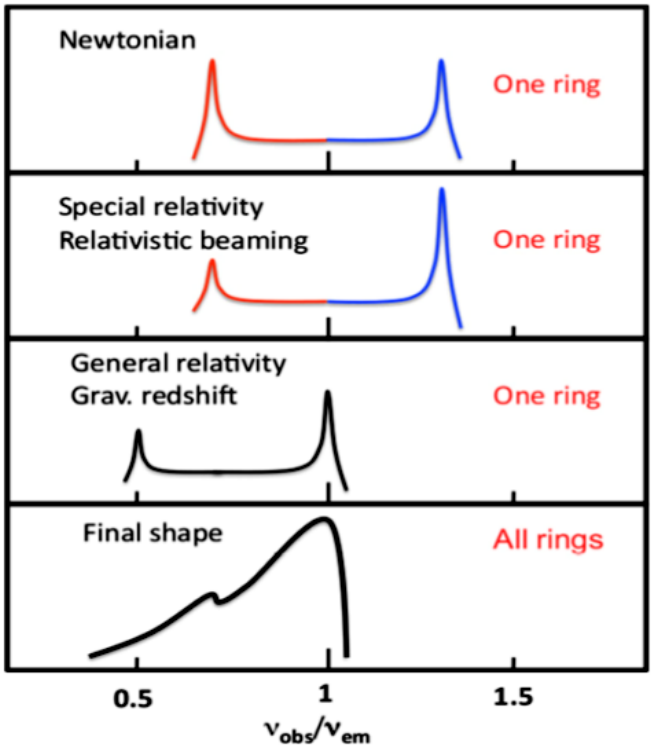

Figure 1.7: Schematic profile of an intrinsically narrow emission line, modified by the interplay of Doppler/gravitational energy shifts, relativistic beaming, and gravitational light bending occurring in the accretion disc. Upper panel: the symmetric double-peaked profile from an annulus of a non-relativistic Newtonian disc. Second panel: the transverse Doppler shifts make the profiles redder; the relativistic beaming enhances the blue peak with respect to the red. Third panel: the gravitational redshift shifts the overall profile to the red side and reduces the blue peak strength. Bottom panel: The integration over all annuli gives rise to a broad, skewed line profile (figure adapted from Ghisellini 2013).

- If the accretion disc is seen from a non-zero angle (not a face on configuration), and the emitting material is moving with a non-relativistic speed, then one expects to see a symmetric double peaked emission line due to Doppler effect. The approaching/receding parts of the disc will emit a line that will be blueshifted/redshifted. The symmetry refers to the fact that all the parts of the ring are emitting at the same flux (see upper panel in Figure 1.7).

- Considering that the material is orbiting with relativistic speed, the Doppler boosting becomes important, and the blue peak will have more flux than the red one (see second panel in Figure 1.7).

- If the emission takes place from material very close to the BH, then in this case gravitational redshift will affect the overall spectrum, all frequencies will be redshifted (the closer to the BH, the higher the redshift), and light

bending becomes important as well, changing the profile of the line and thus the received flux (see third panel in Figure 1.7).

- Integrating over the whole accretion disc and taking into consideration all the aforementioned effects will result in a broad and skewed line profile (see bottom panel in Figure 1.7).

Thus, the black hole spin plays a crucial role in the final profile of the emitted line. In fact, as already mentioned, the higher the spin the closer the ISCO is to the BH. In other words, the emitting material can reach closer distances to the BH where the special and general relativistic effects are maximal. In that way, fitting the observed X-ray spectra with reflection models can potentially be a powerful tool in order to determine BH spins. Figure 1.8 shows the effect of the BH spin on the resulting reflection spectrum. It should be noted that the resulting features depend also on the parameters of the accretion disc (ionization, iron abundance), on the characteristics of the illuminating primary source (see later) and the viewing angle of the observer. For large inclination gravitational lensing and light bending play a crucial role as photons coming from behind the black hole are bent and can reach the observer.

It should be noted that evidence of reprocessing (from the disc or distant material) can be also obtained by studying time delays between various energy bands. In fact, the reprocessed emission should vary in response to the variability of the primary emission (regardless its nature). This is known as "X-ray reverberation" and is due to the different light travel paths between the primary photons that arrive directly to a distant observer, and the ones which reach the observer after being reprocessed by the disc or more distant material. The magnitude of these delays depends on: a) the physical and geometrical properties of the X-ray source, and b) the characteristics and location of the reprocessing material. These reverberations, if caused by reflection off the inner disc where relativistic effects are important, should additionally depend on the spin of the SMBH. The lags can be studied by estimating the temporal correlations between light curves in energy bands which are the most representative of the primary emission, and the ones which can be considered as a proxy of the reflected emission. The delays studies are codified in the so-called 'time-lag spectrum', which consists of studying the delays as function of temporal frequency or photon energy, in order to understand the dependence of these delays on the physics and the geometry of the X-ray emitting source and the reprocessing media. Recent studies (e.g. Emmanoulopoulos et al. 2011b; De Marco et al. 2013; Kara et al. 2016) have revealed the presence of such reverberation where the emission in energy bands which are primary dominated (say 1-4 keV for example)

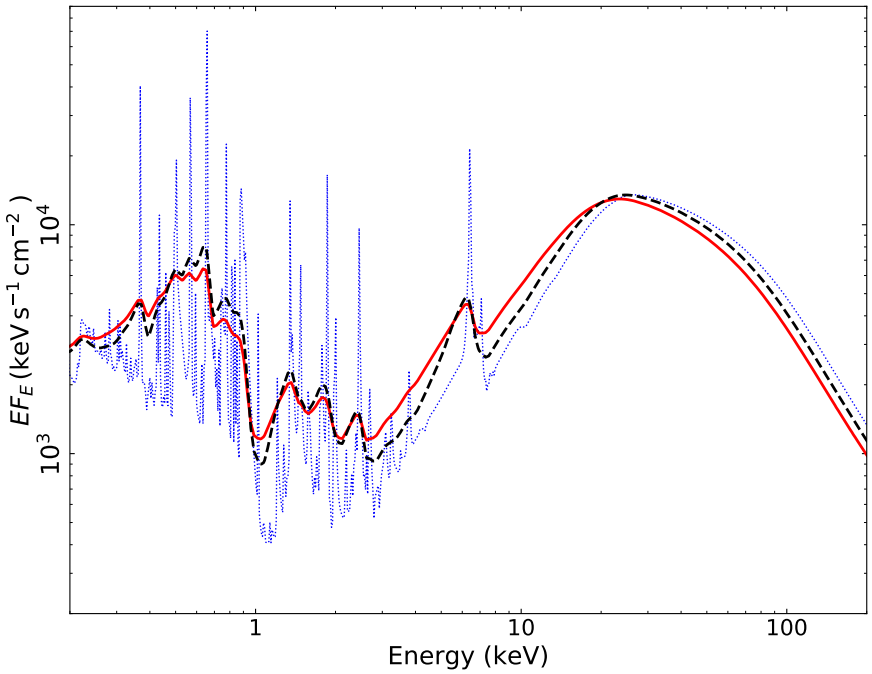

Figure 1.8: The effects of relativistic blurring on the reflection spectrum, assuming a disc with solar abundance and $\log \xi = 2$, which is illuminated by a power-law X-ray source of $\Gamma = 2$ and observed with an inclination of 20°. The dotted line represents the reflection spectrum in the absence of relativistic effects. The dashed and solids lines show the corresponding reprocessed spectrum including relativistic effects for BH spins of 0 and 0.998, respectively. In the latter cases, the disc extends from the ISCO up to 1000 r_g.

leads the emission in the reflection-dominated energy bands (below 1 keV, dominated by the soft excess, or 4-7 keV where the Fe Kα line is prominent, for example) by a few tens up to a few hundreds of seconds, as expected in the case of reverberation (from the inner regions of the disc). If the time delays are due to reprocessing, then the magnitudes of these lags ($|\tau_{\rm lag}|$) are set by the light-crossing time ($t_g = r_g/c$) which is proportional the BH mass ($M_{\rm BH}$). Thus it is expected that $|\tau_{\rm lag}| \propto M_{\rm BH}$. Indeed, De Marco et al. (2013) and Kara et al. (2016) show a positive correlation between these two quantities which is in favour of the reprocessing scenario.

The lamp-post geometry

As discussed earlier, several pieces of evidence suggest that the X-ray emitting region is compact and located close to the BH. This led to the so called "lamp-post" scheme (George et al. 1989; Matt et al. 1991), as shown by a schematic illustration in Figure 1.9, where the corona is assumed to be a point source located at a height (h) on the rotational axis of BH. The idea of a compact X-ray source positioned on the rotational axis of the black hole was also used to explain the observed X-ray

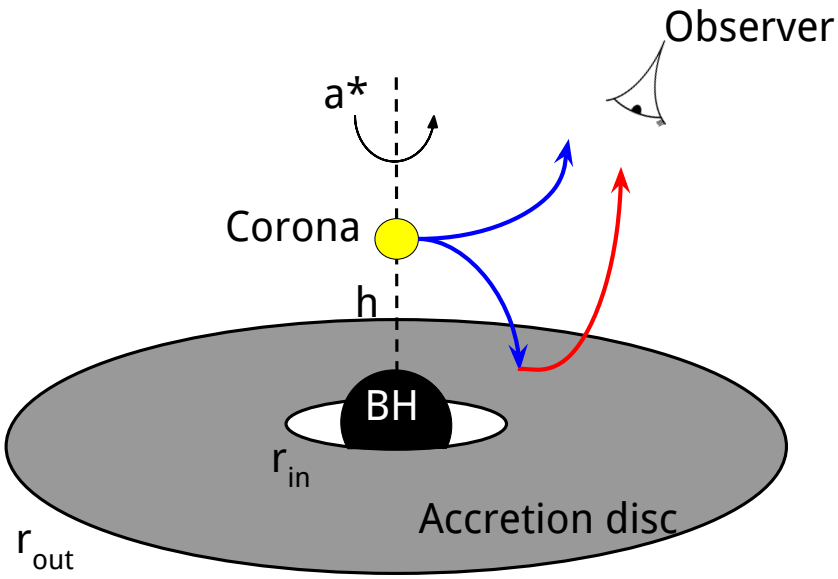

Figure 1.9: Lamp-post geometry scheme.

variability of AGN (Miniutti & Fabian 2004; Niedźwiecki & Miyakawa 2010). The primary flux, that reaches the observer, decreases when the height of the corona decreases because of the larger photon capture by the central black hole. Moreover, at low heights, more primary radiation will be focused towards the innermost regions of the accretion disc due to light-bending and gravitational redshift (see e.g. Martocchia & Matt 1996). The reflection fraction therefore increases in this state (for quantitative estimates see, e.g., Dauser et al. 2013).

However, in a more realistic situation the corona may be a more complex inhomogeneous medium extended in both radial and vertical direction to larger radii (e.g. Wilkins & Gallo 2015). Dovčiak & Done (2016) pointed out that the source needs to be extended to be able to produce sufficiently enough X-ray photons to match the observations. However, the more complex models that would account for the spatial extension of the corona would contain more free parameters that would be difficult to be uniquely constrained with the current quality of the data. Therefore, owing to its simplicity, the lamp-post scheme is still popular and frequently used in the most recent codes for relativistic smearing (Dauser et al. 2013; Dovciak et al. 2014). Besides to an isotropic homogeneous corona, the lamp-post scheme represents a simple approximation of a spatially compact corona, which is concentrated towards the centre.

Often, instead of assuming any particular geometry, the radial emissivity[6] (ϵ)

[6]The emissivity of a body is defined as the ratio of its radiated energy to the corresponding energy radiated by a blackbody of the same temperature

profile can be introduced in the relativistic reflection models,:

$$\epsilon(r) \propto r^{-q}. \tag{1.8}$$

For an isotropic corona, the thermal energy dissipation is assumed to decrease with the third power of radius ($q = 3$), following the standard prescription of the accretion disc temperature (Shakura & Sunyaev 1973). Also, for the lamp-post geometry, the irradiation at distant parts of the accretion disc should follow r^{-3} (Esin et al. 1997). Thus, index $q = 3$ is considered as a "standard" index of the emissivity. However, the emissivity profile in the lamp-post geometry significantly changes in the innermost regions depending on the source height (see e.g. Martocchia et al. 2000, 2002; Dauser et al. 2013; Dovciak et al. 2014). It is very steep at the innermost radii, then it flattens and finally reaches $q = 3$ at further radii, where the contribution to the total reflection spectrum is often relatively small. Therefore, with the current quality of the data, broken (or twice-broken) power laws can be used as adequate approximations of the intrinsic emissivity profiles (e.g. Wilkins & Fabian 2012; Gonzalez et al. 2017).

It should be noted that X-ray photons from the corona which are emitted towards the accretion disc will ionise the matter. Thus, the strong radial dependence of the irradiation will lead to a radial dependence in terms of ionisation as well. The top panel of Figure 1.10 shows the dependence of the ionisation profile of the disc on the height of the lamp-post. By increasing the height of the lamp-post further out regions of the disc are illuminated, which leads to a flattening in the ionisation profile below ~ 20 r_g. The bottom panel of Figure 1.10 shows the emitted reflection spectrum from various rings of an accretion disc illuminated by a lamp-post located at 4 r_g above a maximally rotating Kerr BH. The material becomes less ionised and emits with less flux as the considered ring is far from the center of the system. It should be noted that the gradient of the ionisation of the disc may play a crucial role in determining the emissivity profiles. In fact, many models that are commonly used in spectral fittings neglect the gradient of ionisation and assume instead a constant ionisation. However, as Figure 1.10 shows clearly, the innermost regions of the disc will be more ionised and will have softer reflection spectra with respect to the outer regions of the disc which are less ionised. Thus, a model assuming a single ionisation parameter of the disc will underestimate the ionisation from the innermost regions which will be compensated by requiring a steep emissivity profile ($q \sim 7$; see Svoboda et al. 2012, for more details on this topic).

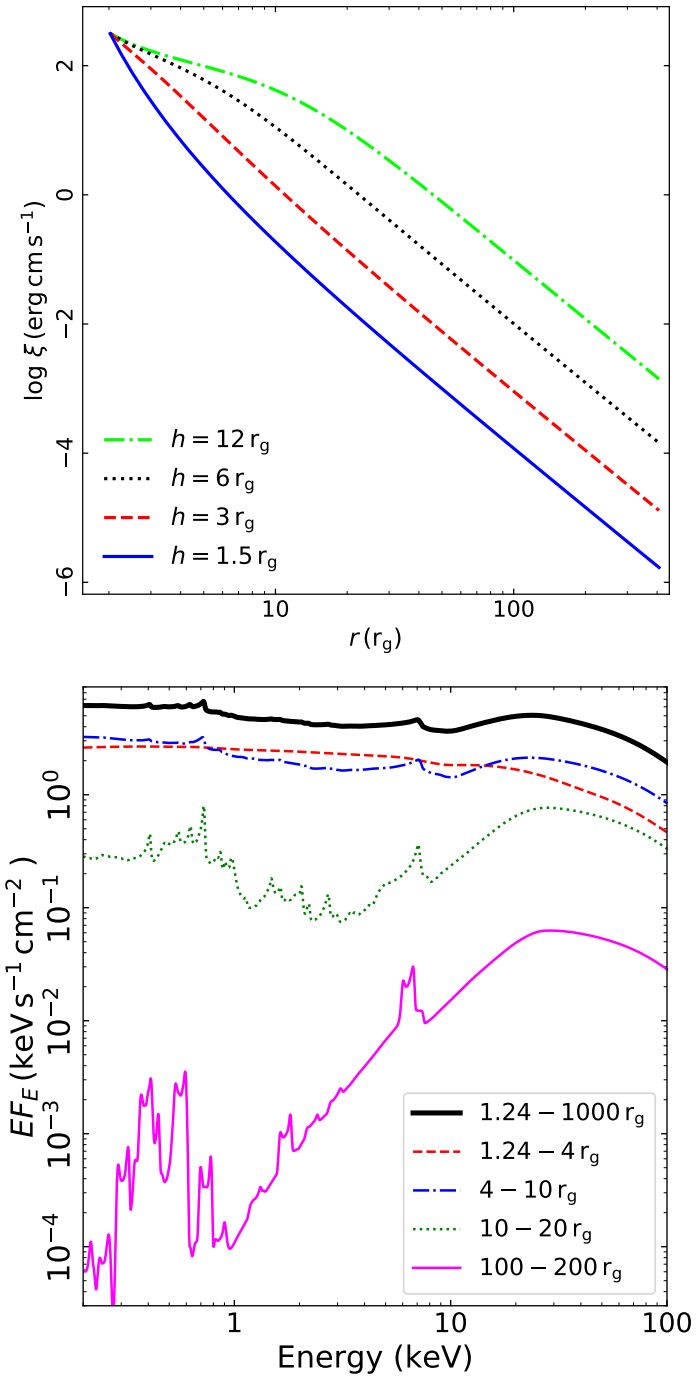

Figure 1.10: Top panel: the radial ionisation profile $\xi(r)$, for various lamp-post heights 1.5 r_g (solid blue line), 3 r_g (dashed red line), 6 r_g (dotted black line), and 12 r_g (dash-dotted green line). I assume the same inner ionisation parameter ($\log \xi_{in} = 2.5$) for all the cases. Bottom panel: eflection spectrum from various annuli of an accretion disc illuminated by a lamp-post (with $\Gamma = 2$) located at 4 r_g above a maximally rotating Kerr BH. The accretion is assumed to have a solar abundance and to be viewed at an angle of 45°. The thick solid line corresponds to the reflection spectrum integrated over the whole accretion disc.

1.5 Outline of the dissertation

As mentioned earlier, the X-ray emission of AGN can be considered as an exceptional means in order to probe the innermost regions of accretion disc, and test general relativity in the strong-field regime. The high sensitivity of *XMM-Newton* (Jansen et al. 2001, in the 0.3–10 keV rangel) combined with that of *NuSTAR* (in the 3–79 keV range; Harrison et al. 2013) allow us to explore, with high precision, the spectral and temporal characteristics of AGN in the broad X-ray range. In this dissertation, I exploit this potential in addition to the development and improvement of various spectral models (e.g. Dauser et al. 2013; Dovciak et al. 2014) in order to get a better understanding of the physics of SMBHs in low- and high-redshift AGN, through spectral and timing analyses.

The physics of the X-ray corona (nature, geometry, heating mechanism, etc.) remain among the main uncertainties in AGN. Assuming that the primary X-ray emission is due to Compton up-scattering of UV photons from accretion disc, the coronal properties (temperature and optical depth) could be then retrieved through the shape of the spectra as discussed earlier. Thanks to the high signal-to-noise ratio (S/N) which can be provided by joint *XMM-Newton* and *NuSTAR* observations in the 0.3-79 keV band, it would be then possible to determine these coronal with higher precision. *XMM-Newton* allows us to characterize the spectral features in the soft and mid-X-ray ranges (below 10 keV) while *NuSTAR* is necessary in order to constrain the spectral (featureless) shape at high energies. In the first part of Chapter 2, I explore the spectral properties of high-redshift AGN. I analyse the joint *XMM-Newton* and *NuSTAR* observations of a luminous non-jetted quasar QSO B2202-209. Considering the previously assumed redshift of this source, $z = 1.77$, $E_{\rm cut}$ is shifted to lower observed energies, helping compensate for the cosmological dimming. In this chapter, I revised the redshift of the source from 1.77 to 0.532, using optical spectra from the Palomar Observatory. Despite the lower estimated redshift, I was able to determine the coronal properties of this quasar showing that they are in agreement with the ones determined for less luminous AGN in the local Universe.

In the second part of Chapter 2, I shed light on the jet emission of blazars in X-rays. Most of this emission is expected to be caused by non-thermal relativistic electrons. However, a population of thermal non-relativistic electrons is expected to be present in the jet. The presence of these electrons can be manifested through the bulk Comptonization of photons from the accretion disc or the BLR, dominating over the non-thermal emission in soft X-rays. Bulk Comptonization is expected to be present in all blazars but has never been confirmed. In this part, I analyse

the simultaneous *XMM-Newton* and *NuSTAR* observations of the FSRQ 4C+25.05 ($z = 2.37$) revealing the presence of an excess at soft X-rays, which I interpreted in the context of bulk Comptonization.

The identification of relativistic reflection X-ray spectra is one of the most robust ways in order to determine SMBH spins in AGN. In Chapter 3, I address the question of how accurate these measurements can be, taken into account the complexity of the X-ray emission in AGN. I attempt to answer this question by fitting blindly high-quality simulated *XMM-Newton* + *NuSTAR* spectra of low-redshift and bright non-jetted AGN. I show in this analysis how the human factor in addition to the characteristics and the complexity of the system may affect the measurements. I show that the major factor in determining the spin, assuming a lamp-post geometry, is the position of the X-ray source with respect to the BH. The closer the source to the BH, the largest the relativistic effects, which leads to a more accurate estimate of the spin, using the current quality of the data.

In Chapter 4, I present a model-independent way (flux-flux analysis) to analyse X-ray light curves of bright and variable AGN. I apply this method to the Seyfert 1 galaxy MCG–6-30-15, one of the sources where the presence of relativistic reflection was questioned. Several authors proposed in the past that the broadening of the Fe line in this source may be due to a complexity in the structure of the absorbing medium. I show that the flux-flux analysis can be a robust and straightforward way to break some degeneracies between various spectral models, since it allows us to identify the various variable and stable components in the X-ray spectra of a given source.

An additional way to probe the innermost regions of AGN is the study of X-ray eclipses by BLR cloud. As a cloud passes through the line of sight, it shades various regions of the accretion disc which are affected differently by special and general relativity (Doppler and gravitational shifts). In Chapter 5, I simulate obscuration events in AGN and analyse their X-ray spectral and polarimetric characteristics. I show that the detection of such events with the next generation of X-ray observatories would improve our understanding the close environment of SMBHs, and would allow us to test the strong-gravity regime in their vicinity. This could be achieved thanks to the emerging field X-ray polarimetry which may open a new window in X-ray astronomy, as it addresses several key questions which could not be answered using neither spectral nor timing analyses. I show in this chapter that X-ray polarimetry could be a key method to constrain not only the emission from the X-ray emitting region and the accretion disc, but it also gives valuable information about the nature and the structure of the parsec-scale material (NLR and torus).

A summary of the results and discussion of future prospects are presented in Chapter 6.

The following cosmological parameters are assumed throughout the manuscript, $\Omega_{\rm M} = 0.27$, $\Omega_{\Lambda} = 0.73$, and $H_0 = 70\,{\rm km\,s^{-1}\,Mpc^{-1}}$.

Wine is sunlight, held together by water.

Galileo Galilei

2

Probing high-redshift quasars

Contents

The unprecedented sensitivity of *NuSTAR* covering the $3-79\,\mathrm{keV}$ band, has allowed us for the first time the to measure spectral parameters in a precise and robust way including both the Compton reflection component and the high-energy cutoff ($E_{\mathrm{cut}} \sim 100-180\,\mathrm{keV}$) in some of the brightest local AGN, with luminosities on the order of $10^{42-44}\,\mathrm{erg\,s^{-1}}$ in the *NuSTAR* energy band (e.g. Marinucci et al. 2014a; Brenneman et al. 2014; Ballantyne et al. 2014; Baloković et al. 2015; Matt et al. 2015). Combining the high sensitivity of *XMM-Newton* at soft X-ray energies with that of *NuSTAR* at hard energies, using simultaneous observations, we are able to investigate the properties of more distant and more luminous quasars. This provides us with the highest signal-to-noise spectra in the broad $\sim 0.3-79$ keV range (observed frame) that can be achieved with the current instruments, allowing us to have a better understanding of the spectral features of high-redshift luminous quasars. The main aim of Section 2.1 is to understand better the coronal physics

and the dependence of the corona on luminosity and redshift, mainly for non-jetted quasars. Section 2.2 shows that simultaneous *XMM-Newton* and *NuSTAR* observations provides valuable information on the hard X-ray spectra of jetted quasars, giving hints on the properties of the material forming the jets.

2.1 The case of QSO B2202-209: Coronal properties

QSO B2202–209 (hereafter B2202) is a non-jetted quasar located at redshift $z = 1.77$ (Reboul et al. 1987). This source is the most luminous non-jetted quasar in X-ray within its redshift ($L_{2-10} \simeq 3 \times 10^{46}\,\mathrm{erg\,s^{-1}}$). I analysed the simultaneous *XMM-Newton* and *NuSTAR* observations of this source with the main aim to measure its coronal properties. Considering the relatively high redshift of QSO B2202–209, $E_{\rm cut}$ will be shifted to lower observed energies compensating for the relative faintness of the source.

2.1.1 X-ray observations

B2202 was observed simultaneously by *XMM-Newton* and *NuSTAR*, on 2015 November 06-07 (Obs. IDs 0764370201 and 60101030002, respectively). The basic observation details are presented in Table 2.1. Here I summarise the data reduction procedures.

XMM-Newton

The *XMM-Newton* data were reduced using `SAS v.15.0.0` and the latest calibration files. I followed the standard procedure for reducing the data of the EPIC-pn (Strüder et al. 2001) and the two EPIC-MOS (Turner et al. 2001) CCD cameras, all operating in full frame mode with a thin filter for the EPIC-pn and a medium filter for the EPIC-MOS cameras. The EPIC-pn and EPIC-MOS data were processed using `EPPROC` and `EMPROC`, respectively. Source spectra and light curves were extracted from a circular region of radius $\sim 25''$. The corresponding background spectra and light curves were extracted from an off-source circular region located on the same CCD chip, with a radius approximately twice that of the source. I filtered out periods with strong background flares estimated to be around 7.5 ks. I corrected the light curves for the background count rate using `EPICLCCORR`. The extracted light curves did not show any significant spectral variability. Response matrices were produced using the FTOOLs `RMFGEN` and `ARFGEN`. I re-binned the observed spectra,

Table 2.1: B2202 net exposure times, and count rates estimated from the background-subtracted data in the 0.5–10 keV range for *XMM-Newton*, and the 4-30 keV range for *NuSTAR*.

Instrument	Net exposure (ks)	Count Rate (count/s)
EPIC-PN	60.5	0.501 ± 0.003
MOS 1	69.7	0.152 ± 0.001
MOS 2	69.4	0.156 ± 0.001
FPMA	106.8	0.0233 ± 0.0005
FPMB	106.5	0.0227 ± 0.0005

shown in the bottom left panel of Figure 2.1, using the SAS task `SPECGROUP` to have a minimum S/N of 5 in each energy bin. The MOS1 and MOS2 spectra are consistent with each others, so I combined them using the SAS command `COMBINE`.

NuSTAR

I reduced the *NuSTAR* data following the standard pipeline in the *NuSTAR* Data Analysis Software[1] (NuSTARDAS v1.4.1), and instrumental responses from *NuSTAR* CALDB v20151008. I cleaned the unfiltered event files with the standard depth correction, with `saamode = optimized` and `tentacle = yes` criteria for a more conservative treatment for the high background in the proximity of the South Atlantic Anomaly. I extracted the time-averaged source and background spectra from circular regions of radii 40″ and 100″, respectively, for both focal plane modules (FPMA and FPMB) using the HEASoft task `NUPRODUCT`, and requiring a minimum of 50 counts per bin. The extracted spectra are presented in the bottom right panel of Figure 2.1. The spectra extracted from both modules are consistent with each other. The background starts to dominate the source above ~ 30 keV. For that reason, I decided to analyse the *NuSTAR* data in the observed $4-30$ keV energy range, which corresponds to the $6-46$ keV energy range in the rest frame of the source. The data from FPMA and FPMB are not combined together, instead they are analysed jointly.

2.1.2 Spectral Analysis

The spectral fitting was done using `XSPEC v12.9` (Arnaud 1996). Unless stated otherwise, uncertainties are listed at the 90% confidence level ($\Delta\chi^2 = 2.71$). I

[1] https://heasarc.gsfc.nasa.gov/docs/nustar/analysis/nustar_swguide.pdf

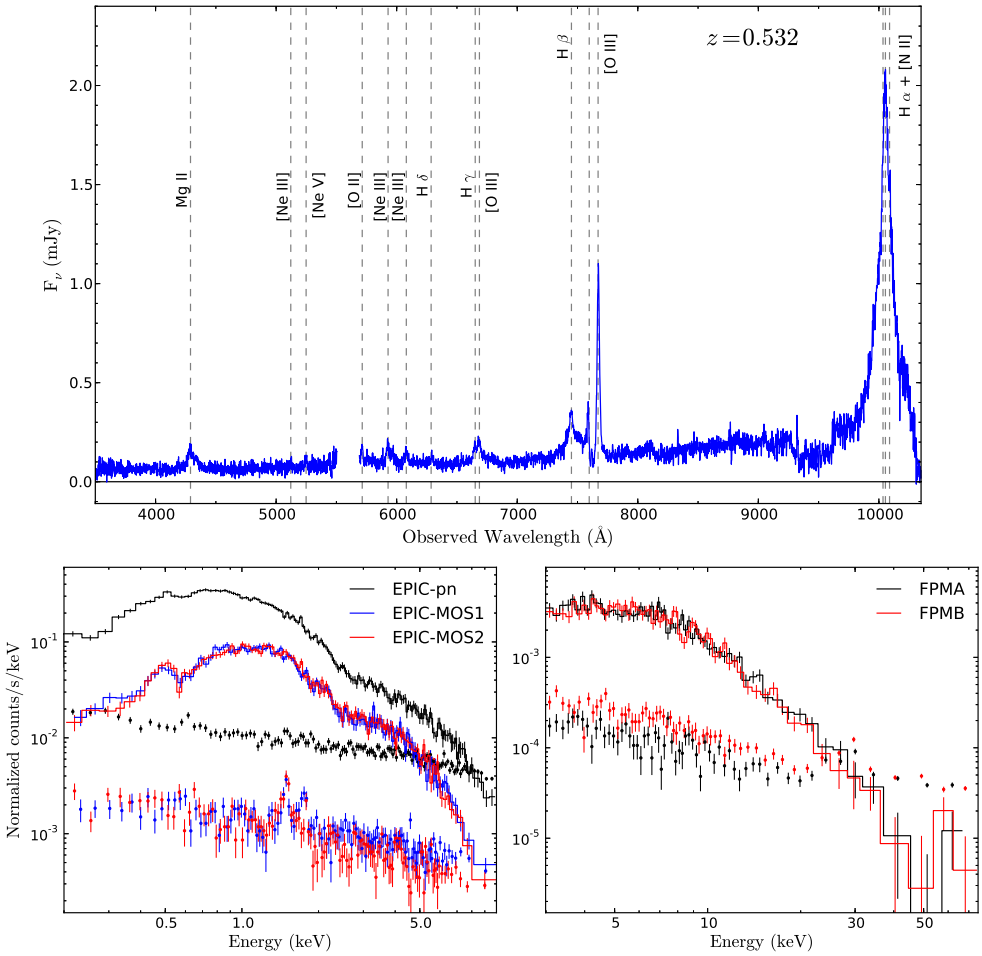

Figure 2.1: Upper panel: optical spectrum obtained using the Palomar DBSP. Lower panels: X-ray background-subtracted source spectra (continuous lines) and background spectra (dots). Left panel: the spectra extracted from the EPIC-pn (black), EPIC MOS1 (blue) and EPIC MOS2 (red) instruments. Right panel: the spectra extracted from the FPMA (black) and FPMB (red) modules.

included a variable constant, for each instrument, in order to account for the residual uncertainties in the flux calibration between the various detectors, fixing the constant for the EPIC-pn data to unity. I considered the EPIC-pn and the merged EPIC-MOS spectra in the 0.5–10 keV range, and the FPMA/B spectra in the 4-30 keV band, as mentioned above.

Identification of the wrong redshift

First, I fitted the spectra with a simple, absorbed power law with an exponential high-energy cutoff (`CUTOFFPL` model in `XSPEC`). I fixed the Galactic absorption to the equivalent hydrogen column density in the line of sight towards QSO B2202–209, $N_{\rm H} = 5.52 \times 10^{20}\,{\rm cm}^{-2}$ (Kalberla et al. 2005). Furthermore, I considered

an intrinsic neutral absorber at the redshift of the source (ZWABS). The model fit is unacceptable (χ^2/dof = 1.32), mostly due to the presence of strong residuals suggesting the need of an additional absorption. For that reason, I added a partial covering absorption by partially ionized material (ZXIPCF) at a free redshift. The fit improved (χ^2/dof = 1.13). However, a significant deficit could be detected in the residuals at energy ~ 1.8 keV, most probably due to inaccuracies in modelling the Si absorption in the CCD detectors. I modelled this deficit using a Gaussian absorption profile with a free centroid energy, width, and normalisation (in the observed frame). The fit improves significantly by adding this line ($\Delta\chi^2/\Delta$dof = 27/3, F-test null probability = 1.95×10^{-5}), resulting in a χ^2/dof = 1.07. I found a high-energy cutoff $E_{\rm cut} = 90.60^{+64.79}_{-31.14}$ keV, in the observed frame, corresponding to an energy of ~ 251 keV in the rest frame of the source, with a slope of the power-law $\Gamma = 1.82^{+0.06}_{-0.05}$. Moreover, I was able to identify a partially ionised absorber with an ionisation parameter $\log \xi = 0.52^{+0.8}_{-0.66}$ situated at a redshift $z = 0.53^{+0.12}_{-0.16}$ covering $\sim 30\%$ of the source, having a relatively large column density $N_{\rm H} \simeq 2.3 \times 10^{23}{\rm cm}^{-2}$. In addition, a neutral absorber at the rest frame of the source can be identified to have a column density $N_{\rm H} = (5.92 \pm 0.09) \times 10^{21}{\rm cm}^{-2}$.

The identification of an ionised absorber at $z = 0.53$, covering only 30% of the source, is unphysical. In fact, if the source is located at $z = 1.77$ then it would be perceived by the absorber as a point-like source. Aiming to have a better idea about the multi-wavelength characteristics of this source, I searched for archival data in order to build the SED of the source. I built the SED of the source using the photometric data from: the Two Micron All Sky Survey[2] (2MASS, observed in 2000; Skrutskie et al. 2006), the 10th data release of the Sloan Digital Sky Survey[3] (SDSS DR10, observed in 2009), and the Wide-field Infrared Survey Explorer[4] (*WISE*, observed in 2010; Wright et al. 2010). I added also the fluxes obtained from the U, W1 and M2 filters of the Optical/UV Monitor Telescope (OM), mounted on the *XMM-Newton* observatory, observed in 2015. After correcting for the Galactic extinction in the line of sight of the source, I compared the SED to a typical SED of a non-jetted quasar (Elvis et al. 1994). I found that the observed SED, especially the *WISE* data points, does not agree with the typical SED (see Figure 2.2). It is clear that the typical SED, assuming that the source is at $z = 1.77$ is systematically shifted to the left with respect to the observed points. In other terms, this may indicate that the source could be at a redshift lower than 1.77. The redshift of

[2] http://irsa.ipac.caltech.edu/Missions/2mass.html
[3] http://skyserver.sdss.org/dr10/en/home.aspx
[4] http://irsa.ipac.caltech.edu/Missions/wise.html

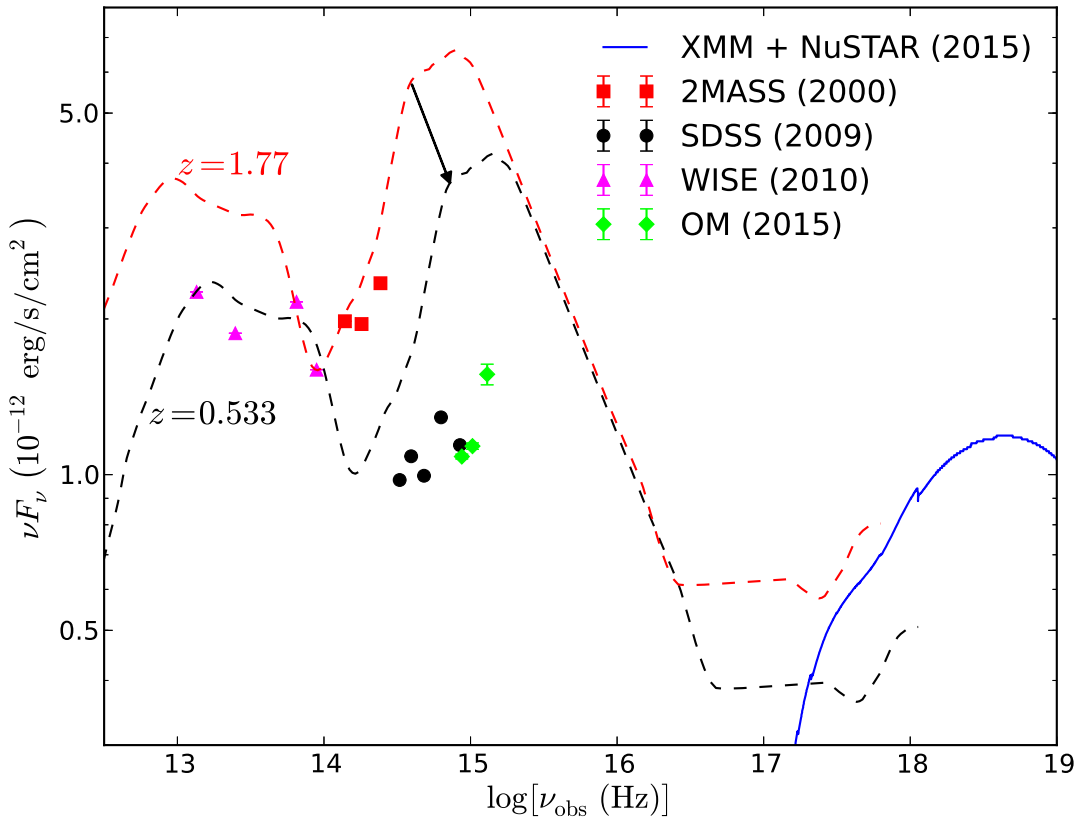

Figure 2.2: The observed spectral energy distribution of the source in the observed frame, corrected for Galactic extinction only, from WISE (magenta triangles), 2MASS (red squares), SDSS (black circles), OM (green diamonds) and the X-ray spectrum from the joint *XMM-Newton* and *NuSTAR* observations (blue solid line). The typical non-jetted quasar SEDs (Elvis et al. 1994) are plotted, for comparison, assuming a redshift of 1.77 (red dashed line) and 0.533 (black dashed line).

the source has been determined by Reboul et al. (1987) who identified a broad emission line to be "most likely" a C IV1549 line. However, if one identifies the emission line to be Mg II2798, then the redshift of the source will be 0.533 and the two SEDs will be in agreement. Interestingly, in this case the redshift of the source will be equal to that of the partially ionised absorber identified earlier. This discrepancy motivated us to obtain a higher quality optical spectrum using the Hale Telescope at Palomar Observatory.

Palomar Observations

We obtained an optical spectrum of B2202 using the dual-beam Double Spectrograph on the 200-inch Hale Telescope at Palomar Observatory. The 900 s spectrum, obtained on UT 2016 May 28 in photometric conditions, used the 1.″5 wide slit, the 5500 Å dichroic to split the light, the 600 $\ell\,\mathrm{mm}^{-1}$ grating on the blue arm

($\lambda_{\rm blaze} = 4000\,$Å; spectral resolving power $R \equiv \lambda/\Delta\lambda \sim 1200$), and the $316\,\ell\,{\rm mm}^{-1}$ grating on the red arm ($\lambda_{\rm blaze} = 7500\,$Å; $R \sim 1800$). We processed the data using standard techniques within IRAF, and calibrated the spectrum using an archival sensitivity function obtained in February 2016 using the same instrument configuration and observing conditions.

The processed spectrum, shown in the upper panel of Figure 2.1, shows the source to be an AGN at $z = 0.532$ with many standard emission features identified, including broad Mg IIλ2800, broad hydrogen Balmer emission lines, and narrow [O III]$\lambda\lambda$4959, 5007; the redshift has been determined from the latter features. In particular, the new data clearly demonstrate that the line at $\sim 4290\,$Å previously identified as C IV by Reboul et al. (1987) is indeed Mg II.

Coronal properties of B2202

Given the correct redshift of the source, I re-fitted the spectra with a simple, absorbed power-law with an exponential high-energy cutoff. I fixed the Galactic absorption to the equivalent hydrogen column density in the line of sight towards B2202, $N_{\rm H} = 5.52 \times 10^{20}\,{\rm cm}^{-2}$ (Kalberla et al. 2005). Furthermore, I considered a neutral absorber at the redshift of the source (`ZWABS`) and a partial covering absorption by partially ionized material (`ZXIPCF`), both being at the redshift of the source. The fit was statistically good ($\chi^2/{\rm dof} = 1.12$). However, a significant deficit could be detected in the residuals at energy $\sim 1.8\,$keV, most probably due to inaccuracies in modelling the Si absorption in the CCD detectors. I modelled this deficit using a Gaussian absorption profile with a free centroid energy, width, and normalisation (in the observed frame). The fit improves significantly by adding this line ($\Delta\chi^2 = -25$ for 3 degrees of freedom less), resulting in a $\chi^2/{\rm dof} = 1.05$. The final model and data/model ratio are presented in the top panel of Figure 2.3. I performed a Monte Carlo Markov Chain (MCMC) analysis to estimate the errors on the parameters, using the Goodman-Weare algorithm (Goodman & Weare 2010) with a chain of 50,000 elements, and discarding the first 5000 elements as part of the "burn-in" period. I found a high-energy cutoff $E_{\rm cut} = 99^{+67}_{-35}\,$keV in the observed frame that corresponds to an energy of $152^{+103}_{-54}\,$keV in the rest frame of the source, with a photon index $\Gamma = 1.82 \pm 0.05$. In the bottom left panel of Figure 2.3, I present the contour plots derived from the MCMC analysis showing the constraints on the photon index Γ and the high-energy cutoff $E_{\rm cut}$ in the rest frame of the source. Moreover, I identified a partially ionised absorber $\left(\log\left[\xi({\rm erg\,cm\,s^{-1}})\right] = 0.39^{+0.80}_{-0.75}\right)$ situated at the redshift of the source covering $\sim 30\%$ of the source and having a column density $N_{\rm H} = 2.32^{+0.83}_{-0.88} \times 10^{23}{\rm cm}^{-2}$. In addition, I identified a neutral absorber

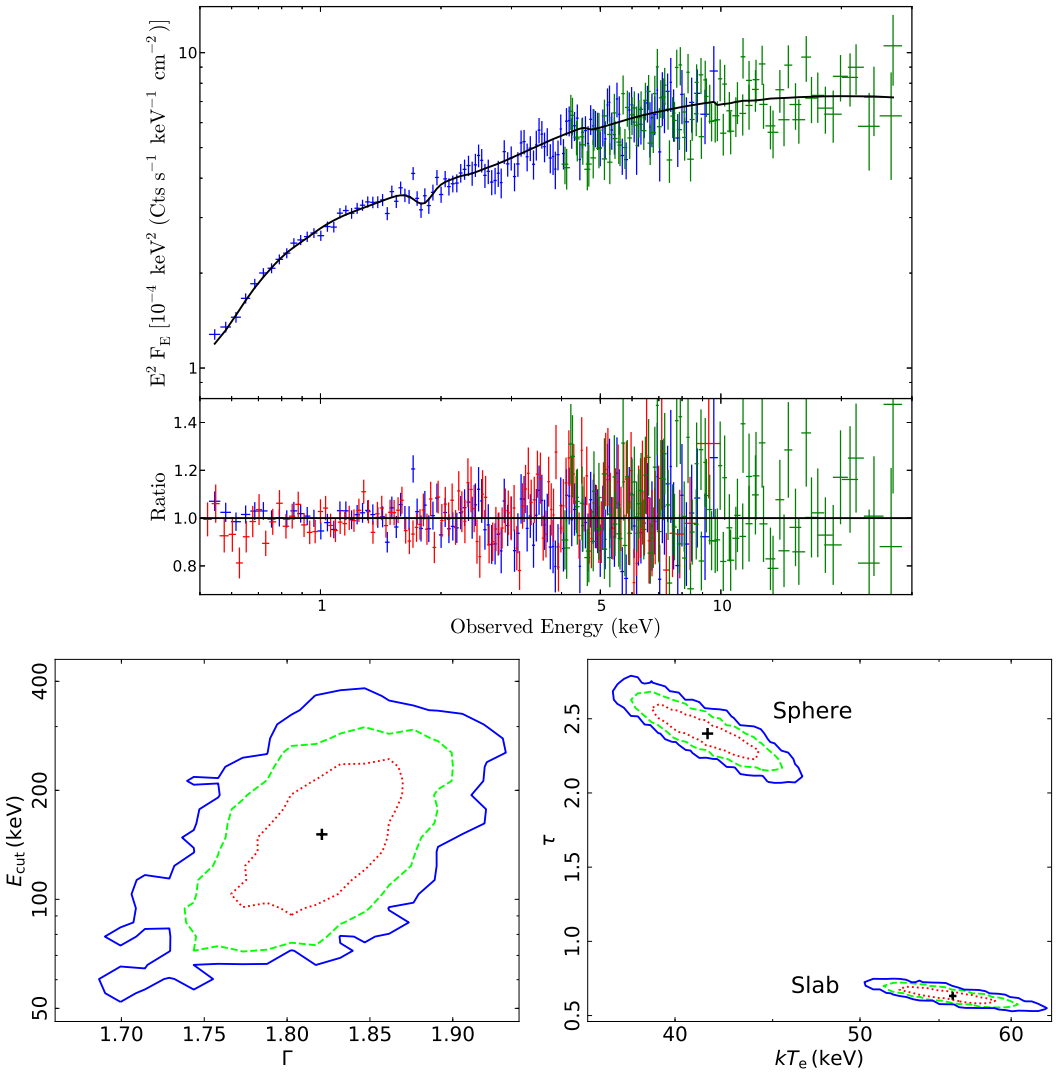

Figure 2.3: Top panel: observed spectra from EPIC-pn (blue) and *NuSTAR* (green) plotted together with the best-fit model (black line) composed of an absorbed cutoff power-law. In addition to the data/model ratio for the EPIC-pn (blue), EPIC-MOS (red), and *NuSTAR* (green) data. Bottom left panel: $\Gamma - E_{\rm cut}$ contour plot (in the rest frame) for the cutoff powerlaw model. Bottom right panel: $kT_{\rm e} - \tau$ contour plot (in the rest frame) for the Comptonisation model assuming a spherical geometry and a slab geometry. I plot the 68% (dotted red lines), 95% (dashed green lines) and 99.7% (solid blue lines) confidence levels.

Table 2.2: Best-fit parameters obtained assuming a cutoff power-law model, and a Comptonisation model for both spherical and slab geometries.

Parameter	Cutoff	Compton (spherical)	Compton (slab)
	`zwabs`		
$N_{\rm H}\,(10^{21}\,{\rm cm}^{-2})$	$1.40^{+0.22}_{-0.20}$	$1.40^{+0.13}_{-0.12}$	$1.38^{+0.15}_{-0.13}$
	`zxipcf`		
$N_{\rm H}\,(10^{23}\,{\rm cm}^{-2})$	$2.32^{+0.83}_{-0.88}$	$2.32^{+0.68}_{-0.55}$	$2.43^{+0.77}_{-0.45}$
$\log\left[\xi({\rm erg\,cm\,s}^{-1})\right]$	$0.39^{+0.80}_{-0.75}$	$0.40^{+0.79}_{-0.47}$	$0.36^{+0.76}_{-0.35}$
CF (%)	30^{+6}_{-5}	30^{+4}_{-3}	29^{+4}_{-3}
	`cutoffpl`		
Γ	1.82 ± 0.05	–	–
$E^{a}_{\rm cut}$ (keV)	99^{+67}_{-35}	–	–
Norm $(\times 10^{-4})$	$5.26^{+0.54}_{-0.41}$	–	–
	`compTT`		
$kT^{b}_{\rm e}$ (keV)	–	42 ± 3	56 ± 3
τ	–	$2.40^{+0.18}_{-0.16}$	$0.63^{+0.06}_{-0.05}$
Norm $(\times 10^{-4})$	–	$4.23^{+0.45}_{-0.41}$	$3.07^{+0.34}_{-0.28}$
	`gaussian (absorption)`		
E (keV)	1.8 ± 0.04	1.8 ± 0.04	1.8 ± 0.03
σ (eV)	72^{+55}_{-40}	72^{+47}_{-34}	73^{+54}_{-38}
Norm $(\times 10^{-6})$	$4.75^{+1.77}_{-2.34}$	$4.73^{+1.47}_{-1.87}$	$4.79^{+1.58}_{-2.17}$
χ^2/dof	363/344	363/344	363/344
	1.05	1.05	1.05

Notes.
[a] The cutoff energy is reported in the observed frame.
[b] The electron temperature is reported in the rest frame of the source.

at the rest frame of the source with a column density $N_{\rm H} = 1.4^{+0.22}_{-0.20} \times 10^{21}{\rm cm}^{-2}$. The best-fit parameters are reported in Table 2.2.

The measurement of $E_{\rm cut}$ could be affected by the presence of a reflection component in the spectrum. In order to test the stability of the measurement, I replaced the power-law model by the neutral reflection model `PEXMON` (Nandra et al. 2007), considering an intermediate inclination of 60° and solar abundances. The fit improves by $\Delta\chi^2 = -6$ for one additional free parameter. I found a low reflection fraction ($R_{\rm frac} = 0.31^{+0.24}_{-0.21}$) and a low high-energy cutoff of $E_{\rm cut} = 69^{+47}_{-25}$ keV in the rest frame of the source, but consistent within the error bars with the value found assuming a simple cutoff power-law model. In addition, I tested the possibility of having relativistic reflection using the `RELXILL` model (Dauser et al. 2013; García et al. 2014; Dauser et al. 2016). The fit was statistically accepted ($\chi^2/{\rm dof} = 1.04$), and $E_{\rm cut}$ was consistent with the values determined above. However, neither the reflection fraction nor the ionisation parameter of the disc could be constrained. This could be due to the high luminosity of the source, which leads to a high ionisation of the disc, thus the reflection parameters could not be well constrained.

Finally, assuming that the power-law spectrum is obtained by Comptonisation of soft photons arising from the accretion disc by hot electrons in a corona, I substituted the cutoff power-law with the Comptonisation model `COMPTT` (Titarchuk 1994). This model allows us to determine the coronal temperature and optical depth assuming either a spherical or a slab geometry. I fixed the temperature of the seed photons, assumed to follow a Wien distribution law, to $kT = 20$ eV. I obtained a fit statistically similar to the one obtained for the cutoff power-law model. I performed an MCMC analysis similar to the one mentioned previously, and found the coronal temperature and optical depth to be $kT_{\rm e} = 42 \pm 3$ keV, $\tau = 2.40^{+0.18}_{-0.16}$ (spherical geometry), $kT_{\rm e} = 56 \pm 3$ keV, $\tau = 0.63^{+0.06}_{-0.05}$ (slab geometry). The electron temperatures are in agreement with the estimation of $E_{\rm cut}$, within the error bars, obtained assuming a high-energy cutoff power-law model ($E_{\rm cut} \simeq 2 - 3kT_{\rm e}$, e.g. Petrucci et al. 2001a). The optical depth is larger for the spherical geometry. This is expected because the optical depth estimated assuming a spherical geometry is the radial (effective) depth, while the slab optical depth is the vertical one that should be lower than the effective one. The $kT_{\rm e} - \tau$ contour plots for both geometries are presented in the lower panel of Figure 2.3. The best-fit parameters are shown in Table 2.2. The observed 2–10 keV flux is $F_{2-10} = (1.43 \pm 0.07) \times 10^{-12}\,{\rm erg\,cm^{-2}\,s^{-1}}$, while the unabsorbed 2–10 keV luminosity, in the rest frame, is $L_{2-10} = (1.93 \pm 0.07) \times 10^{45}\,{\rm erg\,s^{-1}}$.

B2202 was also observed by *XMM-Newton* in May 2001 (Obs. ID 12440301, hereafter obs. 1), for $\sim$ 30 ks. I extracted the EPIC-pn/MOS data in a similar way to that described in Section 2.1.1. I fit the EPIC spectra of this observation by an absorbed power-law model, similar to the best-fit model presented above, but without considering either the high-energy cutoff or the absorption feature at $\sim$ 1.8 keV. The fit is statistically good (χ^2/dof = 0.97) and the parameters of both neutral and ionised absorbers are consistent, within the error bars, with the ones found in 2015. However, I found a steeper power-law with a photon index $\Gamma = 1.97^{+0.05}_{-0.06}$. During obs. 1, the source was $\sim$ 1.5 times brighter than in 2015 (unabsorbed luminosity, $L_{2-10} = 2.92 \times 10^{45}\,\mathrm{erg\,s^{-1}}$) showing a behaviour often observed in AGNs, where the X-ray spectrum gets steeper when the source is brighter (Markowitz & Edelson 2001).

2.1.3 Discussion and conclusions

In order to derive the black hole mass ($M_{\rm BH}$) of B2202, we fit the Hβ line region with the IDL package MPFIT (Markwardt 2009). Approximating the uncertainties to the flux using the standard deviation of the spectrum outside the emission lines, we fit the rest-frame 4200-5600 Å including a power-law continuum, broad and narrow Gaussian components for the Hβ line, narrow [O III]$\lambda\lambda$4959, 5007 doublet, narrow He IIλ4686 and the blended Hγ and [O III]λ4363. The contribution from the Fe II complex is negligible for this target and thus was ignored. The full widths at half maximum (FWHM) and the equivalent widths (EW) of the Hβ lines and the [O III]$\lambda\lambda$4959, 5007 doublet are presented in Table 2.3. Using the width of the broad Hβ line and the monochromatic 5100 Å luminosity (L_{5100}), we get $\log(M_{\rm BH}/M_\odot) = 9.08 \pm 0.18$ from the Jun et al. (2015) estimator. This implies an Eddington luminosity of $L_{\rm Edd} = (1.56 \pm 0.28) \times 10^{47}\,\mathrm{erg\,s^{-1}}$. Note that L_{5100} is derived directly from the spectrum, that was checked to yield consistent i-band magnitude to that from the SDSS imaging, within a 10% difference. We applied then the bolometric correction to L_{5100} suggested by Marconi et al. (2004), $L_{\rm bol}/\nu_{\rm B}L_{\rm B} = 7.9 \pm 2.9$, and we estimate the bolometric luminosity of this source to be $L_{\rm bol} = (5.72 \pm 2.15) \times 10^{45}\,\mathrm{erg\,s^{-1}}$. This means that the source is emitting at $\sim$ 3.66% of its Eddington limit. However, by applying the bolometric correction to L_{2-10} (equation 21 in Marconi et al. 2004), we obtain a higher bolometric luminosity, $L_{\rm bol} = 1.79 \times 10^{47}\,\mathrm{erg\,s^{-1}} \simeq 1.15\,L_{\rm Edd}$.

Moreover, we estimated the monochromatic luminosity of the source at 2500 Å to be $L_\nu(2500\,\text{Å}) = (1.06 \pm 0.02) \times 10^{45}\,\mathrm{erg\,s^{-1}}$, which implies an optical-to-X-ray spectral slope $\alpha_{\rm OX} = -0.384 \times \log[L_{2\,\rm keV}/L_{2500}] = 1.01 \pm 0.02$. This is a strong

Table 2.3: Full widths at half maximum and equivalent widths of the broad and narrow Hβ lines and the [O III]$\lambda\lambda$4959, 5007 doublet seen in the Palomar spectra.

Line	FWHM ($\mathrm{km\,s^{-1}}$)	EW (Å)
Hβ_{broad}	6940 ± 1033	128.4 ± 5.9
Hβ_{narrow}	961 ± 49	18.4 ± 8.5
[O III]λ4959	1144 ± 77	49 ± 3
[O III]λ5007	995 ± 50	145.7 ± 3.4

outlier in the α_{OX}-luminosity relation ($\alpha_{\mathrm{OX}} \sim 1.6$ for typical quasars of the same luminosity, Lusso & Risaliti 2016). However, the large EW of [O III]λ5007 can be indicative of a high inclination angle θ between between the disc axis and the line of sight. In fact, we observe the projected EW along the line of sight, $\mathrm{EW_O} = \mathrm{EW^*}/\cos\theta$, where $\mathrm{EW_O}$ is the observed EW, and $\mathrm{EW^*}$ is the EW as measured in a face-on disc. By considering an average value of $\mathrm{EW^*}$, for all quasars, to be ~ 11 Å(Risaliti et al. 2011c; Bisogni et al. 2017), we obtain $\theta \simeq 85°$. This means that the disc is observed nearly edge-on and can explain the high X-ray loudness of the source. In other terms, having such a high inclination of the disc with respect to the line of sight, the intrinsic UV luminosity should be higher than the observed one. Instead, the inclination will not affect the X-ray primary that is thought to be emitted isotropically. If we assume an intrinsic L_{5100} to be larger than the observed value by a factor of $1/\cos\theta$, then this leads to an intrinsic $\alpha_{\mathrm{OX,\,int}} \simeq 1.43$ comparable to other sources. In addition, using the [O III]λ5007 luminosity ($L_{[O\,\mathrm{III}]} = (2.07 \pm 0.32) \times 10^{43}\,\mathrm{erg\,s^{-1}}$), we estimated the expeected X-ray luminosity, following the correlation found by Panessa et al. (2006), to be $L_{\mathrm{X}} = (3.2 \pm 0.6) \times 10^{45}\,\mathrm{erg\,s^{-1}}$. The estimated value of L_{X} is in agreement within a factor of 1.65 with the value derived from the X-ray spectral analysis. Given the isotropicity of the X-ray primary emission, the high inclination of the disc and the agreement between the X-ray and the [O III] measurements, this is suggestive that, for this source, the measurement of L_{bol} using the X-ray luminosity is more reliable compared to the bolometric correction estimated using L_{5100}.

Interestingly, I found that the coronal properties are in agreement with the ones determined for local less luminous and less massive Seyfert galaxies (e.g. Fabian et al. 2015; Lubiński et al. 2016a, and references therein). Lubiński et al. (2016a) analysed the hard X-ray spectra of 28 Seyfert galaxies based on observations with *INTEGRAL* (Winkler et al. 2003). The values of the electron temperature, photon index and reflection fraction that I found are in good agreement with the median values

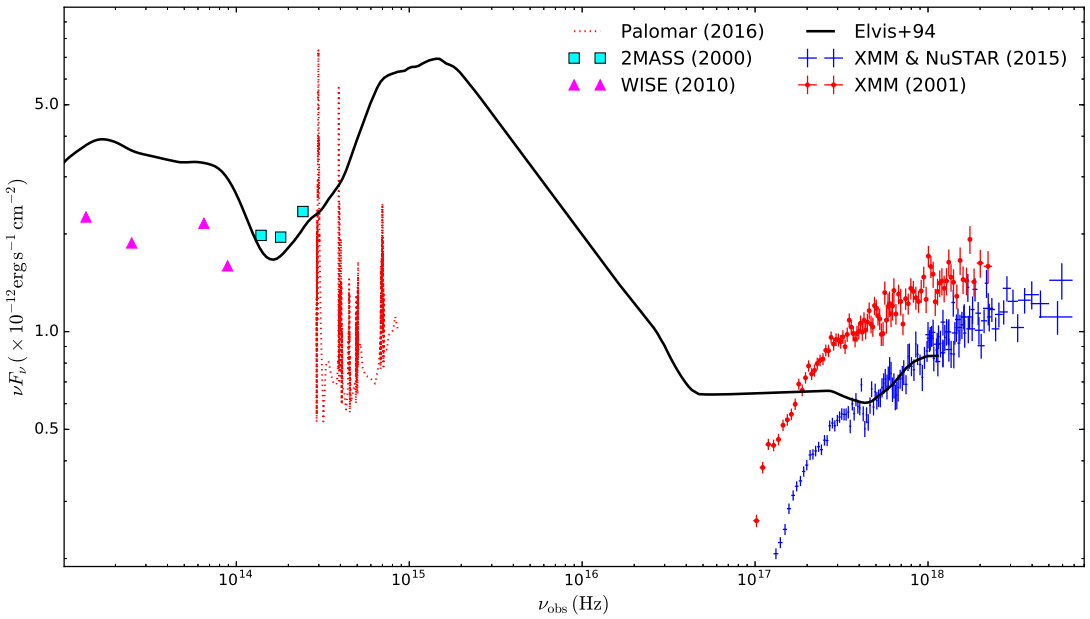

Figure 2.4: The observed SED of the source, obtained using photometric data from *WISE* in 2010 (magenta triangles) and 2MASS in 2000 (cyan squares), in addition to the Palomar Observatory spectrum obtained in 2016 (red dotted line) and corrected for the Galactic extinction and for the Oxygen A-band absorption, the *XMM-Newton* spectrum obtained in 2001 (red dots) and the joint *XMM-Newton* and *NuSTAR* observations in 2015 (blue points). The typical non-jetted quasar SEDs (Elvis et al. 1994) is also plotted (black solid line) for comparison.

of their full sample ($\langle kT_{\rm e}\rangle = 48^{+57}_{-14}$ keV, $\langle\Gamma\rangle = 1.81^{+0.18}_{-0.05}$, and $\langle R_{\rm frac}\rangle = 0.32^{+0.33}_{-0.28}$, respectively). Lubiński et al. (2016a) suggest that the small value of $R_{\rm frac}$ is indicative of a small solid angle under which the corona is seen from the disc. In other terms, this means a reduction in the flux of seed photons emitted by the disc that are cooling the corona. They also suggest the need of an additional process (such as synchrotron self-Compton) that is able to explain the efficient cooling of a compact corona, close to the BH and separated geometrically from the accretion disc.

It should be noted that the low amount of reflection is in agreement with the X-ray Baldwin effect (e.g. Iwasawa & Taniguchi 1993) whereby the equivalent width of the Fe Kα line diminishes with X-ray luminosity. In fact, I modelled the Fe Kα line by adding a Gaussian in emission, to the high-energy cutoff power-law model, and I estimated its EW to be $\leq$ 40 eV.

The weak reflection can be associated with sparse clouds, most likely to be in the broad line region, covering a small fraction of the solid angle. The similarities in both spectral shape and cut-off energy between B2202 and local AGNs are therefore indicative of a universal process determining the spectrum of the X-ray

emission, with the strength of the coupling between disc and corona affecting only the overall normalization of such spectra.

I plot in Figure 2.4 the observed multi-epoch SED of the source by adding the optical data from Palomar observatory to the archival data discussed earlier. I compare the observed SED to a typical SED of a non-jetted quasar (Elvis et al. 1994) trying to match the X-ray spectra obtained in 2015. However, it is obvious that the optical spectrum is fainter and redder compared to a standard SED, but this is expected given the high inclination of the accretion disc, which leads the emission from the host galaxy, usually negligible, to show up. Moreover, interestingly, the IR emission appears to be low compared to the standard quasar SED. Adding to this the fact that the X-ray spectra are barely affected by absorption, and the small amount of reflection, this implies a particular system in which I observe the accretion disc nearly edge-on with no evidence of any Compton thick pc scale reprocessor, indicating a small covering fraction by the torus, if any.

In conclusion, I was able in this study to estimate the coronal properties of the luminous quasar B2202-209. This source was chosen on the basis of the previously reported redshift that mistakenly let it be considered one of the most luminous non-jetted quasars. However, the results of this analysis on a less extreme quasar demonstrate that joint *NuSTAR* and *XMM-Newton* observations with a moderate exposure time are capable of making good measurements of coronal properties for quasars at cosmological redshifts. This significantly ex- tends the previous work done primarily on relatively local and lower luminosity Seyferts (e.g Fabian et al. 2015; Lubiński et al. 2016b).

2.2 The case of 4C+25.05: hints of Bulk Comptonization

In this section I focus on the recent *XMM+NuSTAR* observations of the FSRQ 4C+5.05. FSRQs are typically characterized by photon indices $\Gamma \sim 1.3$–1.5 in the 2–10 keV band (e.g. Wilkes et al. 1992; Boller et al. 2000; de Rosa et al. 2008; Eitan & Behar 2013), which are flatter than usually observed in less luminous jetted quasars ($\Gamma \sim 1.75$; Sambruna et al. 1999) or non-jetted quasars ($\Gamma \sim 1.9$; Piconcelli et al. 2005). Several blazars reveal a flattening in their X-ray spectra at energies below ~ 2 keV with respect to a higher-energy power law (e.g. Fabian et al. 1998; Piconcelli & Guainazzi 2005). The origin of this flattening has been associated with intrinsic cold or warm absorption ($N_{\rm H} \sim 10^{22}\,{\rm cm}^{-2}$; e.g. Worsley et al. 2006) or a break of the continuum due to intrinsic curvature of the EC emission from the jet

(e.g. Ghisellini et al. 2007; Tavecchio & Ghisellini 2008; Paliya et al. 2016). Some sources, instead, reveal the presence of an excess in emission at similar soft energy ranges. Various scenarios have been suggested in order to explain this feature such as an excess due to the contribution of the accretion disc emission to the soft X-rays (Sambruna et al. 2006), similar to the one seen in non-jetted AGNs, or an increase in the contribution of the SSC component (Kataoka et al. 2008). Bulk Comptonization (BC) emission has been proposed as an alternative explanation of spectral flattening and/or excess (e.g. Begelman & Sikora 1987; Sikora et al. 1994; Celotti et al. 2007). In this context, cold (i.e. non-relativistic) leptons, travelling with a bulk Lorentz factor $\Gamma_{\rm bulk}$, would interact with the photons produced by the accretion disc, and with those reprocessed (re-isotropized) in the BLR and/or scattered by free electrons external to the jet. The BC emission of disc and BLR photons would result in an excess emission with respect to the power-law continuum, emerging in the far ultraviolet (hence not accessible) and mid X-ray ranges, respectively. The latter component would correspond to a hump peaking at ~ 3 keV (approximated by a blackbody), accompanied by a flattening towards softer energies, which can mimic absorption. It should be noted that the peak energy of this feature depends on the Lorentz factor of the emitting region and on the viewing angle of the observer. The two flavours of the soft X-ray spectral break (deficit or excess) have been usually treated as originated from different processes. Celotti et al. (2007) modelled the flattening seen in the blazar GB B1428+217 ($z = 4.72$) assuming a transient BC scenario. The flattening in this source had been suggested to be due to the presence of intrinsic absorption with column densities exceeding $10^{22}\,{\rm cm}^{-2}$ (e.g. Boller et al. 2000; Fabian et al. 2001; Worsley et al. 2006). It should be noted that BC is expected to be present in all blazars but has never been confirmed, to my knowledge. Besides the case of GB B1428+217, Kataoka et al. (2008) and de Rosa et al. (2008) presented tentative hints of the presence of BC in the FSRQs PKS 1510–089 ($z = 0.361$) and 4C+04.42 ($z = 0.965$), respectively.

The flat spectrum radio quasar (FSRQ) 4C+25.05 (a.k.a. PKS 0123+257, $z = 2.368$, $\log(M_{\rm BH}/M_{\odot}) = 9.24 \pm 0.44$; Kelly & Bechtold 2007) simultaneously by *XMM-Newton* and *NuSTAR*, on 2017 January 15 (Obs. IDs 0790820101 and 60201047002, respectively). The log of the observations is presented in Table 2.4.

2.2.1 X-ray observations and data reduction

The *XMM-Newton* and *NuSTAR* data were reduced following a similar procedure to the one described in Section 2.1.1. The *XMM-Newton* and *NuSTAR* are analysed in the 0.3–10 keV and 3–30 keV ranges in the observed frame, respectively, which

Table 2.4: Net exposure time, average net count rate and ratio of the source to total counts, in the observed 0.3–10 keV band for EPIC-pn and MOS, and 3–30 keV band for FPMA/B, for 4C+25.05.

Instrument	Net exposure (ks)	Count Rate (Count s^{-1})	Source/total
pn	37.7	0.522 ± 0.003	99%
MOS	49.4	0.305 ± 0.003	98.8%
FPMA	40.4	0.047 ± 0.001	90.3%
FPMB	40.4	0.043 ± 0.001	86.9%

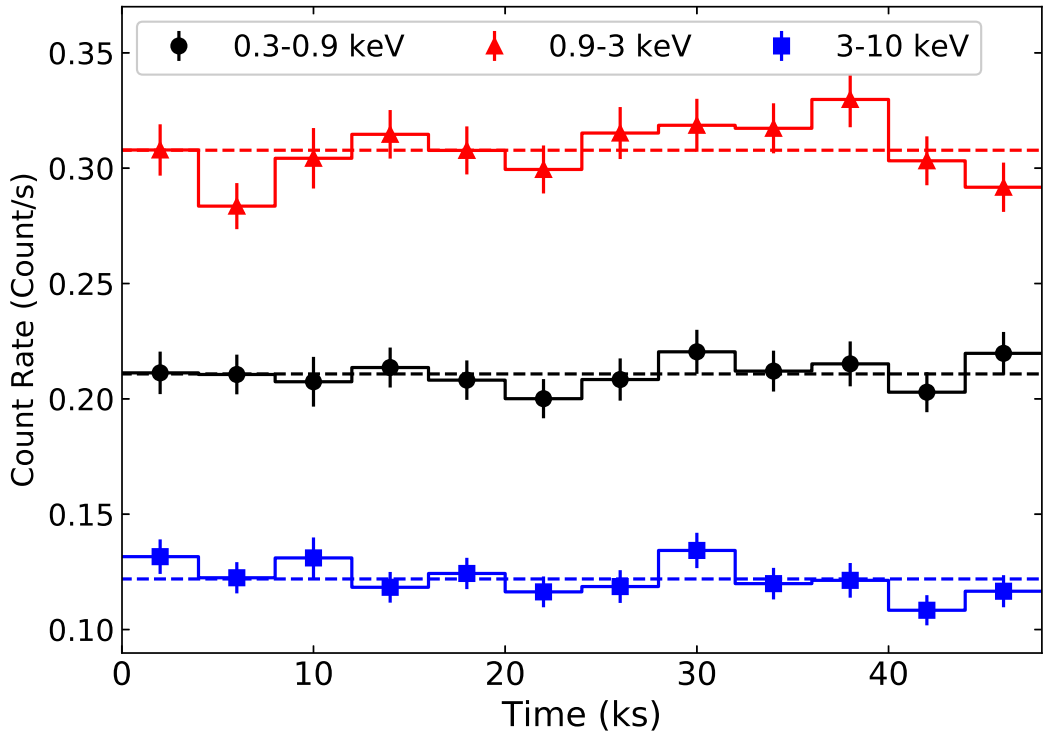

Figure 2.5: *XMM-Newton* light curves (with a time bin of 4 ks) extracted in the 0.3–0.9 keV (black circles), 0.9–3 keV (red triangles) and 3–10 keV (blue squares) observed energy bands, corresponding to the ∼1–3 keV, 3–10 keV and 10–34 keV rest-frame energy bands, respectively. The horizontal dashed lines correspond to the average count rate for each energy band.

correspond to $\sim 1 - 33$ keV and $\sim 10 - -100$ keV in the rest frame of the source. The EPIC-pn light curves, background-corrected using `EPICLCCOR`, are shown in Figure 2.5 in three different bands (soft, medium, hard). The light curves were consistent with the *NuSTAR* ones in the hard range. None of them shows any significant variability, as they are all well-fitted with a constant. The log of the observation is presented in Table 2.4.

2.2.2 X-ray Spectral analysis

In the following, spectral fitting was performed using `XSPEC` v12.9s (Arnaud 1996). Unless stated otherwise, uncertainties on the parameters are listed at the 90 per cent confidence level ($\Delta\chi^2 = 2.71$). I included a multiplicative constant, for each instrument, in order to account for the residual uncertainties in the flux calibration between the various detectors, fixing the constant for the EPIC-pn data to unity. The spectra from the various instruments are shown in Figure 2.6a.

I started by fitting the hard-energy part of the spectra above 3 keV (observed) with a power-law model with a high-energy cutoff (hereafter PL model), taking into consideration the Galactic absorption in the line of sight ($N_{\rm H} = 6.87 \times 10^{20}\,{\rm cm}^{-2}$; Kalberla et al. 2005). The fit is statistically acceptable ($\chi^2/{\rm dof} = 181/220$), showing no systematical trend in the residuals, with a photon index $\Gamma = 1.34 \pm 0.13$. I could only set a 3σ lower limit for the high-energy cutoff of $E_{\rm cut} > 63$ keV (in the rest frame). The cross-calibration factor between *NuSTAR* and *XMM-Newton* was found to be $f_{\rm NuSTAR} = 1.09 \pm 0.06$, consistent with the values reported by Madsen et al. (2015). The extrapolation of this model to lower energies reveals an excess below ∼5 keV (rest-frame), as shown in Figure 2.6b. I re-fitted the same model to the full 0.3–30 keV observed range. The fit is statistically acceptable ($\chi^2/{\rm dof} = 373/359$, $p_{\rm null} = 0.29$). The residuals are not statistically significant, yet, qualitatively, they show a subtle overall curvature, leading to a systematic excess in the ∼1.5–3 keV range. The best-fit photon index is steeper than the previous case ($\Gamma = 1.54 \pm 0.01$). $E_{\rm cut}$ is pegged to its maximum allowed value, with a 3σ lower limit of 387 keV (in the rest frame). The cross-calibration factor between *NuSTAR* and *XMM-Newton* becomes larger, $f_{\rm NuSTAR} = 1.14 \pm 0.04$. I re-fitted the spectra accounting for the possible intrinsic neutral absorption in the rest frame of the source (`zTBabs`; Wilms et al. 2000a). The fit did not show any improvement ($\chi^2/{\rm dof} = 373/358$), revealing an intrinsic absorption that is consistent with zero (I could set a 3σ upper limit on $N_{\rm H}$ to be $9.5 \times 10^{20}\,{\rm cm}^{-2}$). I show the residuals corresponding to this model in Figure 2.6c.

I considered several models, in order to account for the possible excess at soft energies. I first fitted the spectra with a broken power-law model (hereafter BPL model) modified by Galactic absorption only. The fit was statistically acceptable ($\chi^2/{\rm dof} = 343/357$) with the photon indices being $\Gamma_{\rm soft} = 1.56 \pm 0.03$, $\Gamma_{\rm hard} = 1.29 \pm 0.11$. The break and cutoff energies are $E_{\rm b} = 9.2^{+1.2}_{-1.6}$ keV and $E_{\rm cut} = 121^{+139}_{-44}$ keV in the rest frame. The 3σ confidence level gives only a lower limit on $E_{\rm cut} > 60$ keV. The cross-calibration factor is $f_{\rm NuSTAR} = 1.08 \pm 0.05$. The fit improves by $\Delta\chi^2 = -30$ for one extra free parameter with respect to the PL model. This improvement

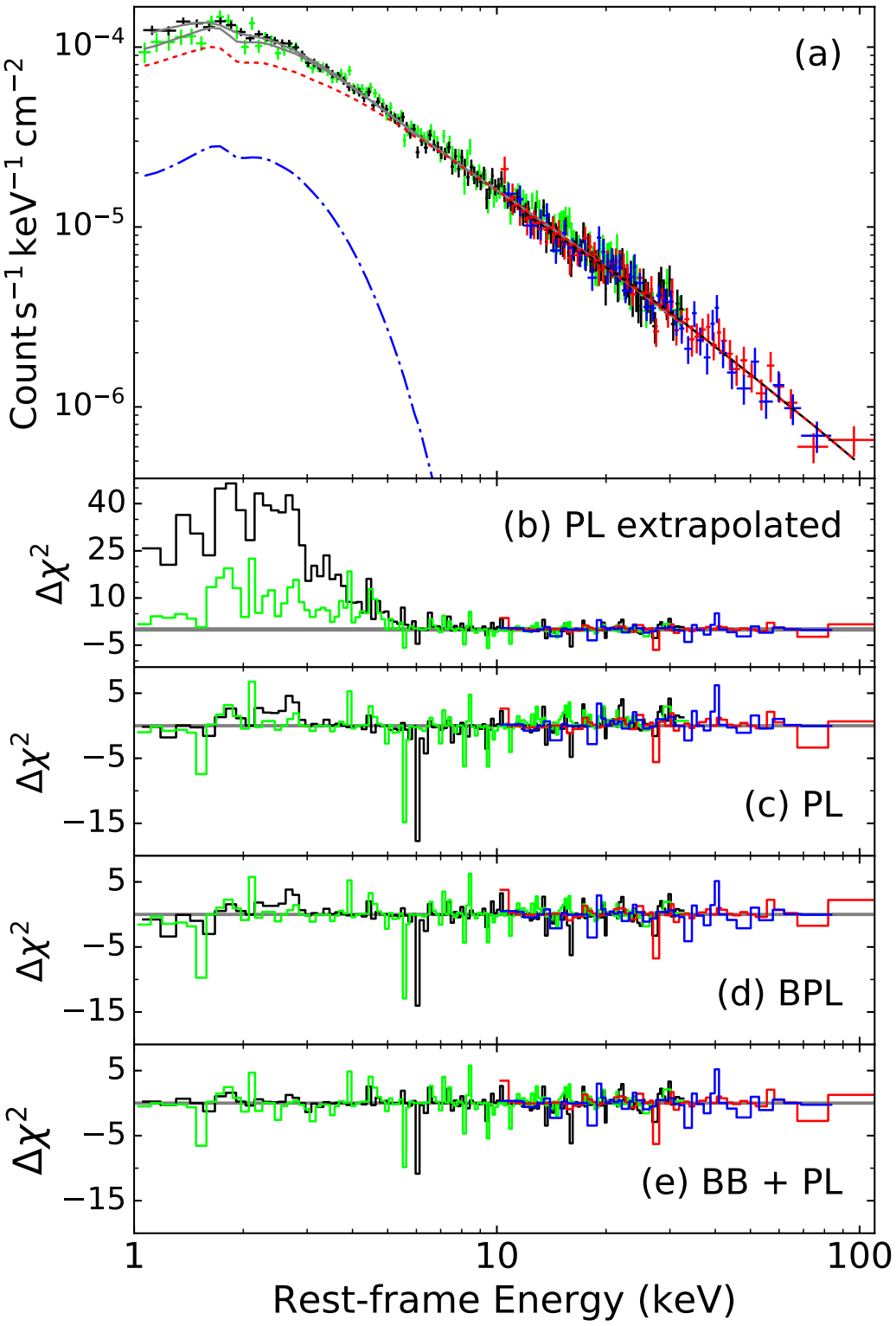

Figure 2.6: Panel (a): Spectra from EPIC-pn (black), EPIC MOS (green) and *NuSTAR* FPMA/FPMB (red/blue) plotted together with the total best-fitting model (grey solid line) composed of a PL (red dotted line) and a BB component (blue dash-dotted line) plotted in the rest-frame energy. Panel (b): residuals obtained by fitting the spectra above 10 keV (rest-frame) with a PL model then extrapolating it to softer energies, showing an excess in the ∼1–5 keV range. Panels (c–e): residuals obtained by fitting the 1–100 keV range with a PL, BPL, and BB+PL models, respectively (see Section 2.2.2 for details).

Table 2.5: Best-fit parameters obtained by fitting the spectra with the PL, BPL and BB+PL models considered in this analysis. $E_{\rm b}$, $E_{\rm cut}$ and $kT_{\rm BB}$ are reported in the rest frame of the source. The last column represents the peak values of the 1D probability distribution obtained from the MCMC analysis.

Parameter	PL	BPL	BB+PL	
$N_{\rm H}$ (10^{20}cm^{-2})	$< 9.5^{\dagger}$	–	–	–
$\Gamma_{\rm soft}$	–	1.56 ± 0.03	–	–
$E_{\rm b}$ (keV)	–	$9.2^{+1.2}_{-1.6}$	–	–
$\Gamma_{\rm hard}$	1.54 ± 0.01	1.29 ± 0.11	$1.38^{+0.05}_{-0.03}$	1.41
$E_{\rm cut}$ (keV)	$> 387^{\dagger}$	121^{+139}_{-44}	205^{+256}_{-54}	210
$N_{\rm PL} \times 10^{-4}$	3.05 ± 0.05	3.13 ± 0.07	$2.63^{+0.11}_{-0.08}$	2.65
$kT_{\rm BB}$ (keV)	–	–	$0.66^{+0.05}_{-0.04}$	0.66
$N_{\rm BB} \times 10^{-5}$	–	–	$1.92^{+0.32}_{-0.51}$	1.8
χ^2/dof	373/358	343/357	322/357	

† 3σ lower/upper limit.

is mainly due to the steepening of the spectrum at soft energies, leading to less prominent residual structures (as shown in Figure 2.6d), contrary to the commonly-seen flattening in other sources (e.g. Piconcelli & Guainazzi 2005).

I also tested a reflection model (`RELXILL`; Dauser et al. 2013, 2016), even though I do not detect any clear presence of either an iron line or a Compton hump. I fixed the spin to its maximum value (0.998) and I assumed a power-law illumination profile ($q = 3$) with a reflection fraction equal to unity. First, I let the inclination free to vary. The fit resulted in a very high inclination of the disc, which is not physical for this system. Then I fixed the inclination to 5°, which corresponds to a nearly face-on configuration. The fit is statistically acceptable (χ^2/dof = 362/357). The best-fit photon index, ionization parameter and iron abundance are: $\Gamma = 1.43^{+0.04}_{-0.08}$, $\log \xi = 3.72^{+0.08}_{-0.47}$, and $A_{\rm Fe} = 3.7 \pm 1.2$ solar, respectively. However, this model cannot be considered as a plausible explanation for the spectrum of 4C+25.05. On the one hand, it gives a statistically worse fit compared to the (phenomenological) BPL model. On the other hand, the Doppler-boosted featureless jet emission is expected to be much stronger than any reflection component, thus diluting all other features. Moreover, if the X-ray source illuminating the disc is a relativistically outflowing corona, then beaming effects would reduce the illumination of the disc, so any reflection component would be negligible (see also King et al. 2017).

Motivated by the BC model (Celotti et al. 2007), I considered a model defined as the sum of a blackbody component and a power law (hereafter BB+PL model). The model fits very well the data (χ^2/dof = 322/357), without any systematic

residuals. The best-fitting BB+PL model and the corresponding residuals are presented in Figure 2.6a,e, respectively. The best-fitting parameters of the BB+PL model, and, for comparison, of the PL and BPL models as well, are presented in Table 2.5. The errors on the parameters, for the BB+PL model, are calculated from an MCMC[5] analysis, starting from the best-fitting model that I obtained. I used the Goodman-Weare algorithm (Goodman & Weare 2010) with a chain of 500,000 elements (100 walkers and 5000 iterations), and discarding the first 75,000 elements as part of the 'burn-in' period. The rest-frame temperature of the blackbody is $kT_{\rm BB} = 0.66^{+0.05}_{-0.04}$ keV, equivalent to a peak energy $E_{\rm peak,\,BB} = 3.93kT_{\rm BB} \simeq 2.6 \pm 0.2$ keV (in νF_ν), consistent with the expected value (e.g. Celotti et al. 2007). In this case, the values of the photon index and the high-energy cutoff are $\Gamma = 1.38^{+0.05}_{-0.03}$ and $E_{\rm cut} = 205^{+256}_{-54}$ keV (rest frame), respectively. These values are consistent with the ones that I obtained by fitting a PL model to the spectra above 3 keV, and the hard component of the BPL model. The 3σ confidence level gives only a lower limit on $E_{\rm cut} > 110$ keV. The results of the MCMC analysis are shown in Figure 2.7. It should be noted that the peak values of the 1D probability distribution obtained from the MCMC analysis (presented in the last column of Table 2.5) do not exactly coincide with the best-fit values obtained by minimizing the χ^2 value, but they are consistent within 1σ. The contours show that the temperature of the blackbody is not degenerate with any other parameter, confirming the presence of a significant excess over this energy range. Instead, I found some degeneracy between the normalizations of the PL and that of the BB and between both normalizations and the photon index. The mild degeneracy between the BB normalization with the photon index indicates that a steepening in the PL slope tends to compensate for the BB component. Furthermore, I determine the flux of the source to be $F_{0.3-10} = 2.25^{+0.01}_{-0.05} \times 10^{-12}$ erg s^{-1} cm^{-2} in the 0.3–10 keV observed energy range, which corresponds to a luminosity of $L_{1-30} = (9.44 \pm 0.07) \times 10^{46}$ erg s^{-1} in the 1–30 keV rest-frame energy range. The errors on the flux and luminosity represent the 1σ confidence level.

2.2.3 Discussion and conclusions

In summary the observed spectrum of the source in the 0.3–30 keV range can be well explained by (Table 2.5):

[5] I use the `XSPEC_EMCEE` implementation of the `PYTHON EMCEE` package for X-ray spectral fitting in XSPEC by Jeremy Sanders (`http://github.com/jeremysanders/xspec_emcee`).

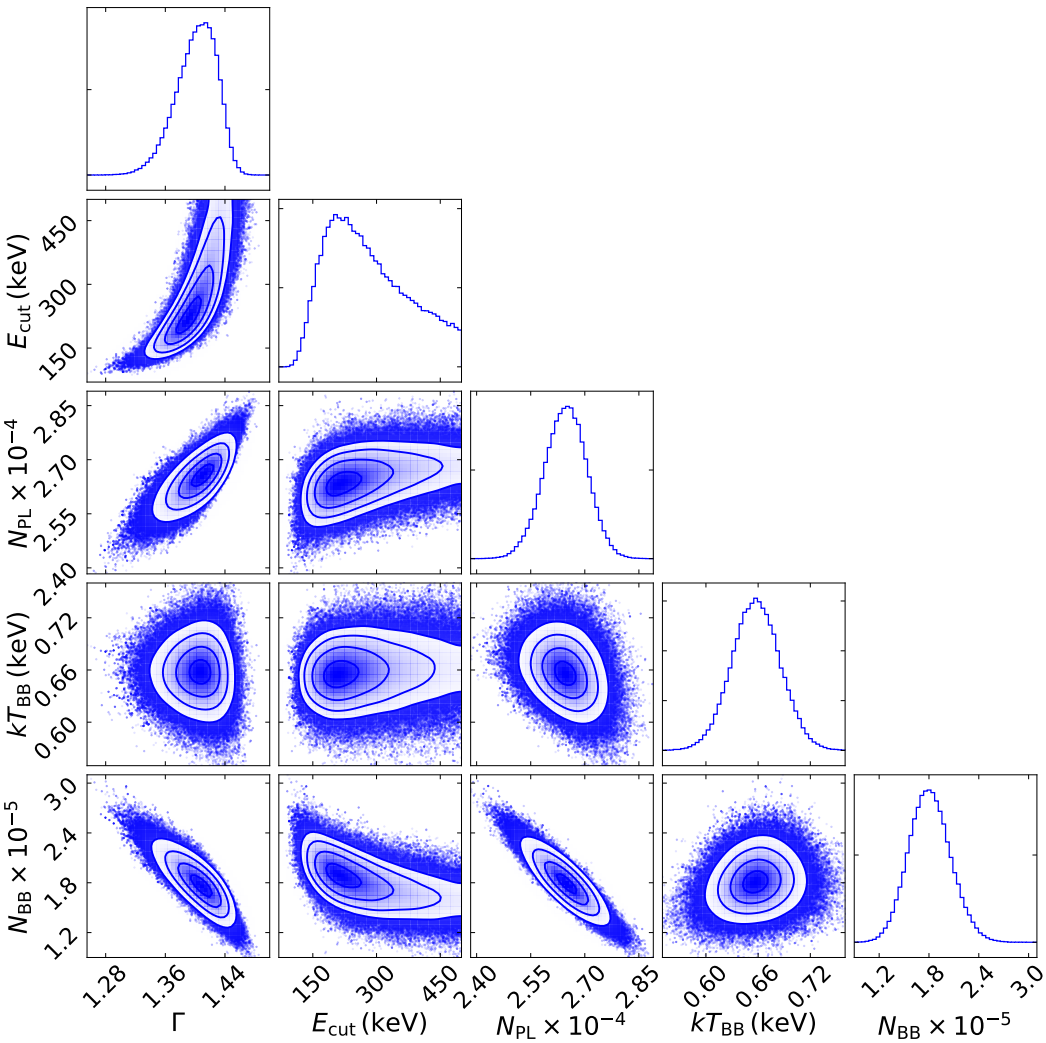

Figure 2.7: Results of the MCMC analysis of the PL+BB model. I show the outputs for photon index Γ, cutoff energy $E_{\rm cut}$ (keV), blackbody temperature $kT_{\rm BB}$ (keV), and normalizations of the power-law and the blackbody components $N_{\rm PL}$ and $N_{\rm BB}$, respectively. The 1D histograms show the probability distribution for each parameter normalized to unity.

(i) A simple power-law model (χ^2/dof = 373/358) of photon index $\Gamma = 1.54$. Only upper and lower limits can be set for any intrinsic absorption and high-energy cutoff, respectively.

(ii) A broken power-law model (χ^2/dof = 343/357), with $\Gamma_{\rm soft} = 1.56$, $\Gamma_{\rm hard} = 1.29$, break energy of $E_{\rm b} = 9.2\,$keV and cutoff at $E_{\rm cut} = 121\,$keV (rest frame).

(iii) A power-law plus blackbody model (χ^2/dof = 322/357), with $\Gamma = 1.38$, $E_{\rm cut} = 205\,$keV and $kT_{\rm BB} = 0.66\,$keV.

The BPL model is largely phenomenological, yet the steeper $\Gamma_{\rm soft}$ with respect to $\Gamma_{\rm hard}$ clearly indicates a softening in the soft X-rays, as opposed to the flattening

(due to either absorption or intrinsic curvature of the EC emission from the jet) usually observed in high-z blazars. This excess favours the possibility that we are witnessing the spectral signature of bulk Comptonization of BLR photons. Indeed, the BB+PL model has the lowest χ^2 among the various models that I have considered. The absence of any absorption in 4C+25.05 is confirmed by the two optical spectra obtained from the Sloan Digital Sky Survey (SDSS-IV; Dawson et al. 2016; Blanton et al. 2017) in 2012 and 2015 (red and blue lines in Figure 2.8, respectively), which do not show any signature of intrinsic cold absorption. It should be noted that the SDSS spectra reveal the presence of narrow 'associated' absorption lines from Lyα, N V, Si IV and C IV (the C IV $\lambda\lambda$1548, 1550 doublet is shown in the inset in Figure 2.8). These features, rather common in flat-spectrum quasars (e.g. Richards et al. 1999; Richards 2001; Baker et al. 2002), indicate the presence of an ionized low-density ($N_{\rm H\,I} \lesssim 10^{17}\,{\rm cm}^{-2}$) absorber close to the central engine. However, it should be noted that this absorption system has been suggested to partially cover the background light (including both the continuum and broad emission-line region) by Barlow & Sargent (1997). I finally point out that the SDSS spectra reveal several broad emission lines, implying the presence of a proper BLR in this source. The BLR component has been already detected and well-discussed in previous studies (e.g. Baldwin 1977; Padovani 1989; Kelly & Bechtold 2007).

Our observation time is around 50 ks that corresponds to ∼15 ks or 4 hr in the rest frame of the source. As no variability has been observed during the observations, this implies that the BC of BLR photons is stable over this timescale. In fact, Celotti et al. (2007) showed that the intensity of the BC spectrum from scattered BLR photons increases with time as the jet is accelerating and remains constant once the jet has reached its maximum bulk Lorentz factor. Given $kT_{\rm BB}$, I can estimate the factor $\delta\Gamma_{\rm bulk}$, where $\delta = \Gamma_{\rm bulk}^{-1}(1-\beta\cos\theta_{\rm V})^{-1}$ is the relativistic Doppler factor and $\theta_{\rm V}$ is the angle between the observer and the jet axis. Following Celotti et al. (2007), I assumed that the BLR emission can be approximated by a blackbody spectrum peaking at the energy of the Lyα, $h\nu_{\rm Ly\alpha} = 2.8kT_{\rm BLR} = 13.6\,{\rm eV}$. The observed temperature of the BC component (in the rest frame of the source) is then $kT_{\rm BLR,\,obs} = \delta\Gamma_{\rm bulk}kT_{\rm BLR}$, from which $\delta\Gamma_{\rm bulk} = 136$. One may also derive the expressions of $\theta_{\rm V}$ and the apparent superluminal speed $\beta_{\rm a}$ as a function of $\Gamma_{\rm bulk}$. For $\Gamma_{\rm bulk} = \delta = 11.7$, I find $\theta_{\rm V} \simeq 5°$ and $\beta_{\rm a} \simeq 11.6$. Note that even if BC requires the presence of cold leptons, the jet is not likely to be pair dominated since in this case the plasma will suffer strong Compton drag and will be significantly decelerated (Ghisellini & Tavecchio 2010). Alternatively, the jet could be magnetically dominated and proton free, but this possibility is unlikely by noting that the SED of this source[6] is very similar to that of a typical FSRQ, for which Celotti & Ghisellini

[6]The archival SED can be built using the tool at https://tools.asdc.asi.it/.

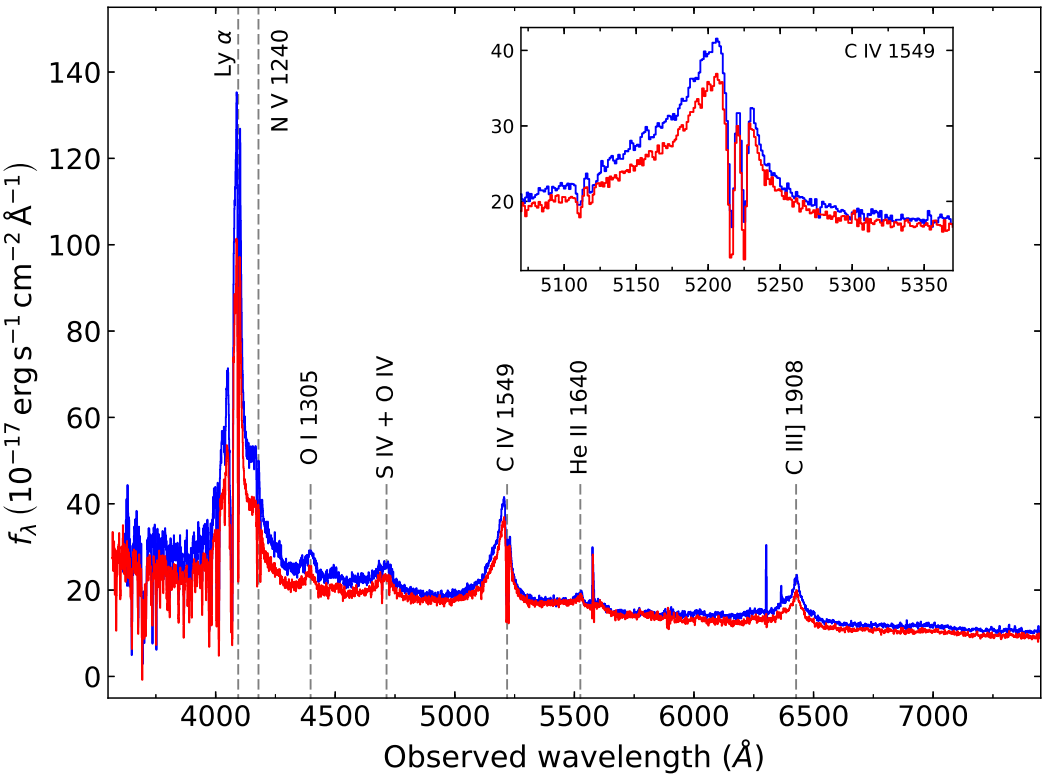

Figure 2.8: Optical spectra of 4C+25.05 obtained from the SDSS-IV. The inset shows the peak of the C IV emission line and the absorption doublet.

(2008) model the high-energy spectrum as inverse Compton emission. The X-ray spectrum of FSRQ 4C+25.05 is rising (in νF_ν) to higher energy, and the luminosity is already similar to that in the lower-energy synchrotron component. If the X-rays are due to inverse Compton scattering, the Compton peak dominates the bolometric electromagnetic output, and the magnetic-field component can only marginally contribute to the jet energy density.

BC emission is expected to be present in the X-ray spectra of all blazars. However, it has not been clearly detected until now. This can be mainly due to the presence of strong SSC and EC emission diluting any other emission features. In powerful FSRQs, the SSC is relatively weak, and the EC spectrum is exceptionally hard. These sources could be therefore the best candidates to search for BC signatures. It should be noted that excesses similar to the one that I have found at soft energies have been reported is several blazars at redshifts below one (e.g. Piconcelli et al. 2005; Sambruna et al. 2006; Kataoka et al. 2008; de Rosa et al. 2008), and modelled with a blackbody component with $kT_{\rm BB} \sim 0.1$–0.2 keV. However, this temperature range is lower than expected for the BC process, leading to low values of $\Gamma_{\rm bulk} \sim 5$–6. This makes 4C+25.05 an exceptional source where a softening in the X-ray spectrum

has been detected for the first time, to my knowledge, above $z = 1$, contrary to the soft X-ray flattening that has been observed up to $z = 4.72$ (e.g. Worsley et al. 2006). In the case of 4C+25.05, the hard X-ray photon index obtained by applying a BB+PL model is only slightly flatter than the one obtained by fitting a simple PL ($\Delta\Gamma \sim 0.15$). This difference would be negligible for low S/N at high energies. The failure in detecting BC, in the past, could be due to the possible overestimate of the slope of the hard X-ray continuum.

I was able in this study to identify the presence of the elusive BC feature at soft energies, that to the simultaneous *XMM-Newton* and *NuSTAR* observations, providing high S/N spectra over the observed 0.3–30 keV band. I finally note that BC is expected to be a transient feature. Hence, a further and longer monitoring of the source, catching it probably in other spectral states, would be needed in order to confirm this scenario. Moreover, it could be worth revisiting the model of BC effects, based on more general assumptions and geometries, including a disc-like structure for the BLR (similar to the one observed in non-jetted AGN) instead of the semi-spherical shell geometry considered by Celotti et al. (2007).

Facts which at first seem improbable will, even on scant explanation, drop the cloak which has hidden them and stand forth in naked and simple beauty.

Galileo Galilei

3

On the accuracy of reflection-based SMBH spin measurements in AGN

Contents

The increase in number and quality of AGN spectra, at various wavelengths, allowed astronomers to attempt a determination of the SMBH spin parameters with a relatively high confidence. A variety of observed features are considered as good indicators of the black hole spin, such as continuum shape (e.g. Done et al. 2013), broad iron Kα line (Fabian et al. 2000b), and quasi-periodic oscillations (QPOs; e.g. Mohan & Mangalam 2014). Recently, the detection of gravitational waves through the coalescence of black hole pairs founded a new technique to constrain the spins of non-accreting black holes and verifying the general relativity

predictions on space metric (Abbott et al. 2016a,b). There are several advantages and caveats relative to each method. Continuum fitting, for instance, can be applied to any AGN for which continuum emission is detected and has been applied to sources out to redshift ~ 1.5 (e.g. Capellupo et al. 2015, 2016). However, one of the main drawbacks of this method is that it requires a broad and simultaneous wavelength coverage, which usually exceeds the capabilities of a single observatory, in order to determine properly the shape of the relevant part of the SED (i.e. optical to X-rays). This method requires accurate estimates for the black hole mass, disc inclination, and distance, which are typically derived from optical data. Furthermore, the continuum fitting method can be applied effectively only when the peak of the emission from the accretion disc can be reasonably probed. Since most AGN spectra peak in the extreme UV, this range is only accessible by current detectors in high-redshift objects, at the expense of a rather modest quality for the corresponding X-ray spectra (e.g. Collinson et al. 2017). As for the QPOs, they are common in Galactic binaries while few examples exist in AGN light curves, most of which are statistically marginal and/or controversial (apart from the notable case of RE J1034+396; Gierliński et al. 2008). Their detection requires long monitoring, high signal-to-noise ratio (S/N), and a proper modelling of the continuum power spectrum (Vaughan & Uttley 2005, 2006).

The most direct and robust measurements to date are those obtained through the detection of a strong relativistic reflection feature in the X-ray spectra. This method can be applied to a wider black hole (BH) mass range. As discussed in Section 1.4, X-ray spectra of AGN can be expressed as a sum of several components, in particular a primary continuum that is well approximated by a power law with a high-energy exponential cut-off and ionized and/or neutral reflection that is detected in most of the sources, arising either from the accretion disc within a few gravitational radii from the BH or from distant Compton-thick material (the broad line region or the molecular torus), respectively (e.g. Lightman & White 1988; George & Fabian 1991; Ghisellini et al. 1994a; Bianchi et al. 2009). The resulting reflection spectrum is characterized mainly by the iron Kα emission line at $\sim 6.4 - 7.0\,\mathrm{keV}$ and a broad component peaked at around 20–30 keV, known as the Compton hump. Special and general relativistic effects result in blurring the ionized reflection spectrum and asymmetrically broadening the Fe Kα emission line owing to the gravitational redshift and the motion of the emitting particles in the disc (see Fabian et al. 2000b; Reynolds & Nowak 2003, for reviews). This method consists in fitting the X-ray spectrum of a given source with a reflection model accounting for the relativistic distortions that affect these features on their way to

the observer. Some of the models that predict the relativistic line profile for a narrow line emitted in the rest frame of the accretion disc are: `diskline`, `laor`, `kyrline`, `kerrdisk`, `relline` as published in Fabian et al. (1989); Laor (1991); Dovčiak et al. (2004); Brenneman & Reynolds (2006); Dauser et al. (2010), respectively. The resulting shape of the reflection spectrum strongly depends on the parameters of the system. Hence, this method can be used not only to determine black hole spins but also to probe the innermost regions of the accretion discs, providing information about its inclination, ionization state, elemental abundance, and emissivity (see Reynolds 2014, for a review). However, there are known difficulties in determining the spins via X-ray reflection, which are mainly due to the complexity of (and some subjectivity in) modelling the AGN spectra, considering the various emission and absorption components that are known to be present, hence requiring high-quality data (e.g. Guainazzi et al. 2006; Mantovani et al. 2016).

An alternative absorption-based interpretation has been proposed to explain the apparent, broad red wing of the Fe line and the spectral curvature below 10 keV (e.g. Miller et al. 2008, 2009). According to this scenario, partial-covering absorbers in the line of sight (having column densities in the 10^{22-24} cm^{-2} range) plus distant (i.e. non-relativistic) low-ionization reflection, can produce an apparent broadening of the Fe Kα line similar to that caused by relativistic effects. Variability in the covering fraction of these absorbers would also provide a complete description of the observed spectral variability.

Contrary to stellar-mass BHs in Galactic binaries, whose spectra are much brighter and typically less complex, both blurred reflection and partial covering are relevant to the X-ray spectra of AGN. In fact, while the former process is able, in principle, to explain the spectral and timing properties of any accreting system, the rapid Compton-thin to Compton-thick (and vice versa) transitions seen in changing-look AGN (after Matt et al. 2003) imply that also partial covering must be taken into account. In a single-epoch AGN spectrum, the effects of disc reflection and partial covering are often hard to separate or distinguish from each other, thus leading to a long-standing debate. However, thanks to the high-quality spectra provided by *XMM-Newton* (Jansen et al. 2001) and *NuSTAR* (Harrison et al. 2013) observations, which jointly cover a wide energy range from 0.3 keV up to 80 keV, it has now become possible to disentangle the two scenarios. This can be clearly seen in the case of NGC 1365 (Risaliti et al. 2013), which is one of the best cases lending weight to the idea that X-ray reflection is indeed an effective means of measuring the spin of SMBHs, even when absorption is present. This source was observed simultaneously for 4 orbits, by *XMM-Newton* and *NuSTAR*, in

2012-2013. Three different variable absorbers with column densities in the range $5 \times 10^{22} - 6.5 \times 10^{24}\,\mathrm{cm}^{-2}$ and variable covering factors would be needed to explain the spectrum of the source below 10 keV. However, this absorption-only model fails to explain the hard X-ray spectrum in the 10–80 keV band, where the inclusion of relativistic reflection provides a statistically better description of the data (Risaliti et al. 2013; Walton et al. 2014). Furthermore, the former model is also preferred on physical grounds, as the inferred bolometric luminosity in absorption-only scenarios is significantly higher compared to other indicators such as the [O III] λ5007 line.

3.1 Motivation

Our main aim is to test the reliability of spin measurements when the spectra include additional components with respect to the simple primary continuum plus disc reflection configuration (i.e. always, in principle). In fact, the innermost emission components are generally subject to absorption by gas with column densities from $N_\mathrm{H} < 10^{21}\,\mathrm{cm}^{-2}$ to $N_\mathrm{H} > 10^{24}\,\mathrm{cm}^{-2}$ and ionization states from neutral to almost completely ionized. As demonstrated by the case of NGC 1365, the presence of a given absorption component can be better identified thanks to its variability. NGC 1365 is one of the unique sources showing frequent changes in its obscuration state. Recently, Risaliti (2016) summarized the various observational aspects of this source and proposed a multi-layer structure of the circumnuclear medium to explain all the observed absorption states and their variability. NGC 1365 has been observed several times in reflection-dominated states, suggesting the presence of a layer of neutral Compton-thick ($N_\mathrm{H} > 10^{24}\,\mathrm{cm}^{-2}$) absorber located at a distance of the order of or larger than that of the broad line region (Risaliti et al. 2007). The source is usually caught in a Compton-thin state, $N_\mathrm{H} \sim 10^{23}\,\mathrm{cm}^{-2}$, but the column can even occasionally drop down to $N_\mathrm{H} \sim 10^{22}\,\mathrm{cm}^{-2}$ (Braito et al. 2014). Furthermore, absorption lines have been detected when the source is not heavily obscured, indicating a stratification of absorbers with ionization states ranging from highly ionized ($\log \xi > 3$) to mildly ionized ($\log \xi \sim 1 - 2$) down to neutral ($\log \xi < 1$). *All* these components and absorption states can be present in *all* AGN. However, their detection in a single source, also at different times, is highly dependent, on the one hand, on our line of sight, and, on the other hand, on the chance to observe any given component when variability is present.

The repetition of measurements (via X-ray reflection) can result in inconsistent values of the spin parameter for a given source. The discrepancy is mainly due to the use of different components in modelling the spectra, such as the use of

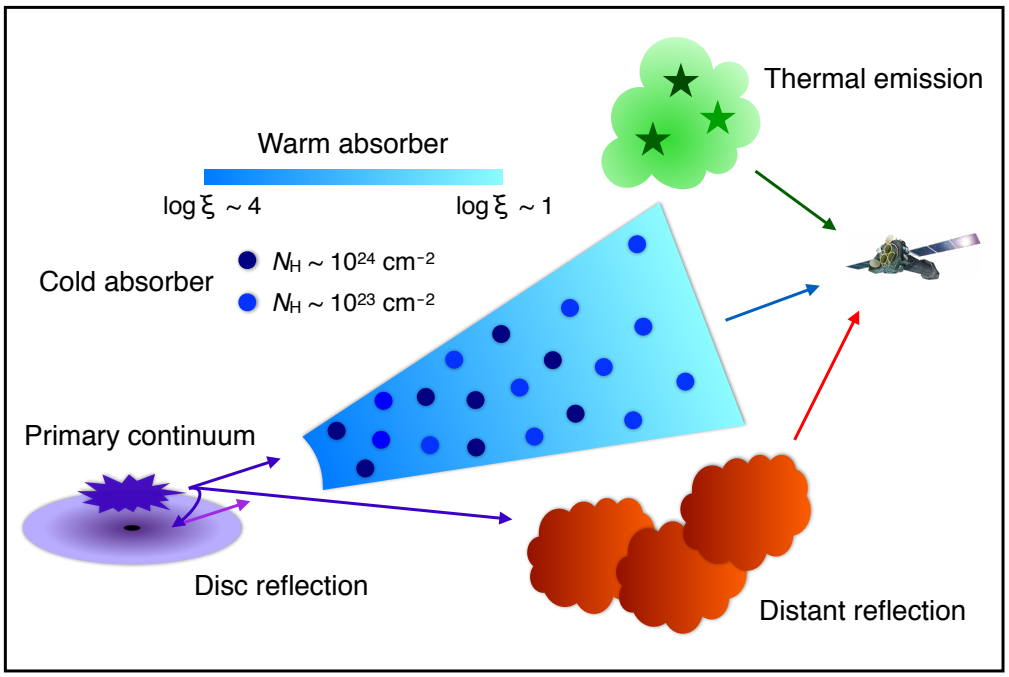

Figure 3.1: Schematic (not to scale) of the proposed configuration, presenting the various emission and absorption features that we consider in the simulations (See Section 3.2 for details).

dual reflectors, partial-covering, and/or warm absorbers. For example, Patrick et al. (2011) analysed the *Suzaku* spectra of NGC 3783, among others, and found the spin parameter in this source is $a^* < -0.04$. This result contradicts the high spin parameter ($a^* \geq 0.88$) found by Brenneman et al. (2011) and Reynolds et al. (2012), who analysed the same observations.

In this chapter, we suggest a preliminary study aiming to test, through the simulation of high-quality *XMM-Newton* and *NuSTAR* spectra (in the 0.3–79 keV range), the reliability of reflection-based SMBH spin measurements that can currently be achieved. A similar approach has been adopted recently by Bonson & Gallo (2016) and Choudhury et al. (2017), who simulated AGN spectra by assuming only two components: primary emission and relativistic reflection. Instead, we assume a more complex spectral configuration, closer to the real general case. This is presented below, along with a detailed description of how we simulated and fitted the data. We note that both of the aforementioned studies neglected the soft X-ray band, in which the soft excess can be a crucial driver of reflection-based spin determinations (e.g. Walton et al. 2013).

3.2 Simulation set-up

As mentioned above, various emission/absorption components can be present in the X-ray spectrum of any AGN. However, depending on the state in which the source is caught, we may be able to observe all or only some of these components. Generally, the Ockham's razor argument is (or should be) applied during the spectral fitting, thereby avoiding the inclusion of unnecessary components. While this is the correct practice, we might miss a component that is actually present in the case of a single-epoch observation, either if the spectra do not cover a broad band or do not have enough S/N. We know from the literature the expected ranges of the parameters for the various components that are observed and are potentially present in any AGN spectrum. Hence, we can simulate the most general spectrum and then examine how well the model parameters are recovered using the common fitting techniques.

We simulated AGN spectra in the 0.3–79 keV band via the XSPEC v12.9.0s (Arnaud 1996) command `FAKEIT` and the *XMM-Newton* EPIC-pn (Strüder et al. 2001) and the *NuSTAR* response matrices in the 0.3–10 keV (with an exposure time of 90 ks)[1] and 3–79 keV (with an exposure time of 100 ks, i.e. 50 ks per focal plane module) ranges, respectively. The spectra were binned not to oversample the FWHM resolution by a factor larger than 3 and 2.5 for *XMM-Newton* and *NuSTAR*, respectively. Then, we grouped the spectra, for both instruments, to ensure a minimum S/N of 5 in each energy channel. The simulations are intended to represent single-epoch observations of bright low-redshift AGN, similar to the observed sources, using *XMM-Newton* and *NuSTAR* simultaneously. Hence, we defined a generic parent model that contains the various expected emission and absorption components. The former are described below through their Xspec spectral counterparts:

- `APEC`: thermal diffuse emission at soft X-rays arising from the host galaxy in the cases when the star formation rate is enhanced and/or from gas photoionized by the AGN in the narrow line region (see Nardini et al. 2015, for the reference case of NGC 1365, and references therein for other notable sources). The parameters of this model that were varied during the simulations are the temperature of the gas (kT) and its abundance in solar units (from Grevesse & Sauval 1998).

[1] This is approximately the maximum effective exposure per *XMM-Newton* orbit in Small Window mode (needed to avoid pile-up in bright sources).

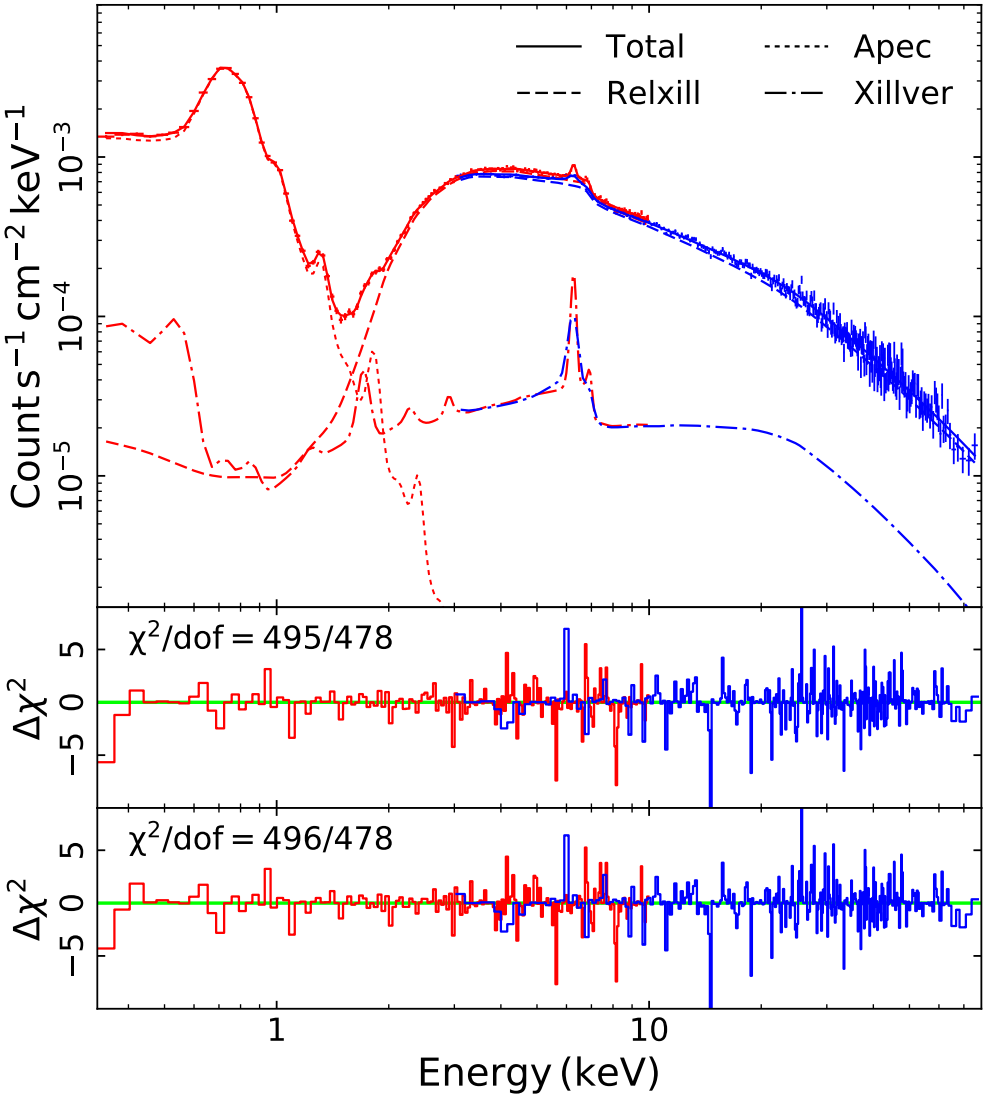

Figure 3.2: Top panel: Example of the simulated *XMM-Newton* (red) and *NuSTAR* (blue) spectra (corresponding to simulation G8) together with the various components of the theoretical model assumed. The primary emission plus ionized reflection (dashed lines), neutral reflection (dash-dotted lines), and thermal emission (dotted lines) are shown. Middle and bottom panels: The χ^2 residuals obtained by the two separate fits are indicated (see Section 3.3 for details).

- `RELXILLLP v0.4a`: primary emission plus blurred relativistic reflection from ionized material, assuming a lamp-post geometry for the emitting source (Dauser et al. 2013; García et al. 2014). The free parameters of this model are the photon index (Γ) of the incident continuum, the height of the lamp post (h, in units of $r_{\rm g}$), the spin parameter (a^*), and the inclination (i), ionization parameter ($\xi_{\rm d}$), and iron abundance ($A_{\rm Fe}$ in solar units) of the accretion disc. We kept the high-energy cut-off fixed to 300 keV. The reflection fraction is computed self-consistently within the model and fixed to the lamp-post value (`fixReflFrac = 1`), as defined in Dauser et al. (2016). This also implies that the disc emissivity as a function of radius is fully determined by the height of the X-ray source.

- `XILLVER`: neutral reflection arising from distant material by fixing the ionization parameter, inclination angle and iron abundance of the reflector to $\log \xi = 0$, $i = 45^\circ$ and $A_{\rm Fe} = 1$, respectively. For simplicity, we tied the values of the photon index and the high-energy cut-off of this component to those of the primary continuum.

As for the absorption components, we modelled the Galactic column using the `PHABS` model and assuming $N_{\rm H} = 5 \times 10^{20}\,{\rm cm}^{-2}$. We assumed that the intrinsic absorption can affect only the innermost emission components (primary continuum and relativistic reflection), and we considered the following configuration:

- `WARMABS`: fully covering warm absorption modelled through an XSTAR table (Kallman & Bautista 2001) having an input continuum with a photon index of 2. Although it is usually seen in outflow (e.g. Braito et al. 2014, and references therein), we assume for simplicity that this component is at rest in the local frame. The free parameters of this model are the column density $N_{\rm H,\,wa}$ and the ionization parameter of the absorber $\xi_{\rm wa}$.

- `ZPCFABS`: two layers of partially covering neutral absorbers that can represent the various neutral-absorption states (from Compton-thin to Compton-thick regimes). We let free to vary the column densities $N_{\rm H,\,1/2}$ and the covering fractions ${\rm CF}_{1/2}$ of both absorbers.

The final model can be written in XSPEC terminology, neglecting Galactic absorption, as follows:

$$\begin{aligned}\texttt{model} = {} & \texttt{WARMABS} \times \texttt{ZPCFABS} \times \texttt{ZPCFABS} \times \texttt{RELXILLLP} \\ & + \texttt{XILLVER} + \texttt{APEC}.\end{aligned}$$

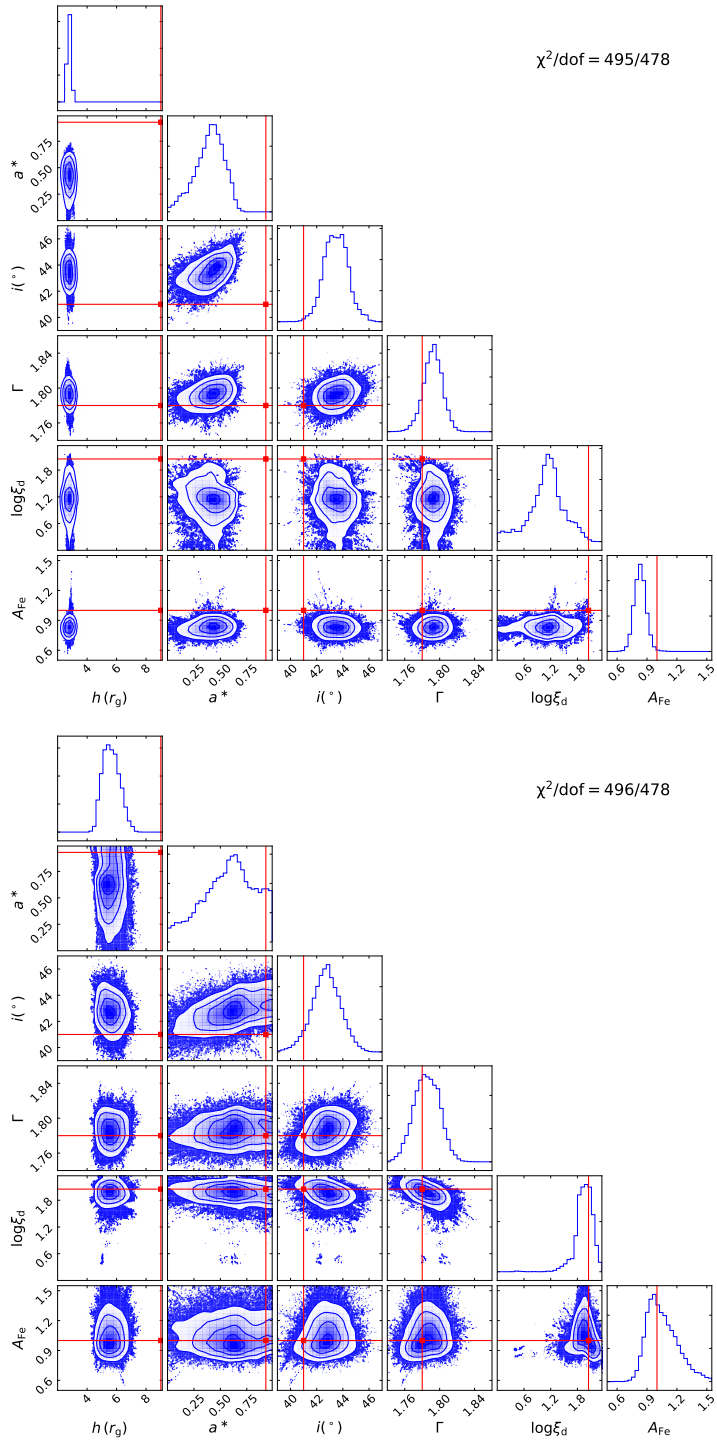

Figure 3.3: Results of the MCMC analysis for the relevant best-fit reflection parameters corresponding to the two different spectral fits shown in the middle and bottom panels of Figure 3.2. The red lines correspond to the input values assumed in order to create the simulations. We show the χ^2 values obtained from the corresponding best fit, whose accuracy as a whole is excellent in both cases. The individual parameters, however, are not all correctly retrieved.

Table 3.1: Key parameters used to perform the simulations with the corresponding input range, for the various emission and absorption components. All the key parameters were allowed to vary freely during the spectral fitting.

Parameter	Input range
Warm absorption	
$N_{\rm H,\,wa}\,(\rm cm^{-2})$	$10^{18} - 3 \times 10^{24}$
$\log[\xi_{\rm wa}\,(\rm erg\,cm\,s^{-1})]$	$0 - 5$
Reflection	
$h\,(r_{\rm g})$	$2 - 100$
a^*	$0 - 0.998$
$i(^\circ)$	$3 - 89$
Γ	$1.5 - 2.5$
$\log[\xi_{\rm d}\,(\rm erg\,cm\,s^{-1})]$	$0 - 4.7$
$A_{\rm Fe}\,(\rm solar)$	$0.5 - 10$
PC neutral absorption	
$N_{H,\,1}\,(10^{22}\,\rm cm^{-2})$	$0.01 - 20$
$\rm CF_1$	$0 - 1$
$N_{H,\,2}\,(10^{22}\,\rm cm^{-2})$	$0.01 - 500$
$\rm CF_2$	$0 - 1$
Thermal emission	
$kT\,(\rm keV)$	$0.1 - 1.5$
Abundance (solar)	$0 - 5$

A scheme of the proposed configuration is shown in Figure 3.1. We report in Table 3.1 the input range chosen for each of the free parameters considered in the simulations. The redshift of the simulated source is fixed at 0.02. We kept the normalizations of the various emission components free, and the only limitation is that the observed flux is between 1 and 3 mCrab in the 0.3–10 keV range (resulting in $\sim 3 \times 10^5 - 10^6$ counts, for the *XMM-Newton* spectra).

We note that the configuration we adopted may have some caveats on physical grounds. For instance, we neglected Compton scattering out of and into the line of sight for partial coverers with column densities $N_{\rm H} > 10^{24}\,\rm cm^{-2}$. In fact, this

would make the structure of the model much more complicated. On the one hand, accounting for the scattering into the line of sight would require arbitrary geometrical assumptions. On the other hand, the combination of partial covering and scattering out of the line of sight is not trivial in terms of model definition and handling. Even if these effects were treated properly, the actual physics of a real system would still be likely much more complex than the model we adopted. For example, the distant reflection is assumed to arise from a plane-parallel slab with an intermediate inclination of 45°, but this is just a coarse representation of the expected geometry of the reflector (see e.g. Yaqoob 2012). Moreover, this component might not be completely neutral; its ionization is low but not negligible, which leads to some heating near to the surface of the reflector (García et al. 2013). This mainly shifts the narrow iron K feature to higher energy. An additional complexity could be also due to the possible presence of multi-temperature thermal emission, a more complex structure of the warm absorption, or other forms of scattering into the line of sight. Finally, it should be kept in mind that the actual geometry of the X-ray corona is largely unknown. The point-like, lamp-post corona is a convenient approximation, but it also has some clear physical limitations, for instance a compactness problem similar to gamma-ray bursts (e.g. Fabian et al. 2015; Dovčiak & Done 2016). It is worth stressing, however, that none of our assumptions affect our results as long as the simulations and spectral fitting are performed in a self-consistent way.

3.3 Fitting procedure

Our group consisted of three people. In order to reduce the observer-expectancy effect, each simulation was created by one member of the group and fitted blindly by the two other members separately. The various spectral components mentioned above were allowed to be present or absent in any simulation (and fit), except for the primary continuum plus ionized reflection component, which was always included by construction. We first simulated a general set of 15 simulations (5 simulations per person; hereafter Set G, we refer to these simulations as G1–G15). The simulated parameters were allowed to vary within the input range, while in the fits they were free to vary without any restriction, apart from neglecting negative spins and heights below $2\,r_{\rm g}$. The Ockham's razor criterion was followed in the spectral analysis. A fit was considered as satisfactory at personal discretion, provided that 1) the overall statitistics was good, 2) the χ^2 value represented a stable minimum, and 3) no obvious residuals were present. This does not ensure that the accepted fit is strictly the best possible. Indeed, in some cases only a

local χ^2 minimum is found, revealing how critical this kind of analysis can be in practice (see Section 3.5 for a more detailed discussion).

An example of the simulated data with the theoretical model and the corresponding residuals from the two different fits is shown Figure 3.2. Errors on the parameters are calculated from Markov chain Monte Carlo (MCMC)[2], using the Goodman-Weare algorithm (Goodman & Weare 2010) with a chain of 510,000 elements (170 walkers and 3000 iterations), and discarding the first 51,000 elements as part of the 'burn-in' period. We show in Figure 3.3 the results of the MCMC analysis for the best-fit reflection parameters found for the simulated spectrum presented in Figure 3.2.

3.4 Results

We present in Table 3.2 a qualitative summary of the results we obtained from the blind spectral analysis, based on the classification criteria defined below. While these criteria are to a certain extent (but unavoidably) arbitrary, none of our conclusions are substantially modified.

• **Individual parameters:** For all the parameters, except for the spin and, to a lesser extent, iron abundance, the measurements are generally very well constrained. Thus, we define both a *full* and a *fair* success criterion. The former (denoted by the ✓ sign) is met when a measurement is consistent with the input value within a confidence level of 90%, while the latter (denoted by the ★ sign) is met when the fitted and input values are formally inconsistent, but agree with each other within a 10% uncertainty[3]. All the other cases are classified as *failures* (denoted by the ✗ sign).

• **Spin classification:** Since the measure of the spin is the main aim of our study and the spin is the parameter that shows the most complex behaviour in the fits, we adopted a different approach to classify the goodness of our constraints on the spin parameter. We divided the 0–0.998 spin range into three bands: low spin ($a^* \in [0, 0.4[$), intermediate spin ($a^* \in [0.4, 0.8[$), and high spin ($a^* \in [0.8, 0.998]$). Hence, we classified the measurements based on the following criteria: (a) full success if the measured value is consistent with the input one within the 90% confidence level and the uncertainty range is within a single spin band; (b) fair success if either the measured value is consistent with the input value within the 90% confidence level but the uncertainty range covers two spin bands, or the measured value is not consistent with the input value but the uncertainty range is within the

[2]We use the `XSPEC_EMCEE` implementation of the `PYTHON EMCEE` package for X-ray spectral fitting in XSPEC by Jeremy Sanders (http://github.com/jeremysanders/xspec_emcee).

[3]We note that we considered the ratios $\xi_{\rm fit}/\xi_{\rm input}$ for the ionization parameters of the accretion disc ($\xi_{\rm d}$) and of the warm absorber ($\xi_{\rm wa}$) rather than the ratios of the logarithms.

Table 3.2: Summary of the success/failure in measuring the relevant parameters for the three simulation sets. Simulations performed assuming a spin parameter < 0.8 are indicated with italics font, while the underline corresponds to a height of the lamp post that is $\leq 5\,r_g$. Symbols for the individual parameters are as follows: full success (✓), fair success (★), undetermined (**?**), added component (+), missing component (−), failure (✗), while blank corresponds to the cases when a given component is neither present in the simulated model nor in the fit. The qualitative classification of the fit as a whole is represented as follows: excellent fit (🟢), good fit (🟡), and inaccurate fit (🔴). See text for details.

Parameter	*G1*	*G2*	G3	G4	*G5*	*G6*	*G7*	G8	G9	*G10*	*G11*	*G12*	G13	*G14*	G15
a^*	✗★	★★	✓★	★★	★?	??	✓★	✗?	★★	?✓	✗✗	✗✗	✓✓	??	✓✓
h	✗✗	✓✗	✓✓	✓✓	✗✗	✓✓	✗✗	✗✗	✓✗	✗✗	✗✗	✗✗	✓★	✗✗	★✓
i	★★	✓✗	✓✓	✓✗	✓★	★★	✓✓	★✓	✗✓	✗✗	✓✓	✓✓	✓✓	✗✓	✓✓
Γ	✓★	✓✓	✓✓	★★	★★	✓✓	★✓	✓✓	✓✓	★✓	✓✓	✓★	✓✓	★✓	★✓
$\xi_{\rm d}$	✓✗	✗✗	✓✓	✓✓	✓✗	✗✗	✓✓	✗✓	✗✓	✗✓	✗✓	✗✓	★★	✗✓	✓✓
$A_{\rm Fe}$	✓✗	✗✓	✓✓	✓✓	✓✗	✓✓	✗✓	✗✓	✗✓	✗✗	✓✓	✗✓	✓✗	✗✓	✓✓
$N_{\rm H,\,wa}$	✓★	✗✗	✓✓	★✗	✓✓	✓✓	✓✓	★✓	✓✓	✗✓	✓✓	✓✓	✓✓	✓✓	✓✓
$\xi_{\rm wa}$	✗✓	✓✓	✓✓	✓✓	✓✓	✓✓	✓✗	✓✓	✓✓	✓✓	✓✓	★✓	✓✓	✓✓	✗✗
$N_{H,\,1}$	−✗	✗✗	✗✗	✓✗	+	✓✓	✓★		✗✓	✓✓	✓✓	−✓	✓✓	✓✓	✓✓
$\rm CF_1$	−✗	✓✓	✓✓	✗✗	+	✓✓	✓✓		✓✓	✓✓	✓✓	−✓	✓✓	✓✓	✓✓
$N_{H,\,2}$	✓★	+	✓✓	+	+	✓✓	✓✓	✗✓	✓✓	−★	✓✓	✓✓	✓✓	✓✓	✓✓
$\rm CF_2$	✓★	+	✓✓	+	+	✓✓	✓✓	✓✓	✓✓	−✓	✓✓	★✓	✓✓	✓✓	✓✓
kT	✓★	✓✓	✓✓	++	✓✓	✓✓	+	✓✓	✓✓	✓✓	✓✓	✓✓	✓✓	✓✓	✓✓
$N_{\rm xillver}$	✓✗	✓✓	★★	✓✓	✓✓	✓✓	✓✓	✓✓	✓✓	★✓	✓✓	✓✓	✓✓	✓✓	✓✓
Fit	🟡🔴	🟢🔴	🟢🟢	🔴🔴	🟢🔴	🟢🟢	🟢🔴	🟢🟢	🔴🟢	🔴🟡	🟢🟢	🟡🟢	🟢🟢	🟡🟢	🟢🟢

Parameter	K1	K2	K3	K4	K5	K6	K7	K8	K9	B1	*B2*	*B3*	B4	B5	B6
a^*	✗✗	✗✓	✗✗	✗✗	★★	★✗	★★	✓✓	✗✗	✗✗	✓★	✗✗	★★	✗✗	★✓
h	✗✗	✗✗	✗✗	✗✗	✓✗	✓✓	★✓	✓✓	✓✓	✓✓	✓✗	✗✗	✗✓	✗✗	★★
i	✓✗	✓✓	✓✓	✗✗	★✓	✓✗	★★	✓✓	✓✓	★★	✓✓	✓✓	✓✓	✓✓	✓✓
Γ	✓★	★✓	✓✓	★★	★★	★★	✓✓	★★	✓✓	✓✓	✓✓	✓✓	✓✓	✓✓	✓✓
$\xi_{\rm d}$	✓✗	✓✗	✓✓	✗✗	✗★	✓✗	✗✗	✓✓	✗✗	★✗	✓✓	✓✓	✓✓	✓✓	✓✓
$A_{\rm Fe}$	✓✗	✗✗	✓✓	✓✗	✗✓	★✗	✓✗	✗✗	✗✗	✓✓	✗✗	✓✓	✓✓	✓✓	✓✓
$N_{\rm H,\,wa}$		✗✗	✓✓	✗✗	✗★	✓✓	✓✗	✓✓	✗✗						
$\xi_{\rm wa}$		✗✓	✓✓	★✓	✗✓	✗✓	✓✓	✓✓	✓✗						
$N_{H,\,1}$	✓✓	✗✗	✓✓	✗✗	✗✓	+	✓✓	✓✓	−−						
$\rm CF_1$	✓✗	✗✓	✗✗	✗✗	✓★	+	✓✓	✓✓	−−						
$N_{H,\,2}$	+	★★	★★	★★	✗★	✓★	★★		✓✓						
$\rm CF_2$	+	★★	★★	★✓	✗★	✓✓	★★		★★						
kT	✓✗	✗✓	✓✓	−✓	★✓	✓✗	✓✓	✓✓	✓✓	++	✓✓	✓✓	✓✓	✓✓	✓✓
$N_{\rm xillver}$	✓✗	✓✓	✗✗	✓✗	++	✓✓	✓✓	✓✓	✓✓	✓✓	✓✓	✓✓	−✗	★★	✓✓
Fit	🟢🔴	🔴🟢	🟢🟢	🔴🔴	🔴🔴	🟡🔴	🟢🟢	🟢🟢	🟡🟡	🔴🔴	🟢🟢	🟢🟡	🔴🟢	🟢🟢	🟢🟢

same single band that contains the input value; (c) *undetermined* (denoted by the **?** sign) if the measured value is consistent with the input one but the uncertainty range covers three spin bands; and (d) *failure* for the other cases.

• **Fit accuracy:** Irrespective of the values of the individual parameters and their degree of adherence to the input values, we also defined the following quality criteria for the accuracy of the whole fit: a) *excellent* if the adopted model is correct and the fit statistic is within a $\Delta\chi^2$ of 2.3 from the putative absolute minimum (see below); b) *good* if either the model is correct and the distance from the absolute minimum is $\Delta\chi^2 < 9.2$, or the model misses a component that turns out to be significant at less than 99%; c) *inaccurate* in all the other cases, including overfitting. The absolute minimum is evaluated as $\min\{\chi^2_0, \chi^2_{\rm a}, \chi^2_{\rm b}\}$, where χ^2_0 is obtained by applying a posteriori the input model and $\chi^2_{\rm a,b}$ are the results from the blind spectral analysis (provided that the correct model is used). We found that 18 out of 30 fits were excellent, 4 out of 30 were good, and 8 out of 30 were inaccurate. We note that the application of the correct model (i.e. corresponding to the input one), as becomes evident below, does not imply that the input parameters are individually recovered with success (see Figure 3.3). We stress again, however, that even inaccurate fits are fully acceptable on statistical grounds and meet the three conditions listed in Section 3.3.

We summarize below the constraints that we obtained on the relevant parameters that are always present in the model by construction, distinguishing between accurate (either good or excellent) and inaccurate fits as follows:

- The measure of the *spin parameter* was a full/fair success in 7+4 cases, while it was undetermined/failed in 5+6 cases out of the 22 accurate fits. In the 8 inaccurate fits, 6 spins were fairly retrieved and 2 were undetermined. Low and intermediate spins (i.e. lower than 0.8) were present in 9 out of 15 simulations (i.e. 18 spectral fits, 13 of which were accurate). A low spin value was determined correctly and well constrained in only 1 out of 18 cases. The measure of the spin was fairly successful in 5 cases and it was undetermined in 6. However, for the 6 high-spin simulations (9/12 accurate fits), the measurements were successful in 10 cases (5 fully, 5 fairly), undetermined once, and the only failure was in a fit classified as excellent. In summary, the two different fits corresponding to the same simulated spectrum might result in different best-fit values of the spin parameter if one of the fits hits a secondary minimum or makes use of a *wrong* model, thus classified as inaccurate. However, even fully successful fits are not always able to recover the correct value of the spin, with a clear preference for high values.

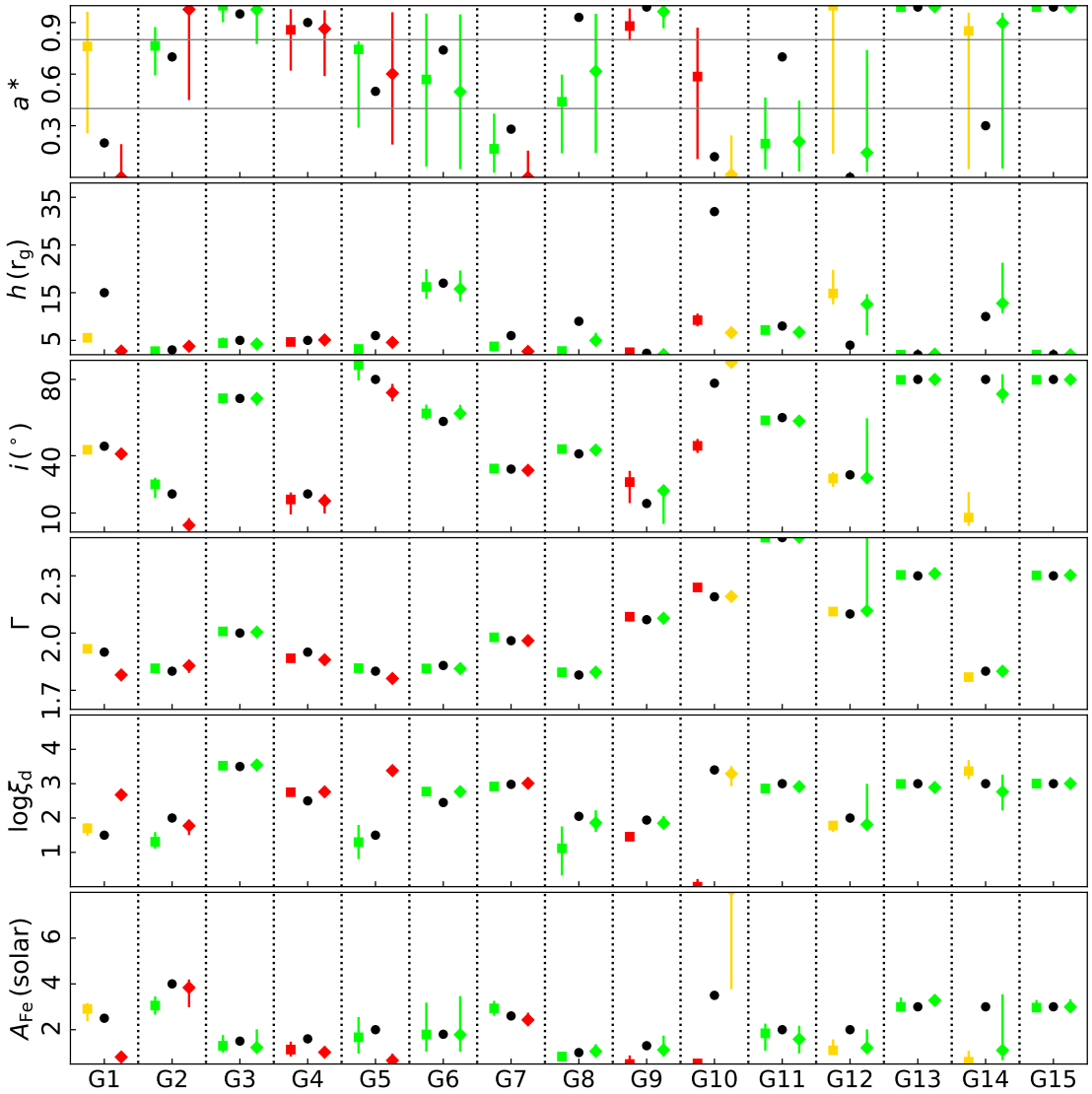

Figure 3.4: Input values (black dots) of the reflection parameters assumed for creating the various simulations (for Set G). The best-fit values obtained for the various parameters are shown as squares and diamonds for the two different realizations. The colour code refers to the quality of the fit as a whole: green for excellent, yellow for good, and red for inaccurate (see text for details). The error bars represent the 90 % confidence levels obtained from the MCMC analysis.

- The *height of the lamp post*, which is the other key parameter that determines the strength of the reflection component in the observed spectra, was measured with success in 7 (full) plus 2 (fair) cases, while it failed in the remaining 13 of the 22 accurate fits. However, 3 more full successes were found among the 8 other fits. The role of the source height is further discussed later on.

- The *disc inclination* was measured with success in 16 plus 4 of the accurate fits (2 failures) and 2 plus 2 of the inaccurate fits (4 failures).

- The *photon index* was measured successfully in all cases, of which 20/30 were a full success. We found a maximum difference between the measured and input photon index of $\Delta\Gamma = 0.12$.

- The disc ionization parameter was retrieved with success in 13 plus 2 of the accurate fits (with 7 failures) and 3 of the inaccurate fits (5 failures).

- The measure of *iron abundance* was fully successful in 15/22 accurate fits and in 4/8 inaccurate fits, and unsuccessful in all the other cases.

As already noted, the failure in measuring the single parameters might also occur in cases in which the fit is highly accurate for both analysts (e.g. G8, G11), which is a possible indication of complex degeneracies.

The various simulated spectra for Set G together with their corresponding residuals are presented in Figure A.1. The best-fit results relative to the reflection components are presented in Figure 3.4, while those for the absorption and thermal components are presented in Figure 3.5. Table A.1 shows the input and best-fit values of the lamp-post height and spin parameters. We report the best-fit χ^2/dof values in the same table.

3.5 Discussion

We simulated high-quality single-epoch spectra of AGN at low redshift in the 0.3–79 keV band using the responses of both *XMM-Newton* and *NuSTAR*. We assumed a general spectrum that includes, in addition to the primary emission, both ionized and neutral reflection, thermal emission, a warm absorber, and two layers of neutral partially covering absorbers. While in most cases the blind fitting procedure should be considered as successful, this fails in retrieving all of the individual input parameters. Below we examine the possible causes.

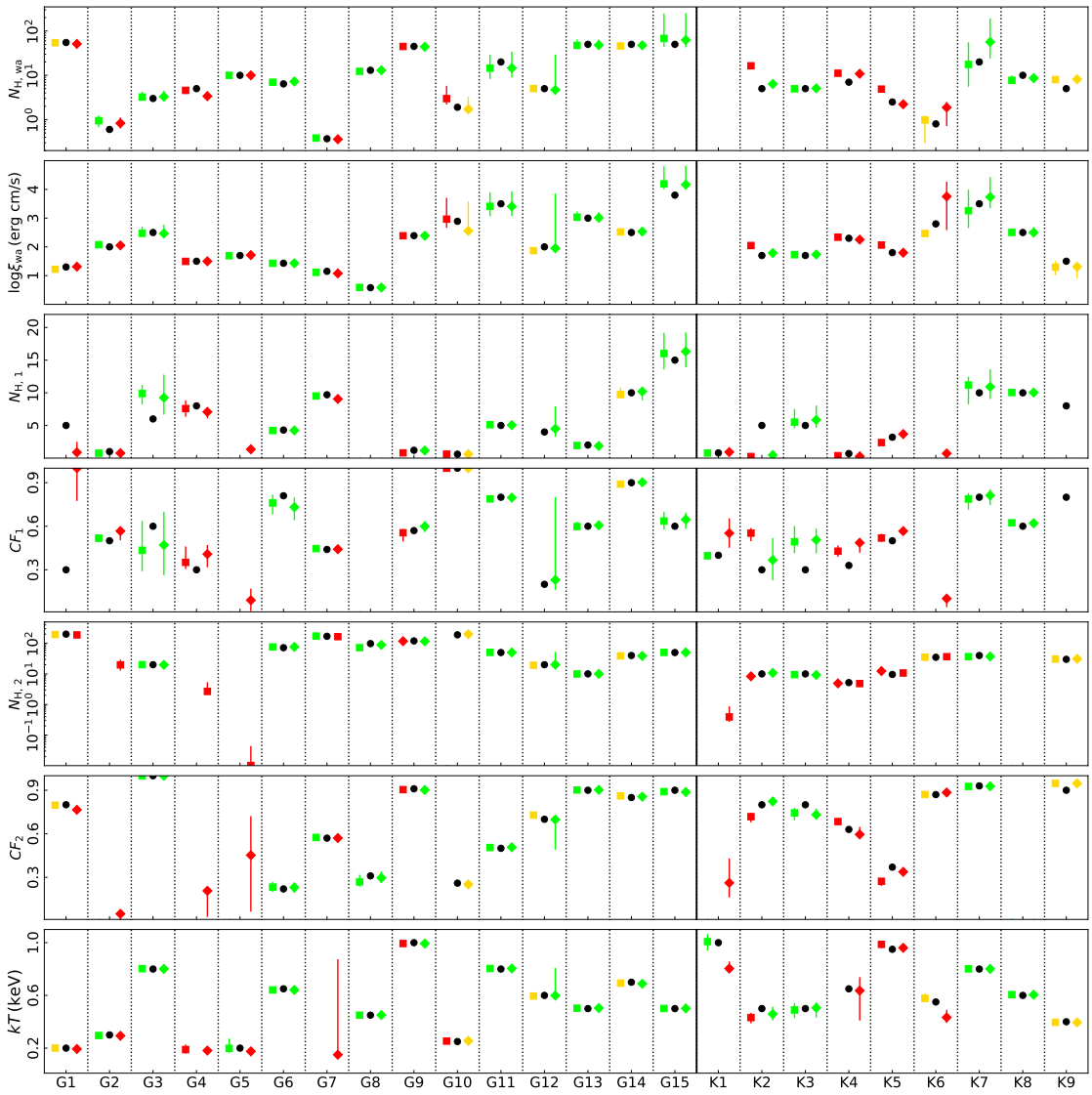

Figure 3.5: Similar to Figure 3.4 but for the absorption parameters (top panels) and the gas temperature of thermal emission component (last panel), presenting the results for Sets G and K. The column densities are in units of 10^{22} cm^{-2}.

3.5.1 The Kerr BH case

As noted in Section 3.4, spectral analysis tends to recover high input spins better than low/intermediate spins: 10 out of 12 high-spin measurements were at least fairly successful, while only 7 out of 18 low/intermediate spins were reasonably retrieved. Furthermore, the measured spin distribution, as reported in the literature, shows a clear tendency towards high spins (e.g. Walton et al. 2013; Reynolds 2014; Vasudevan et al. 2016). This evidence was the main motivation for us to simulate a set of high-spin spectra (hereafter Set K). Thus, we generated a set of 9 simulations (3 simulations per person) by fixing the spin parameter to its maximum allowed

value; we refer to these simulations as K1–K9. However, the spin parameter was free to vary within the 0–0.998 range during the spectral fitting. The constraints on the best-fit parameters of the reflection and absorption components are presented in Table 3.2, and plotted together with the corresponding input values in Figs. 3.6 and 3.5, respectively. The spin was retrieved successfully in 6 (3 fully and 3 fairly) of the 11 accurate fits, with 5 failures, while the 7 inaccurate fits returned 2 fairly constrained spins (with 5 failures). In total, only 18 out of 30 high-spin cases (in sets G and K) were a success: 13 (8 plus 5) are obtained in the 20 accurate fits, while other 5 fair successes still emerge from the 10 inaccurate fits. This suggests that, even though it plays an important role, the spin is not the only factor that may lead to a positive result in recovering its input value. Instead, the height of the source plays a crucial role in determining the spin value as we discuss in Section 3.5.4.

3.5.2 Effects of absorption

We summarize below the constraints we obtained on the absorption components in Sets G and K. We note that these components can be added/removed arbitrarily. 1) The fully covering warm absorber is included in 23 simulations (equivalent to 46 fits). Its column density and ionization parameter were positively recovered in 34 (30 full plus 4 fair successes) and 38 (36 plus 2) cases, respectively. Both rates are higher than the incidence of accurate fits (32/46). 2) The partial-covering low-column absorber is present in 21 simulations. Its column density and covering fraction were measured successfully in 25 plus 1 and in 28 plus 1 cases, respectively, against 25 out of 38 accurate fits (in 4 cases this component is missed in the spectral analysis). 3) The partial-covering high-column absorber is present in 19 simulations. Its column density and covering fraction were measured successfully in 23 plus 12 and 24 plus 12 cases, respectively, when the accurate fits are 24 out of 37 (this component is missed only once).

Summarizing, the properties of the absorbers are correctly estimated in the majority of the blind fits. Even though the number of simulations that we performed is statistically small, we can still derive a general idea of the degeneracy that may be present between the reflection-based models and the complex absorption model. It may happen that the inclusion of an absorber that is not present intrinsically mimics some of the relativistic effects on the spectrum, thus resulting in a wrong measurement of the spin parameter. However, it seems that absorption plays only a marginal role in the ability of measuring spins, as the overall absorption configuration in the fits was correct in 37 out of 48 cases. These issues are further investigated in sections 3.5.5 and 3.5.6.

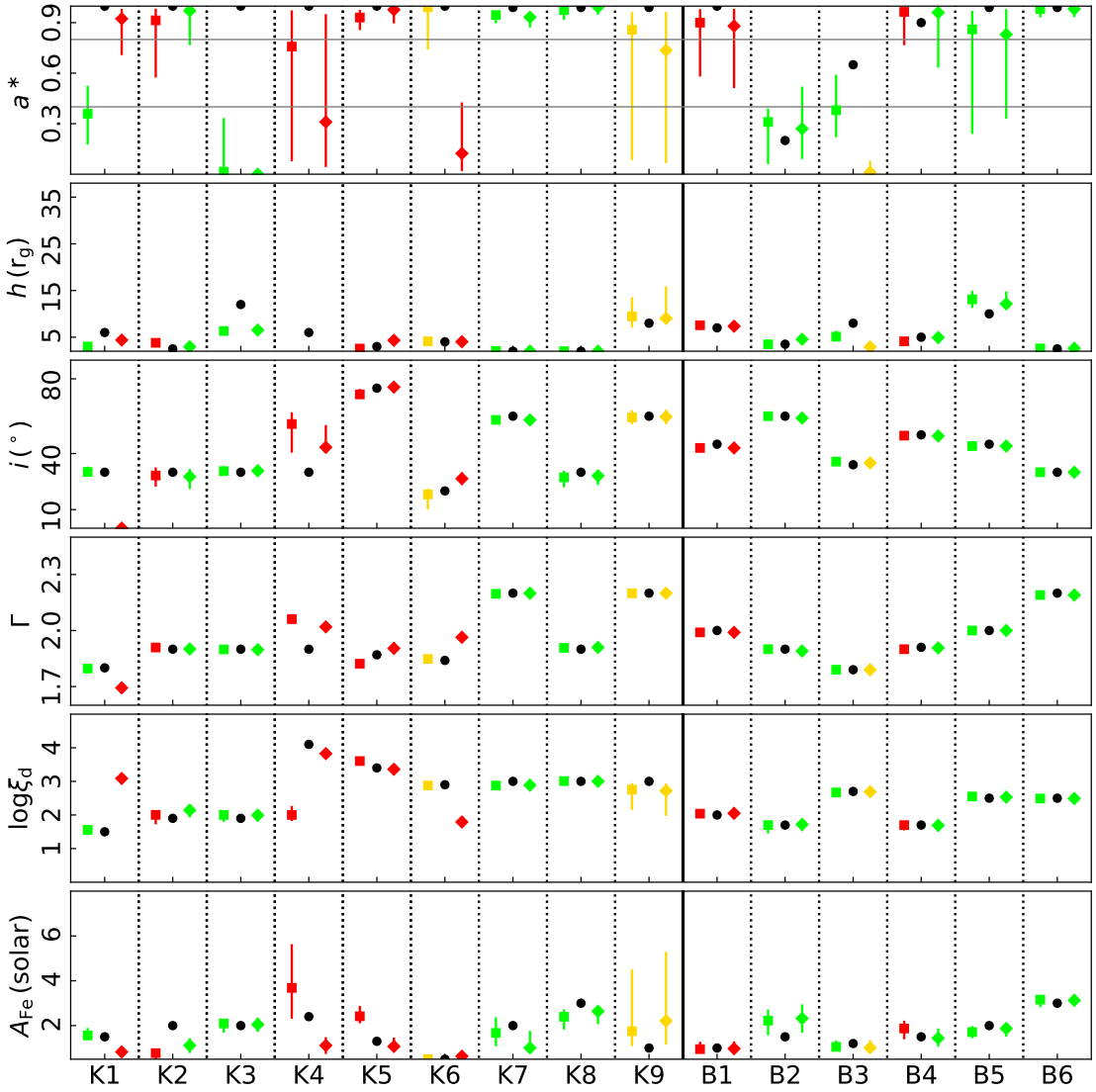

Figure 3.6: Similar to Figure 3.4 but for Sets K and B.

3.5.3 The bare sources case

In order to completely remove the uncertainties associated with absorption effects, we performed an additional set of 6 simulations (two per person) of bare sources, without including any intrinsic absorption (hereafter Set B, we refer to these simulations as B1-B6). The input model of this set can be written in XSPEC terminology, neglecting Galactic absorption, as follows: `model = RELXILLLP + XILLVER + APEC`. The simulated spectra and the χ^2 residuals are presented in Figure A.1. The input parameters together with the best-fit values are plotted in Figure 3.6. We summarize in Table 3.2 the qualitative constraints on the parameters that we obtained for this set. Four of these simulations involved a high spin value, and two cases each correspond to a lamp-post height $\leq$ or $> 5\,r_{\rm g}$. All the successful

spin measures (1 full and 3 fair, with 3 out of 4 accurate fits) occurred for a low height of the source. Interestingly, at low height even a small spin is correctly retrieved (1 full and 1 fair success in 2 out of 2 accurate fits). Conversely, when the height of the lamp post is larger than $5\,r_{\rm g}$, the measure of the spin always fails, irrespective of its value and despite the good rate (4/6) of accurate fits. The other disc reflection parameters were all well constrained in all cases, except for the Fe abundance in a single instance. As for the thermal and distant reflection components, they were both correctly assessed in 10 out of 12 fits.

In total, 19 out of the 30 simulations (i.e. 38 out of 60 fits) were performed asssuming maximally rotating black holes. The spectral analysis resulted in 22 successes in the measure of the spin (9 full and 13 fair), with 1 undetermined and 15 failed cases, for 25/38 accurate fits. Remarkably, when we consider only the simulations performed with a low lamp-post height, the total count features all the 22 successes and only 2 failures, for the same fraction (16/24) of accurate fits. This strongly suggests that the height of the primary X-ray source is the most critical ingredient for an accurate measure of black hole spin.

3.5.4 Effects of the lamp-post height

In the light of these findings, we further explored the dependence of our results on the input lamp-post height. Half of the simulations were perfomed assuming an input lamp-post height lower or equal to $5\,r_{\rm g}$. In general, these heights were measured successfully in 21 (16 plus 5) fits, with 5 full successes coming from the 9/30 inaccurate fits. Three of these 15 simulations were performed assuming a low input spin parameter. The fit was accurate in 5 out of 6 cases, returning 2 successes in the measure of the height and 4 (1 plus 3) in that of the spin.

By considering the second half of the simulations, with a lamp-post height larger than $5\,r_{\rm g}$, we find that the height was correctly estimated in 6/30 fits only despite the 21 out of 30 accurate fits. In 5 out of 30 spectral fits we were able to recover the spin (2 full and 3 fair successes), while in 6 out of 30 cases the spin was undetermined. Eight of these 15 simulations were performed assuming a low spin. As already noted, the high spin and large height case gave 1 undetermined and 13 failures, despite the 9 out of 14 accurate fits. This apparently suggests that, at large heights, the value of the spin has little weight, and the chance of success in its measure is not only small but also random (i.e. depending on several other factors such as iron abundance). In this sense, the preference for low spins is most likely a bias, so any measure at large heights should be taken with caution (see also Fabian et al. 2014).

The full summary is given in Table 3.3.

Table 3.3: Summary of the constraints on determining the spin showing its dependence on the lamp-post height. The values/fractions between parentheses refer to the accurate fits only.

$a^* < 0.8$: 11 models	$a^* \geq 0.8$: 19 models
$h \leq 5\,r_g$: 6 (5) fits	$h \leq 5\,r_g$: 24 (16) fits
- Full success: 1/6 (1/5)	- Full success: 9/24 (9/16)
- Fair success: 3/6 (2/5)	- Fair success: 13/24 (7/16)
- Undetermined: 0/6 (0/5)	- Undetermined: 0/24 (0/16)
- Failure: 2/6 (2/5)	- Failure: 2/24 (0/16)
$h > 5\,r_g$: 16 (12) fits	$h > 5\,r_g$: 14 (9) fits
- Full success: 2/16 (2/12)	- Full success: 0/14 (0/9)
- Fair success: 3/16 (1/12)	- Fair success: 0/14 (0/9)
- Undetermined: 6/16 (4/12)	- Undetermined: 1/14 (1/9)
- Failure: 5/16 (5/12)	- Failure: 13/14 (8/9)

3.5.5 Model dependence

By construction, the disc reflection component is always included in both the simulated models and the fitted models, while the presence of all the other components, either additive (distant reflection, thermal emission) or multiplicative (warm, cold absorption) is arbitrary. This allows us also to investigate the impact of model dependence on the ability to accurately recover the reflection parameters. Considering all the simulations from sets G, K, and B, soft X-ray thermal emission was present in 27 out of 30 cases, and was missed in only one out of the 54 relevant fits (K4a). Of the 3 out of 30 cases where it was not required, it was included in 5 out of 6 fits (G4a,b, G7b, B1a,b). Correctly accounting for this component or not seems to have little effect on the spin determination. Interestingly, its inclusion does not necessarily undermine the measure of the spin, but the accuracy is lower (compare the results of G7b versus G7a; Table 3.2. We note that model G7 is a low-spin, moderate-height case). In total, this component was measured successfully in 50 out of 53 spectral fits.

While the soft thermal component is easier to distinguish from the smooth, blurred reflection, the contribution from the distant reflector can significantly modify the shape of the Compton hump above 10 keV. This is present in 29 out of 30 models. It is missed once, and added instead in both fits of the single model (K5) where it was not originally included. This is a maximum-spin, low-height case, which, as we have seen, should have a higher chance of success. Indeed, both fits meet the fair success criterion for the spin. However, we could argue that the inclusion of distant reflection

prevents us from obtaining more stringent constraints. In total, the normalization of this component was measured succesfully in 51 out of 57 spectral fits.

Absorption is allowed in 24 models only (G and K sets). The fully covering, warm layer is present in 23 out of 24 simulations. Remarkably, it is never missed and never added. This suggests that the features imprinted on the spectrum from mildly (or even highly) ionized gas in the line of sight are relatively easy to identify, at least at the X-ray brightness level of the simulated spectra. Hence, we expect this component to have no significant effect on the measure of the spin. In reality, however, the different treatment of warm absorption might lead to incompatible spin measures for the same data set of the same source, as in NGC 3783 (Brenneman et al. (2011) versus Patrick et al. (2011)). The micro-calorimeters on board of *ATHENA* and, possibly, earlier X-ray missions such as Arcus (Smith et al. 2016) and XRISM will conclusively remove this source of ambiguity.

The lower column partial-covering absorber is included in 21 out of 24 models, while the higher column partial-covering absorber in 19 out of 24. The former is missed 4 times and added in 2 out of 6 fits, the latter is missed once and added in 4 out of 10 fits. Without distinguishing between the relative column densities, the configuration of the partial-covering, cold absorber consists of a single layer in 6 out of 24 cases and of a double layer in 17 out of 24 cases. No cold layers are included in the remaining case (G5), but they are both used in G5b, leading to an undetermined spin measure (as opposed to a fair success for G5a, where the correct model is applied). Two layers instead of the single one required are adopted in 5 out of 12 fits, while one of the two layers is missed in 5 out of 34 fits. Surprisingly, the addition of a layer does not always preclude a decent (or even good) measure of the spin (e.g. G2b), although the statistical significance of the second layer in these cases is most likely marginal. Conversely, all the 5 cases in which a layer is missed correspond to failures or indetermination in the spin measurement. We conclude that the effects of partial covering and of relativistic reflection, when high-quality broadband spectra are available, can be generally well distinguished from each other. We further discuss this point in the next section.

3.5.6 Reflection versus partial covering absorption

According to some interpretations (e.g. Miller et al. 2008), no relativistic signature is needed to explain the spectra (and variability) of most AGN. This is a natural consequence of the substantial statistical equivalence between absorption- and reflection-based models, especially when the spectra are complex and require some combination of both ingredients. The relative dispute was initially concentrated

on the nature of the Fe K line broadening since the partial covering absorption could reproduce both the smooth, extended red wing of the putative relativistic line as a gentle continuum curvature and its blue horn as an absorption edge. The appearance of tentative hard X-ray excesses in the *Suzaku* era added a further controversial element, which could be explained either as a Compton reflection hump (e.g. Walton et al. 2013) or as a signature of Compton-thick absorption (e.g. Tatum et al. 2013), thus reinforcing the polarity between the two mainstream scenarios. The advent of *NuSTAR*, providing high-quality spectra also above 10 keV, accurate background subtraction, and substantial overlap with the band covered by the other X-ray observatories, can greatly reduce this persistent ambiguity.

While, in principle, the ambiguity works in both ways, in our simulations we did not assume any pure partial-covering configuration (i.e. with no disc reflection), so we cannot verify whether an absorption layer could be missed by overestimating the amount of reflection. This is not the scope of our study. In fact, in this context it is more interesting to explore the possibility for the simulated models to be adequately reproduced without considering any relativistic component. We therefore checked the consequences of replacing the `relxilllp` component in our fits with a simple power law, in which the cut-off is fixed at 300 keV for consistency with the primary continuum in the parent model. This is equivalent to fixing the reflection fraction in `relxilllp` to zero. In order to compensate for the lack of disc reflection, we allow for a larger complexity in the absorption configuration. It turns out that only 1 of the 30 simulated spectra could be perfectly described also by a pure partial-covering model, as the relative fits would meet all of our acceptance criteria, namely good statistics and lack of residuals. This is G10 ($\chi^2/\mathrm{dof} = 397/394$), where three cold layers are required: $N_{\mathrm{H},1} = 6 \times 10^{21}$ cm^{-2} ($\mathrm{CF}_1 = 1$), $N_{\mathrm{H},2} = 5.5 \times 10^{23}$ cm^{-2} ($\mathrm{CF}_2 \sim 0.1$), and $N_{\mathrm{H},3} = 3.6 \times 10^{24}$ cm^{-2} ($\mathrm{CF}_3 \sim 0.25$). The fully covering, thinner layer is perfectly matched to a component of the input model, whose second layer has $N_{\mathrm{H}} = 1.9 \times 10^{24}$ cm^{-2} and CF = 0.26. Although G10 is a low-spin ($a^* = 0.12$), large-height ($h = 32\,r_{\mathrm{g}}$) case, a much more complex (and rather extreme) absorption pattern is required to compensate for the lack of disc reflection in the fit.

In three other cases (G14, K4, and K9) the reduced χ^2 is fair (1.02, 1.10, and 1.04, respectively), and two layers have similar (even if not strictly consistent) properties to the input components. There are, however, some clear residual structures that make the absorption-only models not satisfactory. A third partial-covering layer is not statistically required. At low S/N, these spectra (with maximal spin but $h > 5\,r_{\mathrm{g}}$) could be easily misinterpreted. A peculiar case is that of G5, where no cold absorbers are included in the simulation. This spectrum can be well fitted

by a power-law continuum ($\chi^2/\mathrm{dof} = 479/477$) that is subject to warm absorption only with the exact input parameters. Even if the disc reflection component in this case is very smooth and featureless, a model where this is correctly accounted for (G5a; $\chi^2/\mathrm{dof} = 449/473$) is still statistically preferred (at the $> 4\sigma$ level based on the corrected Akaike Information Criterion usually adopted for non-nested models; Akaike 1974). It is likely that the contribution from disc reflection would be missed in lower quality data. A handful (≤ 5) of other cases, in principle, could become acceptable after the inclusion of a third partial-covering layer if the spectra were fainter by at least an order of magnitude with respect to the simulated spectra, which could mask the residuals within the photon noise. We note, however, that such a complex absorption configuration (even if real) should be rejected as a form of data overfitting at low S/N. We conclude that in most cases (26 out of 30), including all the set B of bare spectra, disc reflection cannot be missed or mimicked by absorption effects in high-quality broadband X-ray spectra. The problems with its identification arise when the reflected spectrum is extremely smooth, so this could become a non-negligible issue if the X-ray corona is radially extended and thus responsible for the Comptonization of the relativistic signatures from the inner disc (see Steiner et al. 2017).

An interesting outcome of our analysis is that the failed spin measurements have a nearly flat distribution, which is clearly different from those reported in the literature. We plot in Figure 3.7 the distribution of spin measurements listed in Vasudevan et al. (2016) together with that of wrong and undetermined measurements from our blind spectral analysis. As the uncertainties on the individual entries are rather large for both samples, we do not attempt any statistical test to compare quantitatively the two distributions. We note, however, that, while the selection effects leading to an observed spin distribution peaked towards higher values are well known (e.g. Brenneman et al. 2011), our results seem to discard any systematics or biases associated with possible reflection versus absorption spectral degeneracies.

3.5.7 Simulations with ATHENA

To verify whether the failures require an even larger data quality (hence inaccessible to the current X-ray observatories), we chose two models for which the measured values of the spin were either undetermined (G6) or wrong (G11) despite the excellent accuracy of both fits. Based on our results, both cases are expected to be rather challenging, as they involve intermediate black-hole spin and large lamp-post height. We then simulated the same input model using the response files (with an exposure time of 100 ks) of the Wide Field Imager (WFI; Rau et al. 2013), one of the two

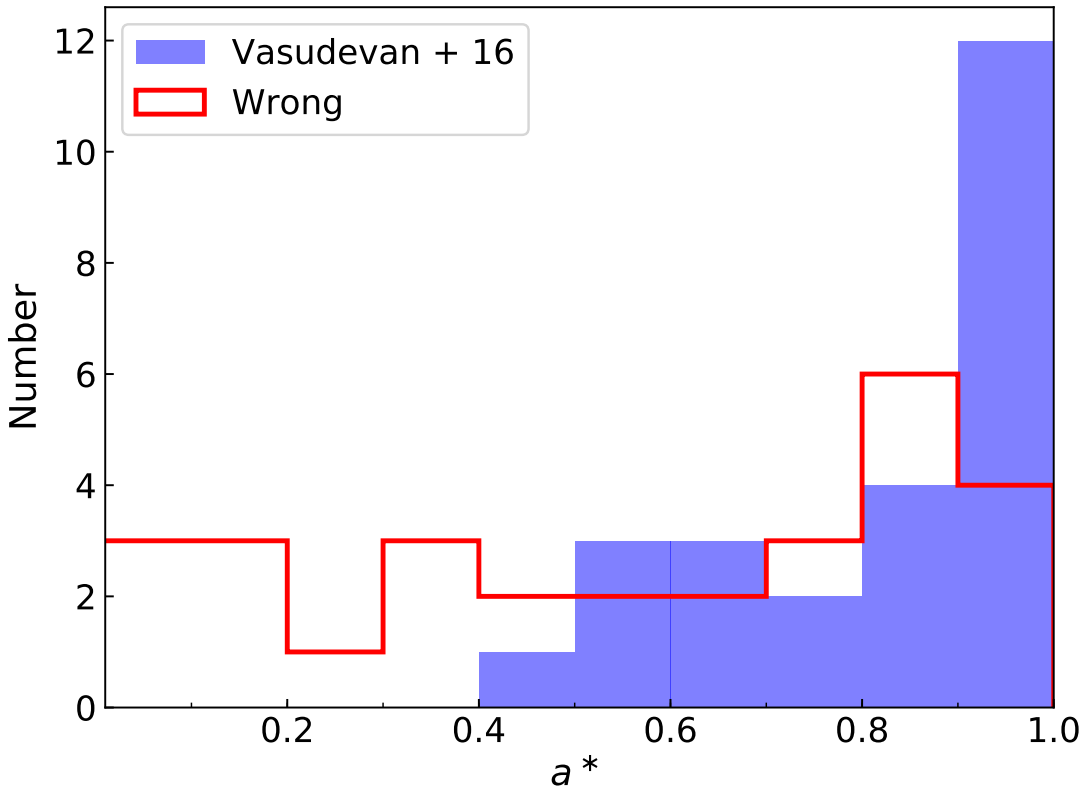

Figure 3.7: Distribution of spin measurements from Vasudevan et al. (2016) (blue histograms) and the distribution of wrong and undetermined measurements (red histograms) obtained from the simulations performed in this chapter.

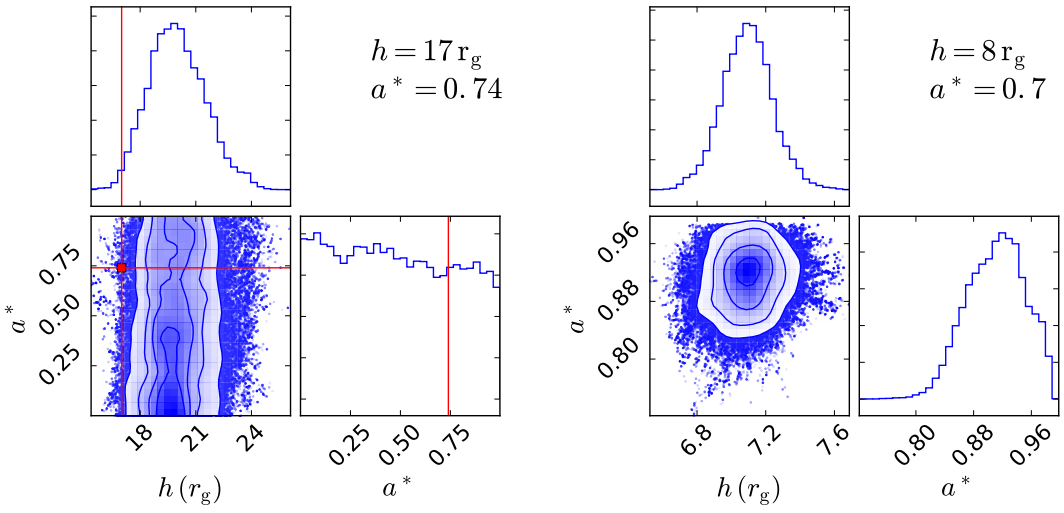

Figure 3.8: Black hole spin vs. lamp-post height contour plots obtained by the MCMC analysis obtained from the best-spectral fits of G6 (left panel) and G11 (right panel), performed using the *ATHENA*-WFI response files. The input spin and height values (red lines) are listed on the top right corner of each panel for the corresponding simulation.

scientific instruments proposed for the *ATHENA* X-ray observatory (Nandra et al. 2013). We performed an MCMC analysis as described in Section 3.3. For model G6, which has $h = 17\,r_{\rm g}$, the results are similar to those obtained by the spectral analysis of the joint *XMM-Newton* and *NuSTAR* spectra. Even with WFI, the measured value of the spin remains undetermined, as shown by the $a^* - {\rm vs} - h$ contour plots in Figure 3.8. For model G11, which has almost the same input spin but lower height ($8\,{\rm r_g}$), the measured spin remains inconsistent with the actual value of 0.7, but it is now much closer to this value (~ 0.9 against 0.2). This test, although unsuccessful, confirms the main indication of our study, i.e. the importance of a small lamp-post height (hence an effective illumination of the innermost disc) for an accurate measure of the BH spin. However, one of the limitations of fitting the spectra with *ATHENA* is the incapability of probing the Compton hump at high energies.

3.6 Conclusions

The measure of black-hole spin in AGN has many important implications in testing strong gravity regimes, and understanding the accretion history of BHs (e.g. Volonteri et al. 2013). The modelling of X-ray reflection features from the inner accretion disc provides a powerful method in this sense. The reliability of the available reflection-based SMBH spin measurements, however, is not fully established yet. In this chapter, we have investigated this issue through the simulation of high-quality broadband spectra, representive of the best possible data that can be achieved with a single simultaneous *XMM–Newton* and *NuSTAR* observation of a local, bright AGN. A similar attempt has been carried out recently by Bonson & Gallo (2016) and by Choudhury et al. (2017). Both studies, however, only considered the spectra in the *NuSTAR* energy range (2.5–79 keV), thereby neglecting the statistically dominant soft X-ray excess component. Moreover, the ideal scenario of pure reflection was assumed in both cases. We allowed, instead, for the general spectral complexity observed in real AGN spectra, including absorption, thermal, and distant reflection components in our parent model. The spectra were simulated by one member of the team and blindly fitted by the other two, where the only constraint was to use the same number of components employed in the parent model or less.

We have shown that the analysis of single-epoch AGN spectra can be really challenging. In fact, our simulations suggest that a correct determination of the BH spin parameter is not straightforward. Our main results are summarized below.

- The height of the X-ray source (in a lamp-post geometry) plays a major role in the spin measurement. By dividing the simulations over the four quadrants of the spin/height plane identified by the $a^* = 0.8$ and $h = 5\,r_g$ values (Table 3.3), we obtain a remarkable 100% success rate for the accurate fits in recovering the correct spin in the high-spin/low-height quadrant. This is not surprising and agrees with the conclusions reached by Fabian et al. (2014), Bonson & Gallo (2016), and by Choudhury et al. (2017): the closer the source to the black hole, the stronger the relativistic distortions that allow an accurate spin measurement.

- We also demonstrated that neither the complex (i.e. partial-covering, multi-layer) absorption nor the additional emission components (i.e. thermal emission and cold reflction) seem to have a critical impact on the ability to measure the spin correctly, at least at very high S/N. In summary, $\sim 70\%$ of the cases turned out to be accurate in that the model employed in the analysis corresponds to the input model and the overall χ^2 is equal or very close to the expected absolute minimum (Section 3.4).

Several lines of evidence suggest a compact primary source that is located at a few gravitational radii from the BH. Spectral-timing and reverberation studies, for example, are suggestive of a physically small corona that lies within 3–10 r_g above the central BH (e.g. Fabian et al. 2009; De Marco et al. 2013; Emmanoulopoulos et al. 2014; Gallo et al. 2015). Moreover, X-ray microlensing analyses of some bright lensed quasars suggest that the hard X-rays are emitted from compact regions with half-light radii less than $6\,r_g$ (Chartas et al. 2009; Mosquera et al. 2013; Reis & Miller 2013). Our findings imply that X-ray reflection is indeed an effective method to measure the BH spin provided that reflection dominates the broadband intrinsic (i.e. before foreground absorption) spectrum, which might not always be the case (e.g. Parker et al. 2017). Furthermore, our analysis implies that the actual nature of the X-ray source (as yet unknown) should heavily affect any reflection-based spin measure. Several other factors may lead to a wrong determination of the spectral parameters in single-epoch observations, such as the choice of a *wrong* model. In fact, at low spectral quality, some absorption configurations can indeed mimic the relativistic effects. Moreover, for large lamp-post heights, the chances of reliably assessing the spin are small, and apparently independent on the value of the spin itself. Simply increasing the total number of counts or effective area does not bring any substantial improvement. For single-epoch, low-resolution spectra, indirect or complementary arguments, such as energy conservation, fractional variability, or

model-independent techniques (see next chapter), are still recommended to support the conclusions of the spectral analysis. Spectral variability, however, could greatly help in constraining the constant parameters in the reflection models, such as the spin, inclination, and iron abundance, as already proved by the NGC 1365 campaign, while high resolution, especially with the next generation of micro-calorimeter which on board of planned missions such as XRISM and ATHENA, can remove the ambiguities associated with the introduction of ad-hoc absorption components.

Air on the G String (Suite No. 3, BWV 1068)

https://open.spotify.com/album/1f3mIaDgN1Zl6PpDtoBl4K

Johann Sebastian Bach

4

Nature of the X-ray variability in MCG–06-30-15

Contents

The flux-flux plot analysis (FFP) is a model-independent method that can provide clues regarding the X-ray variability of AGN. It is straightforward in its implementation and is relatively efficient in detecting spectral components that are less variable than the X-ray primary emission. If present, these components result in positive constants in the FFP plots, which, in general, show a strong positive correlation between the flux in various energy bands (for AGN). The FFP variant of the method is particularly effective when studying the fast spectral variability in AGN on timescales when the flux in various energy bands cannot be accurately determined. This method was first developped by Churazov et al. (2001) and was

applied to the study of the X-ray variability of the BH binary Cygnus X-1. It was first applied to AGN studies by Taylor et al. (2003), with the aim to study the X-ray spectral variability of X-ray bright Seyferts. It has been used since then in numerous AGN X-ray variability studies (Noda et al. 2011, 2013; Kammoun et al. 2015).

In this chapter, I apply the FFP method to the simultaneous *XMM-Newton* and *NuSTAR* observations of the Seyfert 1 galaxy MCG–6-30-15 ($z = 0.00775$), performed in January 2013. The main objective is to study its X–ray flux and spectral variability properties and understand the nature of its various spectral components. MCG–6-30-15 is the archetype of Seyferts with broad iron lines in their X–ray spectra. It was the first source where a broad Fe Kα line with a red tail was detected. The line shape was interpreted as being due to relativistic reflection, implying an almost maximally spinning Kerr black hole (e.g. Tanaka et al. 1995; Iwasawa et al. 1996, 1999; Miniutti et al. 2007; Marinucci et al. 2014b). This interpretation was supported by the detection of short delays between the X–ray continuum and the soft band (i.e. X–rays below ~ 1.5 keV) emission (e.g. Emmanoulopoulos et al. 2011a, 2014; Kara et al. 2014). Epitropakis et al. (2016) showed that the iron line/continuum time delays are consistent with the delays between the hard (i.e. > 2 keV) and soft band variations.

MCG-6-30-15 is highly variable in X–rays. It shows large amplitude flux and spectral variations on short (minutes/hours) and long (days/years) time scales. Its spectral variations have been interpreted within the context of a two component model which consists of: 1) a highly variable power-law (PL) continuum (with an almost constant spectral slope of $\Gamma \sim 2$), and 2) a less variable ionized reflection spectrum arising within a few gravitational radii (Fabian et al. 2002; Lee et al. 2002; Shih et al. 2002; Fabian & Vaughan 2003; Taylor et al. 2003; Parker et al. 2014). The soft X-ray spectrum of the source is affected by a complex warm absorber (e.g. Otani et al. 1996; Reynolds et al. 1997; Branduardi-Raymont et al. 2001; Turner et al. 2003, 2004; Miniutti et al. 2007), whose properties vary in time, and should add to the observed variability of the source. In fact, Miller et al. (2008, 2009) proposed a complex absorption-dominated model in order to explain the red-tail of the iron line and the spectral variability of MCG–6-30-15. According to this model, partial-covering absorbers in the line of sight (having column densities in the $10^{22} - 10^{24}\,\mathrm{cm}^{-2}$ range), can produce an apparent broadening of the Fe Kα line similar to the one caused by relativistic effects (e.g. Miller et al. 2007; Turner et al. 2007). Variability in the covering fraction of these absorbers could also explain the observed spectral variations.

4.1 Observations and data reduction

XMM-Newton

The *XMM-Newton* sattelite observed MCG–6-30-15 simultaneously with *NuSTAR*, starting on 2013 January 29 during three consecutive revolutions (Obs. IDs 0693781201, 0693781301, and 0693781401). The data are available in the *XMM-Newton* Science Archive[1] (XSA). I considered data provided by the EPIC-pn camera (Strüder et al. 2001) only, that was operating in small window/medium filter imaging mode. I do not consider the data from the two EPIC-MOS (Turner et al. 2001) detectors because they were affected by a high level of pile-up (Marinucci et al. 2014b). The EPIC-pn data were reduced following the same procedure described in Section 2.1.1. The background-subtracted light curves were produced using the `SAS` task `EPICLCCORR`.

NuSTAR

MCG–6-30-15 was observed by *NuSTAR* with its two co-aligned telescopes with corresponding Focal Plane Modules A (FPMA) and B (FPMB) starting on 2013 January 29 (Obs. IDs 60001047002, 60001047003, and 60001047005). I reduced the *NuSTAR* data following the standard procedure described in Section 2.1.1. The source and background light curves were extracted from circular regions of radii 1′.5 and 3′, respectively, for both FPMA and FPMB, using the HEASoft task `NUPRODUCT`, and requiring an exposure fraction larger than 50 %. I checked that the background-subtracted light curves of the two *NuSTAR* modules were consistent with each other as follows. I divided the FPMA over the FPMB light curves (binned at $\Delta t = 1$ ks), in all the energy bands I consider in this Chapter (see next Section), and I fitted the ratio as a function of time with a constant, C. The fit was acceptable in all cases, indicating that the FPMA and FPMB light curves are consistent (C being consistent with 1 in all cases). Given this result, I added the FPMA and FPMB light curves in the various energy bands considered in this Chapter, using the `FTOOLS` (Blackburn 1995) command `LCMATH`, in order to increase the signal-to-noise of the *NuSTAR* light curves.

Figure 4.1 shows the *XMM-Newton* and *NuSTAR* light curves in the 3–4 keV band (chosen to be the reference band; see next Section), normalized to the mean average count rate. I plot the data during the four time periods when both satellites were observing the source (I considered data from these periods only, by merging

[1] http://nxsa.esac.esa.int/nxsa-web

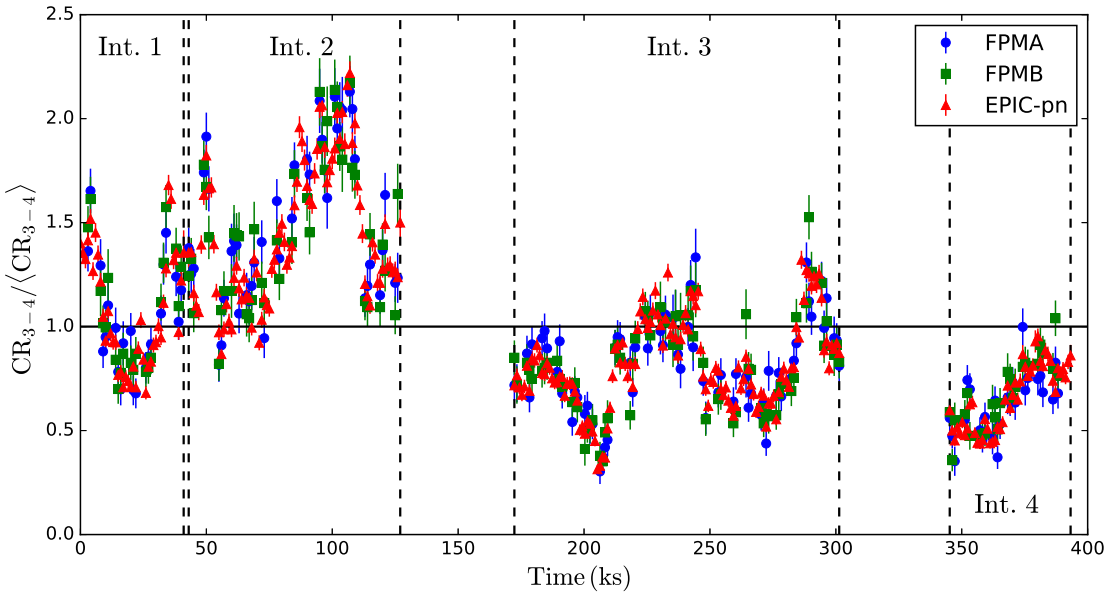

Figure 4.1: The 3–4 keV band EPIC-pn, FPMA, and FPMA (normalized) light curves (red triangles, blue circles, and green squares, respectively). The bin size is 1 ks in all cases and the vertical lines indicate the four intervals when both *XMM-Newton* and *NuSTAR* were observing the source. Time is measured from the start of *XMM-Newton* observations.

the good time intervals tables of the two satellites using the `FTOOLS` command `MGTIME`). This figure shows the large variability range of the source (the max-to-min flux ratio is ~ 7) but also the consistency between the instruments.

4.2 Flux-flux analysis

4.2.1 Choice of the energy bands

The first task in the flux-flux analysis is to define the reference band. Ideally, the flux in this band should be representative of the X-ray primary emission mainly, and should have the largest possible signal-to-noise ratio. In this case this band should also be common in both *XMM-Newton* and *NuSTAR* data. For these reasons, I chose 3–4 keV as the reference band. Table 4.1 lists the net exposure time and the average 3–4 keV count rate for each of the 4 time intervals and for the various detectors.

To construct the FFPs at energies above 4 keV (the high-energy FFPs, hereafter) I divided the 4–40 keV band into 10 sub-bands. The first five were common to both *XMM-Newton* and *NuSTAR*, with $\Delta E = 1$ keV in the energy range 4–8 keV, and $\Delta E = 2$ keV for the fifth sub-band (8–10 keV). Using data from these bands and the reference band I constructed FFPs (plotted in Figure B.1). At energies

Table 4.1: Net exposure time and the average count rate in the 3-4 keV band for the various time intervals and instruments which are considered.

Int.	Exp. time (ks)	$\langle CR_{3-4} \rangle$ (Count s^{-1})	
	EPIC-pn/FPMA,B	EPIC-pn	FPMA(B)
1	41/37	1.23 ± 0.05	0.21(0.22) ± 0.01
2	84/83	1.66 ± 0.04	0.30(0.30) ± 0.01
3	129/129	0.93 ± 0.02	0.17(0.17) ± 0.01
4	48/43	0.76 ± 0.03	0.13(0.14) ± 0.01

larger than 10 keV, I used *NuSTAR* data only (Figure B.2). I considered two sub-bands with $\Delta E = 2$ keV. Then I chose a width of $\Delta E = 3$ keV and 5 keV for the following two sub-bands. I also considered the light curve in the 25–40 keV sub-band ($\Delta E = 15$ keV). I did not consider the data at energies higher than 40 keV, because of the rapid decrease of the signal-to-noise ratio at these energies.

At energies below 3 keV, I extracted *XMM-Newton* light curves from 7 sub-bands in the energy range 0.3–1 keV with a width of $\Delta E = 0.1$ keV. Then I considered two sub-bands with $\Delta E = 0.3$ keV, one with $\Delta E = 0.4$ keV, and $\Delta E = 1$ keV for the last sub-band (2–3 keV). Using these light curves, and the reference band, I constructed the low-energy FFPs (plotted in Figure B.3).

4.2.2 Choice of the time bin size

The time bin size of the light curves, $\Delta t_{\rm bin}$, plays a significant role in the FFP analysis (Kammoun et al. 2015). To investigate this issue, I used *XMM-Newton* and *NuSTAR* light curves with $\Delta t_{\rm bin} = 100$ s, 1 ks, and 5.8 ks (equal to the *NuSTAR* orbit) to create the low and high-energy FFPs (the 100s, 1ks, and 5.8ks FFPs, hereafter). I fitted them with a power-law plus constant (PLc) model of the form,

$$y = A_{\rm PLc} x^{\beta} + C_{\rm PLc}, \tag{4.1}$$

(x in this, and all equations hereafter, represents the count rate in the reference band). I used the `MPFIT`[2] package (Markwardt 2009), taking into account the errors on the y-axis only.

In general, the best-fit parameters in the case of the 1 and 5.8 ks high-energy FFPs are consistent with each other. This is not the case with the low-energy FFPs. This is similar to what was observed in IRAS 13224–3809 (Kammoun

[2] http://code.google.com/p/astrolibpy/source/browse/trunk/

et al. 2015) and suggests that the intrinsic FFPs are not linear at energies below $\sim 2-3$ keV (see Section 4.2.4). The model parameters from the best-fits to the 100 s binned FFPs are significantly different, at all energies. This may be due to Poisson noise that dominates at low count rates.

I chose the 25–40 vs 3–4 keV *NuSTAR* FFP (bottom panel in FigureB.2) to investigate the effects of the Poisson noise on the FFPs, because the mean count rate in these bands is the smallest among all FFPs:

1. I created simulated (*NuSTAR*) 3–4 keV band count rates assuming a log-normal distribution with mean and standard deviation equal to the mean and standard deviation of the observed count rates in this band.

2. Using the resulting values I computed 25–40 keV band count rates based on the best-fit linear relation I obtained from fitting the observed, 1 ks binned FFP.

3. I multiplied the count rates in both bands by a factor equal to 1, 2, 3, 4 and 5×10^3, assuming a Poisson distribution, in order to compute the simulated counts.

4. I divided the resulting counts by the respective factor to get the final, simulated count rate in both bands, and I used them to construct 1, 2, 3, 4 and 5 ks binned, simulated FFPs.

5. Then, I fitted them with a linear model, exactly as I did with the observed FFPs.

Figure 4.2 shows the best fit $A_{\rm L}$ and $C_{\rm L}$ values (top and bottom panels, respectively), as a function of the square root of the average counts in the (simulated) 25–40 keV band light curve. The two panels in Figure 4.2 show that I can retrieve the intrinsic A and C values (indicated by the horizontal line in both panels), only when the average counts in the light curve is at least ~ 200. The mean count rate in the 3–4 keV *NuSTAR* band is ten times larger than the mean count rate in the 25–40 keV band (see Figure B.2). In fact, the average counts in this band is larger than 200 even if the data is binned into 1 ks bins. For that reason, the best-fit $A_{\rm L}$ and $C_{\rm L}$ values are consistent (with the error), irrespective of the bin size of the 25–40 keV light curves. However, they approach the intrinsic values only when the average counts in the 25–40 keV band light curves reaches the limit of 200.

Kammoun et al. (2015) suggested the use of light curves with the shortest possible bin size in order to recover the intrinsic FFP shape in the case of highly

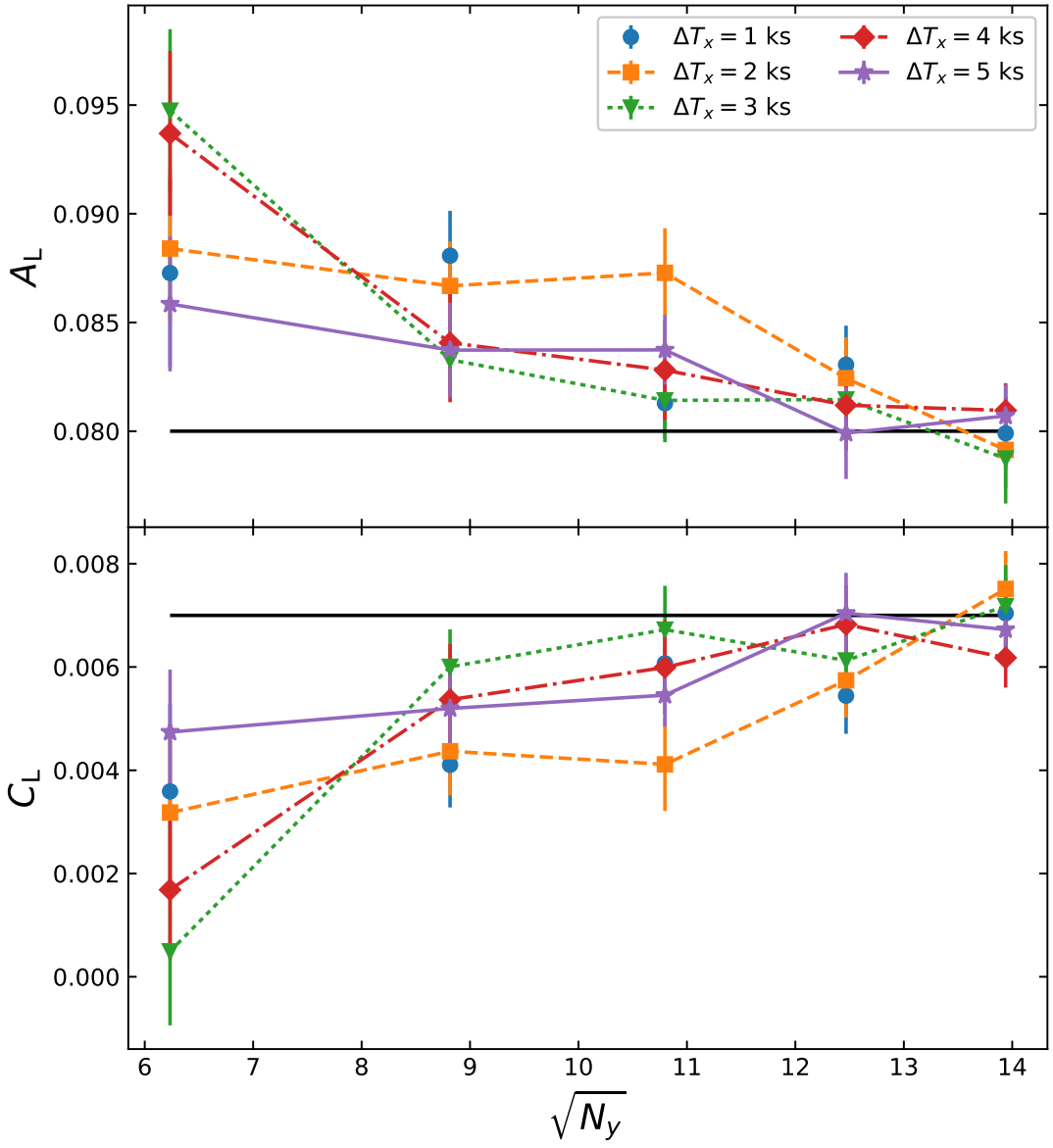

Figure 4.2: The best-fit A_L and C_L constants (top and bottom panels, respectively) of a linear model fit to simulated FFPs, assuming 1, 2, 3, 4 and 5 ksec binned light curves with a mean count rate equal to that of the 25–40 and 3–4 keV band, *Nustar* light curves. The horizontal lines indicate the intrinsic value of the constants.

variable sources and an intrinsically non-linear relation. I show here that in doing so, particular case should be given to Poisson noise effects, which can affect the observed shape of the FFPs. Although it is usually assumed that the Poisson distribution approaches the Gaussian distribution when the mean (i.e. the average counts) is $\sim 20 - 50$, the results indicate that this assumption is not enough to guarantee the correct estimation of the model parameters when fitting FFPs. I suspect that the reason is due to the nature of the intrinsic count rate distribution. As indicated by the plots in Appendix B, there is usually a small number of high flux points, which can span a large range in fluxes. It appears that a truly large number of counts per bin is necessary to guarantee a good approximation to a Gaussian (which is symmetric), so as to not bias the best-fit results to the FFPs to steeper (than intrinsic) slopes (and hence smaller constants).

I considered light curves affected by Poisson noise, because this is usually the case with X–ray light curves, such as the *NuSTAR* light curves. The conclusions should be largely unaffected by the nature of the experimental noise (be it Poissonian or not): as long as the (mean) signal to noise ratio of the observed light curves, defined for example as the ratio of the mean over the mean error, is larger than $(N = 200)/\sqrt{N = 200} \sim 14$, then the resulting FFPs should not be affected by the effects of the observational noise bias. Given this result, and the disagreement between the 1 ks and 5.8 ks results in the low-energy FFPs, I decided to study the FFPs which are constructed with the use of the 1 ks binned light curves at all energy bands, except the two highest *NuSTAR* energy bands, where I used the 5.8 ks binned light curves (to satisfy the high count rate criterion).

4.2.3 The high-energy flux-flux plots

I fitted the high-energy FFPs with the PLc model (eq. 4.1). I fitted both the data of the four time intervals shown in Figure 4.1 separately, and the data from all intervals combined together. The fits were statistically acceptable in all cases, and the best-fit slopes were consistent with one (at all energies). This result suggests that a straight line can also fit the FFPs. So I re-fitted them with a linear model of the form,

$$y = A_{\rm L} x + C_{\rm L}, \tag{4.2}$$

using the `MPFFITEXY` routine (Williams et al. 2010) which takes into account the errors on both x and y variables. Tables B.1 and B.2 list the best-fit results to the individual and the combined FFPs. The solid lines in Figure B.1 and B.2 show the best-fit lines to the combined high-energy FFPs.

The resulting $A_{\rm L}$ and $C_{\rm L}$ values from the best-fits to the FFPs of the individual intervals were consistent within the errors, at all energy bands. Filled symbols in Figure 4.3 show their weighted mean ($A_{\rm L,wm}$ and $C_{\rm L,wm}$) plotted as a function of the mean energy of each energy bin. Empty symbols in the same figure show the best-fit $A_{\rm L,all}$ and $C_{\rm L,all}$ values obtained when I fit the combined FFPs (using the data from all four segments). They are consistent with $A_{\rm L,wm}$ and $C_{\rm L,wm}$ (within 3σ). Since the errors of $A_{\rm L,all}$ and $C_{\rm L,all}$ are smaller than the errors of $A_{\rm L,wm}$ and $C_{\rm L,wm}$, I will use the former in this analysis.

In order to show the consistency of the results derived from the *XMM-Newton* and *NuSTAR* FFPs, one can re-write eq. 4.2 as follows,

$$\frac{y}{\langle y\rangle} = \frac{A_{\rm L}\langle x\rangle}{\langle y\rangle}\frac{x}{\langle x\rangle} + \frac{C_{\rm L}}{\langle y\rangle}, \tag{4.3}$$

where $\langle y\rangle$ and $\langle x\rangle$ are the mean count rates. Figure 4.4 shows the normalized *NuSTAR* best-fit values (i.e. $A' = A_{\rm L,all}\langle x\rangle/\langle y\rangle$ and $C' = C_{\rm L,all}/\langle y\rangle$), versus the respective *XMM-Newton* values. This plot shows that the results from the analysis of the *XMM-Newton* FFPs are consistent with those from the *NuSTAR* FFPs.

The best-fit model constants, $C_{\rm L}$, are significantly larger than zero, even at the highest energy band. This result suggests the presence of a spectral component which is not variable, at least on time scales comparable to the duration of the MCG-06-30-15 observations ($\sim$ 4.5 days). Secondly, the high-energy FFPs are well described by a straight line. This is consistent with the hypothesis of a power-law like X–ray continuum which varies in normalization only. In this case, the slope of the line which fits the FFPs, $A_{\rm L}$, should be equal to the ratio of y over x.

To investigate this issue further, I created fake power-law spectra using the XSPEC command `FAKEIT`, assuming an absorbed PL model with Γ in the range 1.95–2.2, with a step of $\Delta\Gamma = 0.01$. I considered only Galactic absorption in the line of sight of the source ($N_{\rm H} = 3.92 \times 10^{20}\,{\rm cm}^{-2}$; Kalberla et al. 2005), and the response matrices of EPIC-pn and FPMA/B. I estimated the expected count rate in each one of the high energy sub-bands, and I computed their ratio over the 3–4 keV model count rate. In this way, I was able to compute $A_{\rm L,mod}$, and then "$A_{\rm L,mod}$–vs–Energy" data sets for each Γ value.

Then I fitted the observed $A_{\rm L,all} - E$ data (empty symbols in Figure 4.3) to the $A_{\rm L,mod} - E$ lines. I found that the observed $A_{\rm L}$'s are best reproduced in the case when $\Gamma_{\rm X} = 2.04 \pm 0.02$ ($\chi^2_{\rm X}$/degrees of freedom (dof) = 7.4/4), and $\Gamma_{\rm N} =$

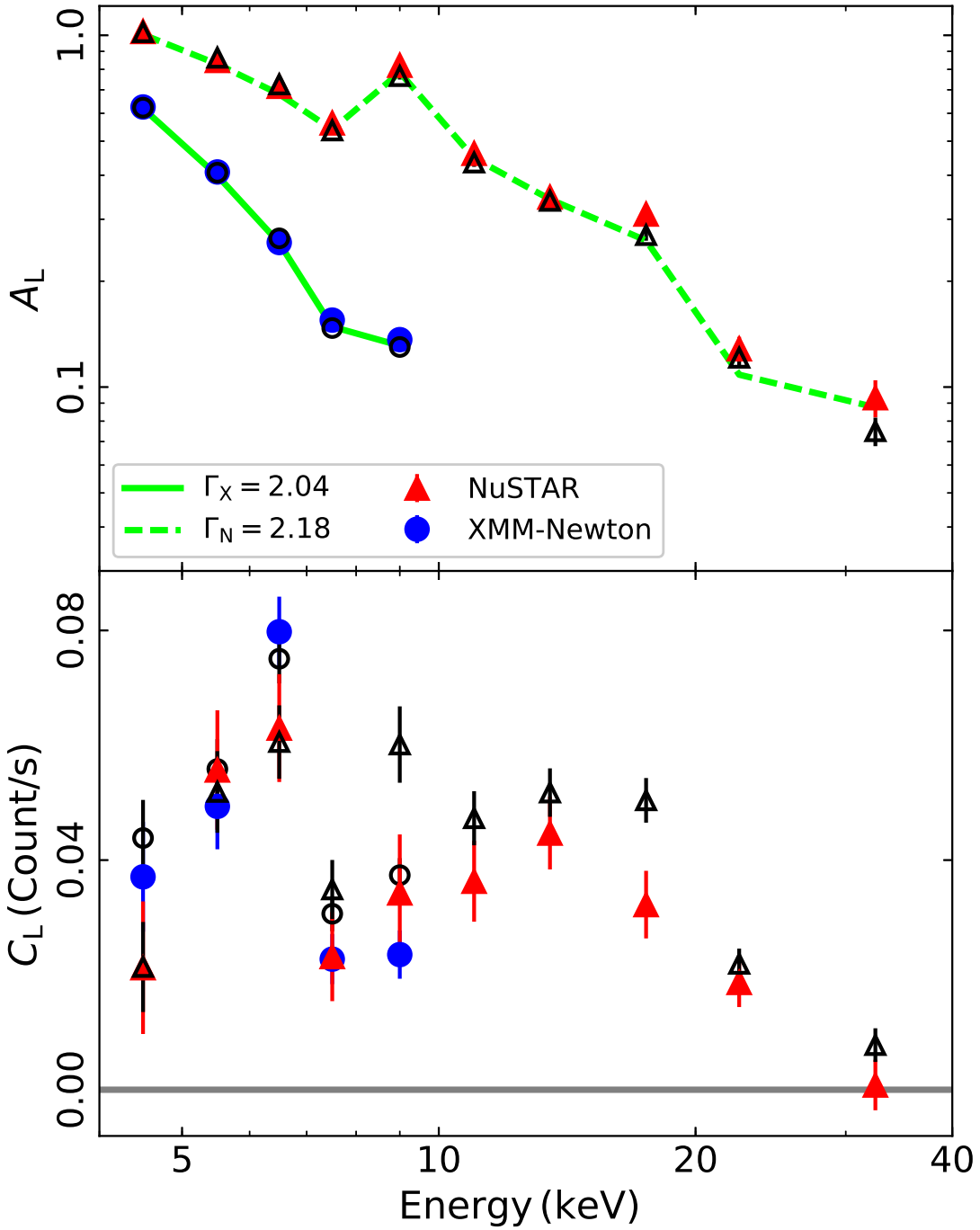

Figure 4.3: The best-fit A_L and C_L (upper/lower panel) parameters derived by fitting a linear model to the *XMM-Newton* (circles) and *NuSTAR* (triangles) high-energy FFPs. Filled/empty symbols show $A_{L,wm}, C_{L,wm}$ and $A_{L,all}, C_{L,all}$, respectively. The solid/dashed lines in the top panel indicate the *XMM-Newton* and *Nustar* A_L model values, assuming a power-law spectrum that varies in normalization only (see Section 4.2.3).

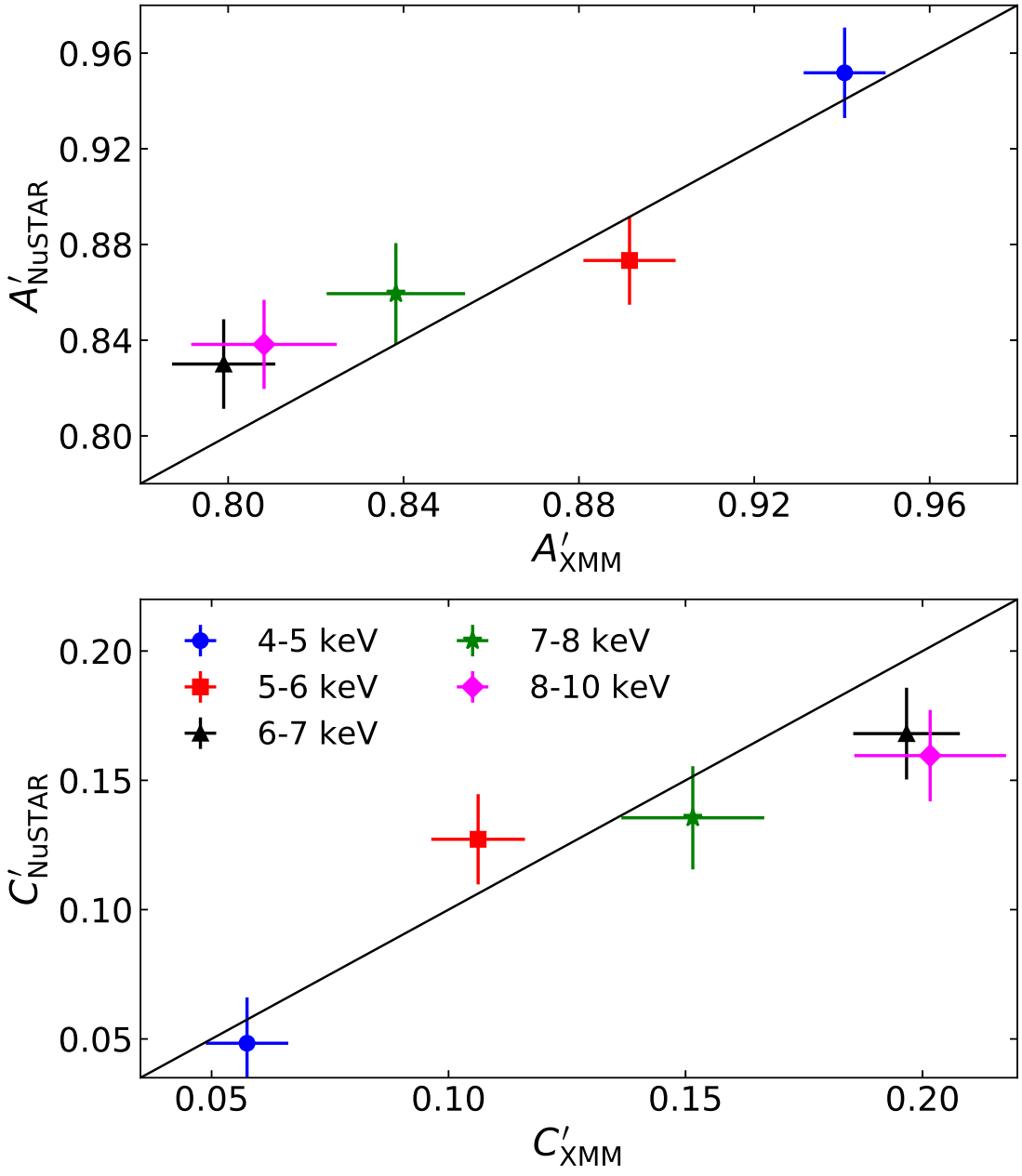

Figure 4.4: Plot of the *NuSTAR* versus the *XMM-Newton* normalized $A_{\mathrm{L,all}}$ (top panel) and $C_{\mathrm{L,all}}$ (bottom panel) best-fit values (see Section 4.2.3). The straight, solid lines indicate the one-to-one relation.

2.18 ± 0.02 ($\chi^2_{\rm N}$/dof = 22/9) for the *XMM-Newton* and *NuSTAR* FFPs[3], respectively. The *XMM-Newton* and *NuSTAR* best-fit $A_{\rm L,mod} - E$ models are plotted with the solid and dashed lines, respectively, in Figure 4.3. It should be noted that the best-fit $A_{\rm L,mod} - E$ lines do not give a statistically accepted fit to the data ($\chi^2_{\rm X+N} = 29.4/13$ dof, $p_{null} = 5.7 \times 10^{-3}$). The weighted mean of the residuals ratio ($|(A_{\rm L,mod} - A_{\rm L,all})/A_{\rm L,all}|$) over the 4–40 keV band is $(1.96 \pm 0.49)\%$. Therefore, a PL component which varies in normalization accounts for most, but not all, of the observed variations. I further discuss this issue in Section 4.3.5.

4.2.4 The low-energy flux-flux plots

As with the high-energy FFPs, first I fit a PLc model to the low-energy FFPs of the individual time intervals. Figure B.3 shows the resulting best-fit PLc models. The best-fit results, the mean value of the best-fit parameters, and the best-fit parameters obtained by fitting all the data together are listed in Table B.3. The model parameters from the best-fits to the individual time intervals were consistent with each other, in all bands. However, contrary to the high-energy FFPs, the best-fit values derived by fitting all the data together do not agree with the mean value of parameters obtained by fitting the FFPs of the individual time intervals.

Strictly speaking, the PLc model is not statistically accepted, neither when I fit the individual nor the combined low-energy FFPs. The residual plots show significant, random data fluctuations around the best-fit models, indicative of short-amplitude, fast variations in the low energy bands which are independent of the continuum variations. When I fit a straight line to the best-fit residuals of the individual FFPs, the best-fit slope turns out to be consistent with zero. This suggests that the PLc model represents rather well the general trend in the low-energy FFPs. It takes account of most of the observed variations in the soft bands, and does not result in any large-scale, systematic trends in the residual plots. On the other hand, the residuals from the best-fits to the combined FFPs show systematic trends. The best-fit results to the individual FFPs can be therefore accepted as representative of the low energy FFPs. Since the best-fit parameters are consistent (within 3σ) at all low-energy FFPs, I use their arithmetic mean[4] in this analysis. Filled symbols in Figure 4.5 show the mean model parameters plotted as a function of the centroid energy of each energy bin.

[3]The difference between the best-fit $\Gamma_{\rm X}$ and $\Gamma_{\rm N}$ slopes ($\Delta\Gamma = 0.14 \pm 0.03$) should be representative of the inter-calibration uncertainties between EPIC-pn and FPMA/B. For example, the difference that is observed is consistent with the $\Delta\Gamma$ differences between the two instruments that Madsen et al. (2015) reported.

[4]Due to the large χ^2 values, the error of the best-fit parameters does not represent their real uncertainty. For that reason I considered the arithmetic mean values of the best-fit parameters for the low-energy FFPs.

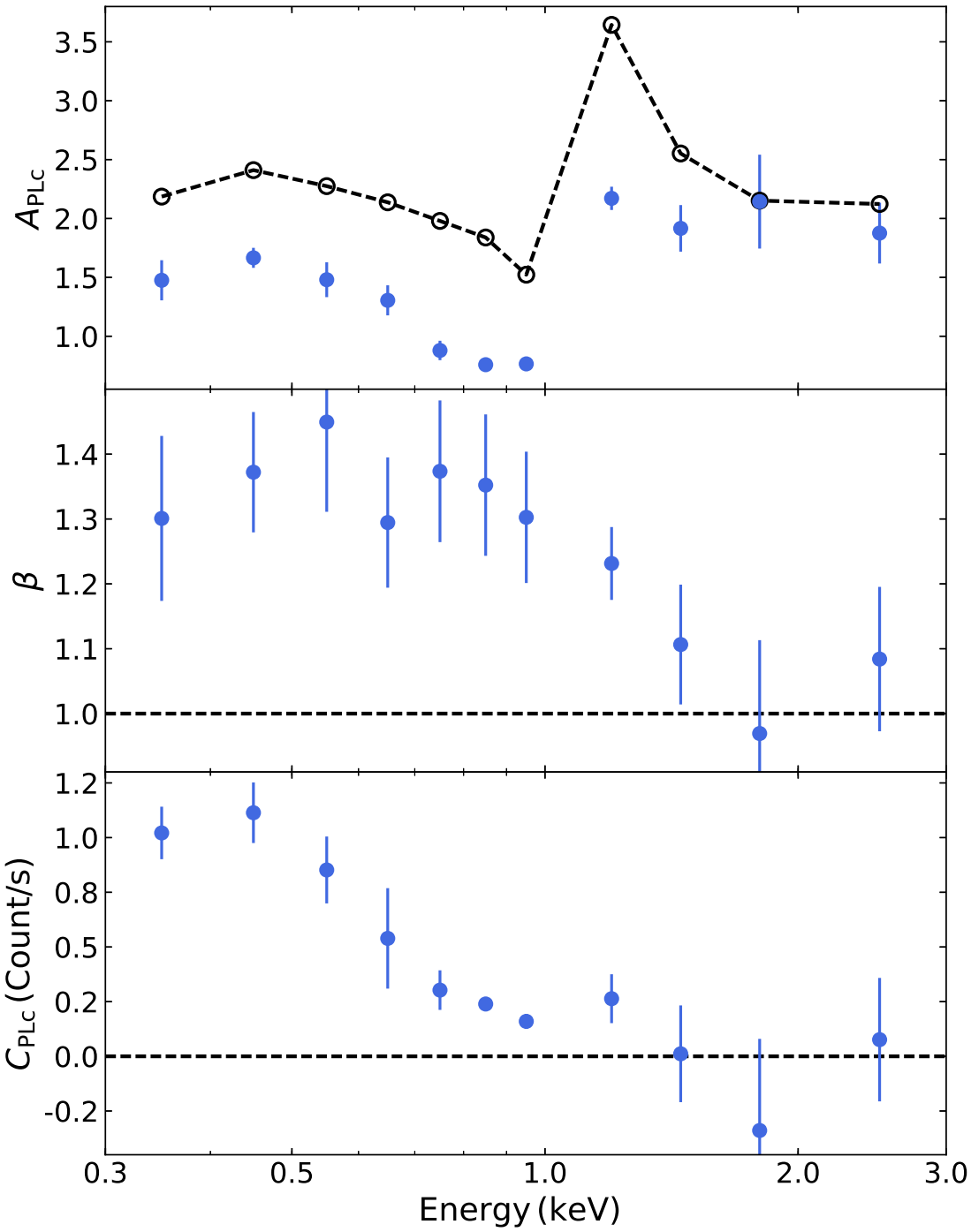

Figure 4.5: Mean best-fit $A_{\rm PLc}$ (upper panel), β (middle panel) and $C_{\rm PLc}$ (bottom panel) values. Empty circles, in the upper panel, show the predicted A_{PLc} assuming a PL spectrum with $\Gamma_{\rm X} = 2.04$ and a variable normalization. (see Sec. 4.2.3 for details).

The best-fit model slopes (middle panel in Figure 4.5) are significantly larger than one at energies below ~ 1.6 keV. Non-linear FFPs can be produced by intrinsic spectral slope variations, as demonstrated by Kammoun et al. (2015). However, these authors showed that Γ variations result in FFP slopes which are flatter than one. In addition, the high-energy FFPs argues against intrinsic Γ variations. I therefore conclude that the non-linear FFPs are not the result of spectral slope variations.

The magenta solid lines in Figure B.3 show the expected FFPs assuming a power-law spectrum with $\Gamma_{\rm X} = 2.04$, which varies only in normalization, as is the case with the high-energy FFPs (the predicted FFP lines are plotted assuming the Galactic absorption, only). The open circles in the top panel of Figure 4.5 show the resulting $A_{\rm PLc}$. At energies $\sim 1.6 - 3$ keV, the observed FFP slopes are consistent with one, and the observed $A_{\rm PLc}$ are consistent with the predicted values. Not surprisingly, the magenta solid lines are also (broadly) consistent with the observed FFPs. I therefore conclude that the FFPs down to ~ 1.6 keV are consistent with a power-law spectrum with $\Gamma_{\rm X} \sim 2$, which varies only in normalization.

The observed FFPs are *below* the magenta solid lines at energies between $\sim 0.6 - 1.6$ keV. Furthermore, the observed $A_{\rm PLc}$ are below the expected values at all energies below ~ 1.6 keV. This result suggests that the count rate in these energies is smaller than what I would expect based on the variable PL model that is consistent with the high-energy FFPs (even when the Galactic absorption is taken into account). The lower than expected count rate can be explained by the well-known variable warm absorber in MCG-6-30-15, which affects mainly the low energy spectrum of the source. At the same time, if the absorber is variable, it can result in FFP slopes which are steeper than one (as shown in Section 4.3.2).

The best-fit model constants ($C_{\rm PLc}$) are positive at all energies below ~ 1 keV (bottom panel in Figure 4.5). This is indicative of the presence of a spectral component at low energies which does not vary on time scales shorter than the duration of the observations. This agrees with the fact that, despite the warm absorption, the observed FFPs are above the predicted ones (magenta line) in the 0.3–0.6 keV range. This can only be explained by the presence of an extra spectral component (in addition to the variable PL and the warm absorber).

4.3 Discussion

4.3.1 Absorption induced X–ray continuum variability

The fact that a straight line fits well the high energy FFPs provides a model independent evidence against variable, clumpy absorption dominating the X–ray

variability in MCG-6-30-15. If that were the case, the observed count rate, $y(t)$, at energy E_y, would be equal to:

$$y(t) = \left\{ \prod_{i=1}^{N} \exp\left[-n_{\rm H,i}(t)\sigma(E_y)\right] \right\} AE_y^{-\Gamma}, \tag{4.4}$$

assuming N obscuring clouds, each one with equivalent hydrogen column, $n_{H,i}(t)$, which is variable in time, while the X–ray continuum spectrum remains constant ($\sigma(E_y)$ is the photo-electric cross-section). The above equation becomes,

$$y(t) = \exp\left\{ \left[-\sum_{i=1}^{N} n_{\rm H,i}(t) \right] \sigma(E_y) \right\} AE_y^{-\Gamma}, \tag{4.5}$$

and should also hold for the count rate at energy E_x,

$$x(t) = \exp\left\{ \left[-\sum_{i=1}^{N} n_{\rm H,i}(t) \right] \sigma(E_x) \right\} AE_x^{-\Gamma}. \tag{4.6}$$

One can solve for $[-\sum n_{\rm H,i}(t)]$ using eq. 4.6, and substitute it in eq. 4.5 in order to reach the following relation between the count rates in the two bands,

$$y = Cx^{\beta}, \tag{4.7}$$

where C is a constant, and $\beta = \sigma(E_y)/\sigma(E_x)$. Equation 4.7 predicts a non linear relation between y and x, contrary to the results obtained from the observed FFPs. Even if N varies with time, eq. 4.7 should still hold. Therefore, my results show that the hypothesis that the X–ray variability in MCG-6-30-15 is due to variable absorption only (on the probed time scales, at least) is not valid.

4.3.2 The effects of the warm absorber to the FFPs

In order to investigate the effect of a variable warm absorber on the low-energy FFPs, I simulated spectra using the XSPEC command `FAKEIT`, and the EPIC-pn responses, assuming the following model (in `XSPEC` terminology):

$$\texttt{model} = \texttt{TBabs} \times \texttt{zxipcf} \times \texttt{powerlaw}, \tag{4.8}$$

where `TBabs` (Wilms et al. 2000b) and `zxipcf` (Reeves et al. 2008) account for the Galactic and the warm asborption, respectively. `powerlaw` varied in normalization ($N_{\rm PL}$) only, with Γ fixed at 2.03. $N_{\rm PL}$ varied between $N_{\rm PL,min}$ and $N_{\rm PL,max}$, so that the respective model count rate, in the 3–4 keV band, were equal to the minimum/maximum observed count rate in the same band. As for `zxipcf`, I fixed $N_{\rm H}$ at $2 \times 10^{22}\,{\rm cm}^{-2}$ and considered 3 different values for the covering fraction

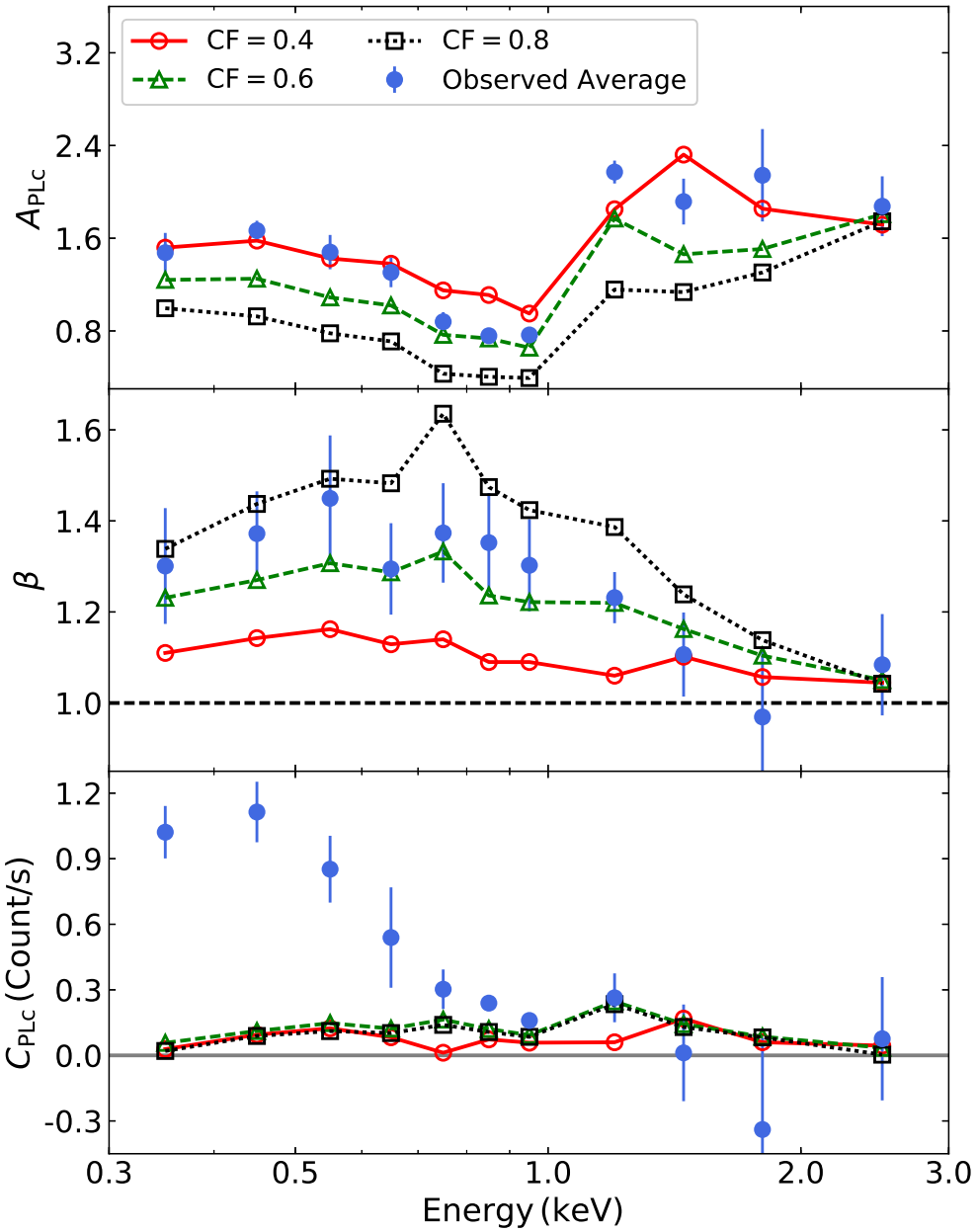

Figure 4.6: The best-fit observed (filled symbols) and simulated (open symbols) parameters obtained by fitting the observed and simulated FFPs with a PLc model.

Table 4.2: The best-fit parameters obtained by fitting the high energy constant component with `pexmon`.

Γ	$2.06^{+0.17}_{-0.19}$	$2.03^{+0.17}_{-0.19}$	$1.99^{+0.18}_{-0.20}$	$1.91^{+0.19}_{-0.20}$
$E_{\rm cut}$ (keV)	27^{+12}_{-7}	26^{+12}_{-7}	26^{+12}_{-7}	25^{+11}_{-6}
$A_{\rm Fe}$	$0.26^{+0.05}_{-0.04}$	$0.26^{+0.05}_{-0.04}$	$0.26^{+0.05}_{-0.04}$	$0.27^{+0.05}_{-0.04}$
$i(^\circ)$	0^f	30^f	45^f	60^f
Norm	$0.026^{+0.009}_{-0.007}$	$0.025^{+0.009}_{-0.007}$	$0.025^{+0.009}_{-0.007}$	$0.026^{+0.009}_{-0.007}$
χ^2/d.o.f.	14.25/12	14.19/12	14.43/12	14.8/12

^{f} Fixed.

(CF): 0.4, 0.6 and 0.8. I assumed that the ionization parameter (ξ) is linearly proportional to the primary flux, as: $\log\xi = \log N_{\rm PL} + 2.97$. The constant was chosen so that the model count rate in the 0.6–0.7 keV band (when CF=0.6 and $N_{\rm PL} = N_{\rm PL,max}$) is equal to the observed largest value. Given the $N_{\rm PL,min} - N_{\rm PL,max}$ range, $\log\xi$ varied between 0.85 and 1.55.

To construct the model FFPs, I estimated the model count rate in the reference and the low-energy bands, assuming 10 different values of $N_{\rm PL}$ (between $N_{\rm PL,min}$ and $N_{\rm PL,max}$). Then I fitted them with a PLc model, exactly as I did with the observed FFPs. The best-fit simulated PLc parameters are plotted as empty symbols in Figure 4.6.

In general, the assumed variable warm absorber model results in FFPs which are, qualitatively, similar to the observed plots. In all cases, $B_{\rm PLc,\,sim}$'s are steeper than one, as observed. Therefore, a variable warm absorber can produce non-linear FFPs, with slopes steeper than one. In addition, variable warm absorption can also result in non-zero, positive constants. But, the value of $C_{\rm PLc,\,sim}$, at all energies, below 1 keV is quite smaller than $C_{\rm PLc,\,obs}$. I also tried different $N_{\rm H}$ and/or CF values, and I saw that in some cases, a variable warm absorber model may even result in negative $C_{\rm PLc,\,sim}$ in the FFPs. In this case, the amplitude of the intrinsic constant spectral component will be larger than what $C_{\rm PLc,\,obs}$'s imply.

4.3.3 The constant high energy X–ray component

The linear model defined by eq. 4.2 consists of two terms. The $C_{\rm L}$ term should be representative of a spectral component, which is not variable (at least over the sampled time scales). I used the best-fit $C_{\rm L,all}$ values to construct the spectrum of this component at energies above 1.6 keV (Figure 4.7). I first created a text file with as many entries as the channels in the original response files of EPIC-pn and

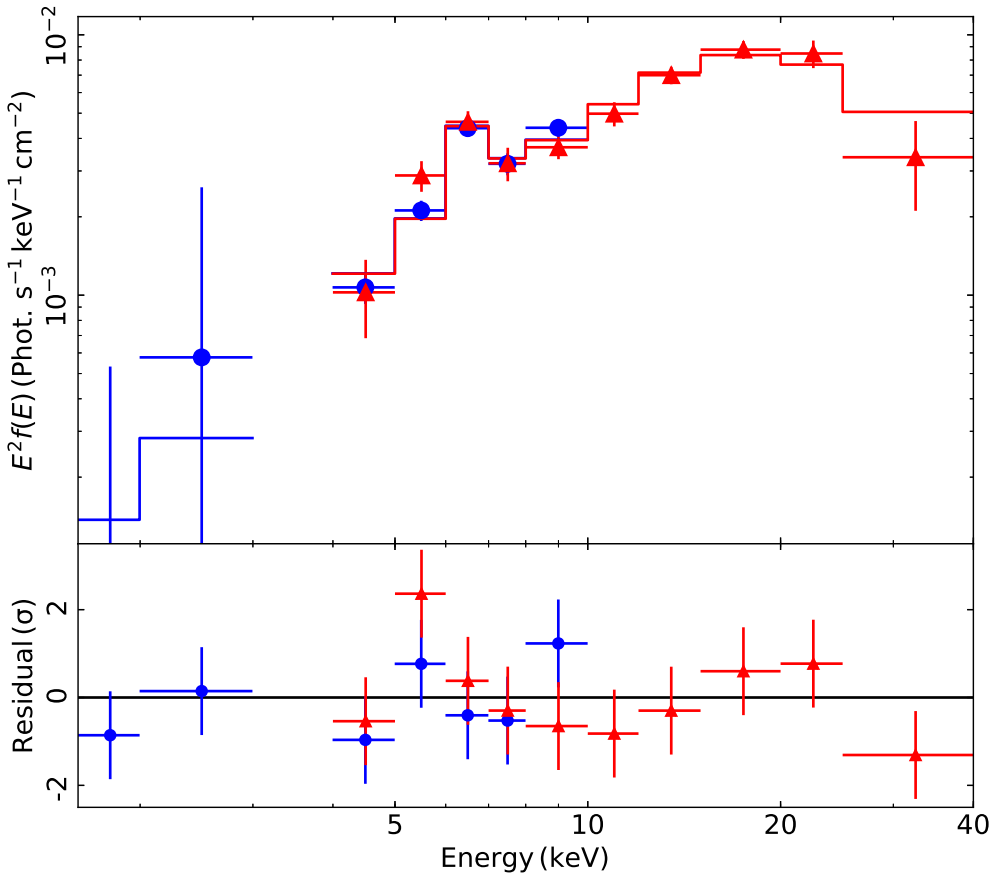

Figure 4.7: The energy spectrum of the constant component (top panel) fitted with a neutral reflection model together with the corresponding residuals (bottom panel) for *XMM-Newton* (blue circles) and *NuSTAR* (red triangles).

FPMA. I assign a value which corresponds to the best-fit FFP parameter value to each channel. Then I used the `ASCII2PHA` tool to create a `pha` file, and I grouped the spectra according to the energy bins that are considered in the FFPs, using the `GRPPHA` task. In the case of *NuSTAR*, the use of the FPMB response matrices gives consistent results with the ones using the FPMA response matrices. I fitted the so-created spectrum with the neutral reflection model `pexmon` (Nandra et al. 2007). I fixed the reflection fraction to minus one (in order to account for the reflection component only) and the abundance of heavy elements to solar but I let the iron abundance and the cutoff energy free to vary. I kept all the parameters tied between the *XMM-Newton* and *NuSTAR* spectra. It should be noted that the values of the constant from *NuSTAR* are estimated by adding the light curves from FPMA and FPMB. For that reason I multiplied the aforementioned model by a constant fixed to 1 for *XMM-Newton* and 2 for *NuSTAR*.

The best-fit results are listed in Table 4.2 for various inclinations, up to 60 degrees. The model fits well the data in all cases, which implies that the inclination

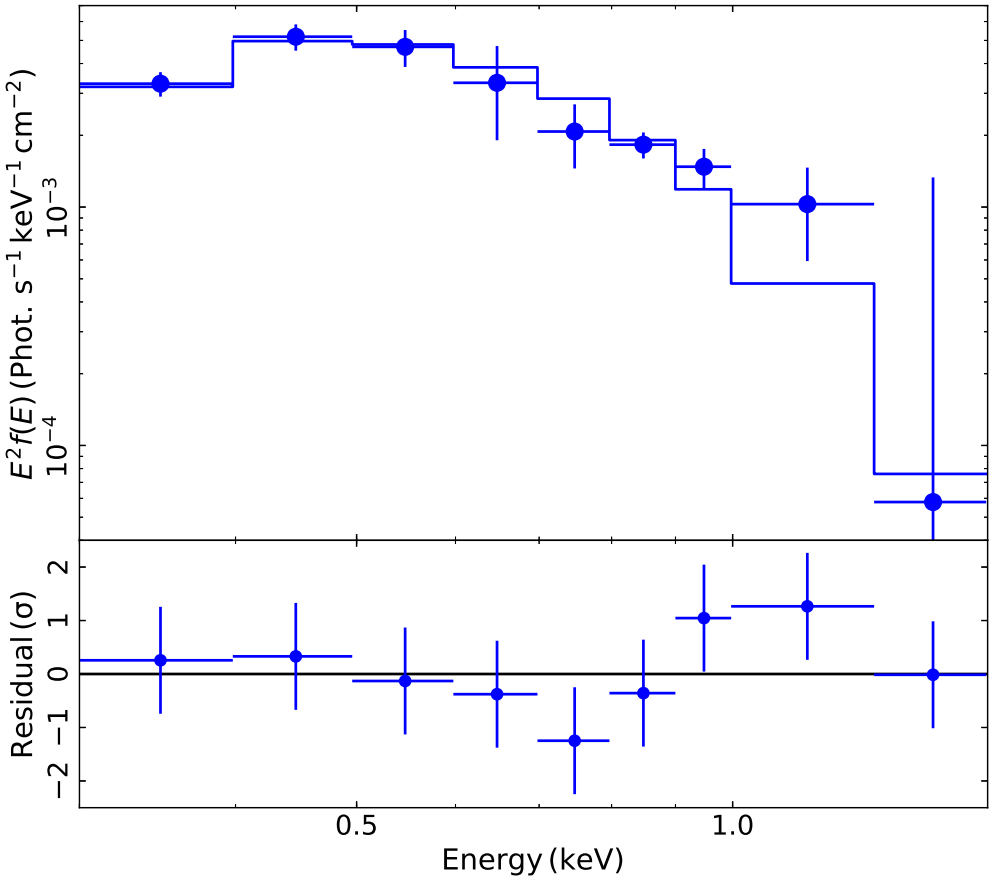

Figure 4.8: The energy spectrum of the low-energies constant component fitted with a black-body model (solid line, top panel), and the corresponding best-fit residuals (bottom panel).

cannot be constrained. The photon index is consistent with 2 (within the errors), and the iron abundance is subsolar in all cases. I also found a low value for the high-energy cutoff, similar to the one found for the variable component in Section 4.3.5 (the $3\,\sigma$ upper limit is 120 keV). The results of the spectral fits indicate that the constant component can result from reflection off neutral material. This component is constant over at least ~ 4.5 days, which places a lower limit on the distance of the reflector from the central source. Assuming that the BH mass is $M_{\rm BH} \simeq 1.6 \times 10^6\, M_\odot$ (Bentz et al. 2016), this implies that the reflecting material is located at a distance $D \geq 5 \times 10^4\, r_{\rm g}$ ($r_{\rm g} = GM_{\rm BH}/c^2$, is the gravitational radius). This is ~ 1.7 times larger than the broad line region radius in this source (Marinucci et al. 2014b).

4.3.4 The constant low energy X–ray component

The model defined by eq. 4.1, which fits well the low-energy FFPs, also consists of two terms. The $C_{\rm PLc}$ term could be representative of a low-energy spectral

component which remains constant on time-scales of a few days (at least). However, this is not straight forward in this case. The soft X-ray spectrum of MCG–6-30-15 is charaterized by complex and variable warm absorption. I demonstrated in Section 4.3.2 that variable warm absorption can result in non-linear FFPs at low energies, with slopes steeper than one, as observed. The simulated FFPs are well fitted by a PLc model, with either positive or negative constants, $C_{\rm PLc,sim}$. In the cases that I considered, the absolute value of these constants is much smaller than the constants I measure in the observed low-energy FFPs, $C_{\rm PLc,obs}$. Although I cannot prove that this will always be the case, it is possible that $C_{\rm PLc,obs}$ are indicative of a spectral component which does not vary, at least over the duration of the observations.

I used the best-fit $C_{\rm PLc,obs}$ values listed in Table B.3 to construct the low-energy, constant spectral component of MCG-6-3015 (plotted in Figure 4.8). I fit the spectrum with an absorbed blackbody (BB) spectrum, taking into account the Galactic absorption only. The fit (blue solid line in Figure 4.8) is statistically accepted (χ^2/d.o.f. $= 4.7/7$). The best-fit temperature and normalization are $kT_{\rm BB} = 100 \pm 6\,{\rm eV}$ and $N_{\rm BB} = (1.99 \pm 0.3) \times 10^{-4}$, respectively.

Such a component could be due to the intrinsic emission of the inner disc. In this case, this component should be variable on the local viscous time scale, which even for a source with a BH mass of the order of a million solar masses could be of the order of many days. In order to investigate the possibility of this component being representative of disc emission, I considered the `optxagnf` model (Done et al. 2012) which gives the spectral energy distribution of an accretion disc around a rotating SMBH, assuming Novikov-Thorne emissivity (Novikov & Thorne 1973). I fitted this model to the data, assuming a BH mass of $1.6 \times 10^6\,M_{\odot}$, a spin parameter of 0.998, and the emission from the inner part of the disc only (i.e. I fixed the model parameter r_{out} to $2\,r_{\rm g}$). The model fits the data well ($\chi^2 = 12.9/8$ dof, $p_{null} = 0.11$), with the best-fit Eddington ratio being $\log L_{\rm Edd} = -1.19 \pm 0.02$. I therefore conclude that, the constant component in the soft-band of MCG–6-30-15 can be indicative of the inner disc emission, if the BH is maximally rotating, and the accretion rate is ~ 6 per cent of the Eddington limit.

It should be noted that the best-fit residuals plot in Figure 4.8 indicate an absorption feature at energies $\sim 0.6 - 0.8$ keV. It is not significant but this feature is reminiscent of warm absorption. It suggests that the constant soft spectral component is emitted by a region close to the central source, in agreement with the assumption that this is the intrinsic emission from the inner disc.

4.3.5 The variable X–ray spectral component

The $A_{\rm PLc}x^{\beta}$ and $A_{\rm L}x$ terms in eqs. 4.1 and 4.2 should account for the variable, X–ray continuum spectral component in MCG–6-30-15, at low and high energies, respectively. I considered the mean 3–4 keV count rate with the best-fit $A_{\rm L,all}$ and $A_{\rm PLc}$ values (at energies above and below 1.6 keV, respectively), to create the spectrum of this component. In principle, I could use any 3–4 keV count rate value to create the spectrum. I chose the mean so that the resulting spectrum is representative of the variable component in the average-flux state of the source (during these observations). The high energy variable component, $y_{\rm var,h}$, is plotted with the filled symbols in the top panel of Figure 4.9 (circles and triangles indicate the data using the best-fit *XMM-Newton* and *NuSTAR* $A_{\rm L,all}$ values, respectively). The low-energy variable component, $y_{\rm var,l}$, is plotted with the open circles in the same panel.

I fitted $y_{\rm var,h}$ with a PL model, taking into consideration the Galactic absorption in the line of sight of the source. The model provides a rather poor fit to the data ($\chi^2 = 30/15$ dof; $p_{null} = 0.01$), in agreement with the results I presented in §4.2.3. The weighted mean of the residuals ratio in the 2–10 keV band is $1.5 \pm 0.5\%$. This in agreement with the results from the principle component analysis (PCA) method which reveals that the variability in the normalization of the PL component can account for $\sim 97\%$ of the variability in this source (Parker et al. 2014, 2015).

The best-fit residuals (shown in the middle panel in Figure 4.9) indicate a deficit at ~ 3 keV and an excess at around ~ 6.5 and 20 keV, and are are suggestive of an X-ray reflection component. I therefore re-fitted $y_{\rm var,h}$ with `relxill` (Dauser et al. 2013; García et al. 2014) (accounting for Galactic absorption). I assumed a maximally spinning black hole, a power-law emissivity profile with $q = 3$, and a reflection fraction of 1. I fixed the inner and outer disc radius to the ISCO and to $400\,r_{\rm g}$, respectively. The model fits the data well ($\chi^2/{\rm dof} = 10.8/11$; the best-fit residuals are plotted in the bottom panel of Figure 4.9).

The best-fit results are listed in the second column of Table 4.3. The best-fit spectral slopes are consistent with the spectral slopes I found in §4.2.3. The best-fit PL cut-off energy is rather low when compared to other AGN (e.g. Marinucci et al. 2016) but it is not well constrained. The 3σ confidence range is [34–295 keV]. It should be noted that the respective $E_{\rm cut}$ range from the `pexmon` best-fit to the constant component (for all inclinations) is [12–120 keV]. When combined together, the two results indicate a cut-off energy between 34–120 keV in MCG-6-30-15. It should be also noted that the best-fit iron abundances from the `relxill` fit to the variable component and from the `pexmon` fit to the constant component are not in agreement. I cannot explain this discrepancy. It could either mean that the spectral

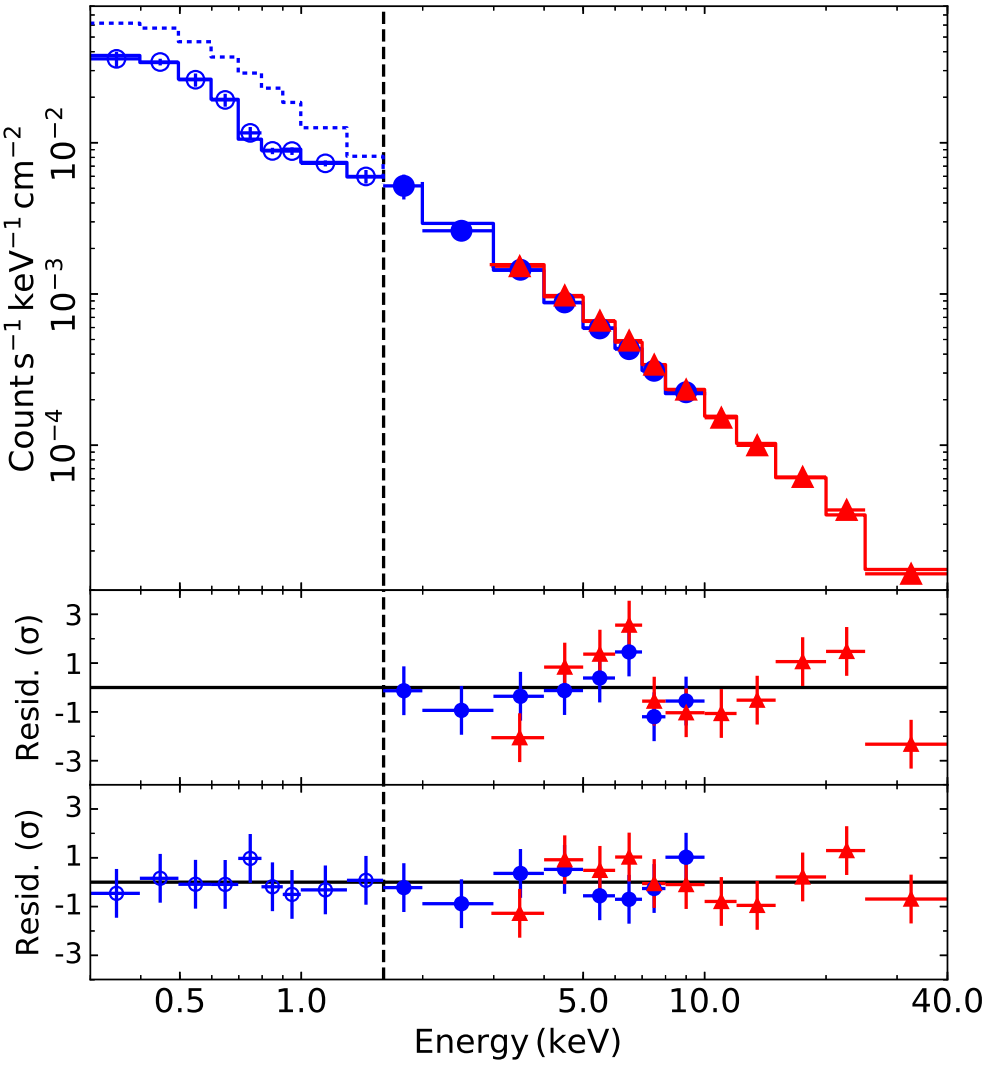

Figure 4.9: *Top panel:* The average, X–ray variable spectrum in MCG-6-30-15 using the best model fit results to the *XMM-Newton* and *NuSTAR* FFPs (circles and triangles, respectively). The vertical dashed line at 1.6 keV indicates the boundary between the high and low energy parts of the spectrum (assuming that the FFPs at energies 1.6–3 keV are similar to the high-energy FFPs, as I argued in Section 4.2.4). The solid line above 1.6 keV indicates the best-fit `relxill` model to the data. The dotted line indicates the extrapolation of the model to lower energies. The solid line below 1.6 keV indicates the best-fit `zxipcf` × `relxill` model to the data. *Middle and bottom panels:* The PL and the `zxipcf` × `relxill` best-fit residuals, respectively (see Section 4.3.5 for details).

Table 4.3: The best-fit `relxill` and `zxipcf` results from the modelling of the variable component in the 1.6–40 keV and the 0.3–40 keV bands (second and third/forth columns, respectively. See Section 4.3.5 for details).

	`relxill`		
$\Gamma_{\rm X}$	2.03 ± 0.03	2.03^{f}	$2.12^{+0.10}_{-0.04}$
$\Gamma_{\rm N}$	2.16 ± 0.05	2.16^{f}	$2.25^{+0.10}_{-0.05}$
$i(^\circ)$	42^{+5}_{-10}	42^{f}	44^{+6}_{-9}
$\log \xi_{\rm d}$	$1.7^{+0.2}_{+0.3}$	1.7^{f}	$1.69^{+0.38}_{-0.40}$
$A_{\rm Fe}$ (solar)	$1.48^{+0.89}_{-0.60}$	1.48^{f}	$0.88^{+0.56}_{p}$
$E_{\rm cut}$ (keV)	60^{+23}_{-15}	60^{f}	81^{+200}_{-64}
	`zxipcf`		
$N_{\rm H}$ (10^{21}cm^{-2})	–	$5.1^{+1.1}_{-0.6}$	$7.1^{+2.3}_{-1.1}$
$\log \xi_{\rm abs}$	–	0.78 ± 0.10	$0.66^{+0.10}_{-0.18}$
CF	–	$0.96^{p}_{-0.08}$	0.88 ± 0.07
χ^2/dof	10.8/11	17/23	10.8/17

^{p} pegged to its maximum/minimum value.
^{f} fixed.

modelling is not complete, or it may be indicative of the degree that one (or both) of the models approximate well the respective spectral components.

The extrapolation of the best-fit `relxill` model to low energies (< 1.6 keV) is indicated by the dotted blue line in the top panel of Figure 4.9. The model exceeds the average variable component in this energy range. This is due to the effects of the warm absorber. Hence, I fitted the full band (0.3–40 keV) variable component with the model: `zxipcf` $\times$ `relxill` (accounting for Galactic absorption). First, I fixed the `relxill` parameters to their best-fit values obtained from fitting $y_{\rm var,h}$. The fit was statistically acceptable (χ^2/dof $= 17/23$). The best-fit warm absorber parameters are listed in the third column of Table 4.3. The best-fit model and the corresponding residuals are shown in the top and bottom panel of Figure 4.9, respectively. I re-fitted the full band variable spectrum with the same model but letting the `relxill` parameters free. The fit was also acceptable (χ^2/dof $= 11/17$). The best-fit parameters are reported in the last column of Table 4.3. There are differences between the best-fit values listed in the first and third columns of Table 4.3, notably in the PL spectral slopes, but they are within $2\,\sigma$.

Our results imply that the observed variations in MCG-6-3015 are due to a PL continuum which is variable in normalization only, and a variable, X–ray

reflection component from the (ionized) inner disc. Various studies in the past have detected short delays between the continuum and the soft band variations in this source (e.g. Emmanoulopoulos et al. 2014; Kara et al. 2014). Recently, Epitropakis et al. (2016) also detected similar delays between the continuum and the iron line variations in MCG–6-30-15. To measure time lags, both the continuum and the reflection components must be variable. The FFP results presented in this chapter confirm this scenario.

4.4 Conclusions

To correctly estimate flux-flux plots, the mean counts per bin in both light curves must be larger than 200 in order to avoid distortions in the FFP shape due to the Poisson noise bias. As long as this criterion is fulfilled, the bin size of the light curves should be as small as possible, in order to avoid further distortions due to binning, in the case when the intrinsic FFP has a non-linear shape.

The FFP analysis can provide model independent information on both the constant and variable spectral components in the X–ray spectra of AGN. The latter possibility has not been explored in detail so far, although it has interesting advantages. For example, the FFP shape (linear or power-law like) can show conclusively, and in a model independent way, whether variable absorption operates or not. The spectrum shown in Figure 4.9 is not a traditional, observed spectrum. It is a representation of the spectral energy distribution of the source at a certain flux level, using the results from the FFP analysis. Its energy resolution is low, but it is free of non-variable spectral components that complicate the subsequent model fitting. I could construct these spectra at various flux levels, and study the spectral evolution of the source in this way. I plan to explore in detail this possibility in the future. The conclusions from the study of the MCG–6-30-15 FFPs are summarised below.

A) The non-variable, X–ray spectral components in MCG–6-30-15.

A1) I detect spectral component(s) that remain constant at least over the duration of the observations I study (i.e. ~ 4.5 days). At energies above ~ 1.6 keV the constant spectral component is consistent with reflection from cold, neutral material, located more than $5 \times 10^4\, r_{\rm g}$ away from the central source. The results presented in this chapter are consistent with the ones of Taylor et al. (2003). At energies below ~ 1.6 keV, the constant component is well fitted by a black-body model with a temperature of ~ 0.1 keV. This component cannot correspond to

the soft-excess expected from X–ray reflection from a mildly ionized disc, as this should be variable (since the reflection at high energies is variable). It could be due to intrinsic thermal emission from the inner disc itself, if the disc extends to the ISCO around a maximally spinning BH.

A2) The 2–10 and 2–40 keV flux of the high energy, constant component is 5×10^{-12} and 1.9×10^{-11} erg s^{-1}cm^{-2}, respectively, which is 10% and 20% of the average X–ray continuum flux. The 0.3–1.6 keV flux of the low energy component is $\sim$ 17% of the average X–ray continuum flux in the same band. These are not negligible fractions so, in addition to a PL continuum plus a relativistically blurred reflection component, modelling of the X–ray spectrum of the source should also add: a) a constant reflection component from cold material, and b) a constant, blackbody-like component at low energies.

B) The variable, X–ray spectral components in MCG–6-30-15.

B1) The FFPs at energies above $\sim$ 1.6 keV are well fitted with a straight line. This result proves that: a) there are no spectral slope variations, and b) the observed variations cannot be caused by variations of the number and/or the covering factor of absorbing clouds. These are straight forward results, which do not depend on any assumptions regarding the model fitting of the source's spectrum.

B2) Both the low and the high energy FFPs are fully consistent with a PL continuum, which varies in normalization, plus a variable (on time scales as short as 1 ks), X-ray reflection component, from ionized material close to the central BH. The variable reflection component is consistent with the detection of "soft" time lags in this source, since in order to detect delays between two components, both of them must vary. Part of the observed variations at energies below $\sim$ 1 keV are due to variations of the warm absorber. The presence of the variable warm absorber is supported by the non-linearity of the FFPs at energies below 1.6 keV are non-linear (like IRAS 13224–3809).

C) The soft excess in MCG-6-30-15.

It consists of both a constant and a variable component. Both could originate from the inner disc, as long as it extends to the ISCO around a fast rotating BH: the former could be due to the disc's intrinsic emission, the latter due to X–ray reprocessing (from the same disc region). Using the best-fit results of the constant and variable components, I estimate that the 0.3–1 keV flux of the constant and the variable component, in excess of the PL, are 6.8×10^{-12} and 4.3×10^{-12} ergs s^{-1}

cm^{-2}, respectively. Therefore, $\sim$ 60 and 40 per cent of the soft excess flux is due to these two components. It should be noted that that the variable component flux is based on the modeling of the variable component I reported in Section 4.3.5, when the source was in its average-flux state during the 2013 observations. Obviously, the contribution of the variable soft excess component (due to X–ray reprocessing) will be larger/smaller during higher/lower flux states of the source.

Prague doesn't let go. Of either of us. This old crone has claws. One has to yield, or else. We would have to set fire to it on two sides, at the Vyšehrad and at the Hradčany; then it would be possible for us to get away.

Franz Kafka

5

Spectral and polarimetric signatures of X-ray obscuration events in AGN

Contents

X-ray emission in AGN is expected to be polarized thanks to the scattering processes happening in the vicinity of the accretion disc, in addition to the possible polarization of the primary emission itself (e.g. Chandrasekhar 1960; Angel 1969; Haardt & Matt 1993). Absorption and line re-emission also contribute to the total polarization by diluting the signal, adding to the spectrum several local depolarized features (Matt 1993). The polarization signal is strongly affected by 1) the geometry of the corona-disc system (e.g. Schnittman & Krolik 2009, 2010) and 2) general relativistic effects that parallelly transport the polarization position angle along the photon null geodesics (see e.g. Matt 1993; Dovčiak et al. 2008, 2011).

Several observational pieces of evidence confirmed the existence of a relativistically blurred reflection component in AGN. In particular, X-ray spectroscopy

has proven to be a powerful tool to identify the reflection features in AGN X-ray spectra, allowing us to probe the innermost regions of AGN (e.g. Fabian et al. 2009). Additionally, this technique may provide estimates of black hole spins (e.g. Risaliti et al. 2013; Walton et al. 2014; Marinucci et al. 2014b). This was achieved thanks to the high-quality spectra provided by *XMM-Newton* and *NuSTAR* in the 0.3–80 keV range. The first observational X-ray feature associated with relativistic effects was the anomalous shape of the aforementioned iron Kα line detected in type-1 AGN, where the observer has a direct view of the central engine through the polar direction of the system (e.g. Pounds et al. 1990; Matsuoka et al. 1990). The shape of the iron line, with an extended red wing spanning over several keV was soon associated with special and general relativistic effects blurring the signal (e.g. Tanaka et al. 1995; Iwasawa et al. 1996; Nandra et al. 1997). By fitting the observed iron line with relativistic models, it became possible to determine the spin of the black hole (BH), its mass and inclination (see e.g. Miller 2007, for a review). Yet, an alternative interpretation, based on partial covering absorption, has been proposed in order to explain the apparent red wing of the Fe line and the spectral curvature at hard X-rays (e.g. Miller et al. 2008, 2009). The two scenarios have different advantages: on the one hand, blurred reflection is able to explain the spectral and timing properties of accreting systems for a wide range of BH mass. On the other hand, the Compton-thin to Compton-thick (and vice versa) rapid transitions that are observed in "changing-look" AGN (Matt et al. 2003) is suggestive that partial covering should be also taken into consideration. In addition, several occultation events, associated with both Compton-thin and Compton-thick clouds in the broad-line region (BLR), have been reported in AGN (e.g. Risaliti et al. 2007, 2011b; Nardini & Risaliti 2011; Sanfrutos et al. 2013; Torricelli-Ciamponi et al. 2014). Markowitz et al. (2014) estimated the probability to observe an X-ray eclipse (of any duration between 0.2 d and 16 yr) in a given source to be in in the ranges $0.003-0.166$ and $0.039-0.571$, for type I and type II AGN, respectively. By studying X-ray eclipses, it might be possible to constrain the importance of partial obscuration, together with the geometry and location of the distant clouds. This is particularly relevant since obscuration events from BLR clouds do not affect only the AGN light curves but they show a strong impact on their spectroscopic and polarimetric properties. Risaliti et al. (2011a) investigated the effects of successive eclipses of the receding and approaching parts of the accretion disc on the shape of the iron line. In fact, due to special and general relativistic effects, obscuring various parts of the disc will result in a variability in the profile of the observed emission line, which provides a new probe of the innermost regions of the disc. In

a similar fashion, Marin & Dovčiak (2015) explored the effects of such events on the polarimetric signal. The authors showed that eclipses induce a variability in the polarization signal due to the covering of different parts of the disc emitting a non-uniformly polarized light, mainly due to relativistic effects.

These pioneering studies predict what a time-resolved spectroscopic or polarimetric observation would detect, provided that the source is bright enough and that a random occultation event is serendipitously caught. Both the aforementioned papers considered a simple geometry for the accretion disc, divided in a receding and an approaching halves, illuminated by a power-law primary continuum. It is now possible to refine those studies by applying the state-of-the-art relativistic modelling to account for a more complex disc flux pattern, together with a better constrained coronal emission. In this chapter, I build upon the previous analyses by Risaliti et al. (2011a) and Marin & Dovčiak (2015) in order to estimate the spectral variability as well as the time-dependent polarization that are induced by obscuration events. In this chapter, I use a full relativistic ray-tracing model that allows us to track the position of a circular cloud as it obscures different regions of the disc. The disc is illuminated by a point-like source located on the axis of rotation of the BH, known as lamp-post geometry.

5.1 Model

Our model consists of a central BH of mass $M_{\rm BH} = 10^7\,{\rm M}_\odot$ that is accreting matter through an optically thick geometrically thin disc. This mass is typical for nearby Seyfert galaxies (see e.g. Lubiński et al. 2016b). The disc is inclined by $\theta = 30°$ or 60° with respect to our line of sight. I consider a Schwarzschild BH ($a^* = 0$) and a maximally rotating Kerr BH ($a^* = 0.998$). The primary source is assumed to be point-like (lamp-post), located on the rotation axis of the BH, emitting a power-law spectrum with a photon index $\Gamma = 2$. I investigate in this chapter the effects of the height of the source by considering a source at heights 2.5, 6 and 10 r_g ($r_g = GM/c^2$). The higher the height the weaker the gravitational redshift and the light bending effect, which will lead to illuminating further out regions of the disc by the lamp-post. The X-ray spectra are simulated using different flavours of the relativistic ray-tracing KYN[1] code (Dovciak et al. 2014), which computes the time evolution of a local spectrum seen by a distant observer. The model allows us to consider obscuration by a circular cloud, as it crosses the line-of-sight of the observer. The cloud is characterized by two numbers (α, β), which represent the

[1] https://projects.asu.cas.cz/stronggravity/kyn

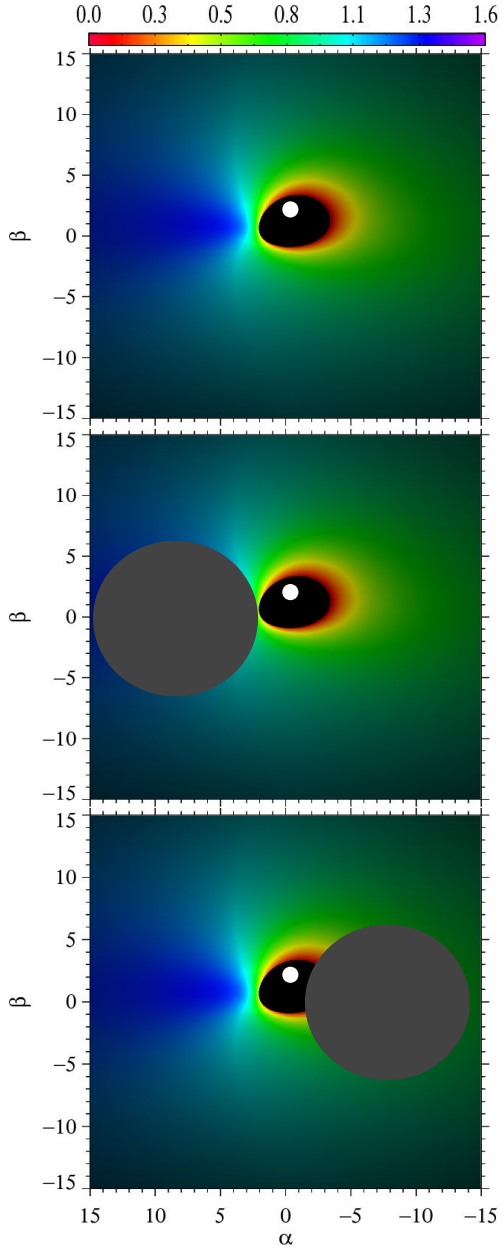

Figure 5.1: Scheme of the configuration which is proposed in this chapter, depicting a circular cloud moving along the line of sight and shading different parts of the accretion-disc and lamp-post (white dot) system. The colour scale represents the energy shift defined as the ratio observed energy over local energy ($g = E_{\rm O}/E_{\rm L}$). α and β represent the coordinates on the sky of the observer in units of r_g (impact parameters) in the $\varphi-$, $\theta-$ direction, respectively.

position of the centre of the cloud on the sky of the observer (impact parameters of the centre) in the azimuth and altitude (φ, θ) direction, respectively, and by its radius R_c. I assume a cloud of radius $30\,r_g$ that is moving with a Keplerian velocity (v_K), in the plane $\beta = 0$, and located at a distance of $10^4\,r_g$ from the central BH (see e.g. Risaliti et al. 2009; Marinucci et al. 2014b) moving from $\alpha > 0$ (the approaching part of the disc) toward $\alpha < 0$ (the receeding part of the disc). This will result in a duration of the eclipse $\Delta t = 2R_c/v_K \simeq 295$ ks. This is in agreement with the duration of the eclipse in MCG–06-30-15 ($M_{BH} \simeq 1.6 \times 10^6\,M_\odot$; Bentz et al. 2016), which was reported by McKernan & Yaqoob (1998), when scaled for the mass of the source[2]. A scheme of the corona-disc-cloud system as projected in the observer's sky is presented in Figure 5.1.

5.2 Spectral signatures

In this section, I compute the predicted spectral signatures of an X-ray eclipse by a Compton-thick cloud orbiting the BH. I assume the following model:

$$\texttt{model} = \texttt{TBabs} \times \texttt{KYNXillver}_{\texttt{abs.}} + \texttt{KYNXillver}_{\texttt{non-abs.}},$$

where `TBabs` (Wilms et al. 2000a) represents a circular cloud of column density $N_H = 10^{24}\mathrm{cm}^{-2}$ (equivalent, for $R_C = 30\ r_g$ and $M_{BH} = 10^7\ M_\odot$, to a number density $\sim 10^{10}\,\mathrm{cm}^{-3}$, which is consistent with the expected values for the BLR clouds), while $\texttt{KYNXillver}_{\texttt{abs.}}$ and $\texttt{KYNXillver}_{\texttt{non-abs.}}$ represent the spectrum that is transmitted[3] through the cloud and the non-absorbed spectrum, respectively. The reprocessing of the primary emission in the ionised disc is estimated according to the `XILLVERD` tables (see García et al. 2016). I considered an ionized disc with density $n_H = 10^{15}\,\mathrm{cm}^{-3}$, ionization parameter $\log \xi_d = 2$, and solar abundance, observed at inclinations of $\theta = 30°$ and $60°$. Figure 5.2 shows the resulting spectra for different positions of a cloud of radius $30\,r_g$ as it passes in the line of sight for Schwarzschild and Kerr BHs (dashed red lines and solid blue lines, respectively) and lamp-post heights of 2.5, 6 and $10\,r_g$, for $\theta = 60°$. The spectral variability for the case of $\theta = 30°$ shows a very similar trend compared to the 60° case.

[2]It should be noted that Iwasawa et al. (1996) has originally considered the flux drop during the ASCA observations of this source (later interpreted by McKernan & Yaqoob (1998) as due to obscuration) to be due to a concentration of the source in small radii (hence light focusing made the "observed" flux low and the line broader, similar to the light-bending model presented by Miniutti & Fabian (2004)

[3]I should be noted that I considered the photoelectric absorption only, neglecting Compton scattering out of and into the line of sight.

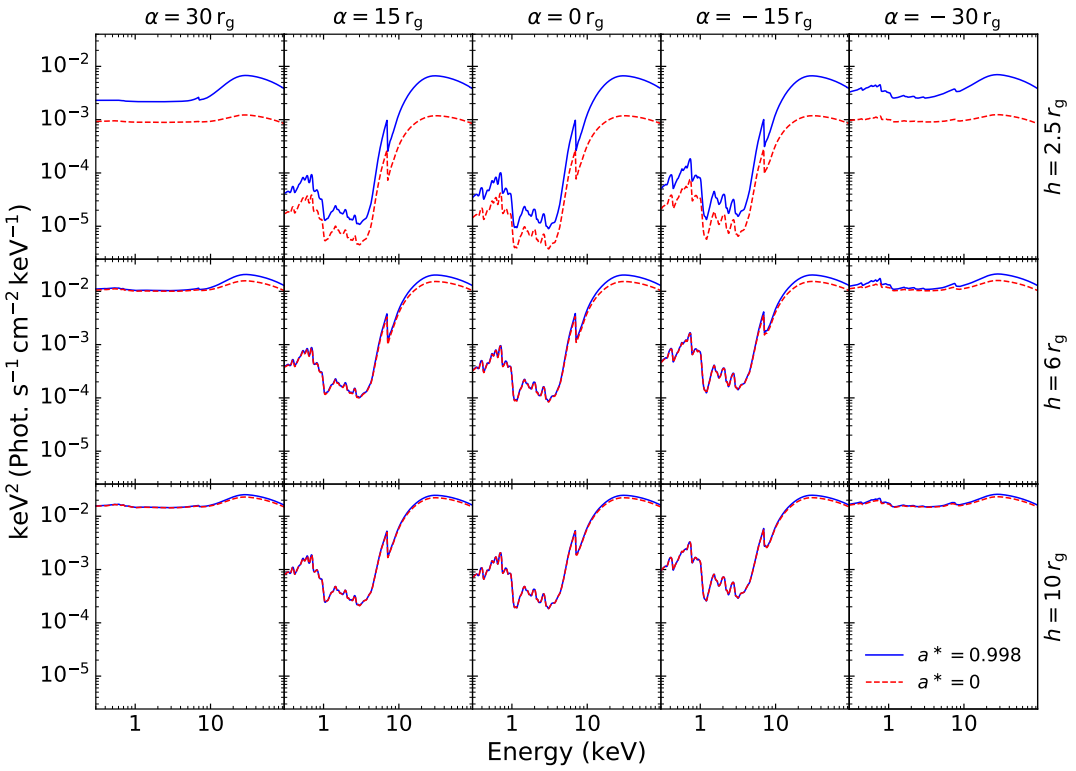

Figure 5.2: The observed spectra resulting from obscuration events as a clouds of radius $30\,r_g$, located at a typical BLR radial distance and orbiting Schwarzschild ($a^* = 0$; dashed red lines) and Kerr ($a^* = 0.998$; solid blue lines) BHs, is passing through the observer's line of sight (i.e. for different values of α, assuming $\beta = 0$). I consider primary sources located at 2.5, 6 and 10 r_g above an accretion disc with an inclination of 60°.

A clear decrease in the flux below ~ 20 keV can be observed when the lamp-post is obscured. The source becomes reflection dominated, since the main contribution is from the unobscured parts of the disc. Below 4 keV, the flux decreases on average by ~ 30 and 100 times, for $h = 10\,r_g$ and $h = 2.5\,r_g$, respectively. In the Fe line band (5-7 keV) a smaller decrease, by a factor of $\sim 7-8$, is seen which is similar for all heights. By comparing positive and negative values of α, this figure clearly shows the asymmetry that is introduced by the relativistic effects as the cloud obscures different parts of the disc. When the cloud is obscuring the receding patches of the disc ($\alpha < 0$) the intensity is typically higher compared to its symmetric position when the cloud is obscuring the approaching patches of the disc ($\alpha > 0$).

It should be noted that the differences in spectral shape and intensity between a BH of spin 0 and 0.998 are larger for lower heights. It is clear from the upper row of Figure 5.2 that the spectra corresponding to the Kerr BH are brighter than the ones corresponding to a Schwarzschild BH. The difference in intensity for $h = 2.5\ r_g$ is mainly due to the fact that, in the latter (Schwarzschild) case, the primary is

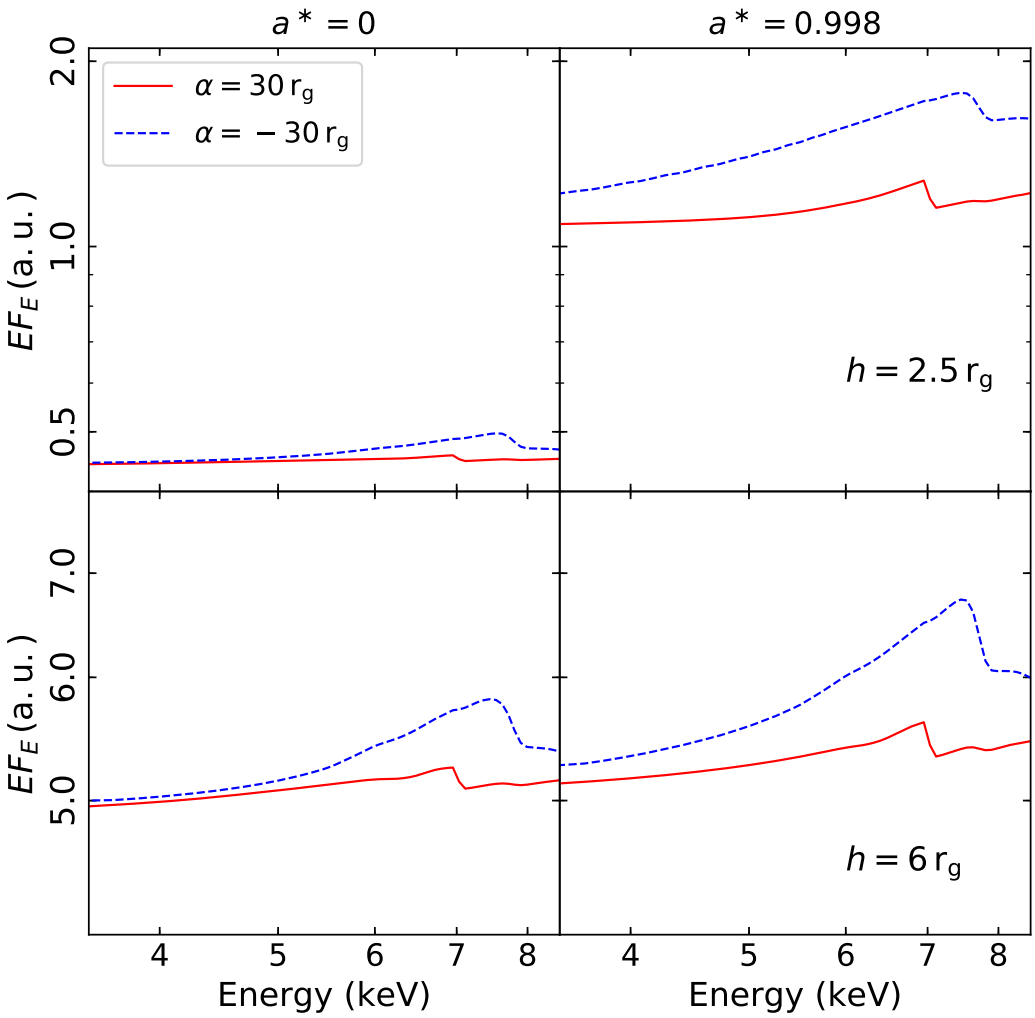

Figure 5.3: The observed spectra, in the 3.5-8.5 keV range, considering a cloud of radius $30\,r_g$ obscuring the approaching ($\alpha = 30\,r_g$, solid red lines) and receding ($\alpha = -30\,r_g$, dashed blue lines) parts of the accretion disc for BH spins of 0 (left panels) and 0.998 (right panels). I consider primary sources located at 2.5 and 6 r_g (top and bottom panels, respectively) above an accretion disc with an inclination of 60°.

much more diluted due to the source being very close to the event horizon (only distant 0.5 r_g as opposed to 1.5 r_g in the former, Kerr, case). Moreover, there is less reflection due to the fact that the innermost stable circular orbit is ~ 5 times farther from the BH. These differences become less prominent for larger heights as light bending gets weaker and the lamp-post can illuminate further out regions of the accretion disc. This is in agreement with previous spectral analyses (e.g. Fabian et al. 2014; Dovciak et al. 2014; Kammoun et al. 2018).

It should be noted also that the profiles of the emission lines differ when different

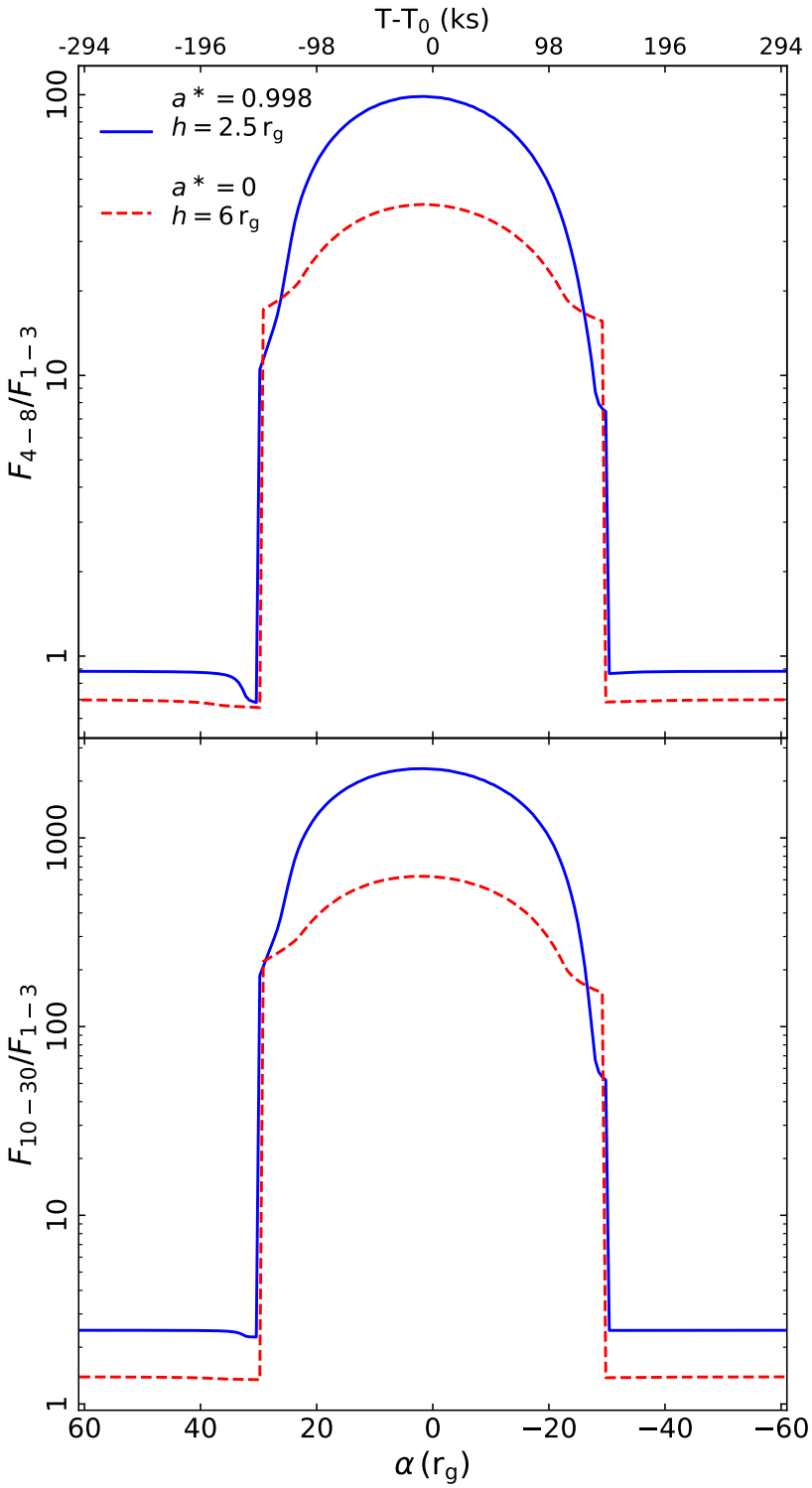

Figure 5.4: Examples of the hard-to-soft flux ratios expected from X-ray eclipses by a cloud of radius 30 r_g, as it moves along the line of sight. I consider the soft band in the 1–3 keV range as a proxy of the primary emission, and two hard bands the 4–8 (top panel) and 10–30 keV (bottom panel) bands, which should be dominated by the FeK line and the Compton hump, respectively. I show the cases of a maximally rotating BH with a lamp-post located at 2.5 r_g (solid blue lines) and a Schwarzschild BH with a lamp-post located at 6 r_g (dashed red lines).

parts of the accretion disc are shaded, as shown in Figure 5.3. This figure presents a zoom-in on the observed spectra in the 3.5–8.5 keV band, which is dominated by the Fe K line, for the cases when the cloud is obscuring the approaching ($\alpha = +30\,r_g$) and receding ($\alpha = -30\,r_g$) parts of the disc. I considered the cases of Schwarzschild and Kerr BHs, for lamp-posts at $h = 2.5$ and $6\,r_g$ above the accretion disc with an inclination of 60°. In addition to the effects mentioned above, this figure clearly shows the variability in the profile of the Fe line owing to shading various regions of the accretion disc. When the cloud is obscuring the receding parts of the disc, the unobscured (approaching) parts of the disc will dominate the observed spectrum. In this case, the spectrum is brighter and the emission line is blueshifted with respect to the case when the cloud is obscuring the approaching part of the disc, thanks to Doppler boosting and Doppler shift effects.

Moreover, this model allows us to estimate the time evolution of the hard-to-soft ratio (HR) light curves during eclipses. Figure 5.4 shows examples of the HR light curves of the fluxes in the 4–8 keV band (characterized by the Fe K line) and the 10–30 keV band (characterized by the Compton hump) over the one in the 1–3 keV band (representing the primary emission) during the eclipse by a cloud of radius 30 r_g. I consider the cases of a maximally rotating Kerr BH with a lamp-post at 2.5 r_g and a Schwarzschild BH with a lamp-post at 6 r_g above an accretion disc with an inclination of 60°. Considering the first case, the HRs are constant when the cloud is obscuring the outer parts of the disc. A small dip can be then observed for $\alpha \simeq 32$ r_g as the cloud obscures the innermost regions of the disc, where Doppler boosting is maximum, leading to a decrease of the flux in the hard bands, where reflection from the disc is important. This dip is smaller for the 10–30 keV band, which will be affected less by absorption for the considered column density ($N_H = 10^{24}\,cm^{-2}$). Once the primary source is obscured, the HRs increase suddenly due to the decrease of the flux in the 1–3 keV band. As the cloud moves into the line of sight, the HR increases until reaching $\alpha \simeq 1.5$ r_g then starts decreasing again. It should be noted that the HR plots show an asymmetric profile, due to relativistic effects as the cloud obscures different regions of the accretion disc. A qualitatively similar behaviour can be also observed for the case of $a^* = 0$ and $h = 6$ r_g. The main differences compared to the previous case are that 1) the obscuration of the primary occurs later due to the fact that the lamp-post is at a larger height and 2) the dip at $\alpha \simeq 32$ r_g is less prominent due to the fact that for low spins the disc does not extend close to the BH, thus the innermost regions which are supposed to be affected the most by relativistic effects do not contribute to the observed signal. The HR light curves were also studied by Sanfrutos et al. (2016),

who assumed instead a radially extended corona. It should be noted that many AGN, at low redshift, show large amplitude variability on timescales of a few tens of kiloseconds. MCG–6-30-15, for example, showed an amplitude variability by a factor of ~ 2 within ~ 20 ks as seen in the previous Chapter. When this variability is caused by a change in the intrinsic luminosity of the primary with a constant power-law slope, the HR light curves are expected to be constant. However, some sources may also reveal a variability in the power-law slope on timescales of a few tens of kiloseconds, as it is the case for IRAS 13224–3809, which shows a positive correlation between the power-law slope and the brightness of the source, i.e. the brighter the source, the softer the power-law (e.g. Kammoun et al. 2015; Jiang et al. 2018). A similar behaviour was observed on longer timescales ($\sim 7 - 11$ yr; e.g. Sobolewska & Papadakis 2009). For such variability scenario, the HR will be larger when the source is dimmer, showing a similar behaviour to the one expected from X-ray eclipses. However, the shape of the HR strongly depends on the variability pattern and such analysis is beyond the scope of this chapter.

5.3 Polarimetric signatures

In this section, I present the effects of obscuration events on the polarization signal. For this reason I use the `KYNlpcr` model that allows us to obtain the Stokes parameters (I, Q, U, V), the polarization degree (P) and the polarization position angle (Ψ) as a function of energy (in the 2–60 keV range), for each position of the cloud. The polarization degree is computed according to the usual Stokes formalism, i.e.,

$$P = \frac{\sqrt{Q^2 + U^2 + V^2}}{I}$$

and the polarization position angle is

$$\Psi = \frac{1}{2} \arctan\left(\frac{U}{Q}\right).$$

The polarization position angle is defined with respect to the system rotation axis, so a value of 0° (90°) will be referred to as parallel (perpendicular) polarization. For this case, the model assumes a neutral accretion disc based on the `NOAR` tables (Dumont et al. 2000), for spectral features of the disc reflection, with single scattering approximation (Chandrasekhar 1960) for local polarimetric properties. It should be noted that reflection tables for the polarization of ionized discs are not available in the literature yet (Goosmann, Marin et al., in prep). The effect of disc ionization

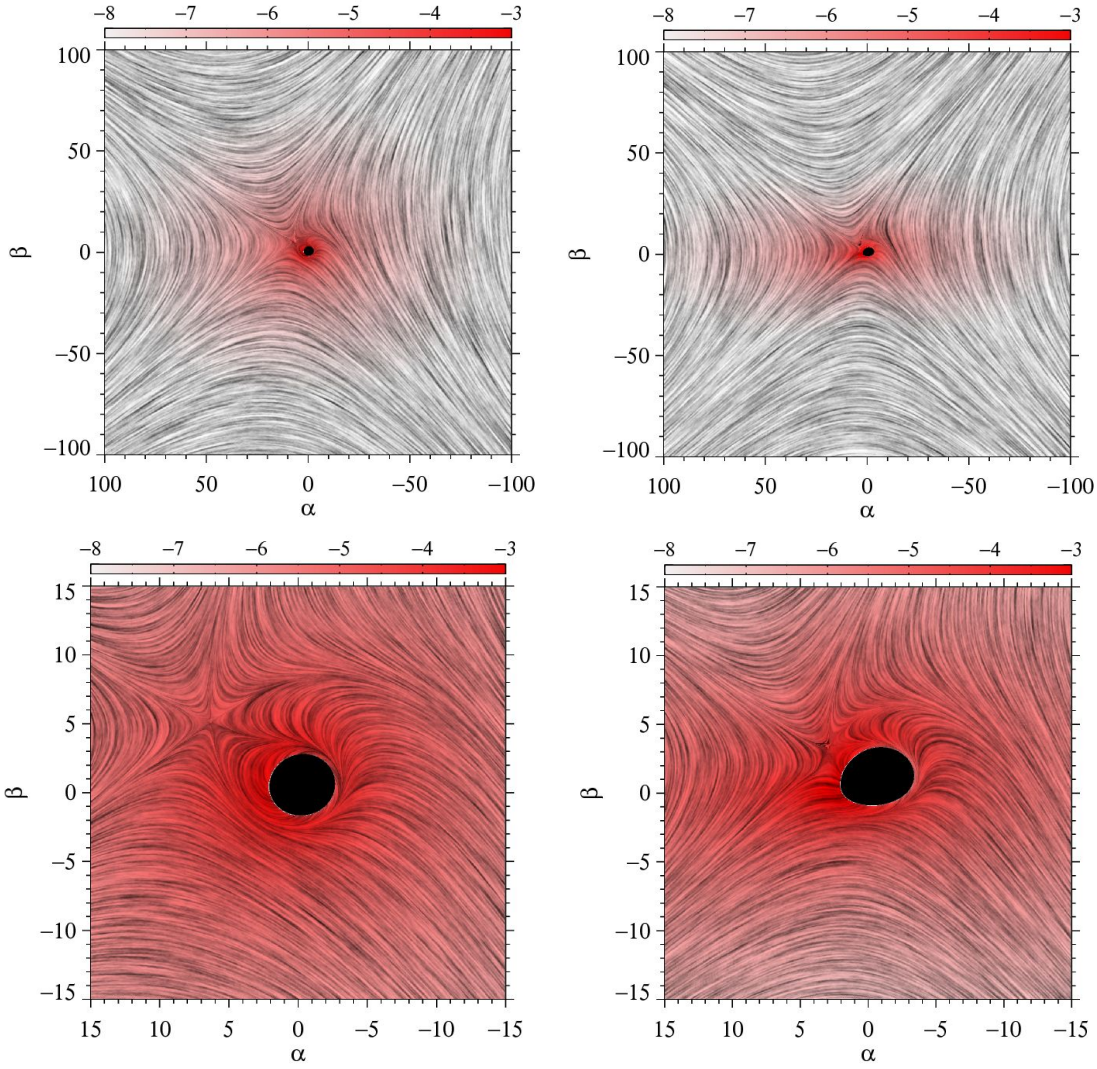

Figure 5.5: The expected polarization, in the 2–8 keV range, throughout the accretion disc (projected in the observer's sky) for a lamp-post located at 2.5 r_g above a Kerr BH. I consider inclinations of 30° (left panels) and 60° (right panels). The black curves depict the direction of the polarization at the detector. It is determined by the local polarization direction induced by disc reflection (for an unpolarized primary) as well as the rotation of the polarization vector between the disc and observer due to relativistic effects. The colour scale represents the polarized flux (defined as total flux times polarization degree, in log scale). The lower panels show a zoomed in snapshot of the innermost regions of the disc, where the relativistic effects dominate.

would be imprinted mainly in the unpolarized emission lines characterizing the reflection component, affecting mainly the soft X-rays. The cloud is assumed to be optically thick ($N_{\rm H} \to \infty$). In reality, the contribution of the transmitted light, through the cloud, to the polarization signal is negligible (see Marin & Dovčiak 2015), hence it can be safely neglected. I consider a primary source at heights 2.5, 6 and 10 r_g, being either unpolarized or polarized with $(P, \Psi) = [(2\%, 0°), (2\%, 90°)]$. The real polarization state of the primary source depends on its geometry, properties (temperature and optical depth), and the viewing angle. Thus I chose these states as an intermediately polarized light, which is expected from a symmetric corona (see Schnittman & Krolik 2010, for more details). I considered both Schwarzschild and Kerr BHs and inclinations of 30° and 60°.

Figure 5.5 shows two examples of the pattern of the polarized light throughout an accretion disc for the two considered inclinations, assuming a lamp-post at 2.5 r_g above a Kerr BH. The zoomed out snapshots (upper panels) show that the contribution to the polarized signal is mainly arising from the innermost regions of the accretion disc. Moreover, it is clear from these panels that, due to the asymmetry caused by the non-zero inclination, the contributions from the 'equatorial' regions of the disc are larger than the ones from the 'polar' zones. It should be noted that this effect is higher for larger inclinations. This figure also shows the dependence of the polarization angle on the location of the emission from the disc. The polarization induced by the scattering process has a perpendicular direction to the scattering plane. Thus the polarization of the rays emitted from the on-axis primary source and scattered from the accretion disc at large radii, where both the special (due to relatively slower orbital speeds) and general relativistic effects (due to the smaller gravity) are weak, will depend only on the azimuth, which determines the scattering plane. For example, the light rays emitted towards or away from the observer that scatter from the accretion disc and reach the observer (polar regions of the accretion disc in Figure 5.5, close to $\alpha = 0$) have a vertical plane of scattering, and thus the polarization direction is horizontal. On the other hand, the light rays emitted to the east or west side of the accretion disc that scatter towards the observer (equatorial regions of the accretion disc in Figure 5.5, close to $\beta = 0$) have a horizontal scattering plane, and thus the polarization direction is vertical.

I should also note the presence of a depolarizing region (a.k.a. "critical point", see Dovčiak et al. 2008) located to the North-West of the BH ($\alpha > 0$ and $\beta > 0$ in Figure 5.5), where the photons are emitted perpendicularly to the disc, due to special relativistic aberration. The location of this region depends on the spin of the BH and on the inclination angle, and it may get closer, or even within the ISCO

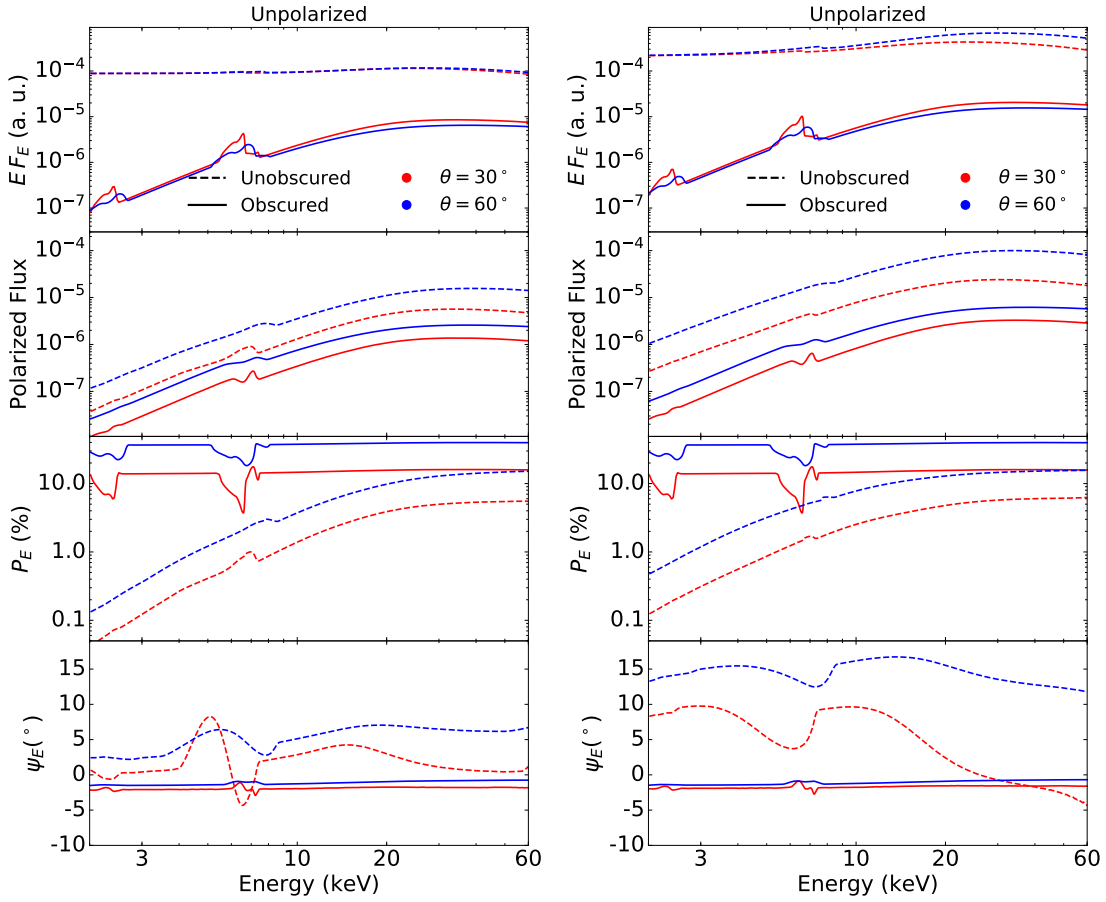

Figure 5.6: X-ray flux (EF_E), polarized flux (EF_E times the polarization degree), polarization degree P and polarization position angle Ψ as function of energy seen by an observer at infinity. I consider an unpolarized point-source corona at 2.5 r_g above the BH spinning with $a^* = 0$ (left panels) and $a^* = 0.998$ (right panels) with an accretion disc that is inclined by 30° (red lines) and 60° (blue lines). The parameters are shown for two configurations: an unobscured system (dashed lines) and a system that is obscured by a cloud, of radius 30 r_g, that is aligned with the BH.

in some cases (see Figure 3 in Dovčiak et al. 2008). Moving closer to the BH from the critical point, the relativistic effects are strong enough to affect the incident and reflection angle of the photons in the local co-moving frame. Therefore also the orientation of the local scattering plane and consequently of the polarization direction will be altered with respect to the cases where relativistic effects are not as prominent. The polarization direction is further changed as the polarization vector is transferred from the inner accretion disc to the observer at infinity. Hence the observed direction of polarization from these regions is not trivial (see the central parts of the accretion disc in Figure 5.5).

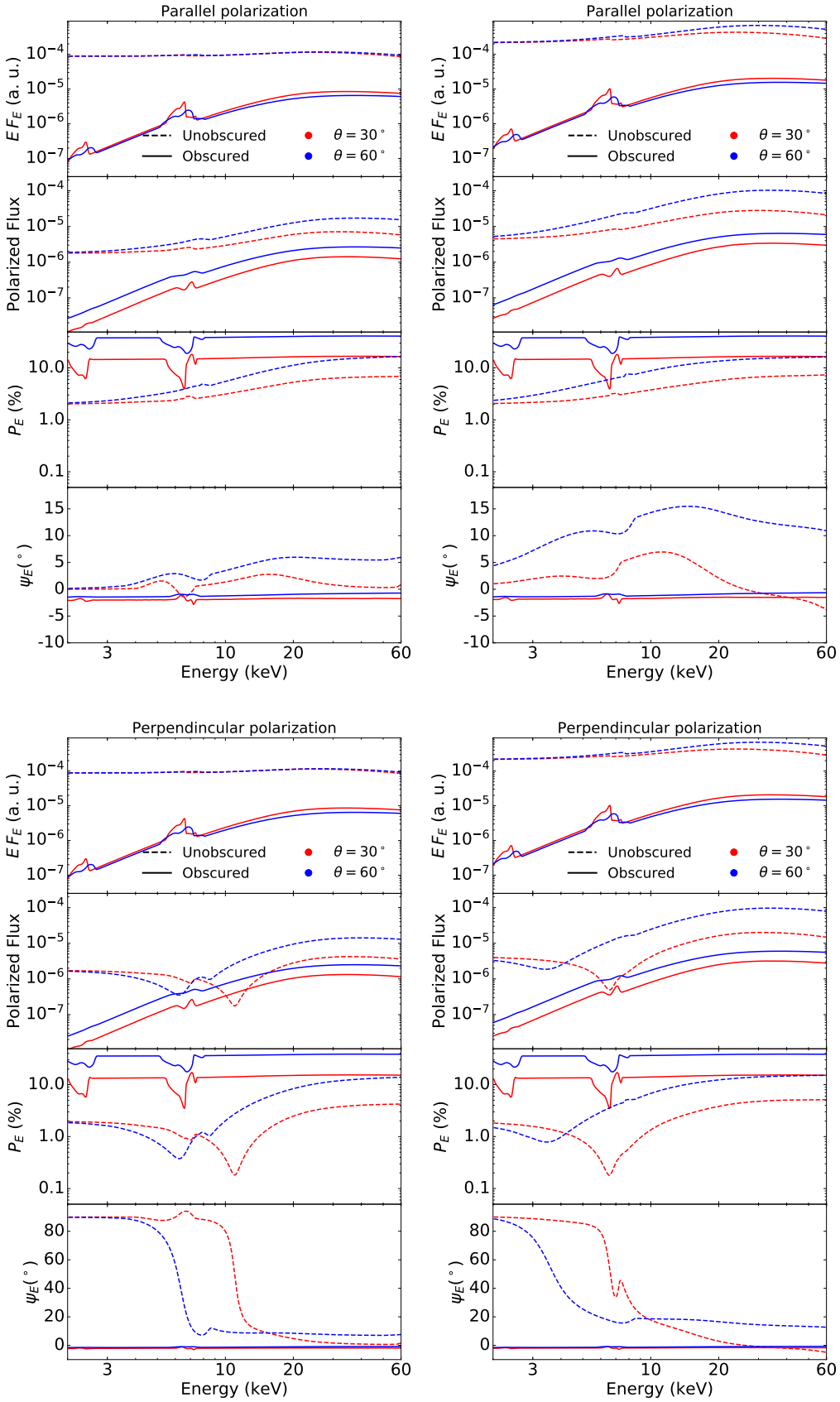

Figure 5.7: Similar to Figure 5.6 but for a 2-percent parallelly (top panels) and perpendicularly (bottom panels) polarized primary.

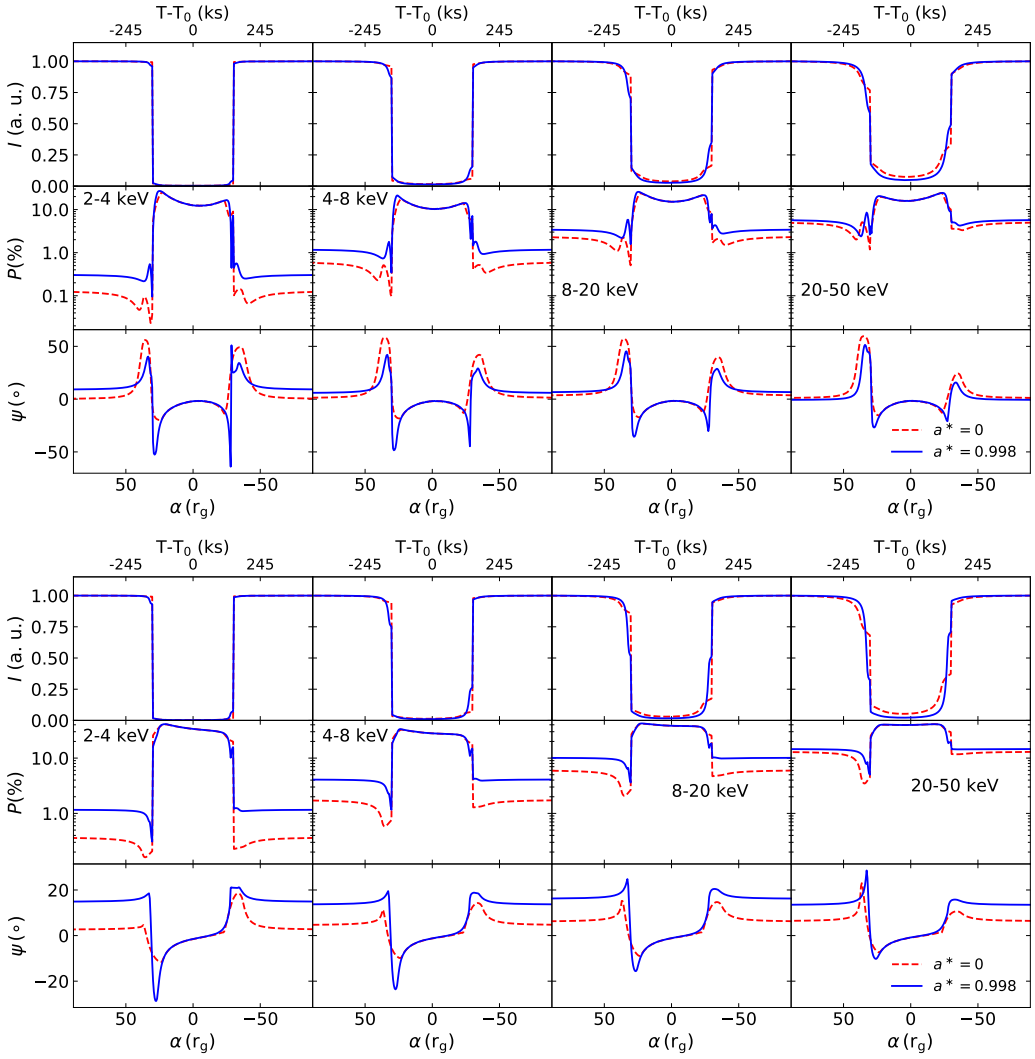

Figure 5.8: Temporal evolution of the X-ray flux, polarization degree (P) and polarization position angle (Ψ) in the 2-4 keV, 4-8 keV, 8-20 keV and 20-50 keV bands. I considered accretion discs with inclinations of 30° (top pannel) and 60° (bottom panel) around Schwarzschild (red lines) and maximally Kerr (blue lines) BHs. I considered an optically thick cloud ($R_{\rm c} = 30\,{\rm r_g}$) eclipsing the system whose primary ($h = 2.5\,{\rm r_g}$) is unpolarized .

5.3.1 Energy dependence

I present in Figure 5.6 and 5.7 the total flux, the polarized flux defined as the total flux times the polarization degree, the polarization degree and the polarization position angle as a function of energy for unpolarized and polarized primary, respectively, located at $2.5{\rm r_g}$ above the disc. I show the results for both Schwarzschild and Kerr BHs (top and bottom panels, respectively). I considered the cases of an unobscured source and the case when the primary is obscured by a cloud ($R_{\rm c} = 30\,{\rm r_g}$) in the line of sight aligned with the BH ($\alpha = 0\,{\rm r_g}$), as an example.

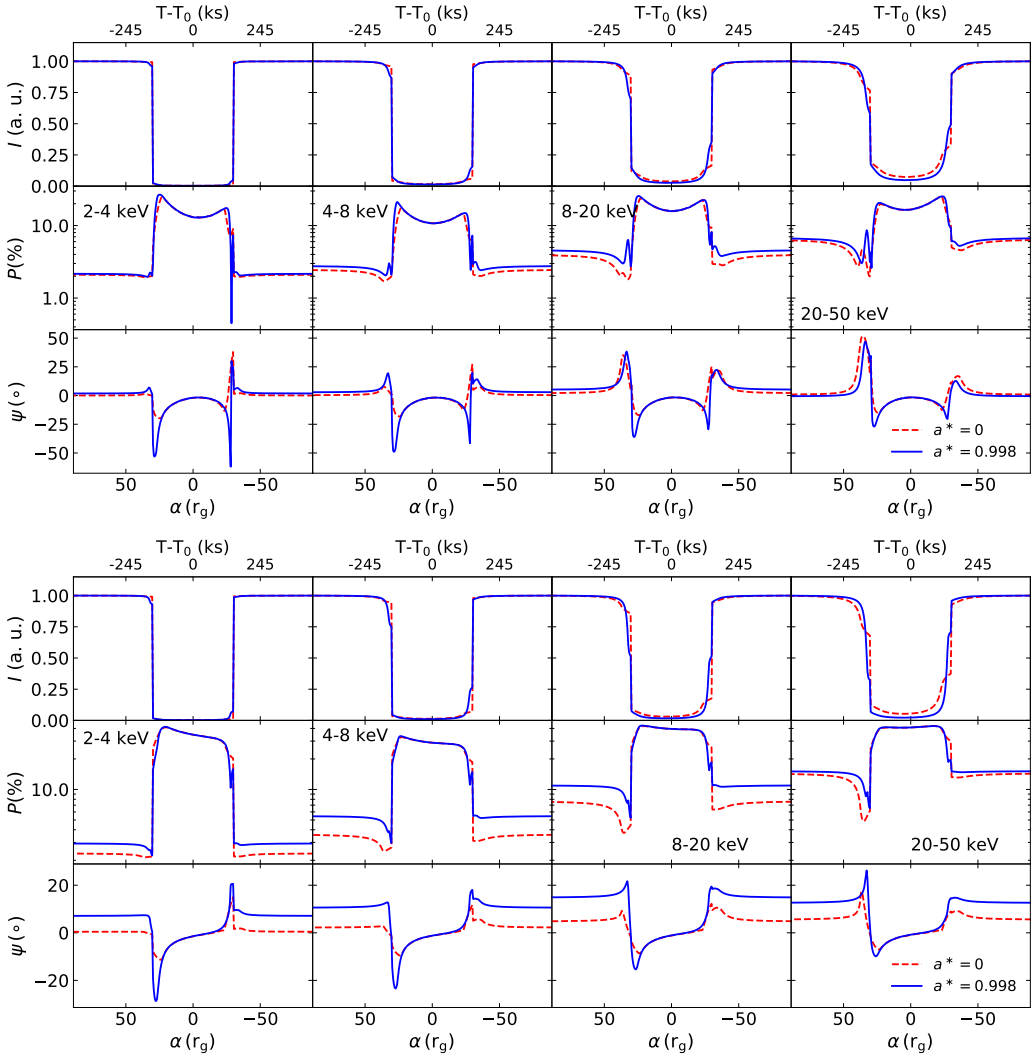

Figure 5.9: Same as Figure 5.8 but considering a 2-percent parallely polarized primary.

Considering the unobscured cases, it should be noted that the higher the inclination the higher the polarization degree, due to special and general relativistic effects (Dovčiak et al. 2011). For the unpolarized and parallelly polarized primary, $P(E)$ increases with energy. At low energies photo-absorption in the disc dominates, thus $P(E)$ is the same as the one of the primary emission. However, for higher energies where the disc reflection becomes more important the polarization varies (increases or decreases) depending on the the polarization angle of the irradiating spectrum. Scattering inside the disc tends to result in parallel polarization angles. If the irradiating emission is parallelly polarized, then the resulting polarization degree increases. Otherwise, the orthogonality between the two vectorial components tends to decrease the net polarization degree. It should be noted that, for the perpendicular polarization, at $\theta = 30°$, the polarization degree shows a dip at

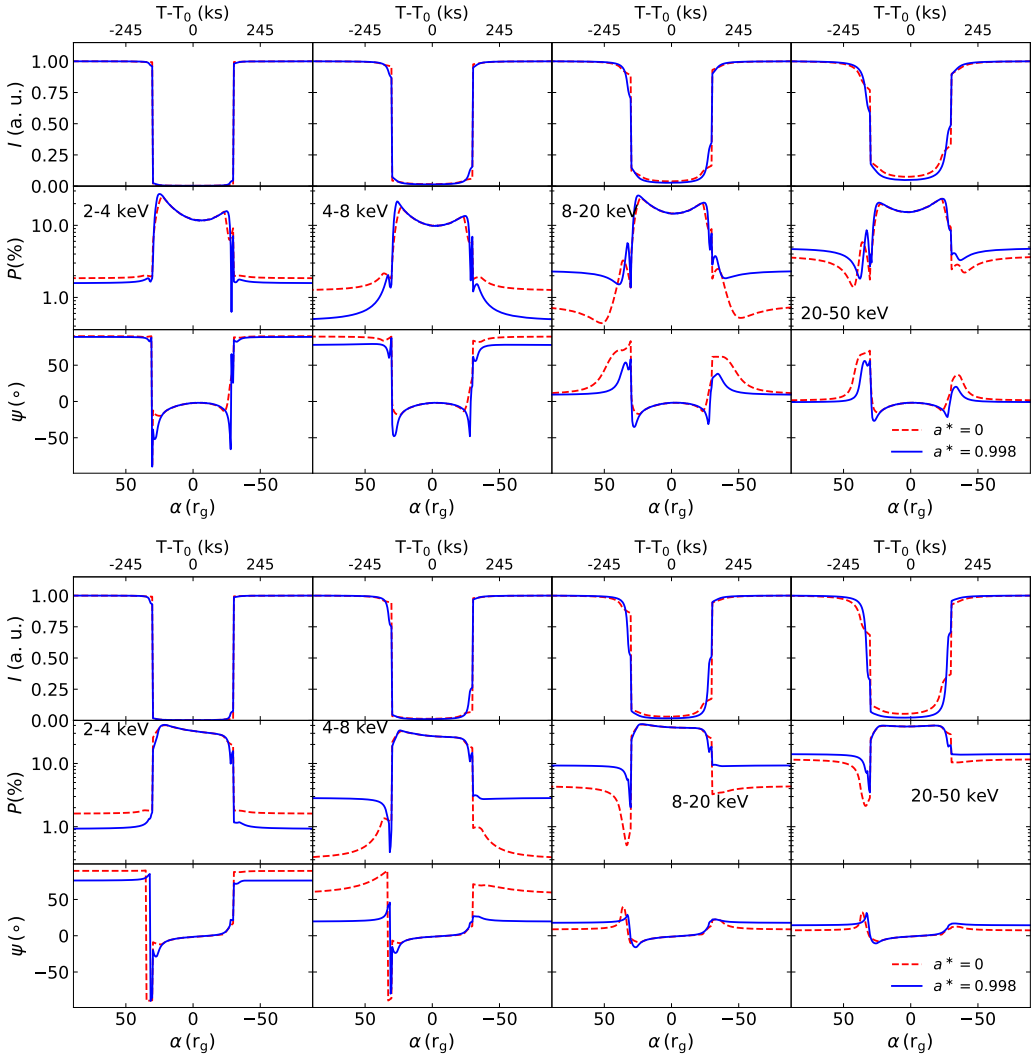

Figure 5.10: Same as Figure 5.8 but considering a 2-percent perpendicularly polarized primary.

energies below ~ 10 keV and 7 keV, for the Schwarzschild and Kerr BHs, respectively. Then it increases continuously at higher energies. A similar behaviour can be seen for $\theta = 60°$ but the transition energies are ~ 7 and 4 keV, respectively. These transitions are accompanied by a decrease in the polarization position angle at higher energies, due to the fact that scattering inside the disc becomes more prominent at higher energies, resulting in parallel polarization angles. The energy at which the rotation occurs depends on the spin of the BH, which determines the location of the ISCO. The higher the spin, the closer the ISCO to the BH, which leads to a variation in Ψ at lower energies.

Considering the obscured spectra, which correspond to pure reflection, the polarization degree is boosted up to $\sim 15\%$ and $\sim 38\%$ for $\theta = 30°$ and $60°$ respectively. This is due to the obscuration of the primary emission, being either

unpolarized or slightly polarized but with a high flux, which tends to dilute the polarization signal from the disc. The $P(E)$ patterns show a clear decrease in polarization due to the broad emission lines from the disc, which are expected to be unpolarized (e.g. Matt 1993). Figure 5.6-5.7 show a decrease in the polarization position angle for all cases. I should be stressed that the behaviours of $P(E)$ and $\Psi(E)$ are highly dependent on the position of the cloud as it eclipses different parts of the accretion disc, as I will discuss in the next section.

5.3.2 Time dependence

I explore in this section the variability (on a timescale up to a few hundred ks) that is introduced in the polarization signal due to obscuration events. Figs. 5.8-5.10 show the temporal evolution of the flux, the polarization degree and polarization position angle as a cloud of radius $30\,r_g$ eclipses the innermost parts of an AGN. I present in Figure 5.8 the results assuming an unpolarized primary located at $2.5\,r_g$ above either a Schwarzschild or a Kerr BH, for inclinations of 30° and 60°. In Figs. 5.9 -5.10, I present the same results for a 2 percent (parallelly and perpendicularly, respectively) polarized primary. I considered 4 energy bands: 2–4, 4–8, 8–20 and 20–50 keV. The polarization signal of the accretion disc is not uniform due to relativistic effects (see e.g. Schnittman & Krolik 2009, 2010), as shown in Figure 5.5. Thus the variability pattern seen in these figures is caused by receiving signal from different patches of the disc as the cloud is moving across the line of sight.

I consider first the unpolarized primary case for an inclination of 30°. In the 2–4 keV band, the polarization degree starts from a negligible value in the unobscured case then it shows a small increase, followed by a decrease, as the cloud is moving closer to the center ($\alpha \simeq 36$ and 32 r_g for the Schwarzschild and Kerr BHs, respectively) that is accompanied by a little decrease in flux and a remarkable variation in polarization position angle. This effect is mainly due to the obscuration of the depolarizing region located to the North-West of the BH (see Figure 5.5). It should be noted that this effect is smaller for higher inclinations and/or low spin values since, in these cases, this region is very close to the horizon. As the cloud moves further it eclipses the lamp-post causing the flux to drop drastically and increasing P, which reaches ∼25% (at $\alpha \simeq 23\,r_g$) and 26% (at $\alpha \simeq 25\,r_g$) for Schwarzschild and Kerr BHs, respectively. However, Ψ rotates to negative values of $\sim -25°$ and $\sim -50°$ for Schwarzschild and Kerr BHs, respectively. $P(t)$ decreases with time and reaches $\sim$ 12% at $\alpha = 0\,r_g$, for both spins, while $\Psi(t)$ increases up to $\sim -1°$. As the cloud is moving away from the center, $P(t)$ increases again up to $\sim$ 16% at $\alpha \simeq -23\,r_g$ and $-25\,r_g$ for Schwarzschild and Kerr BHs,

respectively. This is accompanied by a decrease in $\Psi(t)$. As the cloud is moving further out and uncovering the lamp-post $P(t)$ decreases and re-increases suddenly at $\alpha \simeq -30\,\mathrm{r_g}$ ($\Delta P \simeq 2\%$ and 6.7% for Schwarzschild and Kerr BHs, respectively). As for $\Psi(t)$, its behaviour is inverted for the Kerr BH, while it increases continuously for the Schwarzschild case. This effect is due to unobscuring the depolarizing region described above. It should also be noted that the approaching part of the disc contributes substantially to the polarization degree due to Doppler boosting (as shown in Figure 5.5). This effect becomes more important for higher inclinations. Therefore, obscuring/unobscuring this part of the disc will lead to a decrease/increase in $P(t)$ before obscuring/unobscuring the primary source. As the cloud is moving out of the line of sight all the quantities go back smoothly to their original values. Qualitatively, a similar variability pattern can be seen for all energy bands, having different values as various processes and spectral features dominate in different energy bands. For example, the increase in polarization degree is the smallest in the 4–8 keV band, which is affected by the presence of the broad unpolarized Fe line. In general, the variation of $P(t)$ can be described by an asymmetric double peaked profile, where the peaks correspond to the start and the end of the eclipse, being larger for the former case. However, it should noted that this is inverted for the 20–50 keV band where the second peak is higher. It should be noted that $P(t)$ and $\Psi(t)$ show a qualitatively similar behaviour for the parallelly polarized primary as well.

For a perpendicularly polarized primary, $P(t)$ shows a similar behaviour compared to the other two cases. However, $\Psi(t)$ in the 2–4 keV and 4–8 keV bands starts from $\sim 90^\circ$ when the lamp-post is unobscured then rotates quickly to negative values as soon as the primary is obscured, showing then a variability pattern similar to the parallelly polarized and unpolarized primary. $\Psi(t)$ then increases again to $\sim 90^\circ$ when the cloud is moving away from the line of sight. However, at higher energies, where scattering in the disc is more prominent, leading to a more parallel polarization, $\Psi(t)$ varies in a similar fashion to the previous polarization scenarios. It should be noted that in all cases, both Schwarzschild and Kerr BHs show the same pattern when the innermost regions of the disc are obscured, while the patterns differ once these regions are unobscured. This is due to the fact that in the case of a Kerr BH the accretion disc reaches lower radii with respect to a Schwarzschild BH giving different observed polarization states.

I consider now the case of a higher inclination of $\theta = 60^\circ$. $P(t)$ varies in a similar way to the $\theta = 30^\circ$ case described above. However, it should be noted that on the one hand it reaches higher values during obscuration, $\sim 40\%$. On the other hand, the double peaked features are smoother. As for $\Psi(t)$, it should

be noted that the differences between the Schwarzschild and Kerr BHs, for the uncovered primary, are bigger compared to the case of $\theta = 30°$, being $\sim 2°$ and $15°$, respectively, in the 2–4 keV band (unpolarized and parallelly polarized scenarios). Then Ψ drops to lower values as the primary source is covered and rises again while the cloud is moving towards the receding part of the disc, to reach its initial value when the cloud moves away from the line of sight. Similarly to the lower inclination case, when the source is not obscured, $\Psi(t)$ is larger for energies below 8 keV compared to the one at higher energies.

5.3.3 Effects of the lamp-post height and the cloud radius

I investigate in Figure 5.11 the effects of the height of the primary as well as the size of the cloud on the polarization signal. This figure shows the temporal variability in the 4–8 keV range for a non-rotating and a maximally rotating Kerr BH (top and bottom panels, respectively), for an unpolarized primary source located at 2.5, 6 and 10 r_g above the disc ($\theta = 30°$). I considered cloud radii of 5, 30 and 100 r_g (for $N_H = 10^{24}\,cm^{-2}$, the number density of the clouds will be $\sim 10^{11}$, 10^{10} and $10^{9}\,cm^{-3}$, respectively, covering the whole range of BLR cloud densities). The first immediate difference between the various cloud sizes is the duration of the eclipse which is proportional to the cloud radius.

For $R_C = 5\,r_g$, the obscured regions of the disc are smaller than the other cases. It should be noted that the eclipse occurs earlier when the source is at 2.5 r_g compared to the 6 r_g case. For these two cases, the variations of $P(t)$ while the cloud is moving within the line of sight are smoother for $a^* = 0$. This is due to the fact that the disc does not extend down to the regions, shaded by the cloud, where the effects should be the most intense. However, a larger gradual and asymmetric variability of Ψ is expected, during the motion of the cloud, being $\sim 35°$ for $\alpha = 10$ r_g and decreasing to 1°when the cloud is eclipsing the source, then rising up to $\sim 18°$ for $\alpha = -10$ r_g, for $h = 2.5$ r_g. More features are expected for the rotating BH case, especially for $h = 2.5$ r_g as the ISCO shrinks to lower radii. In these cases, $P(t)$ and $\Psi(t)$ show more variability for low heights. It should be noted that for $a^* = 0.998$, $P(t) \simeq 1\%$ for the unobscured-primary case while it is $\sim 0.3\%$ for $a^* = 0$. For $h = 10$ r_g, despite the fact that the source is not eclipsed at all some small variations are still expected in the polarization signal due to the obscuration of various parts of the accretion disc.

As for $R_C = 30$ and 100 r_g, $P(t)$ shows qualitatively a similar variability pattern for the various heights, which is also consistent with the one described in § 5.3.2. However, the patterns get smoother and flatter for larger heights, during the eclipse

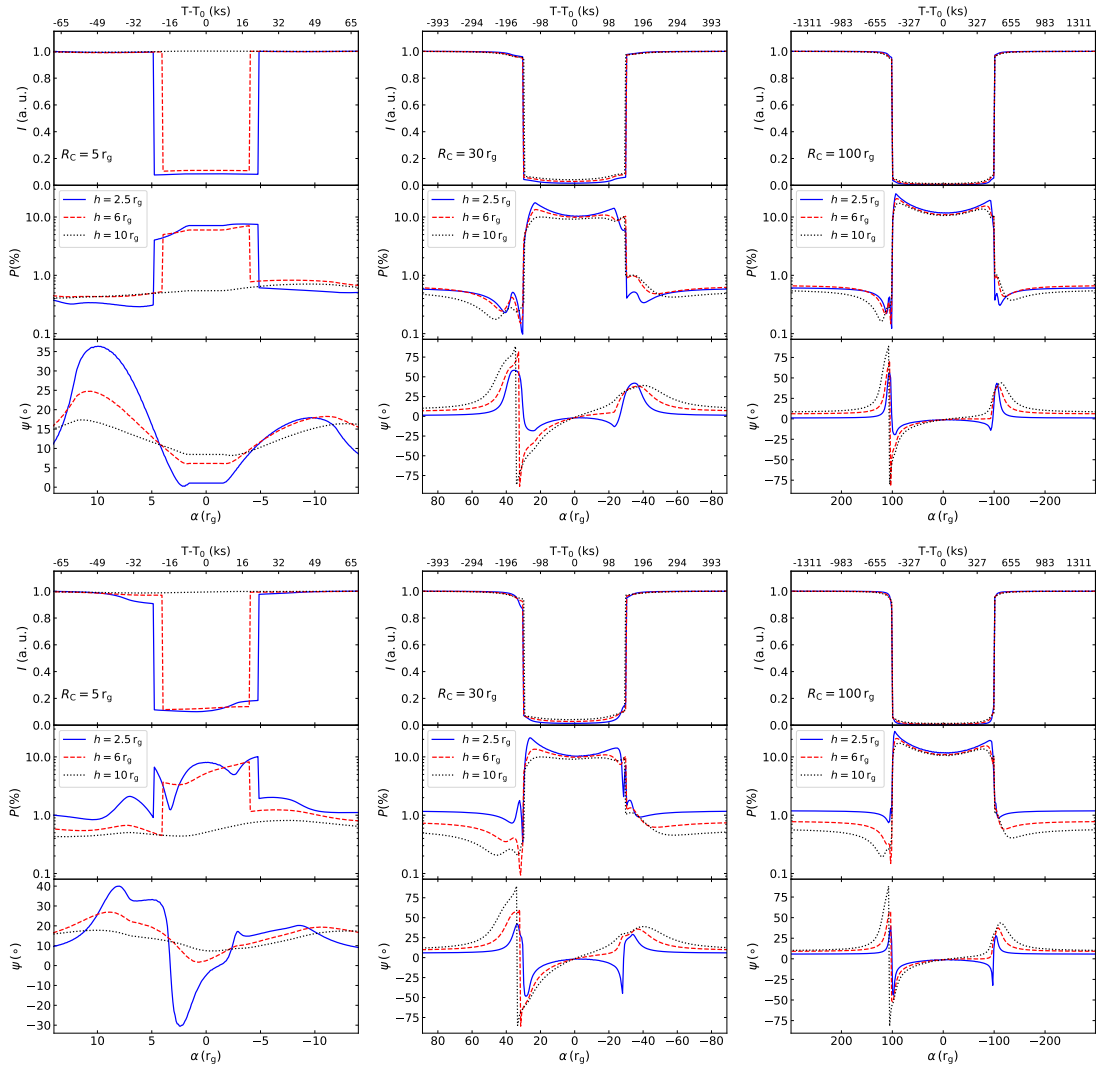

Figure 5.11: Temporal variability of the flux, polarization degree (P) and polarization position angle (Ψ) in the 4–8 keV band for an unpolarized primary at $h = 2.5\,\mathrm{r_g}$ (solid blue lines), $h = 6\,\mathrm{r_g}$ (dashed red lines) and $h = 10\,\mathrm{r_g}$ (dotted black lines), assuming a BH with $a^* = 0, 0.998$ (top and bottom panels, respectively) and an inclination $\theta = 30°$. I considered a cloud of radii 5, 30 and 100 $\mathrm{r_g}$ (left, middle, right columns, respectively).

event. It should be also note that the polarization degree is higher for lower lamp-post heights, as already discussed by Dovčiak et al. (2011). In fact, during the unobscured phases $P(t) \simeq 1.2\%$, 0.7% and 0.5% for $h = 2.5$, 6 and $10\,\mathrm{r_g}$, respectively. Once the primary is obscured, these values reach a maximum of $\sim 21\%$, 13.5% and 10%, respectively, for $R_\mathrm{C} = 30\ \mathrm{r_g}$ and $a^* = 0.998$. The difference in $P(t)$ for different heights is smaller for the Schwarzschild BH case, $P(t) \simeq 0.6\%$ for $h = 2.5$ and 6 $\mathrm{r_g}$ and 0.4% for $h = 10\ \mathrm{r_g}$. $\Psi(t)$ shows a similar variability pattern for the three heights, however the transitions (rise/decay) are more gradual at larger heights (when $\alpha \gtrsim 30$, 100 $\mathrm{r_g}$, for $R_\mathrm{C} = 30$ and 100 $\mathrm{r_g}$, respectively). Instead, for larger

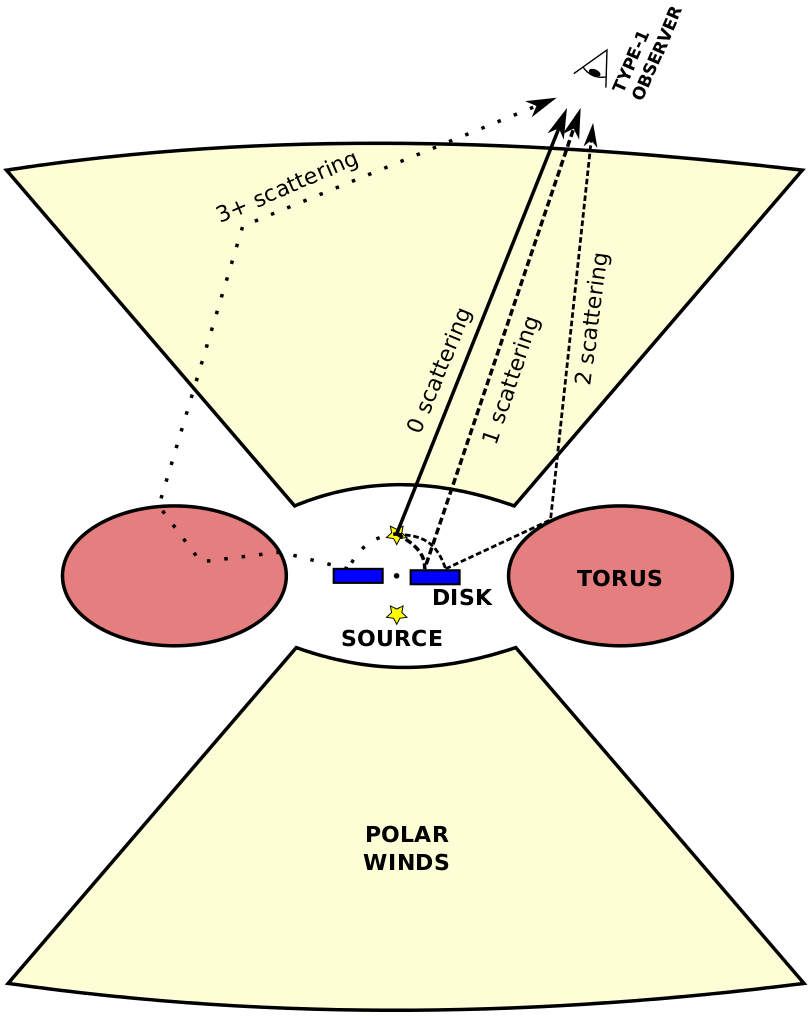

Figure 5.12: Artist representation of the AGN model. Scales have been exaggerated for better visualization of the inner components. The point-like coronas are represented with yellow stars, the cold accretion disk is in blue, the gaseous torus in red and the polar outflows in primrose yellow. The photon trajectories are bend close to the central SMBH and radiation have multiple potential targets for interaction, depending upon the energy of the photon and Compton-thickness of the material. The solid line represents the direct flux from the source (no scattering at all) and the other lines different possible radiation paths with different numbers of scattering. Adapted from Marin et al. (2018a).

heights, $\Psi(t)$ reaches higher values at the beginning of the eclipse, being $\sim 42°$, $60°$, and $90°$ for $h = 2.5$, 6 and $10\,\mathrm{r_g}$, respectively at $\alpha \simeq 35\,\mathrm{r_g}$, for $R_\mathrm{C} = 30\ \mathrm{r_g}$.

5.3.4 Effects of polar winds and torus

In practice the central SMBH, its accretion disc and corona are not isolated from the other AGN components. The impact of absorption, re-emission and scattering of

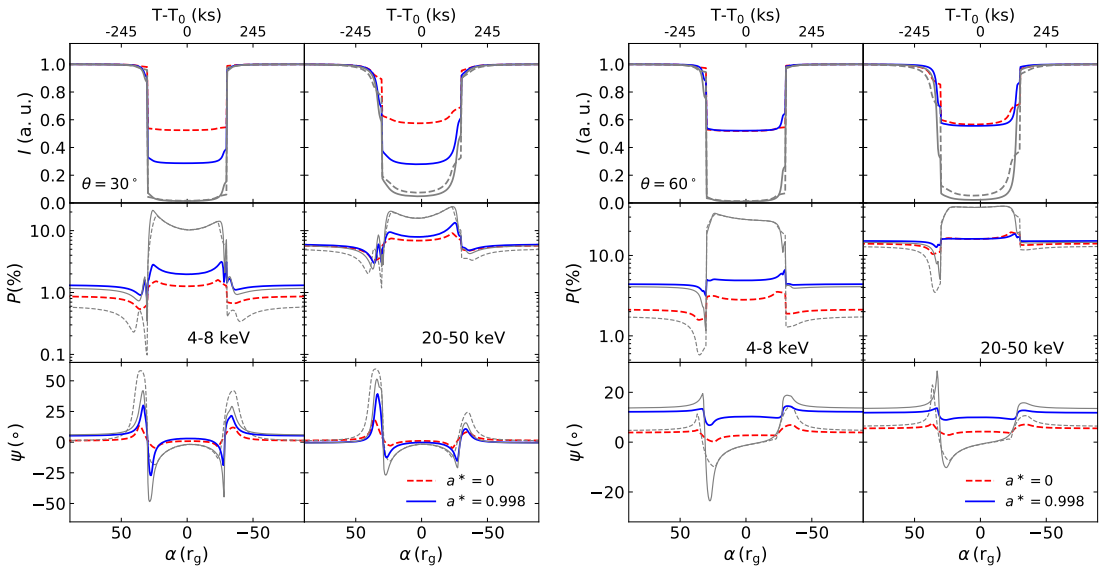

Figure 5.13: Similar to Figure 5.8 but for 4–8 keV and 20-50 keV ranges only, taking into account the contribution from the bi-conical narrow line regions and molecular torus for inclinations of 30° (left panel) and 60° (right panel), for Schwarzschild (dashed lines) and Kerr (solid lines) BHs. The grey lines represent the temporal variations of the polarization degree and polarization position angle without including the effects of the NLR and molecular torus.

parsec-scale structures has been explored in detail for spectroscopic and photometric purposes (see e.g. Ghisellini et al. 1994b). Higher torus hydrogen column density will impact on the Compton hump (Murphy & Yaqoob 2009, 2011). The impact of additional reprocessing from parsec-scale AGN structures on the X-ray polarization signal from type-1 AGN has been neglected until recently. In Marin et al. (2018a), the authors investigate the differences between an isolated central engine and a real type-1 AGN, accounting for biconical narrow line region (NLR) and an equatorial obscuring region. They found that additional parsec-scale scattering increases the expected polarization degree by $0.5 - 1$ percentage points in the case of an unpolarized or a parallelly polarized continuum source. Changes are more profound for a perpendicularly polarized primary.

In order to create a more physical model of X-ray eclipses, we decided to also account for a more realistic geometrical scheme. In addition to the hot corona and the accretion disc, we consider the contribution of an additional equatorial molecular torus and a biconical NLR to the observed polarized light that is scattered along the observer's line of sight, using the STOKES code[4]. STOKES is a Monte Carlo code developed by Goosmann & Gaskell (2007), Marin et al. (2012b, 2015) and Rojas

[4] http://stokes-program.info/

Lobos et al. (2018) that allows us to simulate the radiative transfer of photons in a wide three-dimensional environment. The code accounts for all the physics of scattering, absorption and re-emission from the near-infrared to the hard X-ray band (with the exception of magnetically-driven mechanisms such as synchrotron emission or dichroism that are not relevant in the cases which are considered here). Similarly to the work carried out by Marin et al. (2018a,b), it is possible to use the output from the KY code as input for STOKES. The photons can then propagate in a parsec-scale environment, allowing for a realistic radiative coupling between the central engine and the parsec-scale AGN structure. In this case, we followed the work of Marin et al. (2018a,b) for Seyferts and included a circumnuclear torus with a half-opening angle of 30° from the equatorial plane and a hydrogen column density of $10^{24}\,\mathrm{cm}^{-2}$. The inner radius of the torus is set to a distance of 0.01 pc according to reverberation mapping data (Suganuma et al. 2006; Vazquez et al. 2015), and the outer one to 5 pc. The NLR is bi-conical, optically thin, and have a hydrogen column density of $10^{21}\,\mathrm{cm}^{-2}$. They represent the typical NLR detected in many AGN and extend up to 60 parsecs before mixing with the galactic environment. A schematic representation of the assumed geometry is shown in Figure 5.12.

I present in Figure 5.13 the temporal variations of the polarization parameters that include the extra contributions of the torus and the NLR, in the 4-8 keV and 20-50 keV bands. I also plot the parameters for the same configurations considering only the cloud-corona-disc system, for comparison. I considered only the case of unpolarized primary at $h = 2.5\,\mathrm{r_g}$. First, it should be noted that, for all cases, the inclusion of the contribution from the torus and NLR results in an enhancement in the relative observed intensity during the eclipse. In fact, the contribution of these components to the scattered light in the line of sight is constant for the whole event and not affected by the eclipse itself. As expected, in the unobscured cases, the polarization degree increases when the contributions from the torus and NLR are included, especially for higher energies. The inclusion of torus and NLR result in a small increase in $P(E)$ during the unobscured phase. This is in agreement with the results in Marin et al. (2018a,b) where the authors investigate the effect of the molecular torus and NLR on the polarization signal for type-2 and type-1 Seyferts, respectively. However, this contribution, being stable and non-negligible in terms of intensity, reduces the amplitude of variability, once the primary is obscured. In fact, adding this contribution significantly dilutes the polarization signal leading to lower polarization degrees with respect to the cases when I do not account for these components, thus lower variability amplitude. During the eclipse, $P(t)$ becomes $\sim$ 1.3/2% (7/8%) for the Schwarzchild/Kerr BHs in the 4–8 keV

(20–50 keV) energy bands for an inclination of 30°. While for an inclination of 60°, $P(t)$ becomes $\sim 3/5\%$ for the Schwarzchild/Kerr BHs in the 4–8 keV band, while it is $\sim 16\%$ in the 20–50 keV for both spins. It should be noted, however, that *qualitatively* the same variability pattern can be observed with and without the inclusion of the contribution from the parsec-scale material. The same is seen when comparing the variability patterns of $\Psi(t)$, with the only difference that the inclusion of the torus and NLR tends to reduce the values of the polarization position angles, leading to a more parallel polarization.

5.4 Discussion

I showed that X-ray eclipsing events can be used in order to probe the emission from the innermost regions of AGN. This had been investigated earlier by Risaliti et al. (2011a), Marin & Dovčiak (2015) and Sanfrutos et al. (2016). However, I present in this chapter a new analysis taking into account full relativistic effects and more complex and physical configurations compared to the ones assumed in the aforementioned works. It should be noted that the results depend on several uncertainties, mainly caused by our poor knowledge of the exact geometry of the system.

1. An extended corona would be a more realistic case, and may lead to different spectral and polarimetric signatures with respect to the lamp-post geometry that is assumed in this chapter. This would mainly dilute the sudden changes caused by the high-compactness of the lamp-post. One would expect to observe more gradual patterns during the obscuration of the primary (see e.g. Sanfrutos et al. 2016). However, it should be noted that models with such a geometry are still not available for X-ray polarization.

2. The primary emission, assumed to be a power-law spectrum, is also expected to vary in flux and/or shape during the observation, which I do not take into consideration in this chapter.

3. The structure and geometry of the obscuring material may be more complex having a gradient of column density along the line of sight and a non-spherical shape (Maiolino et al. 2010). It should be also noted that the column density of the obscuring cloud may play a role in modifying mainly the spectral signatures. Obscuration caused by clouds with lower column densities, on the order of $\sim 10^{23}$ cm^{-2} (e.g. Risaliti et al. 2009; Maiolino et al. 2010), will mostly affect the soft X-rays.

Our spectral simulations are promising for the future high-resolution X-ray micro-calorimeters on board of ATHENA and, possibly, earlier X-ray missions such as Arcus and XRISM. The spectra that will be provided by the micro-calorimeters would be of great help in order to track the variability of fine spectral structures (especially the Fe line or the soft bands), during the eclipsing event. This would give us strong hints on the local emissivity of the disc, thus on the geometry of the corona. The detectability of these events and their implications will be investigated in future work. However, it should be noted that it is not yet plausible to detect the effects of obscuration on the polarimetric signals in AGN, on short timescales. In fact, Marin et al. (2012a) showed that more than ~ 1 Ms will be needed for a XIPE-like S-class mission assuming a non variable source with a flux of 3 mCrab in the 2–10 keV band. This is much larger than the timescale of the obscuration event in which the flux drops drastically, making the measurements even harder to be achieved. Instead, it would be possible with the up-coming X-ray polarimeters such as eXTP (Zhang et al. 2016) to catch changing-look (on larger timescales) sources in two different obscured/unobscured states. Sources with high mass and/or large obscuring clouds would be optimal for such analysis, as the duration of the eclipse would be longer in these cases. Combining the spectral and polarimetric capabilities of these missions would allow us not only to probe the innermost regions of the AGN, but it may give us also strong hints about the structure of the parsec-scale material. The presented results clearly show that taking into consideration the contribution from this scattering material would alter the polarization signal in terms of polarization degree and position angle, as well as variability. These effects strongly depend on the structure and the geometry of the parsec-scale material.

5.5 Conclusions

I have shown in this chapter how X-ray eclipses in AGN can affect the observed spectral and polarimetric signals, being then a powerful means to probe the relativistic effects that dominate the innermost regions of these sources. The main conclusions are the following.

1. The observed X-ray spectra show asymmetries during the different phases of the eclipse as the cloud is shading various parts of the accretion disc. These effects depend strongly on the location of the primary source and the size of the obscuring cloud. I also showed that for large heights it becomes harder to determine the BH spin.

2. Considering the corona-disc system only, an asymmetric enhancement in the polarization signal is expected to occur as the cloud is shading the innermost regions of the system. This enhancement is highly dependent on the inclination of the system: the higher the inclination, the larger the polarization degree. In addition, the variability patterns of the polarization degree and the polarization position angle depend strongly on the location of the primary. I also showed that the effect of the spin is less prominent. However, the temporal evolution of the polarization position angle is highly affected by the intrinsic polarization of the primary source.

3. It is crucial to consider a full geometrical configuration of the AGN. Accounting for the polarization signal from parsec-scale AGN components, the expected total polarization from the whole system is strongly altered. The inclusion of the constant scattered light by the torus and NLR in the line of sight tends to increase the degree of polarization when the innermost regions are unobscured. However, once the corona is obscured, the contribution from the torus and NLR, which is not affected by the eclipsing event, tends to smooth out the variability in polarization. This reduces remarkably the degree of polarization, and leads to a more parallel polarization (Ψ closer to 0). It should be noted that, despite the fact that in this case the variability of the polarization signal is lower, its absolute value can provide unique information on the geometry and the properties of the parsec-scale scattering medium.

The butterfly effect cannot be seen,
The butterfly effect will never fade away.

Mahmoud Darwich

6

Conclusions and future prospects

Contents

In this dissertation I studied the X-ray properties of AGN from various perspectives: spectral, temporal and polarimetric. Results from *XMM-Newton* and *NuSTAR* observations of low- and high-redshift AGN were presented, in addition to spectral and polarimetric simulations. I showed in this dissertation how X-rays can shed light on several open questions in AGN physics, serving as a probe of the innermost regions, such as

- the properties of the X-ray emitting region in non-jetted AGN,
- the presence of a population of non-relativistic electrons in the jets of blazars,
- probing general relativity in the strong-field regime, addressing especially the possibility of estimating accurately the SMBH spin in AGN, through the identification of relativistic reflection features in their X-ray spectra and polarization signal,
- the nature of variability in X-ray light curves, and the identification of the different physical components contributing to it.

6.1 General findings

I summarize below the main results and conclusions that were obtained throughout this dissertation:

- The redshift of the non-jetted quasar B2202 was revised from the previously reported value $z = 1.77$ to $z = 0.532$, through an optical observation by the Hale telescope. The observed optical spectra led to a determination of the BH mass and inclination of the system. The *XMM-Newton* and *NuSTAR* spectra of this source led to the determination of its coronal properties, which are comparable to the ones determined for local, less luminous, and less massive Seyfert galaxies, suggesting a unified mechanism coupling the disc and the corona (Chapter 2).

- The *XMM-Newton* and *NuSTAR* observations of the luminous jetted quasar 4C+25.05 ($z = 2.368$, Chapter 2) revealed the presence of a large statistically-significant excess at soft X-rays (below ~ 5 keV, rest frame). The identified excess was interpreted in the context of bulk Comptonisation due to the presence of non-relativistic electrons in the jets that would Comptonize the external light emitted by the BLR in the direction of the jet. This comptonized emission will then be boosted and emitted in the direction of the observer thanks to the bulk motion of the jet, that is assumed to be directed within the line of sight.

- High-quality *XMM-Newton* and *NuSTAR* spectra were simulated and fitted blindly, with the main aim of determining the accuracy of the reflection-based spin measurements in AGN (Chapter 3). The simulated spectra represent single-epoch observations of local AGN. Several components were used in order to give a realistic picture of the complexity that may be found in such systems, such as: blurred and neutral reflection, neutral absorption, warm absorption, and thermal emission from the host galaxy. It has been shown that the complexity of absorption does not seem to play a major role in determining the spin at the high flux level that was considered in the simulations. Instead, the major parameter which may affect the accuracy of the fits is the height of the lamp-post. The lower the lamp-post, the larger the relativistic effects, hence the spin can be recovered more accurately. This may also affect the (non-)identification of the various spectral components, which may be also subject to human bias.

- I proposed in Chapter 4 a potential way to solve the degeneracy between various spectral models (absorption versus reflection) through the flux-flux plot analysis. This method has been already used broadly in the literature, however I presented in this chapter guidelines for its use, by identifying the optimal choice of time and energy bins and the effect of the Poisson noise on its results. Then I applied it to the *XMM-Newton* and *NuSTAR* light curves of the Seyfert 1 galaxy MCG–6-30-15. This analysis led to the identification of variable and stable components in this system. The former component is consistent with a primary power-law plus ionized reflection which vary in normalization and are subject to warm absorption. The latter component consists of a blackbody-like spectrum dominating below 2 keV and a neutral reflection dominating in the 2–40 keV range. These results ruled out the possibility of a variable power-law slope during these observations, and variable partial covering absorbers which may mimic a broad red-wing of the Fe line.

- In Chapter 5, I presented spectroscopic and polarimetric simulations of X-ray eclipses in AGN. The passage of a cloud (assumed to be located in the BLR) within the line of sight will shade the X-ray emitting source (assumed to be a lamp-post) as well as different regions of the accretion disc which are affected differently by special and general relativity. This will lead to asymmetric patterns in the observed spectra as well as the measured polarization parameters. This method could be used in order to probe these effects that are rising within a few gravitational radii from the central BH. Temporal evolution of the polarization parameters were presented, and showed a remarkable increase in the observed polarization degree during the eclipse, due to the obscuration of the primary source (assumed to have low polarization, thus diluting the polarization signal). A more realistic configuration was assumed, taking into account the polarized light which is scattered by parsec-scale structures such as polar winds in the NLR and the circumnuclear torus and emitted in the direction of the observer. The contribution from the parsec-scale structures would lead to an increase in polarization signal for the unobsucred cases. However, the signal would be diluted for the obscured cases, compared to the configuration were these structures are not taken into account.

These findings show the power of X-ray analysis, using current instruments and potential future missions, in shedding light on the properties of the innermost regions in AGN, which are unique laboratories allowing us to understand the strong gravity regime in the vicinity of BHs. It should be mentioned that the recent detections of gravitational waves introduced a robust and complementary method, to accretion flows, in order explore the strong gravity regime.

6.2 Future prospects

The results presented in this dissertation demonstrated that the geometry and physical conditions of the corona are among the most important challenges for spectral analysis of AGN. Thus, a better understanding of the physical properties of the emitting region would be necessary in order to overcome these limitations. This would require a better understanding of the spectral and timing properties of these sources based on physical scenarios which can be achieved thanks to the current improvement of spectral-timing models. This will improve our knowledge and help breaking the degeneracies which are present in the current data.

- For example, it would be interesting to explore in more details a variability scenario in which the corona moves along the rotational axis of the BH. This scenario has been addressed previously by Miniutti & Fabian (2004). However, current (more advanced) models would allow us to track the movement of the corona, and the output radiation taken into account full relativistic effects (light bending, time delays, gravitational redshift). As an output, one could obtain light curves in different energy bands, which would allow us to study the variability in these bands (e.g. estimating the power spectral distributions, fractional variability), to check for correlations between various energy bands, and to estimate the observed energy spectra, for different configurations and parameters (BH mass, spin, accretion rate, luminosity). Comparing these results with the observations would then allow us to confirm or rule out the plausibility of such scenarios.

- As mentioned in Section 1.4.2, the irradiation of the accretion disc by a compact corona would result in a radial ionization profile of the accretion disc. This effect may lead to an artificial increase of the radial-emissivity parameter. It would be then possible with current models to explore and quantify this effect. A possible approach would be to create synthetic spectra assuming a physical radial-ionization profile (within the lamp-post geometry), using

responses of current and/or future instruments, and try to fit them with a single-ionized model (similar to the ones used in the literature) with a radial-emissivity profile (single or broken power law), and explore the parameter space (height, spin, luminosity, ionisation, disc density) trying to understand how would this compare with reported results in the literature, and what parameter(s) would be playing the major role.

Furthermore, it would be equally important to understand how the next generation of high-resolution microcalorimeters on board of XRISM and ATHENA, for example, could improve our understanding of AGN physics. Thus, it would be interesting to test through simulations whether the high-resolution provided by the micorcalorimeters would help in overcoming the limitations of spin determination for local AGN, as well as to test whether it would be also possible to determine BH spins for high-redshift sources. It would be also timely to investigate how the studying the variability with these instruments can help overcoming the difficulties faced in spin determination. Additionally, it would be interesting to investigate the signature of variability on the polarimeteric signal. Long-timescale (on a scale of days/months) variability could be thus tested using the next generation of polarimeters such as IXPE, but more interestingly eXTP which will provide us with spectral and polarization data simultaneously.

On the observational side, it would also important get benefit of the rich archival data of some sources such as NGC 1365, NGC 4051, NGC 4151, MCG–6-30-15, IRAS 13224-3809. In that respect, performing a detailed time-resolved, multi-epoch spectral analysis of these highly variable sources, caught in various spectral states, could be of a great help in order to determine better their physical parameters especially the ones which are supposed to be constant over these timescales: the spin, inclination and iron abundance. Moreover, it may be also helpful in understanding the variability scenario(s) dominating in these sources. This could be accomplished by combining high-quality data from various instruments, probing different energy ranges. It would be important to test the spectral variability in these sources within the context of physical Comptonization models. This would give more clues on the nature and geometry of the corona and its variability which may help in breaking the degeneracies on BH spin measurements.

I have also shown in this dissertation that good measurements of coronal properties for quasars at cosmological redshifts can be achieved. This significantly extends the previous work done primarily on relatively local and lower luminosity Seyferts. Thus, on the one hand, it would be interesting to revisit local bright

sources with already measured coronal properties, especially the ones with extreme cutoff energies such as NGC 5506 that showed a high $E_{\rm cut} = 720^{+130}_{190}$ keV (Matt et al. 2015), and Ark 564 which revealed the presence of one of the coolest coronæ ever found in AGN ($E_{\rm cut} = 46 \pm 3$ keV) showing also large temporal variability (Kara et al. 2017). The aim of such observations is to probe the variability of the coronal properties, in order to understand better the physical behaviour of the corona and the possible corona-disc connection. On the other hand, it would be timely to investigate the coronal properties for a larger sample of optically selected non-jetted quasars at intermediate and high redshifts. This will lead to test whether the same physical conditions hold in 'X-ray normal' quasars at luminosities ~ 100 times higher than those probed so far in the nearby Universe. In addition to the measurement of the coronal properties, this will provide information on the other main X-ray components (such as reflection, the circumnuclear absorber, and possible additional absorbers along the line of sight). This could be achieved by applying for simultaneous *XMM-Newton* and *NuSTAR* observations for the selected sources, with the aim of obtaining a sample with high-quality data allowing us to perform statistical analysis of the coronal properties of intermediate-redshift *typical* quasars. To do so, we must avoid any X-ray-based selection, even if this implies no previous knowledge of the X-ray flux of the selected sources. A possible way to proceed would be to select the optically brightest SDSS quasars at redshifts between 0.5 and 1. Having no prior knowledge of the X-ray emission, the X-ray flux could be then estimated from the SDSS-based flux at 2500 Å (calculated from the fit of the optical spectrum by Shen et al. 2011), adopting the X-ray to UV relation of Lusso & Risaliti (2016). The final choice will be then based on two criteria: 1) The optical spectra of the sources are 'blue', and do not show any hints of strong intrinsic absorption. 2) The 'expected' X-ray fluxes are about the same, within 0.15 dex, of that already observed in the quasar B2202–209 (see Chapter 2).

In addition, the possible identification of bulk Comptonization rises the open question of non-relativistic electrons in AGN jets. Hence, more observations of local and high-z jetted quasars (preferentially FSRQ) would be needed. The joint *XMM-NuSTAR* observations will be necessary in order to constrain more accurately the hard spectra of the sources. It would be also interesting to apply the flux-flux analysis to these sources, which may be of a great help in identifying the presence (or absence) of any component additional to the external Compton emission dominating the hard X-ray spectra of FSRQs, as demonstrated for the case of non-jetted AGNs. Moreover, bulk Comptonization component is expected to be polarized due to 1) Compton scattering, and 2) the directionality of the emission thanks to the

relativistic bulk motion, thus it would be interesting to estimate the expected polarization signature of this component, and its time dependence.

The flux-flux analysis has shown to be a robust way in order to identify the various X-ray spectral component of AGN. A handful of variable local bright Seyferts, which have been observed by *XMM-Newton* and *NuSTAR*, would be interesting for investigation through FFP analysis. Moreover, the results obtained from the FFP can be potentially used in order to explain the commonly used quantities describing variability such as RMS-spectra and excess variance, which show strong correlations with the intrinsic properties of the system (mainly the BH mass). It would be also interesting to understand in more details, through simulations, how various variability scenarios may affect the shape of the FFPs, as well as the effect of time lags on the FFPs.

Appendices

A

Best-fit results of the spectral simulations

I present in this appendix the best-fit results obtained from the blind fitting procedure. I list in Table A.1 the best-fit heights and spin values obtained for each fit, compared to the input values. I also report the minimum χ^2/dof found for each fit and the reference value that I use to evaluate the accuracy of the fit (see Section 3.4 for details). Figure A.1 shows all the simulated spectra in addition to the input models and the residuals of the best-fit model for the two blind spectral fits.

Table A.1: Input and best-fit values of the height (h) and the spin parameter (a^*) found for the two fits performed to the spectra of Sets G, K, and B. I also report the best-fit χ^2/dof I found and the reference value against which the accuracy of a fit is evaluated.

	$h\,(r_\mathrm{g})$	a^*	χ^2/dof		$h\,(r_\mathrm{g})$	a^*	χ^2/dof		$h\,(r_\mathrm{g})$	a^*	χ^2/dof
	Set G										
	15	0.2	538/581		17	0.74	429/441		8	0.7	338/357
G1	$5.55^{+0.96}_{-0.48}$	$0.761^{+0.202}_{-0.506}$	546/583	G6	$16.21^{+3.73}_{-2.50}$	$0.569^{+0.384}_{-0.507}$	429/441	G11	$7.16^{+0.73}_{-0.66}$	$0.196^{+0.269}_{-0.149}$	338/357
	$2.77^{+0.16}_{-0.09}$	$0^{+0.193}_{p}$	597/581		$15.79^{+3.87}_{-2.65}$	$0.498^{+0.450}_{-0.449}$	429/441		$6.71^{+1.04}_{-0.80}$	$0.208^{+0.239}_{-0.173}$	338/358
	3	0.7	370/388		6	0.28	407/455		4	0	410/384
G2	$2.74^{+0.28}_{-0.12}$	$0.765^{+0.109}_{-0.171}$	370/389	G7	$3.74^{+0.40}_{-0.28}$	$0.166^{+0.205}_{-0.139}$	407/455	G12	$14.85^{+4.94}_{-2.28}$	$0.998^{p}_{-0.861}$	418/385
	$3.76^{+0.40}_{-0.32}$	$0.976^{+0.009}_{-0.527}$	383/386		$2.70^{+0.12}_{-0.04}$	$0^{+0.155}_{p}$	418/452		$12.61^{+2.08}_{-6.53}$	$0.143^{+0.597}_{-0.113}$	410/384
	5	0.950	430/419		9	0.93	495/478		2	0.99	431/400
G3	$4.44^{+1.15}_{-0.58}$	$0.998^{p}_{-0.096}$	430/419	G8	$2.77^{+0.21}_{-0.15}$	$0.439^{+0.158}_{-0.299}$	495/478	G13	$2.00^{+0.20}_{p}$	$0.989^{+0.002}_{-0.001}$	431/400
	$4.25^{+1.10}_{-0.39}$	$0.975^{+0.015}_{-0.200}$	430/419		$4.97^{+1.63}_{-0.18}$	$0.617^{+0.334}_{-0.476}$	496/478		$2.13^{+0.14}_{-0.07}$	$0.991^{p}_{-0.003}$	431/400
	5	0.9	410/404		2.3	0.99	392/445		10	0.3	480/481
G4	$4.67^{+0.77}_{-0.35}$	$0.86^{+0.12}_{-0.24}$	401/402	G9	$2.51^{+0.03}_{-0.34}$	$0.880^{+0.102}_{-0.085}$	415/446	G14	360^{+132}_{-143}	$0.851^{+0.106}_{-0.803}$	483/482
	$5.09^{+0.81}_{-0.22}$	$0.86^{+0.12}_{-0.27}$	401/399		$2.02^{+0.16}_{-0.01}$	$0.964^{+0.016}_{-0.097}$	393/445		$12.78^{+8.50}_{-2.06}$	$0.896^{+0.061}_{-0.844}$	479/481
	6	0.5	449/473		32	0.12	381/391		2	0.99	412/412
G5	$3.20^{+0.47}_{-0.23}$	$0.744^{+0.047}_{-0.455}$	449/473	G10	$9.25^{+1.39}_{-1.31}$	$0.586^{+0.284}_{-0.480}$	429/394	G15	$2.04^{+0.14}_{-0.03}$	$0.990^{+0.002}_{-0.001}$	412/412
	$4.58^{+0.90}_{-0.73}$	$0.602^{+0.358}_{-0.411}$	453/468		$6.60^{+1.01}_{-0.77}$	$0.016^{+0.229}_{p}$	385/391		$2.00^{+0.20}_{p}$	$0.990^{+0.003}_{-0.001}$	412/412
	Set K										
	6	0.998	438/433		6	0.998	371/376		2	0.99	400/401
K1	$3.01^{+0.19}_{-0.10}$	$0.359^{+0.167}_{-0.183}$	438/434	K4	134^{+204}_{-57}	$0.758^{+0.215}_{-0.680}$	412/379	K7	$2.04^{+0.15}_{-0.03}$	$0.945^{+0.022}_{-0.049}$	401/401
	$4.39^{+0.54}_{-0.17}$	$0.923^{+0.058}_{-0.216}$	474/433		184^{+56}_{-132}	$0.31^{+0.640}_{-0.268}$	389/376		$2.01^{+0.20}_{-0.01}$	$0.933^{+0.029}_{-0.061}$	400/401
	2.5	0.998	397/443		3	0.998	321/396		2	0.99	384/441
K2	$3.80^{+0.82}_{-0.15}$	$0.913^{+0.069}_{-0.339}$	431/444	K5	$2.57^{+0.45}_{-0.26}$	$0.930^{+0.046}_{-0.075}$	367/395	K8	$2.00^{+0.17}_{p}$	$0.975^{+0.019}_{-0.059}$	385/441
	$2.95^{+0.35}_{-0.22}$	$0.971^{+0.022}_{-0.204}$	398/443		$4.33^{+0.46}_{-0.91}$	$0.977^{+0.019}_{-0.081}$	325/396		$2.00^{+0.17}_{p}$	$0.993^{+0.004}_{-0.046}$	384/441
	12	0.998	472/461		4	0.998	466/449		8	0.99	377/424
K3	$6.32^{+0.75}_{-0.80}$	$0.015^{+0.319}_{-0.008}$	473/462	K6	$4.11^{+0.49}_{-0.21}$	$0.991^{+0.003}_{-0.252}$	471/449	K9	$9.45^{+4.12}_{-2.39}$	$0.857^{+0.105}_{-0.774}$	382/424
	$6.53^{+0.08}_{-1.14}$	$0^{+0.003}_{p}$	472/461		$4.03^{+0.10}_{-0.58}$	$0.123^{+0.303}_{-0.105}$	481/446		$9.03^{+6.83}_{-1.27}$	$0.736^{+0.228}_{-0.670}$	385/424
	Set B										
	7	0.998	350/341		8	0.65	373/383		10	0.99	392/366
B1	$7.56^{+0.95}_{-0.97}$	$0.9^{+0.08}_{-0.32}$	350/339	B3	$5.12^{+1.25}_{-0.50}$	$0.38^{+0.21}_{-0.16}$	373/383	B5	$13.09^{+1.85}_{-1.81}$	$0.86^{+0.11}_{-0.62}$	392/367
	$7.35^{+1.08}_{-0.90}$	$0.88^{+0.10}_{-0.37}$	350/339		$2.91^{+0.08}_{-0.12}$	$0.01^{+0.07}_{p}$	378/382		$12.14^{+2.67}_{-0.98}$	$0.83^{+0.15}_{-0.50}$	392/367
	3.5	0.2	367/372		5	0.9	328/355		2.5	0.99	324/370
B2	$3.47^{+0.40}_{-0.44}$	$0.31^{+0.08}_{-0.25}$	368/373	B4	$4.12^{+0.40}_{-0.24}$	$0.964^{+0.025}_{-0.197}$	350/356	B6	$2.60^{+0.15}_{-0.01}$	$0.981^{+0.006}_{-0.050}$	324/371
	$4.55^{+0.45}_{-0.54}$	$0.27^{+0.25}_{-0.18}$	367/372		$4.93^{+0.64}_{-0.50}$	$0.96^{+0.03}_{-0.33}$	330/355		$2.62^{+0.10}_{-0.06}$	$0.981^{+0.012}_{-0.048}$	324/371

[p] pegged to its maximum/minimum allowed value.

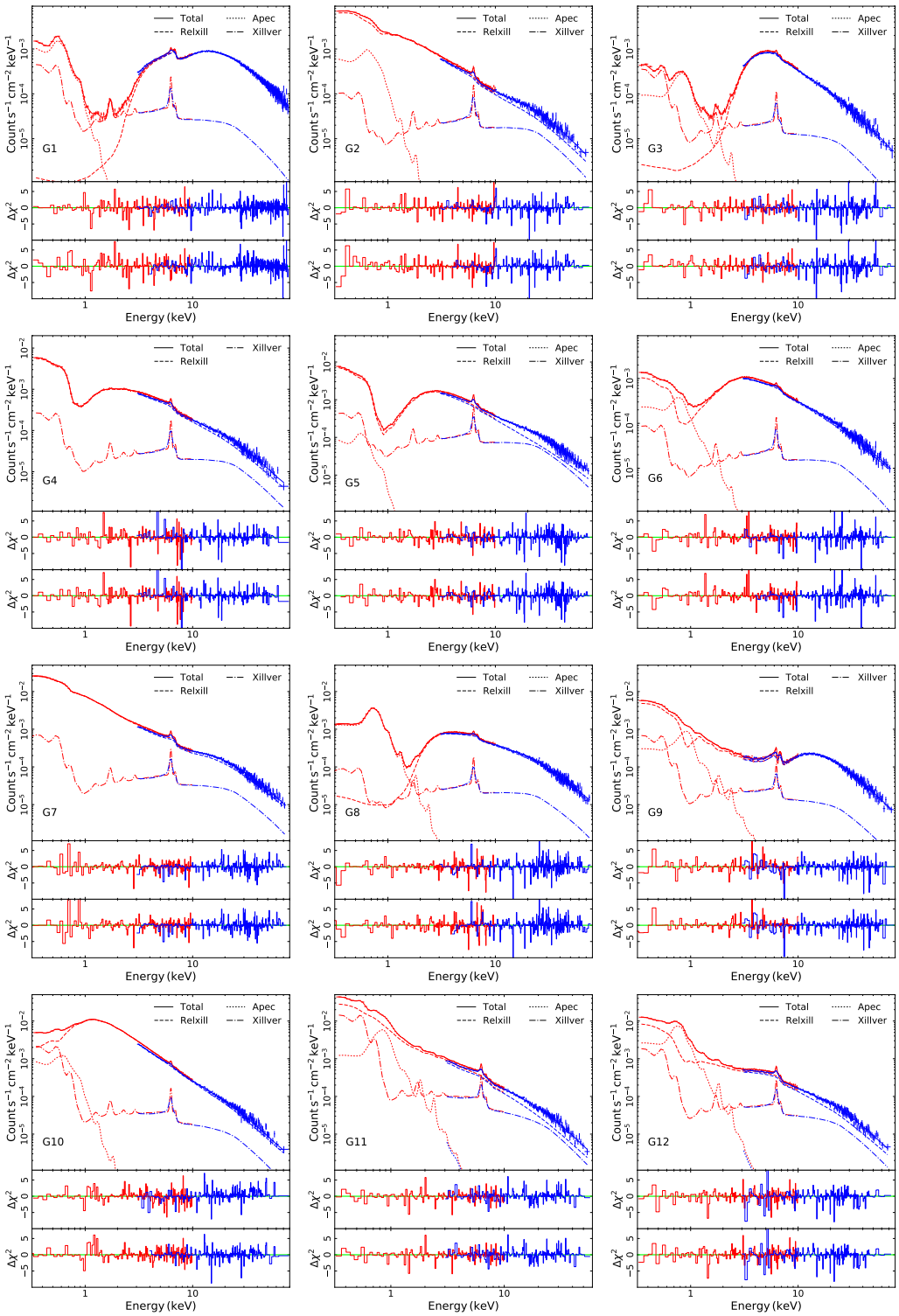

Figure A.1: Top panel: Simulated *XMM-Newton* (red) and *NuSTAR* (blue) spectra together with the various components of the theoretical model assumed. Primary emission plus ionized reflection (dashed lines), neutral reflection (dash dotted lines), and thermal emission (dotted lines) are indicated. Middle and bottom panels: The χ^2 residuals obtained by the two blind fits (See Section 3.3 for details) are shown.

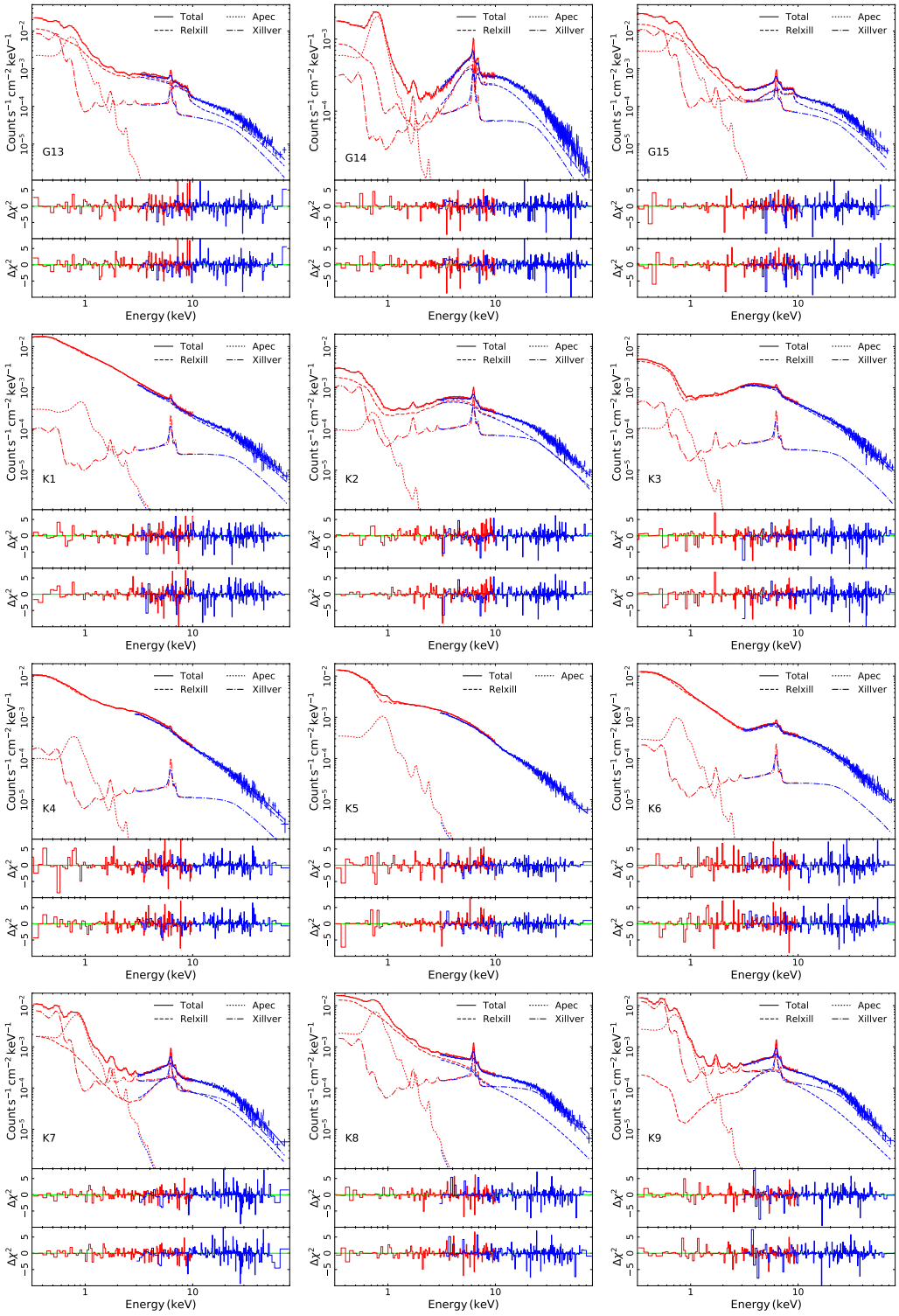

Figure A.1: Continued

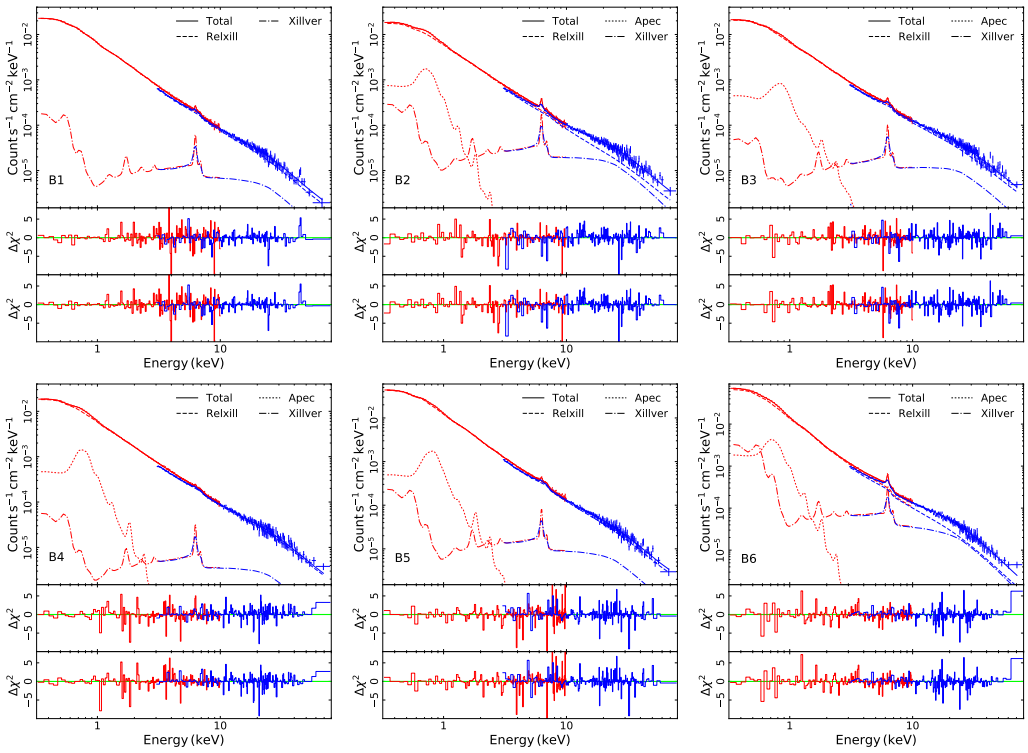

Figure A.1: Continued

B

Flux-flux plot analysis results

I present in this appendix the FFPs obtained from *XMM-Newton* and *NuSTAR* in the various energy bands that are considered in this work. Figs. B.1-B.3 show the observed FFPs in addition to the best-fit models. I list in Tables B.1-B.3 the best-fit parameters obtained by fittin linear and PLc models to the high-energy and low-energy FFPs, respectively.

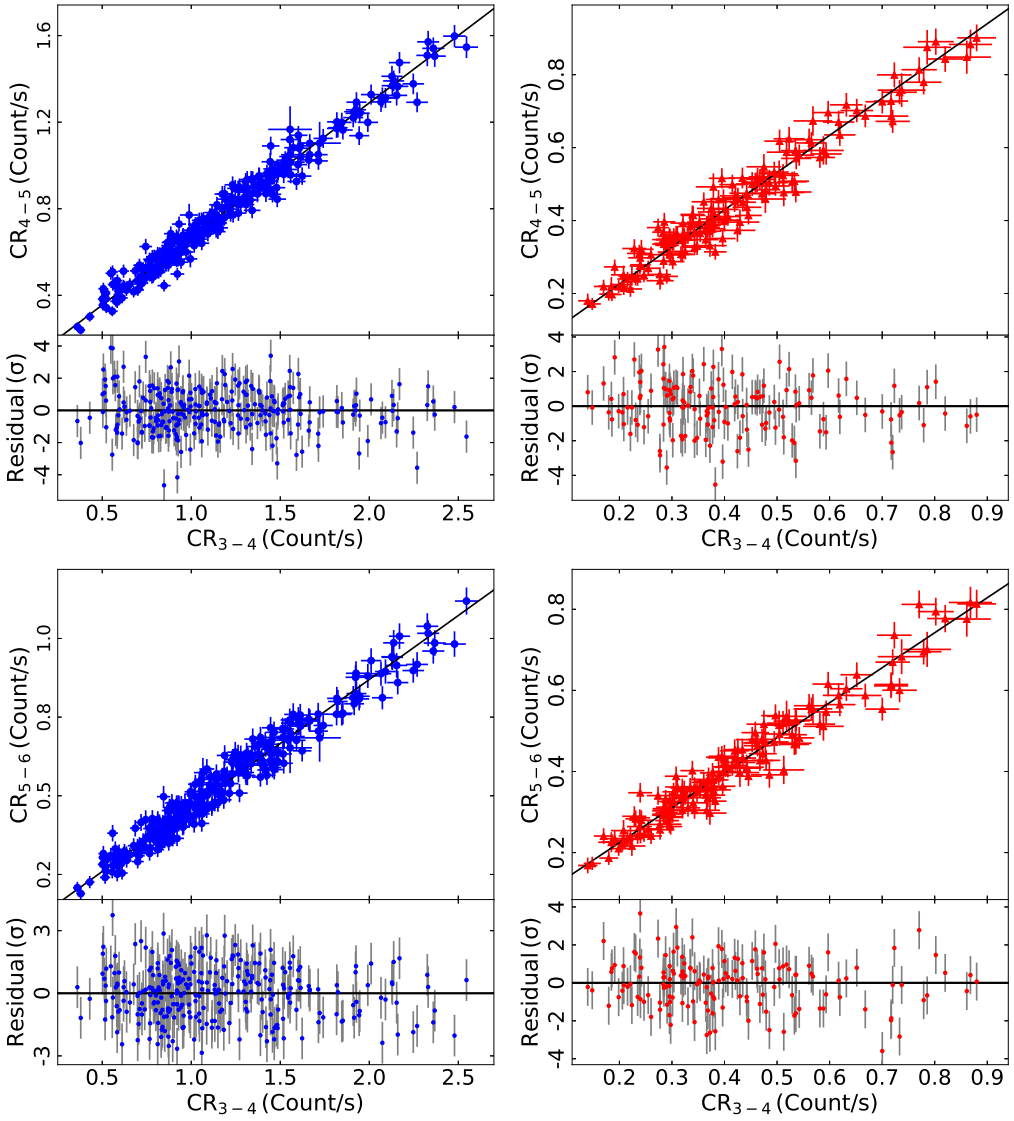

Figure B.1: *XMM-Newton* and *NuSTAR* (left and right column, respectively), high-energy FFPs in the common energy bands (4–10 keV). The solid black line indicates the best-fit linear model to the combined FFPs. Best-fit residuals are plotted in the lower panel of each plot.

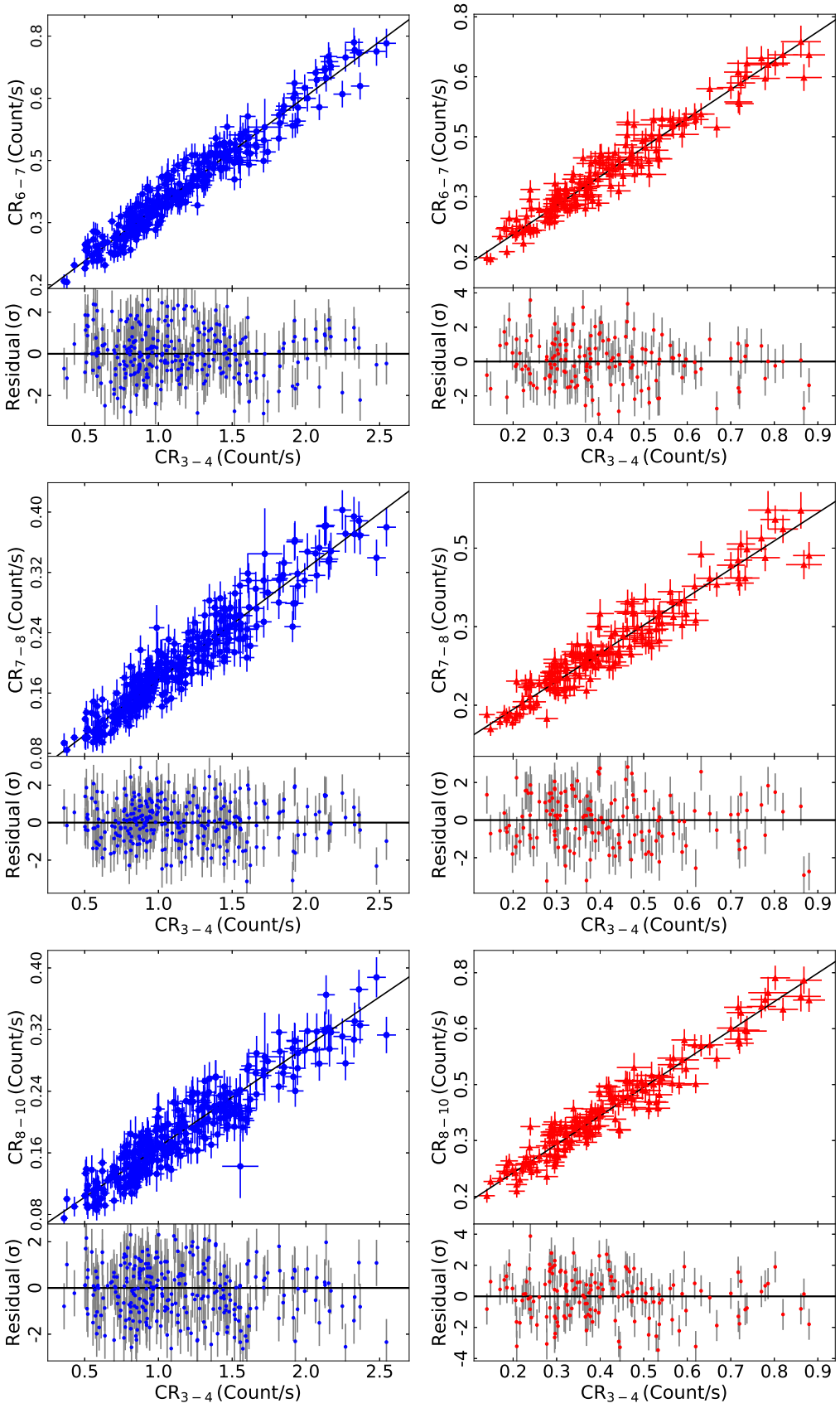

Figure B.1: Continued

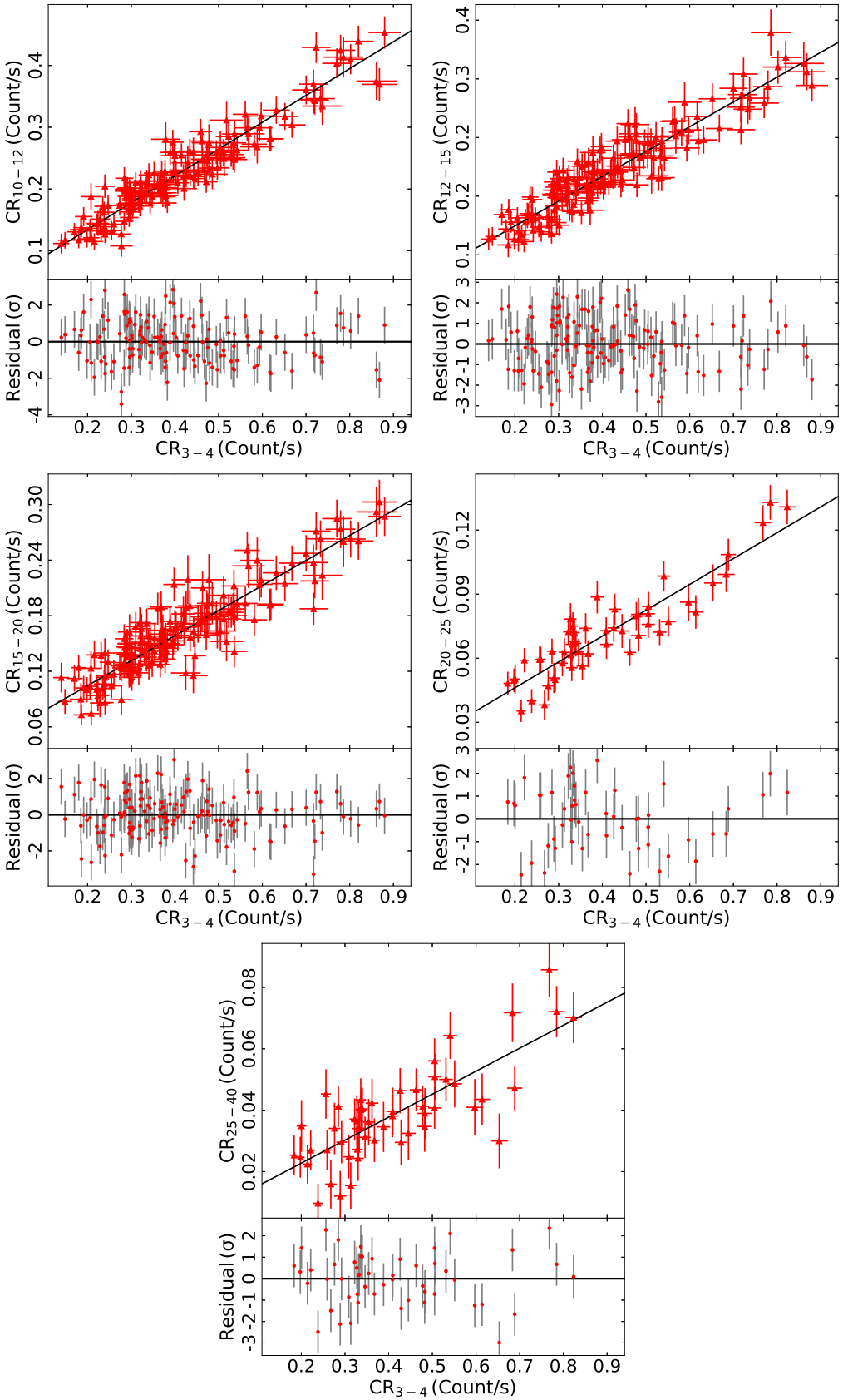

Figure B.2: Similar to Figure B.1 but for the *NuSTAR*-only FFPs, in the energy range 10–40 keV.

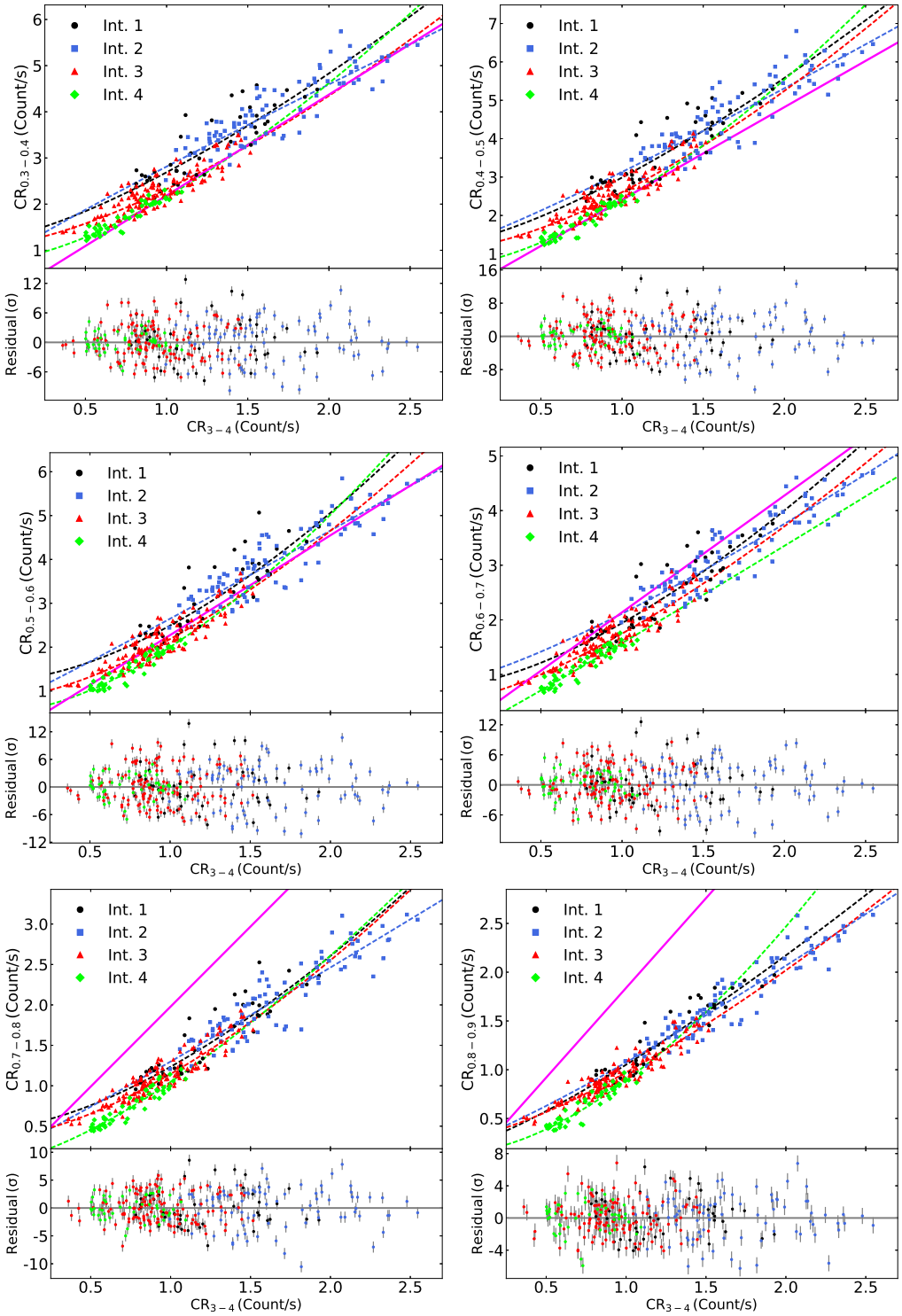

Figure B.3: Low-energy FFPs in the 0.3–3 keV energy range, for the individual time intervals Int. 1-4 (black circles, blue squares, red triangles, green diamond, respectively). The dashed lines correspond to the best-fit PLc model obtained by fitting the data from each time interval separately, using the same color code. The solid magenta line indicates the *predicted* FFPs assuming a power-law spectrum with $\Gamma_X = 2.04$ (see Section 4.2.3 for details). I did not plot the error bars for clarity reasons. The best-fit residuals are plotted in the lower panel of each plot.

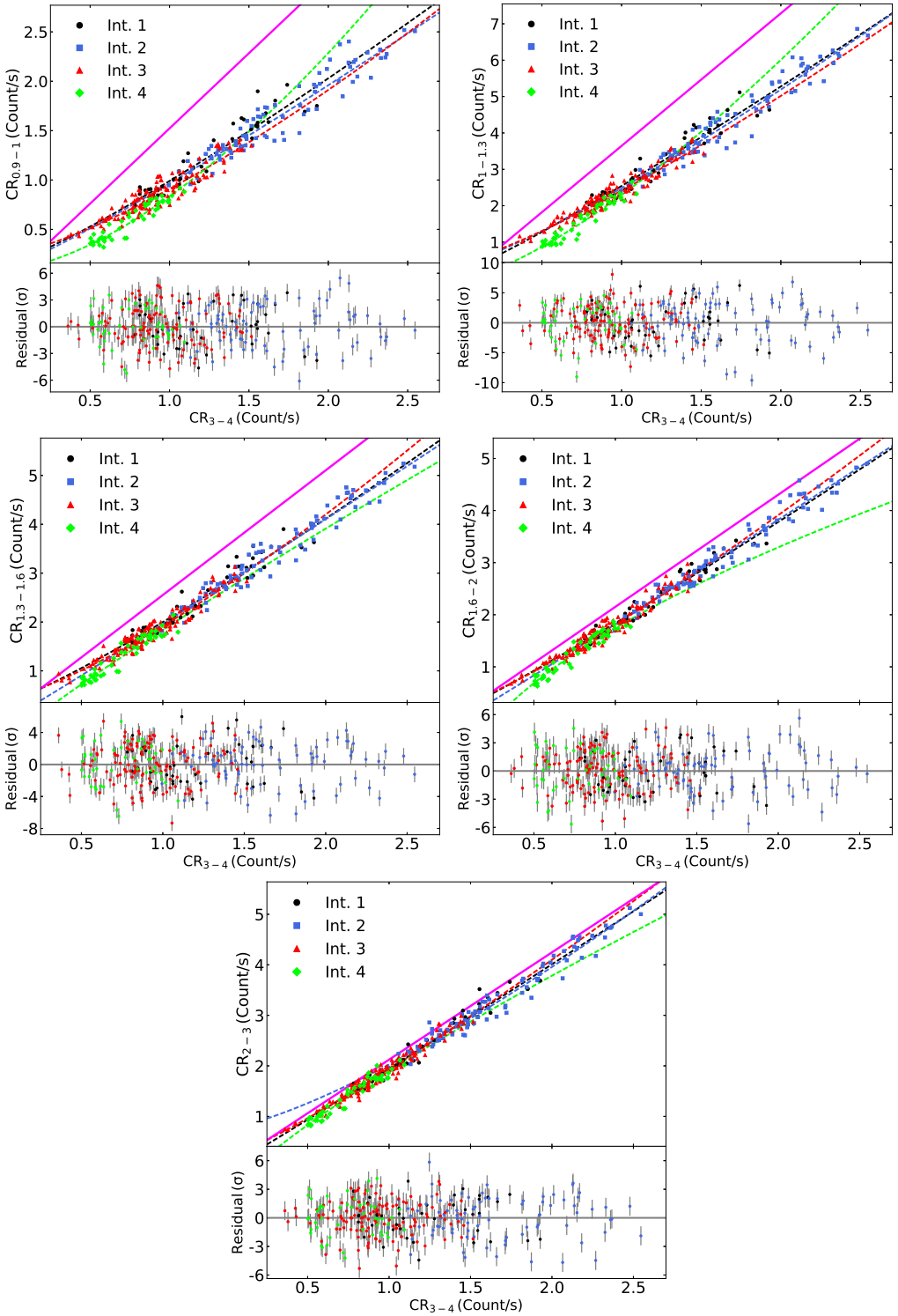

Figure B.3: Continued

Table B.1: Results from the linear model best-fits to the individual and combined *XMM-Newton* high-energy FFPs.

Energy Band (keV)	Int.	$A_{\rm L}$	$C_{\rm L}$ (Count s^{-1})	χ^2/d.o.f.
4 – 5	1	0.66 ± 0.02	0.01 ± 0.03	43/39
	2	0.59 ± 0.01	0.08 ± 0.02	85/82
	3	0.65 ± 0.01	0.01 ± 0.01	128/127
	4	0.55 ± 0.03	0.10 ± 0.02	64/46
	mean	0.625 ± 0.006	0.037 ± 0.009	–
	all	0.622 ± 0.006	0.044 ± 0.006	330/300
5 – 6	1	0.40 ± 0.02	0.06 ± 0.02	54/39
	2	0.39 ± 0.01	0.08 ± 0.02	98/82
	3	0.43 ± 0.01	0.03 ± 0.01	115/127
	4	0.39 ± 0.02	0.08 ± 0.02	62/46
	mean	0.406 ± 0.005	0.049 ± 0.007	–
	all	0.406 ± 0.005	0.056 ± 0.005	337/300
6 – 7	1	0.24 ± 0.01	0.11 ± 0.02	35/39
	2	0.25 ± 0.01	0.09 ± 0.01	108/82
	3	0.27 ± 0.01	0.06 ± 0.01	142/127
	4	0.23 ± 0.02	0.10 ± 0.01	63/46
	mean	0.257 ± 0.005	0.079 ± 0.006	–
	all	0.264 ± 0.004	0.075 ± 0.004	325/300
7 – 8	1	0.15 ± 0.01	0.03 ± 0.01	49/39
	2	0.16 ± 0.01	0.03 ± 0.01	106/82
	3	0.15 ± 0.01	0.02 ± 0.01	126/127
	4	0.17 ± 0.01	0.02 ± 0.01	40/46
	mean	0.155 ± 0.004	0.023 ± 0.004	–
	all	0.147 ± 0.003	0.031 ± 0.003	316/300
8 – 10	1	0.12 ± 0.01	0.04 ± 0.01	42/39
	2	0.13 ± 0.01	0.03 ± 0.01	124/82
	3	0.15 ± 0.01	0.013 ± 0.005	188/127
	4	0.13 ± 0.01	0.04 ± 0.01	47/46
	mean	0.136 ± 0.004	0.023 ± 0.004	–
	all	0.130 ± 0.003	0.037 ± 0.003	344/300

Table B.2: Similar to Table B.1 but for *NuSTAR*.

Energy Band (keV)	Int.	$A_{\rm L}$	$C_{\rm L}$ (Count s^{-1})	χ^2/d.o.f.
4 – 5	1	1.04 ± 0.08	0.01 ± 0.03	29/20
	2	1.02 ± 0.05	0.02 ± 0.03	40/42
	3	1.04 ± 0.05	0.02 ± 0.01	87/68
	4	0.93 ± 0.10	0.05 ± 0.02	27/24
	mean	1.025 ± 0.031	0.021 ± 0.011	–
	all	1.020 ± 0.020	0.021 ± 0.007	162/160
5 – 6	1	0.75 ± 0.06	0.10 ± 0.03	17/20
	2	0.86 ± 0.05	0.05 ± 0.03	45/42
	3	0.88 ± 0.04	0.04 ± 0.01	60/68
	4	0.84 ± 0.09	0.06 ± 0.02	31/24
	mean	0.848 ± 0.027	0.055 ± 0.010	–
	all	0.863 ± 0.018	0.052 ± 0.007	136/160
6 – 7	1	0.61 ± 0.06	0.12 ± 0.02	24/20
	2	0.71 ± 0.04	0.06 ± 0.02	42/42
	3	0.79 ± 0.04	0.03 ± 0.01	72/68
	4	0.58 ± 0.08	0.10 ± 0.02	31/24
	mean	0.716 ± 0.024	0.063 ± 0.009	–
	all	0.724 ± 0.016	0.061 ± 0.006	162/160
7 – 8	1	0.53 ± 0.05	0.03 ± 0.02	31/20
	2	0.55 ± 0.03	0.02 ± 0.01	64/42
	3	0.56 ± 0.03	0.03 ± 0.01	82/68
	4	0.67 ± 0.07	0.001 ± 0.02	22/24
	mean	0.563 ± 0.020	0.023 ± 0.008	–
	all	0.536 ± 0.013	0.034 ± 0.005	182/160
8 – 10	1	0.73 ± 0.06	0.05 ± 0.02	44/20
	2	0.79 ± 0.04	0.03 ± 0.02	55/42
	3	0.87 ± 0.04	0.02 ± 0.01	69/68
	4	0.88 ± 0.09	0.04 ± 0.02	35/24
	mean	0.822 ± 0.026	0.034 ± 0.010	–
	all	0.765 ± 0.017	0.060 ± 0.006	187/160

Energy Band (keV)	Int.	$A_{\rm L}$	$C_{\rm L}$ (Count $\rm s^{-1}$)	χ^2/d.o.f.
10 – 12	1	0.36 ± 0.04	0.07 ± 0.02	12/20
	2	0.48 ± 0.03	0.01 ± 0.01	43/42
	3	0.47 ± 0.03	0.04 ± 0.01	74/68
	4	0.53 ± 0.07	0.03 ± 0.02	29/24
	mean	0.462 ± 0.018	0.036 ± 0.007	–
	all	0.435 ± 0.012	0.047 ± 0.005	161/160
12 – 15	1	0.26 ± 0.04	0.08 ± 0.01	24/20
	2	0.34 ± 0.02	0.04 ± 0.02	55/42
	3	0.35 ± 0.02	0.040 ± 0.008	71/68
	4	0.51 ± 0.06	0.02 ± 0.02	18/24
	mean	0.347 ± 0.016	0.044 ± 0.006	–
	all	0.338 ± 0.011	0.052 ± 0.004	180/160
15 – 20	1	0.24 ± 0.04	0.06 ± 0.01	33/20
	2	0.30 ± 0.02	0.03 ± 0.01	52/42
	3	0.34 ± 0.02	0.025 ± 0.008	82/68
	4	0.37 ± 0.06	0.04 ± 0.01	26/24
	mean	0.310 ± 0.015	0.032 ± 0.006	–
	all	0.270 ± 0.009	0.051 ± 0.004	182/160
20 – 25	1	0.07 ± 0.03	0.04 ± 0.01	8/5
	2	0.15 ± 0.02	0.01 ± 0.01	11/12
	3	0.13 ± 0.02	0.020 ± 0.006	39/21
	4	0.15 ± 0.04	0.02 ± 0.01	2/6
	mean	0.130 ± 0.010	0.019 ± 0.004	–
	all	0.120 ± 0.006	0.022 ± 0.002	83/50
25 – 40	1	0.06 ± 0.03	0.011 ± 0.01	6/5
	2	0.09 ± 0.02	-0.002 ± 0.01	26/12
	3	0.11 ± 0.02	-0.005 ± 0.006	21/21
	4	0.07 ± 0.05	0.02 ± 0.01	5/6
	mean	0.090 ± 0.010	0.019 ± 0.004	–
	all	0.075 ± 0.006	0.008 ± 0.003	73/50

Table B.3: The values of best-fit parameters obtained by fitting the *XMM-Newton* low-energy FFPs with a PLc model (eq. 4.1) for the individual time intervals and their arithmetic mean. In addition I show the best-fit results obtained by fitting the data from the 4 time intervals together.

Energy Band (keV)	Int.	$A_{\rm PLc}$	β	$C_{\rm PLc}$ (Count s^{-1})	χ^2/d.o.f.
0.3 – 0.4	1	1.39 ± 0.21	1.34 ± 0.15	1.30 ± 0.21	968/40
	2	1.97 ± 0.36	0.93 ± 0.11	0.84 ± 0.39	1634/83
	3	1.18 ± 0.06	1.44 ± 0.07	1.14 ± 0.05	1651/128
	4	1.36 ± 0.15	1.49 ± 0.27	0.79 ± 0.15	188/47
	mean	1.47 ± 0.17	1.30 ± 0.13	1.02 ± 0.12	–
	all	2.17 ± 0.04	1.01 ± 0.02	0.25 ± 0.04	6674/304
0.4 – 0.5	1	1.67 ± 0.22	1.35 ± 0.14	1.32 ± 0.22	1166/40
	2	1.860 ± 0.27	1.11 ± 0.10	1.26 ± 0.29	2151/83
	3	1.45 ± 0.05	1.49 ± 0.06	1.15 ± 0.05	2156/128
	4	1.68 ± 0.14	1.52 ± 0.22	0.71 ± 0.15	296/47
	mean	1.66 ± 0.08	1.37 ± 0.09	1.11 ± 0.14	–
	all	2.63 ± 0.05	1.01 ± 0.02	0.07 ± 0.04	8119/304
0.5 – 0.6	1	1.23 ± 0.14	1.63 ± 0.14	1.26 ± 0.14	1080/40
	2	1.90 ± 0.29	1.04 ± 0.10	0.75 ± 0.31	1906/83
	3	1.33 ± 0.05	1.52 ± 0.06	0.86 ± 0.05	2063/128
	4	1.47 ± 0.12	1.61 ± 0.23	0.54 ± 0.12	304/47
	mean	1.48 ± 0.15	1.45 ± 0.14	0.85 ± 0.15	–
	all	2.33 ± 0.04	1.04 ± 0.02	-0.07 ± 0.04	7435/304
0.6 – 0.7	1	1.12 ± 0.15	1.50 ± 0.15	0.82 ± 0.15	988/40
	2	1.21 ± 0.18	1.24 ± 0.11	0.91 ± 0.20	1524/83
	3	1.21 ± 0.05	1.40 ± 0.06	0.54 ± 0.05	1728/128
	4	1.68 ± 0.25	1.04 ± 0.22	-0.11 ± 0.26	293/47
	mean	1.31 ± 0.13	1.30 ± 0.10	0.54 ± 0.23	–
	all	1.99 ± 0.04	1.01 ± 0.02	-0.20 ± 0.04	6072/304

Energy Band (keV)	Int.	$A_{\rm PLc}$	β	$C_{\rm PLc}$ (Count $\rm s^{-1}$)	χ^2/d.o.f.
0.7 – 0.8	1	0.73 ± 0.12	1.52 ± 0.17	0.50 ± 0.11	489/40
	2	1.08 ± 0.20	1.06 ± 0.13	0.22 ± 0.22	1036/83
	3	0.76 ± 0.03	1.52 ± 0.08	0.39 ± 0.03	918/128
	4	0.96 ± 0.11	1.40 ± 0.26	0.09 ± 0.11	191/47
	mean	0.88 ± 0.08	1.37 ± 0.11	0.30 ± 0.09	–
	all	1.29 ± 0.03	1.02 ± 0.02	-0.12 ± 0.03	3435/304
0.8 – 0.9	1	0.83 ± 0.16	1.24 ± 0.19	0.23 ± 0.16	283/40
	2	0.81 ± 0.15	1.16 ± 0.13	0.27 ± 0.17	608/83
	3	0.67 ± 0.04	1.36 ± 0.08	0.31 ± 0.04	602/128
	4	0.74 ± 0.07	1.65 ± 0.29	0.16 ± 0.08	175/47
	mean	0.76 ± 0.04	1.35 ± 0.11	0.24 ± 0.03	–
	all	1.05 ± 0.03	1.04 ± 0.02	-0.07 ± 0.03	2415/304
0.9 – 1	1	0.83 ± 0.17	1.17 ± 0.19	0.16 ± 0.17	211/40
	2	0.84 ± 0.15	1.12 ± 0.13	0.12 ± 0.17	452/83
	3	0.65 ± 0.04	1.34 ± 0.08	0.26 ± 0.03	610/128
	4	0.74 ± 0.08	1.57 ± 0.29	0.10 ± 0.08	198/47
	mean	0.77 ± 0.04	1.30 ± 0.10	0.16 ± 0.03	–
	all	1.00 ± 0.03	1.05 ± 0.02	-0.08 ± 0.02	2127/304
1 – 1.3	1	2.35 ± 0.31	1.11 ± 0.12	0.19 ± 0.30	409/40
	2	2.08 ± 0.21	1.20 ± 0.08	0.40 ± 0.24	946/83
	3	1.94 ± 0.07	1.23 ± 0.05	0.48 ± 0.06	1018/128
	4	2.31 ± 0.16	1.38 ± 0.16	-0.02 ± 0.17	412/47
	mean	2.17 ± 0.10	1.23 ± 0.06	0.26 ± 0.11	–
	all	2.68 ± 0.04	1.04 ± 0.01	-0.27 ± 0.04	4015/304
1.3 – 1.6	1	1.70 ± 0.25	1.17 ± 0.13	0.30 ± 0.24	296/40
	2	2.06 ± 0.26	1.03 ± 0.09	-0.10 ± 0.29	543/83
	3	1.51 ± 0.05	1.33 ± 0.05	0.41 ± 0.05	797/128
	4	2.40 ± 0.36	0.90 ± 0.19	-0.57 ± 0.37	304/47
	mean	1.92 ± 0.20	1.11 ± 0.09	0.01 ± 0.22	–
	all	2.11 ± 0.04	1.03 ± 0.02	-0.19 ± 0.04	2447/304

Energy Band (keV)	Int.	$A_{\rm PLc}$	β	$C_{\rm PLc}$ (Count s^{-1})	χ^2/d.o.f.
1.6 – 2	1	1.72 ± 0.27	1.09 ± 0.14	0.11 ± 0.27	189/40
	2	1.93 ± 0.26	1.03 ± 0.09	-0.11 ± 0.28	393/83
	3	1.60 ± 0.06	1.21 ± 0.05	0.22 ± 0.06	549/128
	4	3.32 ± 0.95	0.55 ± 0.19	-1.58 ± 0.95	255/47
	mean	2.14 ± 0.40	0.97 ± 0.14	-0.34 ± 0.42	–
	all	2.04 ± 0.04	0.99 ± 0.02	-0.23 ± 0.04	1631/304
2 – 3	1	1.97 ± 0.31	1.03 ± 0.13	-0.02 ± 0.31	149/40
	2	1.27 ± 0.15	1.33 ± 0.09	0.75 ± 0.17	384/83
	3	1.74 ± 0.06	1.16 ± 0.05	0.18 ± 0.06	420/128
	4	2.51 ± 0.95	0.55 ± 0.19	-1.58 ± 0.95	255/47
	mean	1.88 ± 0.26	1.08 ± 0.11	0.08 ± 0.28	–
	all	2.08 ± 0.04	0.99 ± 0.02	-0.15 ± 0.04	1170/304

Bibliography

Abbott, B. P., Abbott, R., Abbott, T. D., et al. 2016a, Phys. Rev. Lett., 116, 061102

Abbott, B. P., Abbott, R., Abbott, T. D., et al. 2016b, Phys. Rev. Lett., 116, 241103

Agol, E. & Krolik, J. H. 2000, ApJ, 528, 161

Akaike, H. 1974, IEEE Transactions on Automatic Control, 19, 716

Angel, J. R. P. 1969, ApJ, 158, 219

Antonucci, R. 1993, ARA&A, 31, 473

Antonucci, R. R. J. & Miller, J. S. 1985, ApJ, 297, 621

Arnaud, K. A. 1996, in Astronomical Society of the Pacific Conference Series, Vol. 101, Astronomical Data Analysis Software and Systems V, ed. G. H. Jacoby & J. Barnes, 17

Bañados, E., Venemans, B. P., Mazzucchelli, C., et al. 2018, Nature, 553, 473

Baker, J. C., Hunstead, R. W., Athreya, R. M., et al. 2002, ApJ, 568, 592

Baldwin, J. A. 1977, ApJ, 214, 679

Ballantyne, D. R., Bollenbacher, J. M., Brenneman, L. W., et al. 2014, ApJ, 794, 62

Baloković, M., Matt, G., Harrison, F. A., et al. 2015, ApJ, 800, 62

Bardeen, J. M., Press, W. H., & Teukolsky, S. A. 1972, ApJ, 178, 347

Barlow, T. A. & Sargent, W. L. W. 1997, AJ, 113, 136

Barvainis, R. 1987, in BAAS, Vol. 19, Bulletin of the American Astronomical Society, 718

Begelman, M. C. & Sikora, M. 1987, ApJ, 322, 650

Bentz, M. C., Cackett, E. M., Crenshaw, D. M., et al. 2016, ApJ, 830, 136

Bianchi, S., Corral, A., Panessa, F., et al. 2008, MNRAS, 385, 195

Bianchi, S., Guainazzi, M., Matt, G., Fonseca Bonilla, N., & Ponti, G. 2009, A&A, 495, 421

Bisogni, S., Marconi, A., & Risaliti, G. 2017, MNRAS, 464, 385

Blackburn, J. K. 1995, in Astronomical Society of the Pacific Conference Series, Vol. 77, Astronomical Data Analysis Software and Systems IV, ed. R. A. Shaw, H. E. Payne, & J. J. E. Hayes, 367

Blandford, R. D. & Rees, M. J. 1978, Phys. Scr, 17, 265

Blandford, R. D. & Znajek, R. L. 1977, MNRAS, 179, 433

Blanton, M. R., Bershady, M. A., Abolfathi, B., et al. 2017, AJ, 154, 28

Boller, T., Fabian, A. C., Brandt, W. N., & Freyberg, M. J. 2000, MNRAS, 315, L23

Bonson, K. & Gallo, L. C. 2016, MNRAS, 458, 1927

Böttcher, M., Dermer, C. D., & Finke, J. D. 2008, ApJ, 679, L9

Braito, V., Reeves, J. N., Gofford, J., et al. 2014, ApJ, 795, 87

Branduardi-Raymont, G., Sako, M., Kahn, S. M., et al. 2001, A&A, 365, L140

Brenneman, L. W., Madejski, G., Fuerst, F., et al. 2014, ApJ, 788, 61

Brenneman, L. W. & Reynolds, C. S. 2006, ApJ, 652, 1028

Brenneman, L. W., Reynolds, C. S., Nowak, M. A., et al. 2011, ApJ, 736, 103

Capellupo, D. M., Netzer, H., Lira, P., Trakhtenbrot, B., & Mejía-Restrepo, J. 2015, MNRAS, 446, 3427

Capellupo, D. M., Netzer, H., Lira, P., Trakhtenbrot, B., & Mejía-Restrepo, J. 2016, MNRAS, 460, 212

Celotti, A. & Fabian, A. C. 2004, Monthly Notices of the Royal Astronomical Society, 353, 523

Celotti, A. & Ghisellini, G. 2008, MNRAS, 385, 283

Celotti, A., Ghisellini, G., & Fabian, A. C. 2007, MNRAS, 375, 417

Chandrasekhar, S. 1960, Radiative transfer (New York: Dover, 1960)

Chartas, G., Kochanek, C. S., Dai, X., Poindexter, S., & Garmire, G. 2009, ApJ, 693, 174

Choudhury, K., García, J. A., Steiner, J. F., & Bambi, C. 2017, ApJ, 851, 57

Churazov, E., Gilfanov, M., & Revnivtsev, M. 2001, MNRAS, 321, 759

Collinson, J. S., Ward, M. J., Landt, H., et al. 2017, MNRAS, 465, 358

Crummy, J., Fabian, A. C., Gallo, L., & Ross, R. R. 2006, MNRAS, 365, 1067

Czerny, B. & Elvis, M. 1987, ApJ, 321, 305

Dauser, T., García, J., Walton, D. J., et al. 2016, A&A, 590, A76

Dauser, T., Garcia, J., Wilms, J., et al. 2013, MNRAS, 430, 1694

Dauser, T., Wilms, J., Reynolds, C. S., & Brenneman, L. W. 2010, MNRAS, 409, 1534

Dawson, K. S., Kneib, J.-P., Percival, W. J., et al. 2016, AJ, 151, 44

De Marco, B., Ponti, G., Cappi, M., et al. 2013, MNRAS, 431, 2441

de Rosa, A., Bassani, L., Ubertini, P., Malizia, A., & Dean, A. J. 2008, MNRAS, 388, L54

Dermer, C. D., Schlickeiser, R., & Mastichiadis, A. 1992, A&A, 256, L27

Done, C., Davis, S. W., Jin, C., Blaes, O., & Ward, M. 2012, MNRAS, 420, 1848

Done, C., Jin, C., Middleton, M., & Ward, M. 2013, MNRAS, 434, 1955

Dovciak, M., Svoboda, J., Goosmann, R. W., et al. 2014, ArXiv e-prints [arXiv:1412.8627]

Dovčiak, M. & Done, C. 2016, Astronomische Nachrichten, 337, 441

Dovčiak, M., Karas, V., & Yaqoob, T. 2004, ApJS, 153, 205

Dovčiak, M., Muleri, F., Goosmann, R. W., Karas, V., & Matt, G. 2008, MNRAS, 391, 32

Dovčiak, M., Muleri, F., Goosmann, R. W., Karas, V., & Matt, G. 2011, ApJ, 731, 75

Dumont, A.-M., Abrassart, A., & Collin, S. 2000, A&A, 357, 823

Eitan, A. & Behar, E. 2013, ApJ, 774, 29

Elvis, M., Wilkes, B. J., McDowell, J. C., et al. 1994, ApJS, 95, 1

Emmanoulopoulos, D., McHardy, I. M., & Papadakis, I. E. 2011a, MNRAS, 416, L94

Emmanoulopoulos, D., McHardy, I. M., & Papadakis, I. E. 2011b, MNRAS, 416, L94

Emmanoulopoulos, D., Papadakis, I. E., Dovčiak, M., & McHardy, I. M. 2014, MNRAS, 439, 3931

Epitropakis, A., Papadakis, I. E., Dovčiak, M., et al. 2016, A&A, 594, A71

Esin, A., McClintock, J., & Narayan, R. 1997, ApJ, 489, 865

Fabian, A. C. 2012, ARA&A, 50, 455

Fabian, A. C., Celotti, A., Iwasawa, K., & Ghisellini, G. 2001, MNRAS, 324, 628

Fabian, A. C., Iwasawa, K., McMahon, R. G., et al. 1998, MNRAS, 295, L25

Fabian, A. C., Iwasawa, K., Reynolds, C. S., & Young, A. J. 2000a, PASP, 112, 1145

Fabian, A. C., Iwasawa, K., Reynolds, C. S., & Young, A. J. 2000b, PASP, 112, 1145

Fabian, A. C., Lohfink, A., Kara, E., et al. 2015, MNRAS, 451, 4375

Fabian, A. C., Parker, M. L., Wilkins, D. R., et al. 2014, MNRAS, 439, 2307

Fabian, A. C., Rees, M. J., Stella, L., & White, N. E. 1989, MNRAS, 238, 729

Fabian, A. C. & Vaughan, S. 2003, MNRAS, 340, L28

Fabian, A. C., Vaughan, S., Nandra, K., et al. 2002, MNRAS, 335, L1

Fabian, A. C., Zoghbi, A., Ross, R. R., et al. 2009, Nature, 459, 540

Fath, E. A. 1909, Popular Astronomy, 17, 504

Galeev, A. A., Rosner, R., & Vaiana, G. S. 1979, ApJ, 229, 318

Gallo, L. C., Wilkins, D. R., Bonson, K., et al. 2015, MNRAS, 446, 633

Gammie, C. F., Shapiro, S. L., & McKinney, J. C. 2004, ApJ, 602, 312

García, J., Dauser, T., Lohfink, A., et al. 2014, ApJ, 782, 76

García, J., Dauser, T., Reynolds, C. S., et al. 2013, ApJ, 768, 146

García, J. A., Fabian, A. C., Kallman, T. R., et al. 2016, MNRAS, 462, 751

George, I. M. & Fabian, A. C. 1991, MNRAS, 249, 352

George, I. M., Fabian, A. C., Nandra, K., Pounds, K. A., & Stewart, G. C. 1989, in ESA Special Publication, Vol. 296, Two Topics in X-Ray Astronomy, Volume 1: X Ray Binaries. Volume 2: AGN and the X Ray Background, ed. J. Hunt & B. Battrick

Ghisellini, G., ed. 2013, Lecture Notes in Physics, Berlin Springer Verlag, Vol. 873, Radiative Processes in High Energy Astrophysics

Ghisellini, G., Foschini, L., Tavecchio, F., & Pian, E. 2007, MNRAS, 382, L82

Ghisellini, G., Haardt, F., & Matt, G. 1994a, MNRAS, 267, 743

Ghisellini, G., Haardt, F., & Matt, G. 1994b, MNRAS, 267, 743

Ghisellini, G., Haardt, F., & Matt, G. 2004, A&A, 413, 535

Ghisellini, G., Maraschi, L., & Treves, A. 1985, A&A, 146, 204

Ghisellini, G. & Tavecchio, F. 2008, MNRAS, 387, 1669

Ghisellini, G. & Tavecchio, F. 2010, MNRAS, 409, L79

Ghisellini, G., Tavecchio, F., Foschini, L., & Ghirlanda, G. 2011, MNRAS, 414, 2674

Gierliński, M. & Done, C. 2004, MNRAS, 349, L7

Gierliński, M., Middleton, M., Ward, M., & Done, C. 2008, Nature, 455, 369

Gonzalez, A. G., Wilkins, D. R., & Gallo, L. C. 2017, MNRAS, 472, 1932

Goodman, J. & Weare, J. 2010, Comm. App. Math. Comp. Sci., 5, 65

Goodrich, R. W. 1989, ApJ, 342, 224

Goosmann, R. W. & Gaskell, C. M. 2007, A&A, 465, 129

Grevesse, N. & Sauval, A. J. 1998, Space Sci. Rev., 85, 161

Guainazzi, M., Bianchi, S., & Dovčiak, M. 2006, Astronomische Nachrichten, 327, 1032

Haardt, F. & Maraschi, L. 1991, ApJ, 380, L51

Haardt, F. & Maraschi, L. 1993, ApJ, 413, 507

Haardt, F., Maraschi, L., & Ghisellini, G. 1994, ApJ, 432, L95

Haardt, F. & Matt, G. 1993, MNRAS, 261, 346

Harrison, C. 2014, PhD thesis, Durham University

Harrison, F. A., Craig, W. W., Christensen, F. E., et al. 2013, ApJ, 770, 103

Heckman, T. M. 1980, A&A, 87, 152

Ho, L. C., Filippenko, A. V., & Sargent, W. L. W. 1997, ApJ, 487, 568

Ho, L. C. & Peng, C. Y. 2001, ApJ, 555, 650

Hubble, E. P. 1926, ApJ, 64

Hunt, L. K., Zhekov, S., Salvati, M., Mannucci, F., & Stanga, R. M. 1994, A&A, 292, 67

Iwasawa, K., Fabian, A. C., Reynolds, C. S., et al. 1996, MNRAS, 282, 1038

Iwasawa, K., Fabian, A. C., Young, A. J., Inoue, H., & Matsumoto, C. 1999, MNRAS, 306, L19

Iwasawa, K., Miniutti, G., & Fabian, A. C. 2004, MNRAS, 355, 1073

Iwasawa, K. & Taniguchi, Y. 1993, ApJ, 413, L15

Jansen, F., Lumb, D., Altieri, B., et al. 2001, A&A, 365, L1

Jiang, J., Parker, M. L., Fabian, A. C., et al. 2018, MNRAS, 477, 3711

Jones, T. W., O'dell, S. L., & Stein, W. A. 1974, ApJ, 188, 353

Jun, H. D., Im, M., Lee, H. M., et al. 2015, ApJ, 806, 109

Kalberla, P. M. W., Burton, W. B., Hartmann, D., et al. 2005, A&A, 440, 775

Kallman, T. & Bautista, M. 2001, ApJS, 133, 221

Kammoun, E. S., Nardini, E., & Risaliti, G. 2018, A&A, 614, A44

Kammoun, E. S., Papadakis, I. E., & Sabra, B. M. 2015, A&A, 582, A40

Kara, E., Alston, W. N., Fabian, A. C., et al. 2016, MNRAS, 462, 511

Kara, E., Fabian, A. C., Marinucci, A., et al. 2014, MNRAS, 445, 56

Kara, E., García, J. A., Lohfink, A., et al. 2017, MNRAS, 468, 3489

Karhunen, K., Kotilainen, J. K., Falomo, R., & Bettoni, D. 2014, MNRAS, 441, 1802

Kataoka, J., Madejski, G., Sikora, M., et al. 2008, ApJ, 672, 787

Kelly, B. C. & Bechtold, J. 2007, ApJS, 168, 1

King, A. L., Lohfink, A., & Kara, E. 2017, ApJ, 835, 226

King, A. R., Pringle, J. E., & Hofmann, J. A. 2008, MNRAS, 385, 1621

Laor, A. 1991, ApJ, 376, 90

Lee, J. C., Iwasawa, K., Houck, J. C., et al. 2002, ApJ, 570, L47

Lightman, A. P. & White, T. R. 1988, ApJ, 335, 57

Loaring, N. S., Page, M. J., & Ramsay, G. 2003, MNRAS, 345, 865

Lubiński, P., Beckmann, V., Gibaud, L., et al. 2016a, MNRAS, 458, 2454

Lubiński, P., Beckmann, V., Gibaud, L., et al. 2016b, MNRAS, 458, 2454

Lusso, E. & Risaliti, G. 2016, ApJ, 819, 154

Lynden-Bell, D. 1969, Nature, 223, 690

Madsen, K. K., Harrison, F. A., Markwardt, C. B., et al. 2015, ApJS, 220, 8

Madsen, K. K., Harrison, F. A., Markwardt, C. B., et al. 2015, The Astrophysical Journal Supplement Series, 220, 8

Magdziarz, P., Blaes, O. M., Zdziarski, A. A., Johnson, W. N., & Smith, D. A. 1998, MNRAS, 301, 179

Maiolino, R., Risaliti, G., Salvati, M., et al. 2010, A&A, 517, A47

Mantovani, G., Nandra, K., & Ponti, G. 2016, MNRAS, 458, 4198

Maraschi, L. & Tavecchio, F. 2003, ApJ, 593, 667

Marconi, A., Risaliti, G., Gilli, R., et al. 2004, MNRAS, 351, 169

Marin, F. 2016, MNRAS, 460, 3679

Marin, F. & Dovčiak, M. 2015, A&A, 573, A60

Marin, F., Dovčiak, M., & Kammoun, E. S. 2018a, MNRAS, 478, 950

Marin, F., Dovčiak, M., Muleri, F., Kislat, F. F., & Krawczynski, H. S. 2018b, MNRAS, 473, 1286

Marin, F., Goosmann, R. W., Dovčiak, M., et al. 2012a, MNRAS, 426, L101

Marin, F., Goosmann, R. W., & Gaskell, C. M. 2015, A&A, 577, A66

Marin, F., Goosmann, R. W., Gaskell, C. M., Porquet, D., & Dovčiak, M. 2012b, A&A, 548, A121

Marinucci, A., Matt, G., Kara, E., et al. 2014a, MNRAS, 440, 2347

Marinucci, A., Matt, G., Miniutti, G., et al. 2014b, ApJ, 787, 83

Marinucci, A., Tortosa, A., & NuSTAR AGN Physics Working Group. 2016, Astronomische Nachrichten, 337, 490

Markowitz, A. & Edelson, R. 2001, ApJ, 547, 684

Markowitz, A. G., Krumpe, M., & Nikutta, R. 2014, MNRAS, 439, 1403

Markwardt, C. B. 2009, in Astronomical Society of the Pacific Conference Series, Vol. 411, Astronomical Data Analysis Software and Systems XVIII, ed. D. A. Bohlender, D. Durand, & P. Dowler, 251

Martocchia, A., Karas, V., & Matt, G. 2000, MNRAS, 312, 817

Martocchia, A. & Matt, G. 1996, MNRAS, 282, L53

Martocchia, A., Matt, G., & Karas, V. 2002, A&A, 383, L23

Matsuoka, M., Piro, L., Yamauchi, M., & Murakami, T. 1990, ApJ, 361, 440

Matt, G. 1993, MNRAS, 260, 663

Matt, G., Baloković, M., Marinucci, A., et al. 2015, MNRAS, 447, 3029

Matt, G., Guainazzi, M., & Maiolino, R. 2003, MNRAS, 342, 422

Matt, G., Perola, G. C., & Piro, L. 1991, A&A, 247, 25

McHardy, I. M. 1989, in ESA Special Publication, Vol. 296, Two Topics in X-Ray Astronomy, Volume 1: X Ray Binaries. Volume 2: AGN and the X Ray Background, ed. J. Hunt & B. Battrick

McKernan, B. & Yaqoob, T. 1998, ApJ, 501, L29

McKinney, J. C. & Gammie, C. F. 2004, ApJ, 611, 977

Miller, J. M. 2007, ARA&A, 45, 441

Miller, L., Turner, T. J., & Reeves, J. N. 2008, A&A, 483, 437

Miller, L., Turner, T. J., & Reeves, J. N. 2009, MNRAS, 399, L69

Miller, L., Turner, T. J., Reeves, J. N., et al. 2007, A&A, 463, 131

Miniutti, G. & Fabian, A. C. 2004, MNRAS, 349, 1435

Miniutti, G., Fabian, A. C., Anabuki, N., et al. 2007, PASJ, 59, 315

Mohan, P. & Mangalam, A. 2014, ApJ, 791, 74

Mosquera, A. M., Kochanek, C. S., Chen, B., et al. 2013, ApJ, 769, 53

Murphy, K. D. & Yaqoob, T. 2009, MNRAS, 397, 1549

Murphy, K. D. & Yaqoob, T. 2011, MNRAS, 415, 3962

Nandra, K., Barret, D., Barcons, X., et al. 2013, ArXiv e-prints [arXiv:1306.2307]

Nandra, K., George, I. M., Mushotzky, R. F., Turner, T. J., & Yaqoob, T. 1997, ApJ, 477, 602

Nandra, K., O'Neill, P. M., George, I. M., & Reeves, J. N. 2007, MNRAS, 382, 194

Narayan, R. & Yi, I. 1994, ApJ, 428, L13

Nardini, E., Gofford, J., Reeves, J. N., et al. 2015, MNRAS, 453, 2558

Nardini, E. & Risaliti, G. 2011, MNRAS, 417, 2571

Nayakshin, S. & Melia, F. 1997, ApJ, 490, L13

Netzer, H. 2015, ARA&A, 53, 365

Niedźwiecki, A. & Miyakawa, T. 2010, A&A, 509, A22

Noda, H., Makishima, K., Nakazawa, K., et al. 2013, PASJ, 65, 4

Noda, H., Makishima, K., Uehara, Y., Yamada, S., & Nakazawa, K. 2011, PASJ, 63, 449

Novikov, I. D. & Thorne, K. S. 1973, in Black Holes (Les Astres Occlus), ed. C. Dewitt & B. S. Dewitt, 343–450

Osterbrock, D. E. & Pogge, R. W. 1985, ApJ, 297, 166

Otani, C., Kii, T., Reynolds, C. S., et al. 1996, PASJ, 48, 211

Padovani, P. 1989, A&A, 209, 27

Padovani, P. 2011, MNRAS, 411, 1547

Padovani, P. 2017, Nature Astronomy, 1, 0194

Paliya, V. S., Parker, M. L., Fabian, A. C., & Stalin, C. S. 2016, ApJ, 825, 74

Panessa, F., Bassani, L., Cappi, M., et al. 2006, A&A, 455, 173

Parker, M. L., Fabian, A. C., Matt, G., et al. 2015, MNRAS, 447, 72

Parker, M. L., Marinucci, A., Brenneman, L., et al. 2014, MNRAS, 437, 721

Parker, M. L., Miller, J. M., & Fabian, A. C. 2017, ArXiv e-prints [arXiv:1710.11166]

Patrick, A. R., Reeves, J. N., Lobban, A. P., Porquet, D., & Markowitz, A. G. 2011, MNRAS, 416, 2725

Peterson, B. 1997, The Observatory, 117, 314

Petrucci, P. O., Haardt, F., Maraschi, L., et al. 2001a, ApJ, 556, 716

Petrucci, P. O., Merloni, A., Fabian, A., Haardt, F., & Gallo, E. 2001b, MNRAS, 328, 501

Petrucci, P.-O., Paltani, S., Malzac, J., et al. 2013, A&A, 549, A73

Petrucci, P.-O., Ursini, F., De Rosa, A., et al. 2018, A&A, 611, A59

Piconcelli, E. & Guainazzi, M. 2005, A&A, 442, L53

Piconcelli, E., Jimenez-Bailón, E., Guainazzi, M., et al. 2005, A&A, 432, 15

Pounds, K. A., Nandra, K., Stewart, G. C., George, I. M., & Fabian, A. C. 1990, Nature, 344, 132

Rau, A., Meidinger, N., Nandra, K., et al. 2013, ArXiv e-prints [arXiv:1308.6785]

Reboul, H., Vanderriest, C., Fringant, A. M., & Cayrel, R. 1987, A&A, 177, 337

Reeves, J., Done, C., Pounds, K., et al. 2008, MNRAS, 385, L108

Reis, R. C. & Miller, J. M. 2013, ApJ, 769, L7

Reynolds, C. S. 2014, Space Sci. Rev., 183, 277

Reynolds, C. S., Brenneman, L. W., Lohfink, A. M., et al. 2012, ApJ, 755, 88

Reynolds, C. S. & Nowak, M. A. 2003, Phys. Rep., 377, 389

Reynolds, C. S., Ward, M. J., Fabian, A. C., & Celotti, A. 1997, MNRAS, 291, 403

Richards, G. T. 2001, ApJS, 133, 53

Richards, G. T., York, D. G., Yanny, B., et al. 1999, ApJ, 513, 576

Risaliti, G. 2016, Astronomische Nachrichten, 337, 529

Risaliti, G., Elvis, M., Fabbiano, G., et al. 2007, ApJ, 659, L111

Risaliti, G., Harrison, F. A., Madsen, K. K., et al. 2013, Nature, 494, 449

Risaliti, G., Nardini, E., Elvis, M., Brenneman, L., & Salvati, M. 2011a, MNRAS, 417, 178

Risaliti, G., Nardini, E., Salvati, M., et al. 2011b, MNRAS, 410, 1027

Risaliti, G., Salvati, M., Elvis, M., et al. 2009, MNRAS, 393, L1

Risaliti, G., Salvati, M., & Marconi, A. 2011c, MNRAS, 411, 2223

Rojas Lobos, P. A., Goosmann, R. W., Marin, F., & Savić, D. 2018, A&A, 611, A39

Ross, R. R. & Fabian, A. C. 2005, MNRAS, 358, 211

Salpeter, E. E. 1964, ApJ, 140, 796

Sambruna, R. M., Eracleous, M., & Mushotzky, R. F. 1999, ApJ, 526, 60

Sambruna, R. M., Gliozzi, M., Tavecchio, F., Maraschi, L., & Foschini, L. 2006, ApJ, 652, 146

Sanders, D. B., Phinney, E. S., Neugebauer, G., Soifer, B. T., & Matthews, K. 1989, ApJ, 347, 29

Sanfrutos, M., Miniutti, G., Agís-González, B., et al. 2013, MNRAS, 436, 1588

Sanfrutos, M., Miniutti, G., Dovčiak, M., & Agís-González, B. 2016, Astronomische Nachrichten, 337, 546

Schmidt, M. 1963, Nature, 197, 1040

Schmidt, M. & Olsen, E. T. 1968, The Astronomical Journal Supplement, 73, 117

Schnittman, J. D. & Krolik, J. H. 2009, ApJ, 701, 1175

Schnittman, J. D. & Krolik, J. H. 2010, ApJ, 712, 908

Seyfert, C. K. 1943, ApJ, 97, 28

Shakura, N. I. & Sunyaev, R. A. 1973, A&A, 24, 337

Shapiro, S. L., Lightman, A. P., & Eardley, D. M. 1976, ApJ, 204, 187

Shen, Y., Richards, G. T., Strauss, M. A., et al. 2011, ApJS, 194, 45

Shih, D. C., Iwasawa, K., & Fabian, A. C. 2002, MNRAS, 333, 687

Sikora, M., Begelman, M. C., & Rees, M. J. 1994, ApJ, 421, 153

Sikora, M., Błażejowski, M., Moderski, R., & Madejski, G. M. 2002, ApJ, 577, 78

Singh, K. P., Garmire, G. P., & Nousek, J. 1985, ApJ, 297, 633

Skrutskie, M. F., Cutri, R. M., Stiening, R., et al. 2006, AJ, 131, 1163

Slipher, V. M. 1917, Lowell Observatory Bulletin, 3, 59

Smith, R. K., Abraham, M. H., Allured, R., et al. 2016, in Proc. SPIE, Vol. 9905, Space Telescopes and Instrumentation 2016: Ultraviolet to Gamma Ray, 99054M

Sobolewska, M. A. & Papadakis, I. E. 2009, MNRAS, 399, 1597

Steiner, J. F., García, J. A., Eikmann, W., et al. 2017, ApJ, 836, 119

Stickel, M., Padovani, P., Urry, C. M., Fried, J. W., & Kuehr, H. 1991, ApJ, 374, 431

Strüder, L., Briel, U., Dennerl, K., et al. 2001, A&A, 365, L18

Suganuma, M., Yoshii, Y., Kobayashi, Y., et al. 2006, ApJ, 639, 46

Svoboda, J., Dovčiak, M., Goosmann, R., et al. 2012, A&A, 545, A106

Tanaka, Y., Nandra, K., Fabian, A. C., et al. 1995, Nature, 375, 659

Tatum, M. M., Turner, T. J., Miller, L., & Reeves, J. N. 2013, ApJ, 762, 80

Tavecchio, F. & Ghisellini, G. 2008, MNRAS, 386, 945

Taylor, R. D., Uttley, P., & McHardy, I. M. 2003, MNRAS, 342, L31

Thorne, K. S. 1974, ApJ, 191, 507

Titarchuk, L. 1994, ApJ, 434, 570

Torricelli-Ciamponi, G., Pietrini, P., Risaliti, G., & Salvati, M. 2014, MNRAS, 442, 2116

Turner, A. K., Fabian, A. C., Lee, J. C., & Vaughan, S. 2004, MNRAS, 353, 319

Turner, A. K., Fabian, A. C., Vaughan, S., & Lee, J. C. 2003, MNRAS, 346, 833

Turner, M. J. L., Abbey, A., Arnaud, M., et al. 2001, A&A, 365, L27

Turner, T. J., Miller, L., Reeves, J. N., & Kraemer, S. B. 2007, A&A, 475, 121

Urry, C. M. & Padovani, P. 1995, PASP, 107, 803

Vasudevan, R. V. & Fabian, A. C. 2007, MNRAS, 381, 1235

Vasudevan, R. V., Fabian, A. C., Reynolds, C. S., et al. 2016, MNRAS, 458, 2012

Vaughan, S. & Uttley, P. 2005, MNRAS, 362, 235

Vaughan, S. & Uttley, P. 2006, Advances in Space Research, 38, 1405

Vazquez, B., Galianni, P., Richmond, M., et al. 2015, ApJ, 801, 127

Véron-Cetty, M.-P. & Véron, P. 2003, A&A, 412, 399

Volonteri, M., Sikora, M., Lasota, J.-P., & Merloni, A. 2013, ApJ, 775, 94

Walter, R. & Fink, H. H. 1993, A&A, 274, 105

Walton, D. J., Nardini, E., Fabian, A. C., Gallo, L. C., & Reis, R. C. 2013, MNRAS, 428, 2901

Walton, D. J., Risaliti, G., Harrison, F. A., et al. 2014, ApJ, 788, 76

Wilkes, B. J., Elvis, M., Fiore, F., et al. 1992, ApJ, 393, L1

Wilkins, D. R. & Fabian, A. C. 2012, Monthly Notices of the Royal Astronomical Society, 424, 1284

Wilkins, D. R. & Gallo, L. C. 2015, MNRAS, 449, 129

Williams, M. J., Bureau, M., & Cappellari, M. 2010, MNRAS, 409, 1330

Wilms, J., Allen, A., & McCray, R. 2000a, ApJ, 542, 914

Wilms, J., Allen, A., & McCray, R. 2000b, ApJ, 542, 914

Winkler, C., Courvoisier, T. J.-L., Di Cocco, G., et al. 2003, A&A, 411, L1

Worsley, M. A., Fabian, A. C., Pooley, G. G., & Chandler, C. J. 2006, MNRAS, 368, 844

Wright, E. L., Eisenhardt, P. R. M., Mainzer, A. K., et al. 2010, AJ, 140, 1868

Yaqoob, T. 2012, MNRAS, 423, 3360

Zel'dovich, Y. B. 1964, Soviet Physics Doklady, 9, 195

Zhang, S. N., Feroci, M., Santangelo, A., et al. 2016, in Proc. SPIE, Vol. 9905, Space Telescopes and Instrumentation 2016: Ultraviolet to Gamma Ray, 99051Q